Multiscale Mechanics of Shape Memory Alloy Knitted Architectures

A DISSERTATION
SUBMITTED TO THE FACULTY OF THE GRADUATE SCHOOL
OF THE UNIVERSITY OF MINNESOTA
BY

Kevin Paul Eschen

IN PARTIAL FULFILLMENT OF THE REQUIREMENTS
FOR THE DEGREE OF
DOCTOR OF PHILOSOPHY

Julianna Abel

August, 2020

Acknowledgements

I would like to thank my advisor, Dr. Julianna Abel, for her support throughout the past five years of graduate work. She trusted me to be her first graduate student, guided and directed my studies, and always showed great care for her students. I am also grateful for my committee members, Dr. Susan Mantell, Dr. Brad Holschuh, Dr. Richard James, and Dr. Arthur Erdman for their feedback and support.

My labmates have also greatly contributed to the success of my studies. Firstly, I would like to thank Rachael Granberry for being a great collaborator, researcher, and friend. Specifically, the close collaboration with Rachael led to shared first authorship of the publications included as Chapters 6 and 7. I would also like to show gratitude to Charles Weinberg, Henry Koon, Makella Daley, Atharva Mahabaleshwarkar, Evan Harris, Tim Anderson, and Sean Dalton, who made every day in the lab more enjoyable. Dr. Javier Garcia-Barriocanal has not only been a great teacher at the Characterization Facility, but has been a great joy to work and chat with.

Most importantly, I want to thank my family, especially Julie, Paul, Frank, Sabine and Joanna who have greatly supported me throughout this time.

Finally, I would like to acknowledge the kind financial support from MnDRIVE Robotics, Sensors, and Advanced Manufacturing (RSAM) and thank the University of Minnesota Informatics Institute (UMII) for the award of the UMII-MnDRIVE Informatics Graduate Assistantship.

Dedication

To Julie, Paul, and future children.

Abstract

Fully-integrated, wearable garments with intrinsic active properties and a small form factor are bound to replace wearable designs with attached actuators and sensors in the next years. One of the promising intrinsically-active garment implementations is the shape memory alloy (SMA) knitted architecture. SMA knitted architectures provide spatially-distributed, three-dimensional actuation deformations and forces upon thermal stimuli. This thesis provides the fundamental understanding of the contractile shape memory alloy knitted architecture mechanics, which enables the predictable design of these novel intrinsically-active garments. SMA knitted architectures are manufactured from a single shape memory filament which is assembled into a network of interlacing loops. The connection of nonlinear geometry and material governs the SMA knitted architecture performance spanning from the macroscale (knit pattern) to the mesoscale (knitted loop) and microscale (SMA material).

Macroscopic experiments are conducted to identify the dependence of force-extension properties on the number of loops in the knitted architecture, operation strategies and cyclic performance. The knitted architecture actuation and relaxation temperatures were defined and their variation was studied through variation of loop geometries and applied loading. Geometric loop properties were correlated to the knitted architecture thermo-mechanical performance on the mesoscale and microscopic phase fraction analysis was conducted to identify highly-stressed segments of the knitted loop and derive the primary deformation modes that contribute to the SMA knitted architecture performance. An empirical and a finite beam element method (FEM) model were implemented to provide predictive capabilities of the SMA knitted architecture performance. The FEM model includes textile specific modules and enables verification of simulation results by comparison to experimental results on all scales.

The new understanding of the SMA knitted architecture mechanics was applied to design wearable garments with self-fitting and compression capabilities utilizing body heat for actuation through novel operation strategies. This research sets up the design of complex applications, optimization of SMA knitted architectures, and provides transfer knowledge that can be applied broadly in the up-and-coming intrinsically-active wearables space.

Contents

List of Tables

List of Figures

Abbreviations

CASMART	Consortium for the Advancement of Shape Memory Alloy Research and Technology
CG	cooling garment
CNT	carbon-nanotube
CPI	counts-per-inch
CSZ	Cincinnati Sub Zero
DEA	dielectric elastomer
DOF	degrees of freedom
DMS	deformed martensite state
DRMS	donned relaxing martensite state
DSC	differential scanning calorimetry
EAP	electro-active polymer
FEM	finite element method
FPAS	fitted, partially austenitic state
GADDS	General Area Detector Diffraction System
GUI	graphic user interface
ISO	International Organization for Standardization
LCG	liquid cooling garment
PDMS	pre-donned martensite state
PE	piezo-electric
RMS	relaxed martensite state
RSG	recovery stress generation
SE	superelasticity
SMA	shape memory alloy
SME	shape memory effect

TPAS	tight, partially austenitic state
TWME	two-way shape memory effect
XRD	x-ray diffraction

Symbols

Some symbols have duplicate naming due to the use in different publications. In case that the same symbol was used, parentheses indicate the relevant Chapter.

A_f	stress-free austenite finish temperature
A_l	loop enclosed area
A_s	stress-free austenite start temperature
b, c	fitting parameter
B	binormal vector
c_b	body circumference
C_a	austenite transition constant
C^E	empirical coefficient
C_m	martensite transition constant
c_g	garment circumference
c_{Ni}, c_{Ti}	Nickel/Titanium concentration
C	course height
C_p	projected course height
d	atomic spacing (Chapter 4)
d	filament diameter
d_n	needle spacing
d_{ms}	minimum separation distance
e_x	Euclidean error
E	modulus of elasticity
E	Energy (Chapter 4)
f	scattering factor
f'_x	local tensile forces

$f'_{y,z}$	local shear forces
F	force
F	structure factor (Chapter 4)
F_{app}	applied force
F_{con}	contact force
F_{eqi}	equivalent force
$F_{thermal}$	thermally-recoverable force
$\dot{F}$	force-rate
g	number of wale-wise loops
G	shear modulus
h	number of course-wise loops
i_k	knit index
I	second moment of area
I	diffracted intensity (Chapter 4)
$\dot{l}$	length-rate
k	stiffness
l_a	partially-austenitic knit length or actuated knit length
l_m	martensitic knit length
l_r	relaxed knit length
L	loop length
m	mass
m'_x	local torsional moment
m'_y	local bending moment
m'_z	local bending moment
M	moment
M_f	stress-free martensite finish temperature
M_s	stress-free martensite start temperature
n	number of cycles
N	normal vector
n_e	number of elements
n_n	number of nodes
p	multiplicity factor
p	pressure

q	force-relaxation rate
r	filament radius
R	reflection matrix
s	arc length
S_{hkl}	scaled intensity
T	temperature
T	tangent vector (Chapter 5)
T_a	actuation temperature
T_r	relaxation temperature
$\dot{T}$	temperature-rate
u'	local tensile displacement
v'	local shear displacement
V_{hkl}	volume-corrected intensity
w'	local shear displacement
w	deflection curve (Euler-Bernoulli beam)
W	wale width
W	work (Chapter 3)
z	perpendicular distance to the neutral axis (Euler-Bernoulli beam)
α	thermal expansion/contraction coefficient
γ	shear strains
$\dot{\delta}$	displacement-rate
δ_n	needle displacement
Δ	displacement
ΔF	generated force
ε	strain
ε_b	bending strain
ε_{eq}	equivalent strain
ε_L	maximum residual strain
ε_t	tensile strain
ε_{TWME}	recoverable two-way shape memory effect strain
ε_{TWMS}	residual two-way shape memory effect strain
ζ	%-actuation contraction
η	relative error

θ	loop rotation angle
2θ	detector angle (Chapter 4)
Θ	thermal modulus
κ	curvature
κ_t	rotational spring stiffness
$\lambda_{Co-k\alpha}$	Cobalt-$k\alpha$ wave length
λ	attenuation length
μ	static friction coefficient
ν	Poisson's ratio
ξ	austenite volume fraction
ξ_s	stress-induced martensite volume fraction
ξ_t	temperature-induced martensite volume fraction
ρ	density
σ	stress
σ_{eq}	equivalent stress
$\sigma_{f,cr}$	critical transformation finish stress
σ_p	plateau stress
$\sigma_{s,cr}$	critical transformation start stress
τ	torsion
Φ_x	local torsional rotation
Φ_y	local bending rotation
Φ_z	local bending rotation
χ	goniometer angle (Chapter 4)
χ	loop angle
ω	incident beam angle

Chapter 1

Introduction

Passive fabrics have protected from harsh weather conditions, granted comfort, and served as a platform to express individualism through color and patterns throughout modern humankind. Through the development of fabric manufacturing technologies, utilization of various materials, and advancements in fabric system design, passive textiles have continuously been improved to enable novel applications. [7] The design and manufacturing of passive fabrics has benefited from thorough analytical, numerical, and experimental investigation. [8, 9] However, the passive nature of fabrics has remained a constant until recently.

A new age in fabric technologies has recently begun with the introduction of the first active, multifunctional fabrics. [10, 11] Such fabrics utilize a multifunctional fiber, e.g., shape memory alloys (SMA) [6], shape memory polymers (SMP) [12], carbon-nanotubes (CNT) [13], piezoelectric fibers (PE) [14], electro-active polymers (EAP) [15], and photosensitive fibers [16] as the filament in a traditional fabric architecture and provide actuator, sensor, energy harvester, or communication capabilities. While many multifunctional fabrics have been proposed and their exciting capabilities have been showcased, the current understanding of multifunctional fabric mechanics and design trade-offs remains too limited to enable reliably-performing applications.

The goal of this research is to address the unmet need of understanding the contractile SMA knitted architecture multiscale mechanics in order to accurately predict and optimize their performance to enable novel designs and applications. In this chapter, the conducted research is further motivated and the fundamental concepts of SMA knitted architectures are introduced.

1.1 Multifunctional Fabrics Market Need

Multifunctional fabrics with smart capabilities are increasingly recognized as a technology to satisfy urgent needs within healthcare, aerospace, national security, and many other industries. [17] The recent emergence of multifunctional fabrics is caused by their ability to provide actuation, sensing, energy harvesting, perform in response to unconventional inputs (temperature, electricity, photons), and meet important user specifications such as wearability, flexibility, haptic experience, and comfort.

Their placement within rapidly expanding markets, specifically the medical wearable technologies market, which is projected to grow at compounded annual rates of 25% to a global market size of US$82 billion by 2023 renders the potential for future applications of multifunctional fabric technologies highly likely. [18, 19] Medical compression and health monitoring garments can greatly benefit from multifunctional fabric capabilities such as spatial contraction to prevent orthostatic intolerance or assist with scoliosis treatment, [20, 21] complex geometry fitting for sensor attachments, [22] integrated sensing to monitor breathing and other bodily activities [23], or smart sensing and adjustment of hospital beds to prevent pressure ulcers. [24] Similarly, the aerospace industry, which has historically been an incubator for advanced material technologies, [25, 26] has recently been granted increased national funding to accomplish lunar and Martian missions including smart wearable [20] and multifunctional textile-based [27] applications. For example, three-dimensional shape changes can improve aircraft maneuverability [28] and efficiency [29] through in-flight wing morphology and aircraft skin adjustment. Multifunctional fabrics can also provide complex motions and forces for deployable space structures such as satellite antennae [30] or solar arrays [31] while maintaining a light weight and small volume.

1.2 State of the Art

Traditional actuators operate in one-dimensional spaces providing linear displacements of point geometries. The primary conventional actuators are pneumatic, hydraulic, and electromagnetic actuators with large force and displacement capabilities. In addition to the limitation to 1D-displacements, conventional actuators are subject to a constraining trade-off between large supporting infrastructure (hydraulics) and lower energy density (pneumatic, electromagnetic). [1]

Smart material actuators enable novel actuation mechanisms and intriguing actuator performance. The most common multifunctional materials, shape memory alloys, shape memory polymers, piezoelectrics, electro-active polymers, and carbon nanotubes translate between different energy domains and excel at distinct performance metrics. For example, piezoelectric materials enable highest actuation frequencies, however, their actuation strains are small ($\varepsilon_a \approx 10^{-4}$). Shape memory alloys excel at traditional mechanical engineering performance metrics and provide a stress-strain product similar to conventional actuators while being a lightweight material. This renders SMAs as a very attractive smart material choice for architectural design considerations. The actuation frequency of SMA is relatively low due to the limitations introduced by heat transfer in these temperature-dependent materials, however, miniaturization research has proven as a potential pathway to increase the actuation frequency significantly. [32]

Shape memory alloys have been established as a viable solid-state actuator material through extensive research of their thermo-mechanical actuator properties. [33, 34] SMAs recover considerable material strains (up to 8%) against significant forces when thermally actuated. [35] The optimization of the SMA actuator performance can be accomplished by improving the material itself or by incorporating it into designed geometric arrangements that amplify certain performance metrics. The geometric design can include external mechanisms that direct and amplify the smart material performance as well as internal-leveraging imposing a beneficial stress-strain profile within the material. External mechanisms include simple ratcheting [36] or gripping [37] mechanisms, as well as more complex mechanisms such as morphing wings [38] and standardized actuator modules. [39] Pseudo-distributed two-dimensional actuation has been accomplished through structural attachment of SMA actuators to otherwise standalone traditional textiles. Such architectures have been developed to tailor the textile bending stiffness [40] and to increase the mechanical work performed by SMA springs through their parallel assembly in a textile. [41]

Internal mechanisms describe the SMA performance amplification capabilities introduced through the geometric design of shape memory alloys that create unique stress-strain states. Internal leveraging has been utilized in SMA contractile actuators in the form of SMA bundles, [42] helical springs, [43] and cables, [44] resulting in significant performance improvements with regards to the ability to recover actuation strains and performing mechanical work. [45, 46] While the structural integration of SMA wire

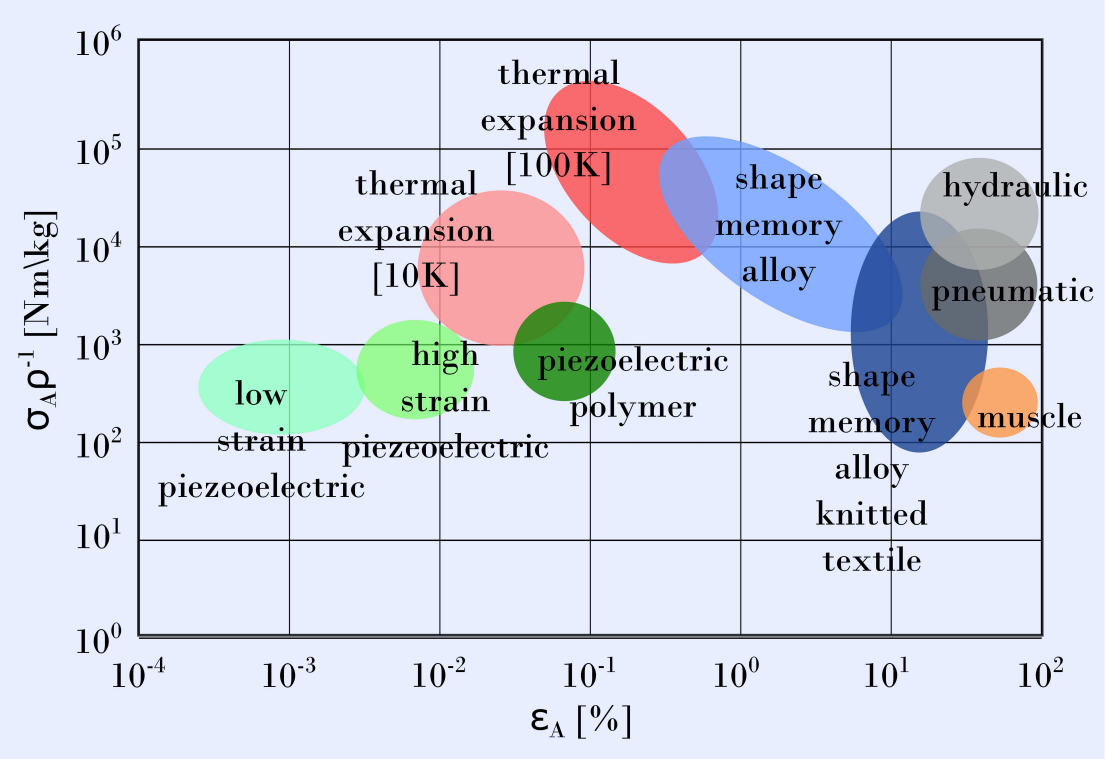

Figure 1.1: **SMA Knitted Actuator Design Space:** Shape memory alloy knitted textiles occupy a valuable actuator design space with large actuation strains and specific actuation stresses due to their lightweight properties. Comparative actuator performance values extracted from literature. [1]

within these geometry-leveraging architectures increases the actuation performance in comparison to simple monofilament SMA wire actuators, they are still restricted to point-wise actuation.

1.3 SMA Knitted Architectures

SMA knitted architectures are internally-leveraged SMA textiles which enable large, truly distributed three-dimensional deformations and can generate significant forces in response to thermo-mechanical loading. Depending on the knit pattern, SMA knitted actuators can accommodate various actuation deformation modes, e.g., contraction, rolling or corrugation. [6] The geometric architectural design enables the amplification

and direction of specific SMA material performance metrics and widens the smart material design space significantly. Figure 1.1 displays an Ashby plot representation of the actuator design space including smart actuators such as piezoelectrics, shape memory alloys and muscles, as well as classic actuators such as hydraulics and pneumatics. [1] The similarity between natural muscle and SMA knitted architectures is a major reason for the tremendous potential of SMA knitted architectures as wearable systems. Due to the combination of large actuation strains and stresses, as well as their lightweight characteristics, SMA knitted actuators capture a previously unattainable design space for smart material architectures.

1.3.1 Shape Memory Alloys

Shape memory alloys are nearly equi-atomic nickel-titanium alloys (NiTi) that have been implemented in many medical, rehabilitation and aerospace applications, mainly because of their inherent thermo-mechanical properties that enable superelasticity (SE) and the shape memory effect (SME). SMAs undergo a reversible, solid-to-solid phase transformation between a high-symmetry austenite and a low-symmetry martensite phase with varying mechanical properties as a function of the applied temperature, strains, and stresses. In the high-symmetry austenite phase, the SMA crystal is a B2 cubic lattice whereas the low-symmetry martensitic lattice is B19' monoclinic. The transition between the austenitic and martensitic lattices can be introduced through thermal (SME) and mechanical (SE) loading. The material-specific phase transition properties are among others the characteristic stress-free transition temperatures - martensite start temperature (M_s), martensite finish temperature (M_f), austenite start temperautre (A_s), and austenite finish temperature (A_f) - as well as phase transition stresses. The phase transition properties can be customized through changes in chemical composition and heat treatments such as annealing. [47]

Figure 1.2a displays the thermo-mechanical coupling of SMAs. In the thermo-mechanical loading of the shape memory effect (SME), the cold ($T \leq M_f$) martensitic SMA is mechanically strained to a maximum of 8% [35] causing the self-accommodated martensitic phase to de-twin and assume an orientation. Upon heating above the austenite start temperature, the SMA material begins to undergo the solid-to-solid phase transformation to the high-symmetry, stiffer austenite phase. Because of the symmetric incompatibility between the two phases, multiple martensitic variants can form in the

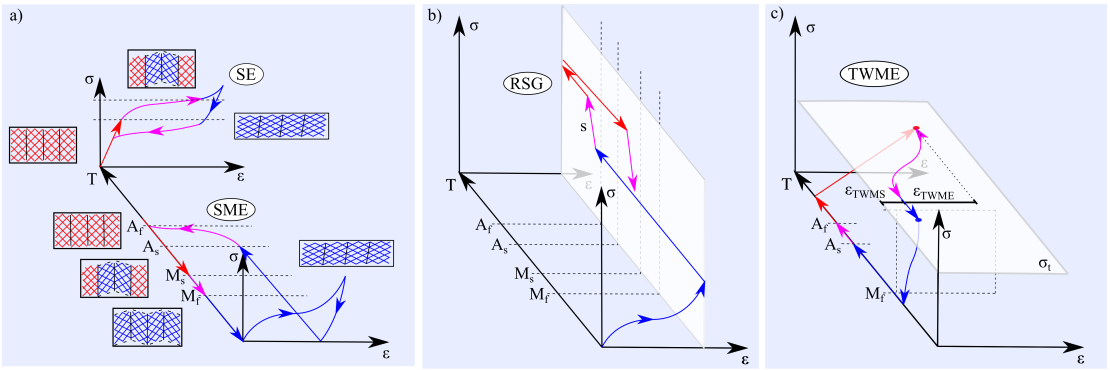

Figure 1.2: **SMA Thermo-Mechanical Coupling:** a) The superelastic (SE) and shape memory effect (SME) are based on the reversible solid-to-solid phase transition between the high-symmetry austenite and low-symmetry martensite phases as functions of the applied temperature, strain, and stresses. Figure inspired by [2, 3]. b) Recovery stress generation is (RSG) a working mode of shape memory alloys that is also commonly employed to generate forces upon heating in a constrained displacement configuration. c) The two-way shape memory effect (TWME) can be accomplished in a constant stress condition after training of the material, where a third, stable state can be accomplished upon cooling and heating with a recoverable strain (ε_{TWME}) and a residual strain (ε_{TWMS}).

phase transition to accommodate the phase interface. In the hot ($T \geq A_f$) austenitic phase, the previously introduced deformations from the memorized state are fully recovered. The reverse phase transformation occurs upon cooling and the initial self-accommodated martensite phase is introduced. [33] The mechanically-introduced phase transition between martensite and austenite above the austenite finish temperature is called superelasticity (SE). The onset of martensitic transformation and de-twinning occurs at a critical transformation stress after the initial elastic straining of the austenite lattice. A force plateau signifies the de-twinning of the martensitic phase. A material-specific stress level marks the full transition to oriented martensite and the stiffness increases while remaining lower than in the austenite phase. The reverse transition to austenite upon unloading takes place at lower stresses when compared to the loading curve.

Recovery stress generation (RSG) is produced by deforming and constraining the material in its martensite phase and subsequently transforming the material to a high-stress austenite state through thermal loading (Figure 1.2b). [48] RSG phase transformation occurs at temperatures higher than the stress-free transformation temperatures

due to the applied pre-straining in the martensite phase. The slope of the stress generation ($s = \frac{\mathrm{d}\sigma_{tr}}{\mathrm{d}T}$) is often assumed to be nearly linear and dependent on micro-structural material parameters, specifically preferential crystal orientation which can be tailored through thermo-mechanical training. [49] The reverse transformation occurs upon cooling and starts at temperatures higher than the stress-free martensite start temperature. Increasing material strain produces increasingly greater SMA recovery stresses. [50, 51] While higher applied temperatures produce larger stresses per fixed material strain, higher thermal loads are required to fully transform SMA into an austenitic state as tensile strain increases. [51] At sufficiently high materials strains, the martensite start temperature (M_s) can be shifted high enough to surpass the austenite start temperature (A_s), resulting in a switch to a Class II thermoelastic transformation (as opposed to a Class I thermoelastic transformation where $M_s < A_f$). [52, 51]

The two-way shape memory effect (TWME) is another hybrid thermal and mechanical load path that can produce desirable material performance. Training crystal preferential orientation through cyclic loading plays a significant role in the TWME. [53] As a first step, the material is heated from a temperature below the martensite finish temperature to a temperature above the austenite finish temperature (Figure 1.2c). The material is subsequently stressed to a training stress level (σ_t), resulting in a strained austenite phase. While the stresses are kept constant, the material is repetitively cooled below the martensite finish temperature and subsequently heated. A residual strain, the two-way martensite strain (ε_{TWMS}) emerges from the training procedure. The two-way shape memory strain (ε_{TWME}) is recoverable upon heating and cooling introducing a third, stable state – in addition to the self-accommodated martensite state and the austenite state. The TWME was long considered to be a weak effect that would only occur at low training stresses; however, stress recovery up to 100 MPa have been reported previously. [54, 55] The outlined procedures separate the mechanical and the thermal loading into distinct steps; however, engineering applications usually impose simultaneous thermal and mechanical loading conditions with varying strain- and stress-levels throughout. In addition to the significant shape memory material path-dependency, [56, 57] variable stresses, strains, and temperatures, can cause a partial occurrence and superposition of the shape memory, superelastic, recovery stress, and two-way shape memory loading paths. [58]

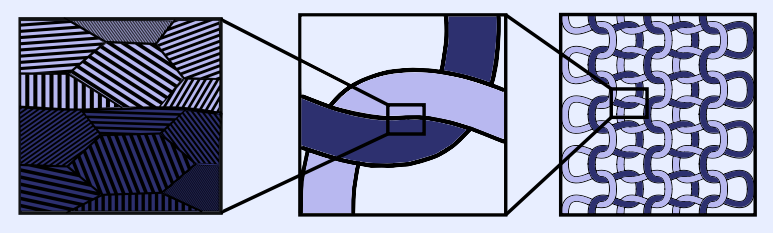

Figure 1.3: **Multiscale Mechanics:** SMA knitted architecture mechanics are described on the micro-, meso-, and macroscales to capture the SMA material, knitted loop, and knitted actuator mechanics.

1.3.2 SMA Knitted Architecture Geometry

SMA knitted architectures are inherently soft and compliant textiles that provide large, distributed, three-dimensional and recoverable actuation deformations in response to controlled changes in thermo-mechanical conditions. During the knit manufacturing process, a single flexible SMA filament is manipulated into a constrained architecture of interlacing, adjacent loops to build a network of consecutive wales (columns) and courses (rows). This process creates nearly planar structures with anisotropic elastic stiffness in the textile plane. SMA knitted architectures are hierarchical as their performance relies on mechanics that span the microscale (material properties), the mesoscale (knitted loop properties), and the macroscale (knitted actuator properties) (Figure 1.3).

Microscale descriptions of SMA knitted architectures are concerned with the material physics at the atom, lattice, and grain resolution, as well as the contact mechanics between the interlacing SMA filaments. The mesoscale is an intermediary scale between the micro- and macroscale, which examines the textile at a unit cell level. The unit cell of a textile is commonly defined as its smallest repetitive geometric element, for knitted actuators usually represented by a quarter/half/full knitted loop element. The macroscopic investigation of textiles is involved with the performance and behavior of the complete textile. The division of the textile mechanics into multiple scales allows an investigation of various levels of granularity. While this multiscale approach fits textiles in general, the hierarchical nature of functional SMA knitted architectures is not fully captured by this description. Additional layers of hierarchy are added on the macroscale to characterize the range of kinematic actuation motions and establish a formalized functional SMA knitted actuator classification. This hierarchy includes four levels of detail, which are from the lowest to the highest level: the knitted loop, the knit

pattern, the grid pattern, and the restructured grid. [6]

The first level of the active knitted architectural hierarchy, the knitted loop is concerned with two fundamental configurations, the knit loop and the purl loop (Figure 1.4). Knit and purl loops are mirrored opposites and only differentiated by the direction in which they are passed through the interlocking loop of the previous course.

The second level, the knit pattern, describes the homogenous assembly of knitted loops that form the SMA knitted actuator. Various combinations of knit and purl loops in both the horizontal and vertical directions result in knit patterns that achieve different homogeneous actuation deformations. Common knit patterns - such as stockinette, garter, or rib - provide homogeneous actuation deformations and are described on this level of architectural hierarchy.

The combination of various knit patterns in a single fabric is described on the third level of hierarchy, the grid pattern. While knit patterns are homogenous in their assembly of knitted loops, grid patterns form a heterogeneous structure with variable mechanical properties and actuation deformations distributed throughout the functional fabric. Grid pattern architectures expand the range of kinematic motions afforded by knitted SMA architectures and enable the controlled distribution of complex actuation deformations in a single knitted architecture.

The highest level of hierarchy, the restructured grid, describes the post-processing of planar knit patterns and grid patterns into three-dimensional, spatial architectures. This level can be achieved through a post-knitting connection of knitted loops, course-wise restructuring, grid cell merging, or re-ordered grids. Restructured grids further expand the range of attainable actuation motions. [6]

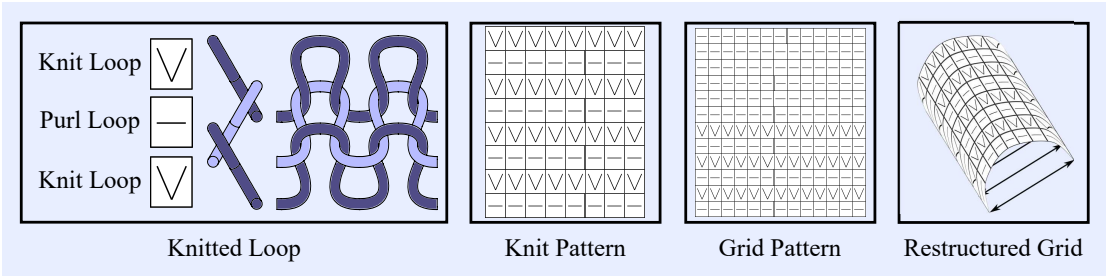

Figure 1.4: **Active Knit Hierarchy:** SMA knitted architectures exist on multiple macroscopic levels of hierarchy that enable homogenous, heterogeneous and restructured actuation deformations. The levels are the knitted loop, the knit pattern, the grid pattern, and the restructured grid.

The kinematic actuation motions of SMA knitted architectures are governed by the hierarchical composition of the knit and purl loops within the SMA knitted architectures. The fundamental homogenous deformation modes are a function of the selected knit pattern, which represents the second level in the active knit hierarchy. The most basic knit pattern, the stockinette pattern, is an assembly consisting of uniquely one type of knitted loops. As knit and purl loops are equal in geometry, but opposite in direction, stockinette patterns can be created from both types of knitted loops. Stockinette knit patterns produce asymmetric actuation deformations resulting in arching or scrolling of the fabric into a cylindrical shape (Figure 1.5, left). Knitted fabrics made of interchanging columns of knit and purl loop are called rib knitted architectures (Figure 1.5, middle). The columns of purl and knit loops bend into opposite directions upon actuation, causing the formation of corrugated actuation displacements. The garter pattern uses a similar architectural approach as the rib pattern. However, the interlacing knit and purl loops are not aligned as columns, but as rows in the knitted architecture (Figure 1.5, right). Garter knitted architectures produce macroscopically planar actuation contraction of up to 50%, which can be primarily attributed to recoverable bending deformations and relative sliding of the interlacing loops. While these are the most fundamental knit patterns, additional homogeneous knit patterns exist and can produce exciting multifunctional properties.

Contractile SMA knitted architectures based on the garter knit pattern are an intriguing functional fabric because of their large structural contractions (up to 50%), and their ability to actuate against significant forces while being a biocompatible, lightweight

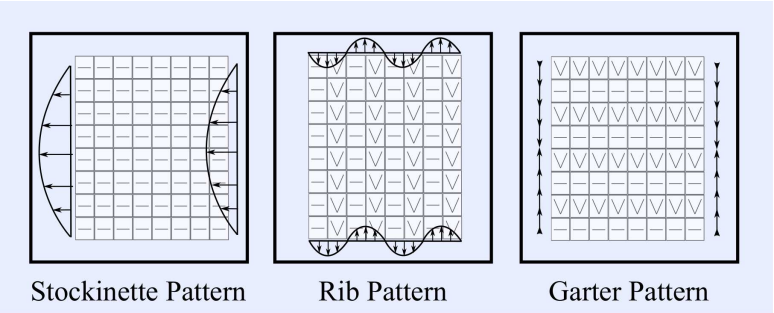

Figure 1.5: **SMA Knitted Architecture Knit Patterns:** Planar knit patterns produce homogenous actuation deformations. The stockinette knit pattern bends out of plane, the garter knit pattern produces uniaxial contractions, and the rib pattern forms a corrugation deformation upon thermal actuation.

architecture. Due to the geometric simplicity (macroscopically planar, uniaxial contraction) in comparison to other SMA knitted actuators, the contractile SMA knitted architecture is a gateway geometry to understand the fundamental mechanics of more complex topologies.

1.3.3 Contractile SMA Knitted Architectures

Contractile SMA knitted architectures consist of horizontally aligned rows of interlacing knit and purl loops manufactured from a single strand of monofilament SMA filament. As the knitted loops are repetitive elements, the geometry of contractile SMA knitted architectures is largely dependent on geometric loop parameters (Figure 1.6a). The course height (C) is defined as the distance between vertices of two interlacing loops. The vectors between the vertices of two interlacing loops and the horizontal baseline enclose the loop angle (χ). At a loop angle of $\chi = 90°$, the course height (C) equals the projected course height (C_p). The loop length (L) is the length of the spline defining a single loop, which surrounds the loop enclosed area (A_l). The wale width (W) is defined as the horizontal distance between the vertices of two adjacent loops. The side-view (Figure 1.6a) of the contractile SMA knitted architectures illustrates the difference between a knit loop and a purl loop, which interlock with knitted loops of the previous course in opposite direction. Figure 1.6b displays a prototype of a SMA knitted architecture.

The active properties of contractile SMA knitted architectures are achieved through

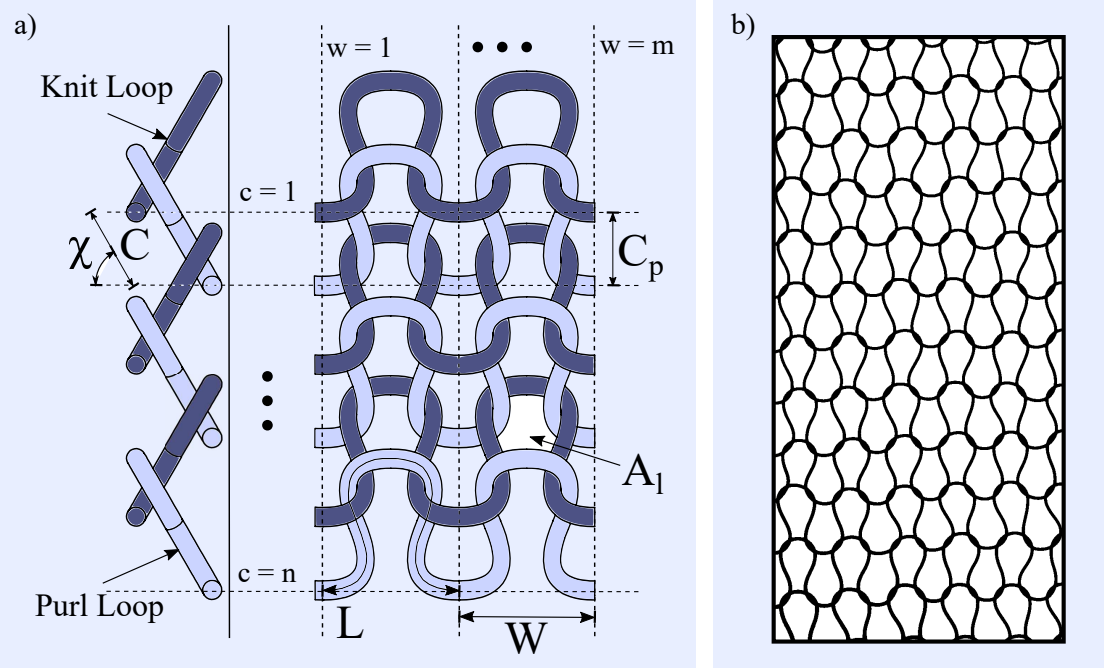

Figure 1.6: **Contractile SMA Knitted Actuator Geometry:** a) Contractile SMA knitted actuators consist of interlacing rows of knit and purl loops. Their geometry can be defined by the course height (C), projected course height (C_p), loop angle (χ), loop enclosed area (A_l), loop length (L), and wale width (W). There are ($w = m$) loops in the walewise direction and ($c = n$) loops in the coursewise direction. b) A knitted actuator prototype.

the integration of the straight-annealed SMA wire within the constrained knitted architecture. Bending deformations are introduced to the SMA wire in the loop forming process and cause internal material stresses, even in the macroscopically unloaded configuration. SMA knitted actuators exhibit variable force-extension behavior, dependent on thermo-mechanical loads. Under temperatures below the martensite finish temperature of the SMA material, contractile SMA knitted actuators exhibit a textile-characteristic strain-hardening behavior. When the temperature raises above the austenite finish temperature, contractile SMA knitted actuators display an initial high-stiffness regime, followed by a low-stiffness plateau and strain-hardening behavior.

Three fundamental paths can be utilized to characterize the low- and high-temperature profiles of contractile SMA knitted. All of them are based on a control input, a measured

quantity and a swept quantity. The force-control path mechanically loads the macroscopic actuator while the displacements are measured and the temperature is swept (Figure 1.7a). Upon heating, the knitted actuator, whose constrained geometry results in a range of spatially-distributed material stresses and strains, recovers macroscopic displacements as it contracts from its fully-martensitic, relaxed profile length (l_M) to its partially-austenitic, actuated profile length (l_A). The %-actuation contraction (ζ) is defined as the engineering strain between the martensite profile length and the austenite profile length. Alternatively, the displacement-control path constrains the contractile SMA knitted actuator to a defined length while contractile forces build in the knitted architecture upon heating from the low-temperature state (Figure 1.7b). In this path, displacements are controlled, forces measured and temperatures swept. Lastly, in a temperature-controlled operation, the forces are measured and the displacements swept. The SMA knitted architecture is displaced under fixed temperatures and either is operated similar to the superelastic SMA material operation if the temperatures are high enough to induce the high-temperature profile, or similar to a passive textile with pure strain-hardening behavior if the temperatures are chosen to induce the low temperature profile (Figure 1.7c).

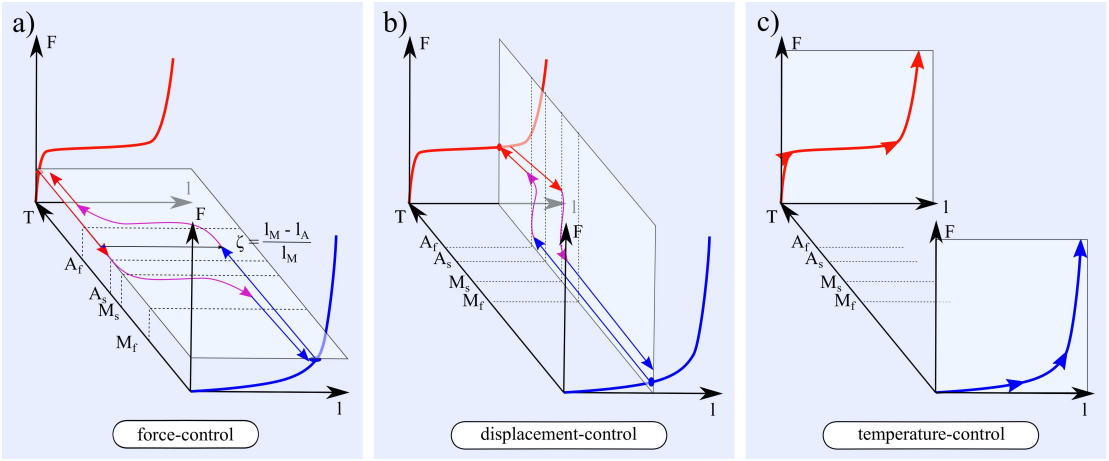

Figure 1.7: **Contactile SMA Knitted Architecture Characterization Strategies:** Contractile SMA knitted actuators can be characterized and operated using the a) force-control strategy, in which the force is constrained, temperatures are swept, and displacements are measured b) the displacement-control strategy, in which the displacements are constrained, temperatures are swept, and forces are measured, and c) the temperature-control strategy, in which the temperatures are constrained, displacements are swept, and forces are measured.

1.4 Research Issues

The potential of multifunctional fabrics, and specifically SMA knitted architectures, as technologies that present additional design spaces for high-demand applications has been established previously. [20, 59, 60, 61] The realization of such applications, however, requires an understanding of the relationship between SMA knitted architecture design parameters and their resulting thermo-mechanical performance. Consequently, the SMA knitted architecture must be understood as a system that relies on mechanics on multiple scales including the micro-, meso-, macro- and application scales.

1.4.1 Macroscale SMA Knitted Architecture Mechanics

The contractile SMA knitted architecture performance can be described as the set of outputs that can be exploited from the change in thermo-mechanical loading of designed SMA textile architectures. The macroscopic approach to SMA knitted architectures disregards the internal mechanics, i.e., the micro- and meso-scale mechanics, of the fabric and reduces the complexity to the relation between macroscopic design inputs and

outputs. As a first step, the formalized definition of such inputs and outputs is necessary. Established definitions exist for passive knitted architectures [62, 63] regarding knit geometric properties and performance metrics. First adaptions of these definitions, specifically measurable in- and outputs for the smart textile space have been generated, but are not yet extensive. [64] Macroscopic input categories that have been identified are (1) the knitted architecture geometry consisting of the loop geometry and the number of loops, and (2) the thermo-mechanical loading conditions which include single-actuation or cyclical displacement-, force-, or temperature-controlled procedures. The effect of the variation of these inputs on the actuator force-extension profiles, actuator transition temperatures, and performance repeatability must be understood to realize SMA knitted actuator applications.

1.4.2 Mesoscale SMA Knitted Architecture Mechanics

The loop geometry is a mesoscopic knitted architecture property that has been identified to be one of the most potent input parameters to alter the knitted architecture mechanics. The knit loop geometry is commonly used as the repetitive volume element in analytical and numerical mechanical modeling and must therefore be captured accurately. Traditional cotton- or polyester-based yarn knitted textiles have been modeled as a network of perfectly-elastic knitted loops, where the loop geometry is solely dependent on the knit loop length. [65] SMA knitted loops, however, are non-traditional knitted loops and may vary significantly in geometry. Understanding the knitted loop geometry, and how it affects the thermo-mechanical performance of the SMA knitted actuator will significantly improve the ability to design SMA knitted textiles and provide a starting point for the description of other non-traditional knitted architecture mesoscopic properties.

1.4.3 Microscale SMA Knitted Architecture Mechanics

The ability of SMA knitted architectures to provide large deformations is enabled by a solid-to-solid transition between its austenitic and martensitic material phases. As the material phases have unique physical properties, such as stiffness and conductivity, the designed phase transition is ultimately responsible for the SMA knitted actuator behavior. Thus far, the microstructural properties of SMA knitted architectures have

not been utilized in the SMA knitted architecture design process, despite their potency for large performance improvements and variations.

Stresses and strains introduced in the SMA knitting procedure and the application of thermo-mechanical loads stem from a variety of loading modes (normal, bending, torsion, shear) and can largely vary in magnitude depending on the spatial position along the knitted loop. Due to the complexity of the loading conditions, it is currently not known which loading modes are most influential on the SMA knitted architecture performance. Understanding the phase distribution in SMA knitted loops as a function of thermo-mechanical loading conditions is necessary to identify potential pathways for the microstructural SMA knitted architecture performance optimization.

1.4.4 SMA Knitted Architecture Design Studies

While the SMA knitted architecture is best studied for its thermo-mechanical properties as an isolated textile, system integration is necessary for utilization in applications. SMA knitted design studies that may not accomplish a complete system design, but highlight specific aspects of a system integration, are necessary to position SMA knitted architectures as an improvement compared to traditional actuator alternatives. While potential application industries have already been identified, the medical and aerospace wearables market is continually investing in novel wearable systems, specific applications need to be determined. Furthermore, operation strategies that complement wearables design, physical requirements, and economic considerations should be developed and highlighted.

1.5 Research Goals & Objectives

The goal of this research is the elucidation of fundamental contractile SMA knitted architecture mechanics to enable the design for specific performance metrics and applications. The following objectives are formulated to accomplish this research goal:

- **Derive guidelines for the design, operation, and characterization of contractile SMA knitted architectures:** The SMA knitted architecture material properties and geometric design parameters determine the thermo-mechanical performance. An empirical investigation correlating the effect of defined geometric

design parameters and operation strategies on specific SMA knitted architecture performance metrics establishes the macroscopic design space and performance trade-offs for the derivation of specific design guidelines.

- **Provide fundamental mechanistic understanding on the microscale:** Develop in-situ microstructural analysis of SMA knitted architectures as a method to identify the dominant deformation modes and establish a connection between the macroscopic and microscopic knitted architecture design.
- **Predict the SMA Knitted Architecture Performance:** Formulate and verify a flexible, accurate, and computationally efficient SMA textile modeling tool that captures the three-dimensional kinematics and material mechanics of SMA knitted architectures and provides the ability to rapidly predict the textile thermomechanical performance.
- **Demonstrate New Design Capabilities in Applications:** Establish the capability of the new understanding and predictive tools to design SMA knitted architecture properties and operation modes for specific application requirements.

1.6 Research Approach

The research goal is accomplished through specific research items focused on the objectives outlined previously. This section organizes the research items of the publications that make up the body of this document, and highlight the contributions to the satisfaction of the defined objectives and goals.

1.6.1 Derive guidelines for the design, operation, and characterization of contractile SMA knitted architectures

The intriguing combination of high stress-strain product and low density is a consequence of the geometric design and operation of SMA knitted architecture. As SMA knitted architectures combine two highly non-linear systems, the SMA material system and the knitted textile architecture, a variety of design trade-offs occur when the geometric parameters of the knitted architecture are changed. Additionally, SMA knitted architecture performance metrics are defined in accordance with existing passive textile and smart material standards to appropriately measure the performance.

Effect of Mesoscopic Parameters on Macroscopic Performance: An empirical study is needed to understand the effect of geometric parameters and operation strategies on the SMA knitted architecture performance. The mesoscopic loop geometry is correlated to the macroscopic knitted architecture performance under the variation of SMA filament diameters and knit manufacturing parameters. A dimensionless geometric parameter that compares the mesoscopic loop geometry inspired by beam bending strain considerations is derived and correlated to SMA knitted architecture performance metrics (Section 3.3). As the induced pre-stresses in the SMA filament from the knit manufacturing procedure are dependent on loop geometric parameters, thermo-mechanical properties of the knitted architecture can vary as a function of them. In distinction to the material specific transition temperatures, knitted architecture actuation and relaxation temperatures are defined and their variation based on the mesoscopic parameters is experimentally-investigated. (Section 2.7)

Effect of Macroscopic Parameters on Macroscopic Performance: The variation of macroscopic parameters and the resulting variation of the SMA knitted architecture performance is also investigated experimentally. The number of knitted loops in the course-wise and wale-wise directions affect the SMA knitted architecture performance. An abstraction of knitted loops as non-linear springs with linear properties in specific ranges allows the application of classic serial and parallel spring design rules for SMA knitted architectures. This approach has been verified for homogenous knitted architectures consisting of a single mesoscopic loop geometry (Section 2.8) as well as inhomogeneous knitted architectures with varying mesoscopic loop geometries (Section 2.9). The minimum number of loops in both the wale- and course-wise directions required for scalability is identified as knitted architectures that consist of few loops in either direction are dominated by their boundary conditions and scalability rules may not apply.

Effect of Operational Conditions on the Macroscopic Performance: SMA knitted architectures can be operated in a force-controlled, displacement-controlled, or temperature-controlled environment. As the knitted architecture and the SMA material introduce hysteresis to the system and frictional conditions change between operational modes, differences in the SMA knitted architecture performance can occur as the operational strategy changes (Section 2.4). A first study of the cyclic performance of SMA knitted architectures, motivated by the prevalence of material and textile shakedown

effects studied in SMA and passive textiles has been performed to identify the initial cyclic performance up to 80 cycles (Section 2.6).

The description of the interrelation of geometric parameter variations in the meso- and macro-scale, as well as knit operation strategies, and the SMA knitted architecture performance provides a broad understanding of design and performance trade-offs in SMA knitted architectures. This empirical study establishes a useful set of design rules and bolsters the understanding of the thermomechanics of this highly non-linear system. A detailed discussion of the empirical study of mesoscale, macroscale, and knit operational parameters can be found in Chapters 2 and 3.

1.6.2 Provide fundamental mechanistic understanding on the microscale

The micromechanics of the SMA filament in the SMA knitted architecture have thus far not been considered in scientific research despite the fact that micromechanical effects are responsible for the intriguing SMA knitted architecture performance. In-situ and in-operando x-ray diffraction experiments are gaining increasing traction, especially for SMA analyses since their highly nonlinear behavior often prohibits highest-accuracy prediction of the micromechanics in complex systems. To capture micromechanical properties, an in-situ study of the SMA knitted architecture in a 2D x-ray diffractometry experiment has been conducted while controlling the applied temperature and macroscopic strains applied to the knitted architecture. Through the study of multiple measurement positions along the SMA knitted loop, the spatially-distributed, temperature- and strain-dependent variation of the material phase fraction can be analyzed and conclusions regarding the dominant deformation modes and critically loaded loop segments can be drawn. Through the study of micromechanical effects, design decisions can be based on microstructural understanding, and performance optimization strategies can be derived based on knowledge of the phase distribution in the SMA knitted loop. A detailed description of the micromechanical study of SMA knitted architectures can be found in Chapter 4.

1.6.3 Predict the SMA Knitted Architecture Performance

To study SMA knitted architecture, understand the underlying multiscale mechanics, and provide a rapid design tool, SMA knitted architecture models are proposed based on

empirical data and fundamental physical concepts. Utilizing the large data set collected in the empirical studies, algebraic functions are formulated that connect the cluster of data along the filament diameter and loop geometry dimensions and provide predictions of the knit performance of knitted architectures within the range of the tested prototypes. Further information on this empirical model is presented in Section 3.7.

A physics-based higher fidelity model has been developed using finite beam element theory. The repetitive contractile SMA knitted architecture unit cell, a quarter knitted loop can be geometrically represented as a spline and discretized into a defined number of connected beam elements. Appropriate material models, specifically a phenomenological 1D SMA constitutive model, have been implemented and the contact between knitted loops has been captured through kinematic periodicity conditions. A differential geometry-based manufacturing model prescribes the initial conditions of every beam element in the computation and boundary conditions are applied to satisfy kinematic constraints, constrain the appropriate degrees of freedom, and apply forces and moments in the knitted loop unit cell. Consequently, the SMA knitted architecture finite beam element model produces predictions on the macroscale and the microscale which are verified experimentally. Macroscopic simulation results of the knitted architecture force-extension properties, the %-actuation contraction, and geometric predictions were verified quantitatively against experimental data. Relative errors over the entire force-extension profile averaging under 5% were reported across simulated SMA knitted architectures of varying filament diameters and knit indices. Microscopic simulation outputs qualitatively matched the trends of the phase distributions obtained experimentally in x-ray diffraction experiment. Chapter 5 discussed the finite beam element model in detail.

1.6.4 Demonstrate New Design Capabilities in Applications

While the promising performance of SMA knitted architectures can be demonstrated well in the laboratory environment, it is necessary to highlight SMA knitted architecture capability and operation strategies for applications. In collaboration with researchers at the Wearable Technology Laboratory first SMA knitted actuator applications have been demonstrated. At the intersection of the medical device and aerospace markets, two markets with comparatively high familiarity with SMAs as outlined in Section 1.1, a self-fitting garment has been developed for the lower limb. A design strategy to

identify the required contractile ability to enable donning over the lower limb and satisfy self-fitting requirements along largely varying lower leg anatomy have been developed. Topographical fitting has been accomplish by strategically varying the knit pattern and has been varyfied for the topographically challenging knee anatomy. Such a self-fitting garment provides solutions for accurate health monitoring sensor placement by accomplishing accurate topographical fitting in a stiff textile that can be easily donned and doffed. It also serves as a precursor for the compression garment development with constant or intentionally-distributed pressure application, a subject that is further developed by the researchers in the Design of Active Materials and Structures (DAMSL) and Wearable Technology Laboratory (WTL). The conclusive description of the self-fitting garment can be found in Chapter 6.

Additionally, research on the integration of SMA knits into novel applications demands the establishment of customized operating modes and creation of innovative design features. TSelf-fitting and compression garment design has raised a need for shifted operation temperatures and increased forces that has previously not been investigated in SMA knitted architectures. An application-specific operation mode based on pre-straining and utilization of both the solid phase transformation and thermal contraction upon cooling can shift material transformation temperatures into desirable ranges for applications, shrink the temperature-difference between the actuated and relaxed states, and increase the forces generated upon actuation. The characterization of this adjusted operation mode and its utility to smart compression as required in compression garments and other applications is outlined in Chapter 7.

1.7 Outcomes & Contributions

While the potential of SMA knitted architectures to be high performance, lightweight actuators and energy dampers has been demonstrated in prior research, their mechanics are currently not understood to a degree that permits the derivation of design rules. This research closes the knowledge gap for contractile SMA knitted architectures and enables their design with reproducible and predictable performance based on scientific evidence.

Guidelines for trade-offs between geometric design, operational strategies, and thermo-mechanical SMA knitted architecture performance have been derived from experimental

data and attributed to SMA material properties and knitted architecture mechanics. A dimensionless parameter, the knit index, has been defined to predict the SMA knitted architecture maximum contractile ability. The establishment of experimentally verified design rules for the contractile SMA knitted architecture provides the background for the formulation of physics-based models, serves as the training data for an empirical model and contributes as a starting point for the research on other SMA knit patterns.

Opening the SMA knitted architecture design space to the microscale through x-ray diffraction experiments provides a set of microscopic design parameters that have previously not been considered in SMA knitted architectures. An in-situ/in-operando SMA knitted architecture x-ray diffraction experiment has been built and proven successful for the identification of the spatial distribution of the SMA material phase fraction as a function of the applied temperature and macroscopically-applied strain. The x-ray diffraction analysis elucidates the predominant deformation modes in SMA knitted architectures, shows which segments of the SMA knitted loop contribute to the performance, and motivates the optimization of local SMA material properties and knitted loop geometries to further increase the exploitable performance. Additionally, this experiment is proof of concept for the in-operando analysis of the SMA knitted architecture micro-structure, and further impactful micro-structural parameters could be investigated in the future, especially with higher energy beams that enable the complete micro-structural analysis.

Predictive capabilities of the contractile SMA knitted architecture performance are presented in an empirical model based on algebraic functions and trained by the large experimentally obtained data set for various contractile SMA knitted architectures as well as a high-fidelity, physics-based finite beam element model. The empirical model serves as a tool for the quick and simple prediction of the SMA knitted architecture thermo-mechanical macroscopic performance for loop geometries and filament diameters within the range of the experimentally-investigated architectures and for Dynalloy Flexinol® material. The high-fidelity, finite beam element SMA textile model is a comprehensive tool that processes several material input parameters and loop geometric inputs to predict the macroscopic performance and micro-structural parameters. The various sub-models implemented in the SMA textile model are described in detail and their interfaces defined. The sub-model approach was chosen to provide a flexible skeleton for the variation of textile architectures, switch model components (e.g., test various

material models) and simplify the addition to the modeling architecture. With the availability of a quick and simple empirical SMA knitted architecture thermo-mechanical model, as well as a high-fidelity finite beam element SMA knitted architecture model, the wide range of needs for desired predictive capabilities can be satisfied. Both models have been verified against experimentally-collected data to ensure their accuracy.

The capabilities of the derived design guidelines and predictive models have been demonstrated through the design of meaningful SMA knitted architecture applications. The market need for applications, identified design requirements, design procedures, and verification are laid out in detail. Through the challenges posed by real application design, novel SMA knitted architecture operation modes, mechanical behaviors, and performance verification techniques have been established with further impact to general SMA actuator design or garment fit analysis.

Beyond the contractile SMA knitted architecture, this research established fundamental principles for other knit patterns, textile architectures, and active filament systems such as electro-active polymers or carbon nanotubes. The sub-model based high-fidelity textile modeling architecture is set up to foster modeling attempts with other textile architecture and material combinations. Similarly, this research provides the basis for the transition to spun fiber knitted architectures from entirely active microfilaments or blended yarns with active and passive elements with improved comfort characteristics. This research provides the fundamental understanding of the mechanics and tools to design SMA knitted architecture applications, which have tremendous potential, specifically in the medical and aerospace world.

Chapter 2

Guidelines on the design, characterization, and operation of shape memory alloy knitted actuators

K Eschen, R Granberry and J Abel
Department of Mechanical Engineering, University of Minnesota,
111 Church Street SE, Minneapolis, MN 55455, USA
Published in **Smart Materials & Structures**
Vol **29**
Pages **035036**
DOI **10.1088/1361-665X/ab6ba7**
Date **January 2020**

Abstract

Textile actuators combine the intriguing mechanics of textile architectures with the multifunctional capabilities of active materials to provide large, distributed and three-dimensional deformations and forces. SMA knitted actuators, a type of textile actuator, are specifically alluring because of their high energy density and mechanical performance. The study of textile actuators in general, and SMA knitted actuators in specific, is currently confined to small parameter studies and application-driven research resulting in a scarcity of conclusive, universal guidelines and standards for the design, operation, and characterization of these compliant smart actuators. This paper identifies the predominant functional dependencies between the knitted actuator geometry, thermo-mechanical loading, and the knitted actuator performance to derive guidelines for the design, operation, and characterization of SMA knitted actuators. Through this first conclusive description of SMA knitted actuators, we significantly advance their research, design, and usability, while providing transferable insight into other active textile implementations and encouraging the standardization of language and procedures across this novel research field.

2.1 Introduction

Shape memory alloys (SMAs) are increasingly implemented in complex geometry systems to utilize the design space afforded by the combination of their nonlinear material behavior, specifically the intriguing superelastic (SE) and the shape memory effects (SME), [34, 35] and the nonlinear geometry that enable extreme applications. Such applications include extra-terrestrial rover tires using spring [66] and knit [67] architecture designs, active self-fitting [68] and compression garments, [69, 20] and soft robotics applications. [60, 61]

The NiTi-based SMA specific shape memory and superelastic effects are based on solid-to-solid phase transitions and can be induced thermally (SME) and mechanically (SE) to provide and recover large strains (up to 8%) and lift significant loads. [33] SMA geometric assemblies of varying complexity - from simple wires [70] to bundles, [42] cables, [44] and springs [43, 45] have been proposed to further optimize and tailor the unique performance of the material. The limitation of only providing one-dimensional actuation deformations shared by the previously listed geometric SMA implementations is overcome by smart textile actuators. Compliant, smart textile actuators are created from active material fibers through traditional textile manufacturing processes (knitting, [6] weaving, [15] embroidering [71]) to provide scalable, three-dimensional actuation deformations. While other active materials such as carbon nanotubes [13] and shape memory polymers [15] have also previously been investigated in textile actuators, SMA knitted actuators render themselves specifically appealing because of their superior actuation contractions ($\zeta > 40\%$) while working against loads (F) of 1-100 N magnitude. [72]

Preliminary studies [73] and applied research showcase the potential of SMA knitted actuators and provide insight into the thermo-mechanical performance of SMA knitted actuators within confined parameters. The current limited state of the SMA knitted actuator design becomes apparent when compared to the one-dimensional actuator geometries (wire, spring, cable, etc.), for which the fundamental thermo-mechanical properties and their dependency on geometric design parameters have already been derived. A first step towards the derivation of the functional dependency between the knitted actuator geometry and thermo-mechanical performance has been accomplished through

the definition of the knit index, a non-dimensional geometric loop parameter which predicts the achievable %-actuation contractions of contractile SMA knitted actuators. [74] In spite of first accomplishments in relating the fabric architecture to the performance of multifunctional knitted actuators, many fundamental properties of the knitted actuator design, characterization, and operation have not yet been researched. This knowledge gap inhibits the employment of multifunctional fabrics as the challenges of manufacture and operation without clear guidelines pose significant cost to researchers and users.

This paper presents guidelines on the design, characterization, and operation of SMA knitted actuators and establishes the relationship between knitted textile geometric parameters and their fundamental active properties - displacement, force, and temperature. Uniaxial tensile characterization strategies are compared and the repeatability of the SMA knitted actuator performance between prototypes is examined. The performance within the first 70 cycles of the SMA knitted actuator is evaluated and the actuation and relaxation temperatures are introduced to describe the required thermal loading for phase transition in the mechanically loaded architecture. Additionally, design rules are established paralleling the serial/parallel connection of springs to describe the actuation performance of SMA knitted actuators with varying numbers of loops in the course- and wale-wise directions. Through this research, we elucidate the thermo-mechanical performance trade-offs of contractile SMA knitted actuators. As a result of this research, the essential thermo-mechanical actuation properties of contractile SMA knitted actuators can be related to geometric design parameters. The derived guidelines will have a broad impact on active textiles research as the established principles can be translated to other multifunctional materials and textile architectures.

2.2 SMA Knitted Actuators

SMA knitted actuators are inherently soft and compliant textiles that provide large, three-dimensional and recoverable actuation deformations and forces in response to controlled changes in temperature. [6] SMA knitted actuators realize these characteristics through their hierarchical architecture which relies on mechanics that span the nano-, and microscales (material properties), the mesoscale (knitted loop properties), and the macroscale (knit pattern properties) as shown in Figure 2.1a.

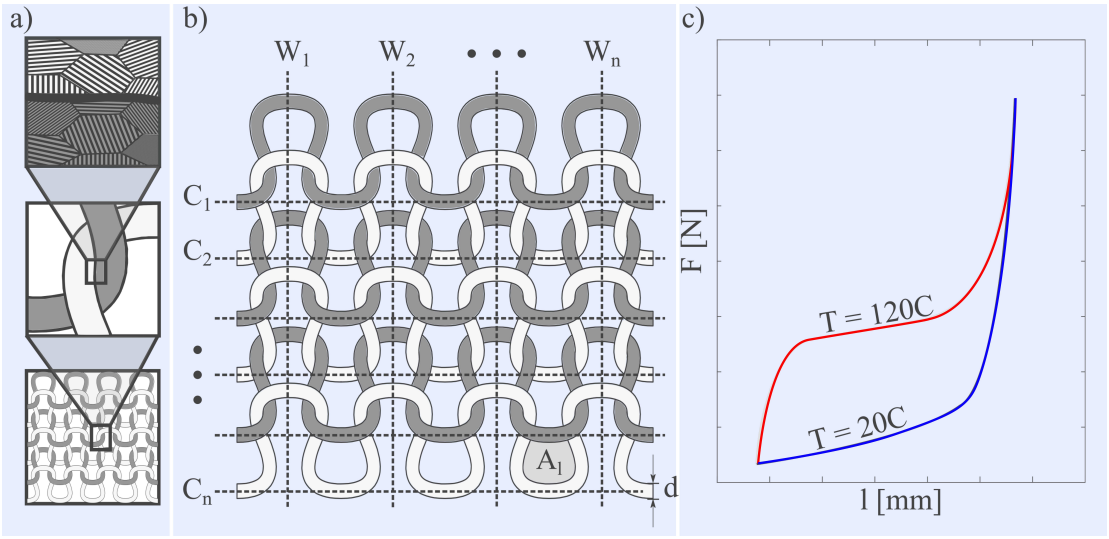

Figure 2.1: **SMA Knitted Actuators:** (a) SMA knitted actuators are hierarchical architectures with multiscale design parameters ranging from the nano-,micro-, and mesoscale to the macroscale. (b) They consist of interlocking adjacent loops formed from a single active fiber, are assembled into rows (courses, C) and columns (wales, W), and are defined by their loop enclosed area (A_l) and the fiber diameter (d). (c) The SMA knitted actuator active ability is visualized force-knit length profiles, which shows a tri-linear behavior in the partially-austenitic, actuated state ($T > A_f$) as opposed to a bi-linear behavior in the fully-martensitic, relaxed state ($T < M_f$).

2.2.1 SMA Knitted Actuator Fundamentals

The active characteristics of SMA knitted actuators are afforded by reversible temperature-, strain-, and stress-dependent transformations between a cubic austenite and a monoclinic martensite phase. The two phases differ in their atomic assembly and their unique micro-mechanical properties which results in variable stiffness that can be induced thermally (SME) and mechanically (SE). In the knit manufacturing process, SMA filament is bent into an interlocking network of adjacent knitted loops. Upon thermal actuation, the austenite volume fraction increases resulting in a higher bending stiffness of the SMA fiber and causing partial recovery of the imposed bending deformations. Based on the presence of the different material phases, the actuated, partially-austenitic, SMA knitted actuator state properties are subscripted with the letter (a), and the fully-martensitic, relaxed knitted actuator state with (m). The magnitude of the loop bending recovery is dependent on the mesoscopic knit geometry and the macroscopically applied external

loads. The dimensionless knit index (i_k) [74] describes the mesoscopic loop geometry of ideal knitted loops whose geometry is entirely dependent on the loop length. [65] Practically, the knit index can be interpreted as a knit-specific parallel to the spring index that relates the void area enclosed by the knitted loop (A_l) and the filament diameter (d).

$$i_k = \frac{A_l}{d^2} \tag{2.1}$$

The number of loops in the horizontal/wale-wise (g) and vertical/course-wise (h) directions are macroscopic geometric properties that describe the SMA knitted actuator dimensions (Figure 2.1b). Knitted actuators that consist of loops of constant knit index are called homogenous. Knitted actuators that consist of knitted loops with multiple knit indices are called inhomogenous.

2.2.2 SMA Knitted Actuator Performance

The contractile SMA knitted actuator performance is a function of the fundamental metrics force, knit length and temperature from which additional metrics, such as work and %-actuation contraction, are derived. The fundamental metrics mirror the SMA material dependency on the applied stresses, strains and temperature. The variation of the knitted actuator's mechanical response is introduced by thermal transition between the martensitic and austenitic phases. For temperatures below the SMA martensite finish temperature, the knitted actuator is fully-martenstic and follows a knit-characteristic bi-linear strain-hardening behavior (Figure 2.1c). For temperatures above the SMA austenite finish temperature, which is defined under stress-free conditions, the SMA knitted actuator is partially-austenitic with residual stress-induced martensite introduced in the manufacturing process. The force-knit length profile in the tri-linear partially-austenitic state is characterized by an initial structural stiffness regime, followed by a force-plateau and a subsequent strain-hardening regime. The strain-hardening regime approaches the fully-martensitic profile as a result of increasing stress-induced martensite volume fractions under higher external loads. The scaled difference between the the high-temperature partially-austenitic knit length (l_a) and the low-temperature fully-martensitic knit length (l_m) at a constant load

$$\zeta = 1 - \frac{l_a}{l_m} \tag{2.2}$$

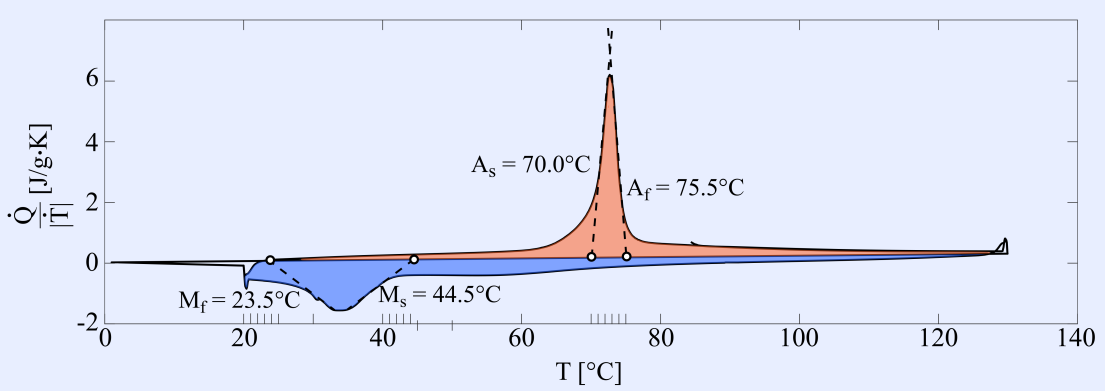

Figure 2.2: **Differential Scanning Calorimetry:** DSC provides the stress-free transformation temperatures (A_s, A_f, M_s, M_f) for the filament ($d = 0.203\,\text{mm}$) used for knitting the contractile SMA knitted actuator.

is the %-actuation contraction (ζ). Contractile SMA knitted actuators provide %-actuation contractions of over 40%, a property that is directly predicted by the SMA knitted actuator's knit index. [74]

2.2.3 Understanding the Filament

Prior to any SMA knitted actuator characterization or operation, it is advisable to understand the thermo-mechanical properties of the SMA filament which can be in the form of wire, yarn or other geometric assemblies. For the most basic filament, plain wire, differential scanning calorimetry is employed for the filament characterization. For more complex geometries with internal stress fields such as yarns, stress-free material samples should be characterized and the filament geometry should be taken into consideration. Differential scanning calorimetry (DSC) reveals the stress-free transformation temperatures - austenite start (A_s), austenite finish (A_f), martensite start (M_s), martensite finish (M_f) - that induce the martensitic and austenitic phases of SMA. [75, 76] These transformation temperatures are useful for the identification of the appropriate temperature range for the thermo-mechanical characterization of SMA knitted actuators. Dynalloy Flexinol® filament samples of 10 mg were prepared and analyzed in a TA Instruments Q-1000 Differential Scanning Calorimeter. The Dynalloy Flexinol® filament, which is used for every prototype presented in this manuscript, undergoes its

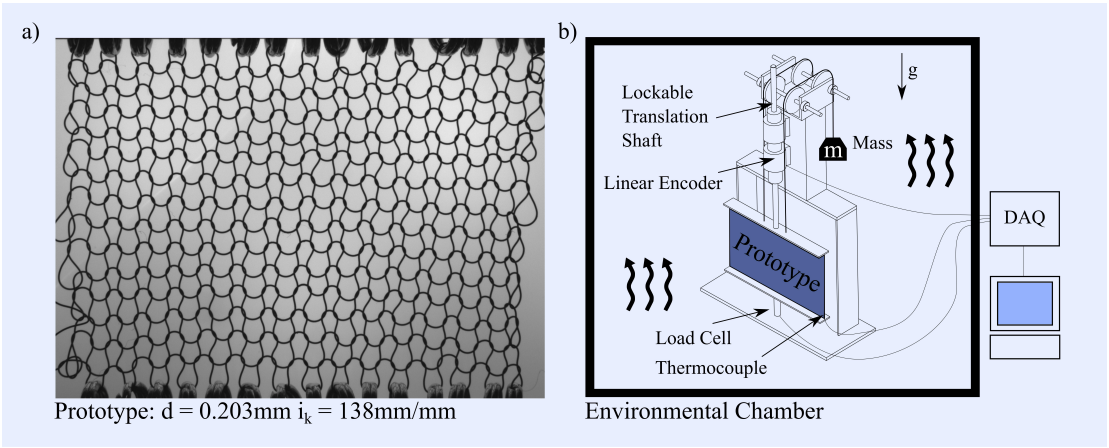

Figure 2.3: **Reference Prototype & Experimental Setup:** (a) The reference prototype used in the publication consists of straight-annealed Dynalloy Flexinol® wire of the diameter ($d = 0.203\,\text{mm}$), has a knit index ($i_k = 138\,\text{mm}^2\,\text{mm}^{-2}$) and 15 loops in the course- and walewise direction ($g = h = 15$). (b) The custom-made uniaxial tensile tester enables temperature-, force-, and displacement-control and measurement.

phase transitions from martensite to austenite between the austenite start temperature ($A_s = 70.0\,°\text{C}$) and the austenite finish temperature ($A_f = 75.5\,°\text{C}$) (Figure 2.4). The phase transition from austenite to martensite occurs between the martensite start temperature ($M_s = 44.5\,°\text{C}$) and the martensite finish temperature ($M_f = 23.5\,°\text{C}$).

2.3 Prototypes & Experimental Setup

The experiments were conducted with SMA knitted actuators manufactured with straight-annealed Dynalloy Flexinol® wire of the diameter ($d = 0.203\,\text{mm}$) as their active filament. The SMA knitted actuators were manufactured on a manually-driven Taitexma TH-860 knitting machine that provides enhanced control of the knit geometric parameters. Every set of experimental data used in this publication is obtained from SMA knitted actuators that have not undergone thermo-mechanical treatment aside from the manufacturer pre-conditioning and the knitting process. All prototypes are related and compared to a reference prototype, which consists of constant mesoscopic knitted loop parameters ($i_k = 138\,\text{mm}^2\,\text{mm}^{-2}, d = 0.203\,\text{mm}$) and a constant number of loops in the wale- and course-wise directions ($g = h = 15$) (Figure 2.3a). All prototypes are homogenous knitted actuators with constant knit index unless specified otherwise. The

experimental characterization that underlies the derivation of guidelines for this publication was conducted in a custom-built uniaxial tensile experimentation setup that enables displacement-control and displacement measurement through a lockable translational shaft connected to a US Digital linear encoder (accuracy 0.012 mm), tensile force-control through manual application of weights, force measurement through a Honeywell M34 miniature 5lbs load cell with temperature compensation (accuracy 0.2% full scale), temperature-control through housing within a CSZ environmental chamber, and temperature measurement using k-type thermocouples (Figure 2.3b).

Strategy	**T**	$\dot{T}$	**F**	$\dot{F}$	**l**	$\dot{l}$
Temperature-control	control	0	measure	N/A	sweep	$5 \times 10^{-4}\mathrm{s}^{-1}$
Displacement-control	sweep	$0.11\frac{^{\circ}\mathrm{C}}{s}$	measure	N/A	control	0
Force-control	sweep	$0.11\frac{^{\circ}\mathrm{C}}{s}$	control	0	measure	N/A

Table 2.1: **Characterization Strategies:** Overview of the different characterization strategies, temperature-, force- and displacement-control, and the employed temperature- ($\dot{T}$), force- ($\dot{F}$), and displacement-rates ($\dot{l}$)
.

2.4 Thermo-mechanical Characterization Strategies

The three fundamental SMA actuator characterization strategies are force-, displacement-, and temperature-control experiments as defined by their control variable (Table 2.1). Best practices have been established for the characterization of less complex SMA systems and can be translated to SMA knitted actuators. For example, low force-, displacement-, and temperature-rates are employed to create a well-controlled, quasi-static experiment. [77] This section introduces different thermo-mechanical characterization techniques and compares the resulting mechanical performance.

2.4.1 Temperature-Control

The quickest SMA knitted actuator characterization strategy is the temperature-control characterization, which is also referred to as the pullout test. [78] This characterization strategy commands the operation under two constant temperatures that induce the SMA knitted actuator's relaxed, fully-martensitic and actuated, partially-austenitic states. In

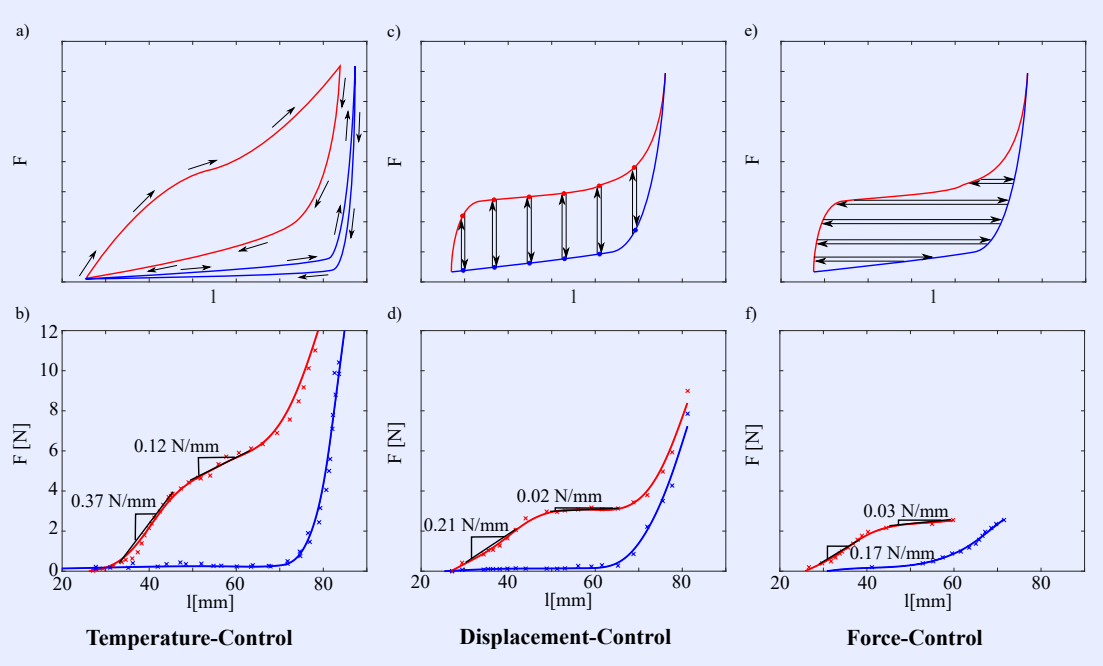

Figure 2.4: **Characterization Strategy Comparison:** Force-knit length data of different characterization strategies is shown schematically and with experimentally obtained data for (a,b) the temperature-control characterization strategy, (c,d) the displacement-control characterization strategy, and (e,f) the temperature-control characterization strategy. The experimental data is collected with SMA knitted actuators with the geometric properties $d = 0.203\,\mathrm{mm}$, $i_k = 138\,\mathrm{mm}^2\,\mathrm{mm}^{-2}$, and $C = W = 15$.

these states, the SMA knitted actuator is displaced under low displacement rates ($\dot{\delta}$) to full extension while forces are measured continuously. Low displacement rates are necessary to accomplish near-isothermal conditions as large-displacement rates result in the release of heat without sufficient heat transfer. For highest accuracy results, displacement rates between $5\times10^{-5}\mathrm{s}^{-1} \leq \frac{\dot{\delta}}{l} \leq 4\times10^{-4}\mathrm{s}^{-1}$ are recommended for straight wire characterization. [70] Variable strain rates of the SMA material depending on the position on and geometry of the knitted loop prohibit the prescription of a uniform strain rate. Macroscopic displacement rates as recommended for SMA wire are employed as a best approximation for isothermal conditions. Figure 2.4a displays the schematic temperature-control characterization strategy. The black arrows indicate the load path in a generic force-knit length profile on both the actuated (red) and relaxed (blue) states. This characterization strategy is the simplest and fastest to conduct and is therefore

employed when a fast bounding characterization is required. Applications that require the change of load-displacements behavior at a specific temperature, e.g., for safety mechanisms, are best characterized by the temperature-control strategy.

Figure 2.4b shows experimental results for a temperature-control characterization of a contractile SMA knitted actuator ($i_k = 138\,\mathrm{mm^2\,mm^{-2}}$, $d = 0.203\,\mathrm{mm}$). The actuated force-knit length data (red) shows three distinct stiffness regimes - initial structural high-stiffness, force plateau, and strain hardening regime. The initial structural high-stiffness regime ($k_{Tc,i} = 0.37\,\mathrm{N\,mm^{-1}}$) under low forces begins at displacements of approximately 30 mm and ends at 42 mm and forces of approximately 3.5 N. The force plateau is between 42 mm and 69 mm and the stiffness drops by a factor of 3 to $k_{Tc,p} = 0.12\,\mathrm{N\,mm^{-1}}$. The final strain hardening regime begins at 69 mm and the stiffness continuously increases with the application of additional strains. The relaxed force-knit length data (blue) of the contractile SMA knitted actuator exhibits the same strain-hardening behavior starting at 69 mm. However, for knit lengths below 69 mm the contractile SMA knitted actuator generates no force and can be displaced freely.

2.4.2 Displacement-Control

Displacement-control SMA knitted actuator characterization is the preferred characterization method for accurate predictions of the ability to generate forces while operating under constrained displacements. [77] In this characterization procedure, the SMA knitted actuator length is incrementally increased while the forces generated by the thermal transition from the fully-martensitic to the partially-austenitic states are measured. This characterization strategy resembles strain-controlled characterization strategies when the geometry of the specimen allows for the direction translation between displacements and strains. A generic force-knit length profile with the displacement-control characterization thermo-mechanical load path are presented in Figure 2.4c. Applications that utilize this load path, and are therefore best characterized by the displacement-control strategy, include compression garments for medical applications and mechanical counter-pressure space suits. [20]

Figure 2.4d displays the displacement-control characterization profiles of a contractile SMA knitted actuator ($i_k = 138\,\mathrm{mm^2\,mm^{-2}}$, $d = 0.203\,\mathrm{mm}$). The partially-austenitic profile exhibits the tri-linear behavior with a initial structural high-stiffness

regime ($k_{Dc,i} = 0.21\,\mathrm{N\,mm^{-1}}$) between 27 mm and 45 mm followed by the nearly horizontal force-plateau ($k_{Dc,p} = 0.02\,\mathrm{N\,mm^{-1}}$) up to 70 mm and the strain hardening regime with continuously increasing stiffness. The relaxed, fully-martensitic profile as characterized with the displacement-control method remains at a zero-load level up to 66 mm and enters the strain hardening regime at displacements larger than that.

2.4.3 Force-Control

Force-control SMA knitted actuator characterization is based on the measurement of the knit length while incrementally increasing the applied external force and sweeping through temperatures that transition the actuator between its fully-martensitic and partially-austenitic states at each force level. The force-control characterization strategy often materializes as a stress-controlled characterization when the geometry of the specimen allows for the direct translation between forces and stresses as is the case for uniaxial testing of wires. [79, 80] Figure 2.4e shows the generation of a generic force-knit length profile using the force-control characterization thermo-mechanical load path. The selection of the appropriate force-increment depends on the goal of the characterization. A finer characterization with around the actuator's natural operation points - maximum %-actuation contraction or maximum mechanical work - is often desirable.

The experimentally obtained force-control characterization of a contractile SMA knitted actuator ($i_k = 138\,\mathrm{mm^2\,mm^{-2}}$, $d = 0.203\,\mathrm{mm}$) are displayed in Figure 2.4f. The actuated, partially-austenitic profile shows a stiffness of $k_{Fc,i} = 0.17\,\mathrm{N\,mm^{-1}}$ in the initial structural high-stiffness regime which occurs at actuation forces between 0 N and 2 N. The force-plateau starts at 2 N with a stiffness of $k_{Fc,p} = 0.03\,\mathrm{N\,mm^{-1}}$. The relaxed, fully-martensitic profile exhibits its characteristic strain-hardening behavior, however, forces start increasing at knit lengths of approximately 50 mm using this characterization technique.

2.4.4 Thermo-mechanical Characterization Strategies Discussion

The three characterization strategies - temperature-, force- and displacement-control - produce force-knit length profiles of contractile SMA knitted actuators that are similar, but can show significant differences in mechanical behavior. This differences are discussed to derive universal qualitative trends based on the quantitative data of this

prototype. Most notable is the deviation of the partially-austenitic force-knit length profile obtained in the temperature-control (Figure 2.4b) characterization from those of the other two characterization strategies (Figure 2.4d,f). The initial structural high-stiffness regime is approximately twice as stiff in the temperature-control experiment when compared to the force- and displacement-control experiments. This high initial stiffness of $k_{Tc,i} = 0.37\,\mathrm{N\,mm^{-1}}$ (compared to $k_{Fc,i} = 0.17\,\mathrm{N\,mm^{-1}}$ and $k_{Dc,i} = 0.21\,\mathrm{N\,mm^{-1}}$) in the temperature-control experiment is caused by a superposition of characterization strategy-dependent frictional and displacement-rate effects. While the macroscopic displacement-rate ($4 \times 10^{-4}\mathrm{s^{-1}}$) of the temperature-control characterized knitted actuator is within the recommended range for SMA wire ($5 \times 10^{-5}\mathrm{s^{-1}} \leq \frac{\dot{\delta}}{l} \leq 4 \times 10^{-4}\mathrm{s^{-1}}$), the actual displacement rate of the knitted SMA wire is distributed along the highly-bent knitted loop and may exceed these limits. Increasing displacement-, force-, or temperature-rates can result in an artificial stiffening of the SMA knitted actuator through the exothermic release of heat that can cause local phase transitioning to the stiffer austenitic phase. [70] The effect is mitigated in the force- and displacement-control strategies as the knit undergoes a complete cooling and heating cycle after every incremental change in mechanical loading.

An additional factor to the larger stiffness in the temperature-control strategy is the increased contribution of frictional effects to the SMA knitted actuator performance based on the strategy-specific thermo-mechanical load path. Frictional effects are important for SMA knitted actuators because of the many contact points between interlocking loops. Frictional forces generally inhibit the motion (elongation and contraction) of the knitted actuator, resulting in an artificial stiffening of the knitted actuator. In the temperature-control characterization strategy, the contractile SMA knitted actuator is heated to a temperature above the austenite finish temperature to characterize the actuated force-knit length profile. Under zero mechanical loading conditions, the SMA knitted actuator contracts into its initial high stiffness state with a contact angle (α) that leads to large frictional contributions that dominate the force equilibrium (Figure 2.5). Under these conditions, the forces on each loop contact point in the contractile SMA knitted actuator increase as the knitted actuator is elongated. The large angle between the normal contact and the externally applied forces contribute to the relatively stiff actuated force-knit length profile using the temperature-control experiment as opposed to the similar actuated force-knit length profiles obtained in the force- and

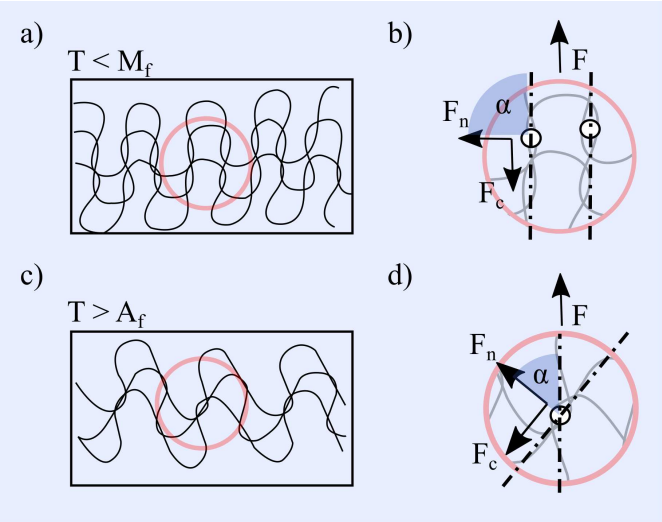

Figure 2.5: **Frictional Artificial Stiffening:** The SMA knitted actuator loop geometries under small externally applied forces (F) are unequally favorable for relative sliding. (a) In the fully-martensitic state, knitted loops are well aligned with (b) the external loading direction resulting in negligible normal (F_n) and contact ($F_c = \mu F_n$) forces. (c) In the partially-austenitic state, the knitted loops interlock into a configuration (d) less favorable to relative sliding as the normal contact force has large components in the externally applied loading direction.

displacement-control characterization strategies.

The other force-knit length variation occurs in the relaxed force-knit length profile. The relaxed force-knit length profile of the force-control characterization strategy displays an earlier onset (at 50 mm as opposed to 68 mm) of strain-hardening when compared with the other characterization strategies. This difference between characterization strategies is predominantly caused by the thermal cycling at constant low macroscopically applied forces in the force-control characterization strategy. The frictional mode at the interlacing points of contractile SMA knitted actuators is stick-slip. Under low constantly applied forces as present in the force-control characterization strategy, the static friction resists the full potential elongation of the knitted actuator as slipping does not occur or only partially occurs. In the other characterization strategies, the knitted actuator is subject to larger forces as a result of the varied thermo-mechanical load path, and the actuator extends to larger lengths at the respective forces.

Understanding the differences between the characterization strategies is of acute importance when attempting to operate SMA knitted actuators. The experimental data

discussed in this section shows that the characterization strategy can affect the operational performance as found for other SMA systems by the Consortium for the Advancement of Shape Memory Alloy Research and Technology (CASMART). [77] It is advisable to utilize the appropriate characterization strategy for the desired actuator functionality: temperature-control for binary stiffness/displacement application, force-control for displacement-generation applications and displacement-control for force-generation applications.

2.5 Performance Repeatability

The derivation of guidelines and standards for design, characterization, and operation of SMA knitted actuators requires knowledge of the reproducibility of the SMA knitted actuator performance between same parameter prototypes. Performance repeatability is the consistency of SMA knitted actuator performance metrics when SMA knitted actuator prototypes of constant material and geometric properties are analyzed. Multiple instances of the reference prototype ($i_k = 138\,\mathrm{mm^2\,mm^{-2}}, d = 0.203\,\mathrm{mm}$) are investigated for the consistency of their thermo-mechanical performance using the force-control characterization strategy, specifically their temperature-dependent force-knit length response as well as their %-actuation contraction profiles.

2.5.1 Performance Repeatability Results

Figure 2.6a displays the partially-austenitic (red) and fully-martensitic (blue) force-knit length profiles of three constant property prototypes. The experimental data of the different data sets is indicated by the geometry (rectangle, circle, diamond) of the data points. The solid lines represent the mean force-knit length profiles of the tested prototypes in their fully-martensitic ($\bar{l}_m$) and partially-austenitic ($\bar{l}_a$) states. The mean partially-austenitic stiffness in the initial structural high-stiffness regime $\bar{k}_{fc,i} = 0.17\,\mathrm{N\,mm^{-1}}$ as well as in the force-plateau regime $\bar{k}_{fc,i} = 0.03\,\mathrm{N\,mm^{-1}}$ are comparable to the data collected for the characterization strategy comparison of Section 2.4.3. It is apparent that the prototype represented by the circular symbols is on average 3 mm longer when compared to the other two prototypes at respective forces. This occurs in both the partially-austenitic as well as the fully-martensitic curve.

The actuation-contraction plot (Figure 2.6b) shows the %-actuation contraction (ζ)

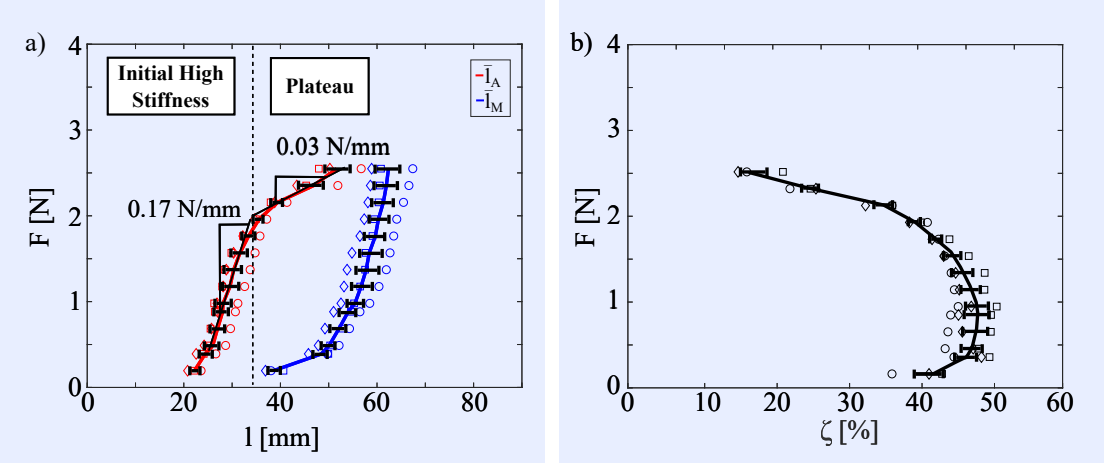

Figure 2.6: **Performance Stability:** (a) Three reference prototypes with constant mesoscopic ($d = 0.203\,\text{mm}$ and $i_k = 138\,\text{mm}^2\,\text{mm}^{-2}$) and macroscopic ($g = h = 15$) properties present consistent temperature-dependent force-knit length responses. The maximum percentual difference between the mean (solid line) and the prototype performance at respective forces is less the 9%. (b) The %-actuation contraction profiles show consistent performance between the prototypes with increasing consistency at increasing forces.

plotted against the applied force in the force-control characterization. All three prototypes have their maximum %-actuation contraction at $F_{\hat{\zeta}} = 1\,\text{N}$ ranging between $\hat{\zeta} = 44 - 49\%$.

2.5.2 Performance Repeatability Discussion

The tested prototypes produce repeatable performance. The maximum absolute difference between the prototype knit length and the mean under constant applied forces ($|l_{max} - l_{min}|$) is smaller than 5 mm which corresponds to a maximum percentual deviation of 7%. The measured deviations of the mean knit length are consistent between the partially-austenitic and the fully-martensitic profiles, i.e., prototypes that are consistently above the mean knit length in the partially-austenitic state are also consistently above the mean knit length in the fully-martensitic state. This consistent knit length deviation is likely caused by a slight variation in the manufacturing process or attachment to the testing fixture. The actuation plot shows increased repeatability between prototypes for higher applied forces as opposed to low applied loads. Frictional effects

are most affected by slight manufacturing inconsistencies and represent a large contributor to the force equilibrium at low applied forces resulting in the larger inconsistency of the actuation profiles. The performance repeatability is a metric of the manufacturing consistency. It is therefore advised to understand the repeatability of the manufacturing method.

2.6 Thermo-mechanical Shakedown

A prominent and well-researched SMA material phenomenon is the material shakedown, which describes the degradation of the SMA recoverable strain within the first one-hundred thermo-mechanical cycles. [81, 82] The thermo-mechanical material shakedown response generally stabilizes after a load-dependent number of cycles. The Dynalloy Flexinol® SMA filament is thermo-mechanically conditioned by the supplier to overcome these effects and provide SMA filament with stable performance within the specified loading limits of the SMA wire. Traditional knitted architectures are also often subjected to conditioning processes such as mechanical and chemical treatment (dry or wet relaxation, washing processes, and ultrasonic waves) to achieve consistent loop geometries and mechanical performance. [83, 9]

2.6.1 Thermo-mechanical Shakedown Results

Architectural and thermo-mechanical shakedown effects were investigated in thermo-mechanical cyclic loading experiments under uniaxial repetitive loading and unloading using the reference prototype geometry ($i_k = 138\,\mathrm{mm^2\,mm^{-2}}, d = 0.203\,\mathrm{mm}, g = h = 15$). Three prototypes were thermally loaded for 70 cycles under constant applied loads $F = [1.0, 2.0, 2.5]$N in the force-control characterization strategy. The number of cycles was chosen to resolve initial effect while being considerate of experiment run times. The schematic temperature-knit length diagram (Figure 2.7a) shows the decrease of knit length at temperatures above the stress-free austenite finish temperature (A_s) and the increase of knit length when the temperature approximates the martensite start temperature (M_s).

The thermo-mechanical uniaxial cyclic loading experiments resolved the initial (70 cycles) displacement response of contractile SMA knitted actuators upon controlled applied loads and temperatures swept between $T = 20 - 120$°C. Figure 2.7b-d show the

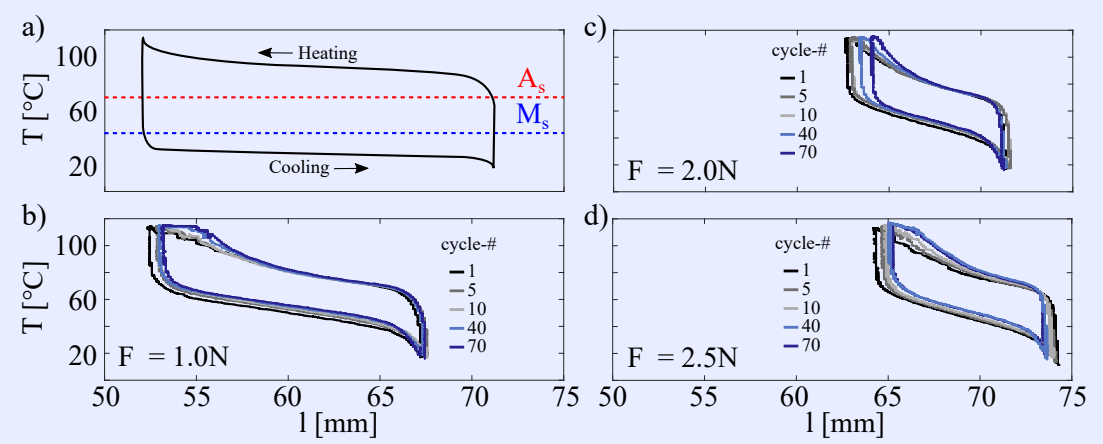

Figure 2.7: **Thermo-mechanical Architectural Shakedown:** The schematic temperature-knit length plot indicating (a) the heating and cooling directions as well as the three thermo-mechanical shakedown temperature knit length profiles at the externally applied loads (b) $F = 1.0\,\mathrm{N}$, (c) $F = 2.0\,\mathrm{N}$, (d) and $F = 2.5\,\mathrm{N}$. Displayed are the cycles $n = [1, 5, 10, 40, 70]$.

three cyclic responses, specifically thermal cycles $n = [1, 5, 10, 40, 70]$, in the temperature-knit length profiles at the forces $F = [1.0, 2.0, 2.5]$N, respectively. At all applied forces, a shakedown, i.e an increase of the partially-austenitic knit length occurs within the first 70 cycles. At $F = 1.0\,\mathrm{N}$, the partially-austenitic knit length increases by $\Delta_{a,1.0\,\mathrm{N}} = 0.89\,\mathrm{mm}$ (1.6%) in the first 70 cycles. Similarly, at $F = 2.0\,\mathrm{N}$ the partially-austenitic knit length increases by $\Delta_{a,2.0\,\mathrm{N}} = 1.4\,\mathrm{mm}$ (2.2%) and $\Delta_{a,2.5\,\mathrm{N}} = 1.38\,\mathrm{mm}$ (2.2%) under constantly applied forces $F = 2.0\,\mathrm{N}$ and $F = 2.5\,\mathrm{N}$, respectively. Similarly, the fully-martensitic knit length first increases and subsequently decreases after reaching its peak. At $F = 1.0\,\mathrm{N}$, the fully-martensitic knit length peaks at cycles $n = 30$ and decreases by $\Delta_{m,1.0\,\mathrm{N}} = 0.51\,\mathrm{mm}$ (0.7%) until cycle 70. At $F = 2.0\,\mathrm{N}$ and $F = 2.5\,\mathrm{N}$, the fully-martensitic knit length decreases from cycle 9 on by $\Delta_{m,2.0\,\mathrm{N}} = 0.5\,\mathrm{mm}$ (0.7%) and from cycle 2 on by $\Delta_{m,2.5\,\mathrm{N}} = 0.81\,\mathrm{mm}$ (1.1%), respectively. Consequently, the envelope of actuation decreases until stable actuation is accomplished. Under all applied loads, an initial phase of variability in %-actuation contraction occurs until the 5-th cycle. From then on, the contractile ability of the knitted actuator slowly degrades. Between the cycles 5 and 70, the contractile SMA knitted actuator's contractile ability decreases by $\Delta_{\hat{\zeta},2.5\,\mathrm{N}} = 1.29$pp, $\Delta_{\hat{\zeta},2.0\,\mathrm{N}} = 1.23$pp, and $\Delta_{\hat{\zeta},1.0\,\mathrm{N}} = 0.75$pp showing the trend of larger degradation under higher applied mechanical loads.

2.6.2 Thermo-mechanical Shakedown Discussion

The SMA knitted actuator performance decreases at a larger rate initially and stabilizes in the first 70 cycles for the three prototypes subjected to different constant mechanical loads. Two major effects contribute to low-cycle SMA knitted actuator performance: architectural and material shakedown. The initial increase in fully-martensitic knit length and partially-austenitic knit length are caused by a resolution of inconsistencies in the knitted actuator architecture from manufacturing when cycled under applied loads. Larger applied loads result in a quicker resolution of the manufacturing inconsistencies - the peak fully martensitic knit length occurs in cycle 2 under $F = 2.5\,\mathrm{N}$, cycle 9 under $F = 2.0\,\mathrm{N}$ and cycle 30 under $F = 1.0\,\mathrm{N}$

Additionally, material shakedown is likely responsible for the degradation of the fully-martensitic knit length. Certain portions of the knitted loop experience significant overloading from large bending stresses while others operate within the supplier specified load limits (138 MPa leads to 1% plastic strain at 100,000 cycles). Local stresses within the knitted loop may exceed these manufacturer limits significantly which can lead to a local deterioration of the material performance [82] that can be caused by microstructural effects such as the increase in R-phase upon thermal cycling. [84]

Higher applied external loads result in faster architectural and material shakedown of the SMA knitted actuator. The austenite knit length only increases by 1.6% under applied loads of $F = 1.0\,\mathrm{N}$ whereas it increases by 2.2% under $F = 2.0\,\mathrm{N}$ and $F = 2.5\,\mathrm{N}$. Similarly, the martensite knit length decreases by 0.7% under applied loads of $F = 1.0\,\mathrm{N}$ and $F = 2.0\,\mathrm{N}$, whereas it decreases by 1.1% under $F = 2.5\,\mathrm{N}$.

The low-cycle performance is affected by architectural and material shakedown. While architectural shakedown produces larger actuator performance, the material shakedown results in a degradation of the actuator performance. Large bending radii and smaller applied loads limit the material shakedown due to overloading of the active material. For lifetime performance predictions, an investigation of the initial architectural and material shakedown up to a larger cycle number is desirable.

2.7 Actuation & Relaxation Temperatures

The phase transformation temperatures of SMAs, the austenite start (A_s), austenite finish (A_f), martensite start (M_s), and martensite finish (M_f) temperatures under

stress-free conditions are specific to the filament material. The specific transition temperatures of the Dynalloy Flexinol® filament used in this publication can be found in Section 2.2.3. As the SMA filament in the knitted architecture is not stress-free, the phase transition temperatures may not resemble the actuation and relaxation of SMA knitted actuators. This section defines the SMA knitted actuator actuation and relaxation temperatures and compares them to the filament phase transition temperatures to discuss the relevant factors that result in the variation of the actuation temperatures.

2.7.1 Actuation & Relaxation Temperature Definition

The definition and analysis of the actuation (T_a) and relaxation (T_r) temperatures is conducted from uniaxial tensile experimental data that relates the knit length, actuation forces, and temperature as thermoanalytical procedures such as DSC are inapplicable for knitted actuators. The tangent-intercept method [85] which has been used to determine the phase transition temperatures of SMA from temperature-extension profiles is employed for the definition of the actuation and relaxation temperatures of SMA knitted actuators (Figure 2.8). The actuation temperature is defined as the point at which plateau tangents intercept in the heating portion of the temperature-knit length profile, whereas the relaxation temperature is the point at which plateau tangents intercept in the cooling cycle of the temperature-knit length profile.

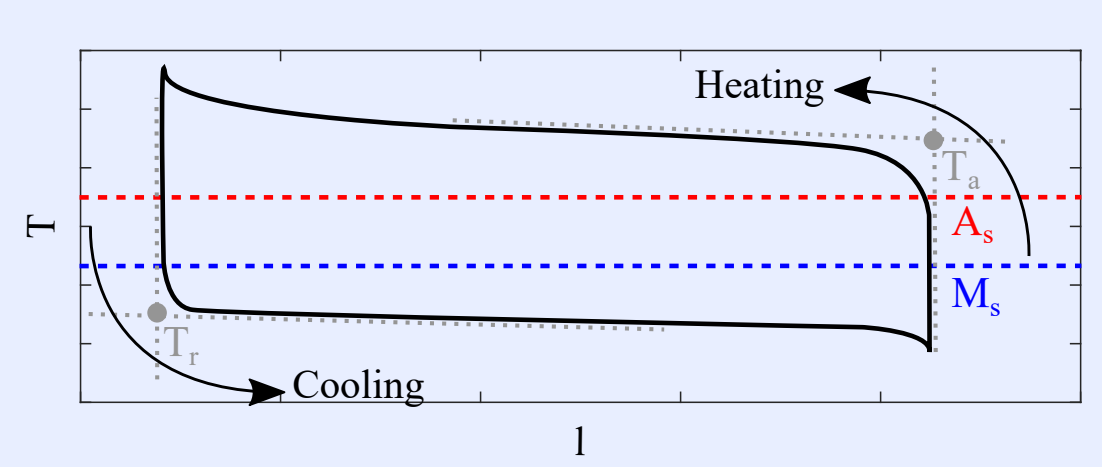

Figure 2.8: **Relaxation and Actuation Temperatures:** The actuation (T_a) and relaxation (T_r) temperatures are determined using the tangent-intercept method in the temperature-knit length profile.

2.7.2 Actuation & Relaxation Temperature Results

Figure 2.9a shows the actuation and relaxation temperatures increase with increasing applied forces on constant geometric parameter prototypes. Under small applied loads ($F = 0.4\,\mathrm{N}$), the relaxation temperature ($T_{r,0.4N} = 20.5\,^{\circ}\mathrm{C}$) is below the martensite finish temperature of the SMA filament. With increasing externally applied loads, the relaxation temperature steadily increases to levels above the stress-free martensite start temperature. Knit relaxation occurs at a temperature of $T_{r,2.2N} = 58\,^{\circ}\mathrm{C}$ under the highest applied load ($F = 2.2\,\mathrm{N}$). Similarly, the actuation temperature increases with increasing externally applied loads. The actuation temperatures range from $T_{a,0.4N} = 67\,^{\circ}\mathrm{C}$ to $T_{a,2.2N} = 96\,^{\circ}\mathrm{C}$.

The SMA knit geometry, defined by the SMA filament wire diameter and the knit index, also affects the actuation and relaxation temperatures. Figure 2.9b displays temperature-extension plots for prototypes of varying knit indices between $i_k = 39\frac{\mathrm{mm}}{\mathrm{mm}}$ and $i_k = 138\,\mathrm{mm}^2\,\mathrm{mm}^{-2}$ under constant wire diameters ($d = 0.203\,\mathrm{mm}$) and constant applied external loads ($F_{app} = 1.5\,\mathrm{N}$). Scaling of prototypes' knit lengths (l) by their partially austenitic knit length (l_a) was performed due to the large differences of absolute knit lengths between the analyzed prototypes. The relaxation temperatures increase with increasing knit indices from $T_{r,39\,\mathrm{mm}^2\,\mathrm{mm}^{-2}} = 34\,^{\circ}\mathrm{C}$ to $T_{r,138\,\mathrm{mm}^2\,\mathrm{mm}^{-2}} = 40.5\,^{\circ}\mathrm{C}$. The actuation temperatures decrease with increasing knit indices from $T_{a,39\,\mathrm{mm}^2\,\mathrm{mm}^{-2}} = 92.5\,^{\circ}\mathrm{C}$ to $T_{a,138\,\mathrm{mm}^2\,\mathrm{mm}^{-2}} = 81.5\,^{\circ}\mathrm{C}$.

2.7.3 Actuation & Relaxation Temperature Discussion

It is important to understand the differences between the actuation/relaxation temperatures and stress-free SMA filament transition temperatures. While the transition temperatures are a material property, the actuation and relaxation temperatures are a combination of material and knit architecture properties. The SMA knit actuation and relaxation temperatures are dependent on the SMA knitted actuator stresses and the structural friction within the SMA knitted actuator. The increase of relaxation temperatures with increasing applied loads in Figure 2.9a is caused by the increased stresses within the SMA knitted actuator under higher externally applied loads. The drop of relaxation temperatures under low applied loads $T_{r,0.4N} = 20.5\,^{\circ}\mathrm{C}$ below the martensite start temperature ($M_s = 44\,^{\circ}\mathrm{C}$) is a knit architectural phenomenon and stems from the

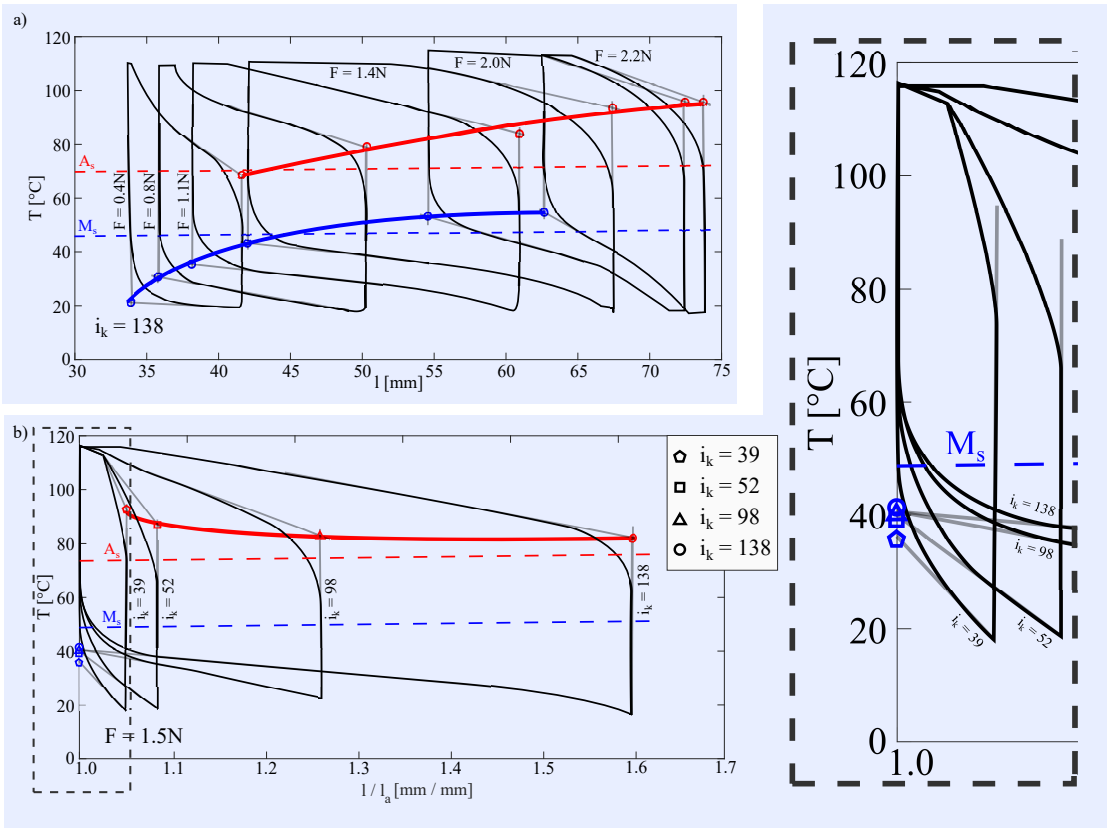

Figure 2.9: **Actuation & Relaxation Temperature Dependencies:** (a) Temperature-length profiles for $d = 0.203\,\text{mm}$ and $i_k = 138\,\text{mm}^2\,\text{mm}^{-2}$ contractile SMA knitted actuators under various constant applied forces show increasing actuation and relaxation temperatures with increasing applied forces. (b) The scaled temperature-knit length profiles of varying knit indices show increasing actuation and relaxation temperatures with decreasing knit indices.

limitation of actuation displacements through frictional forces at the loop interlocking points. Only under sufficiently high externally applied loads ($F > 1.4\,\text{N}$) shift the balance between relaxation-temperature increasing stresses on the material and relaxation-temperature suppressing frictional effects to levels above the stress-free martensite start temperature. Material stresses and architectural friction also shape the actuation temperature behavior of constant geometry SMA knitted actuators. However, since the contractile SMA knitted actuator displaces in the opposite direction when heated, frictional effects and material stresses both result in an increase of actuation temperatures.

Additionally, frictional effects contribute to a lesser degree to the change in actuation temperatures as friction contributes only marginally to the force-equilibrium in the displacement path upon heating from the highly regular fully-martensitic loop configuration to the partially-austenitic loop configuration. Consequently, the actuation temperature approximately equates the austenite start temperature under low applied forces ($F = 0.4\,\mathrm{N}$). The increasing stresses in the SMA material under higher applied loads result in an increase of the actuation temperature.

The actuation and relaxation temperatures of variable knit geometry prototypes under constant applied forces also shift with the varying contribution of material stresses and architectural friction. The small knit index prototypes are close looped knitted with larger contact angles which increase the contribution of knit architectural frictional effects. The decrease of relaxation temperatures from the high knit index prototype ($i_k = 138\,\mathrm{mm^2\,mm^{-2}}$) to the low knit index prototype ($i_k = 39\,\mathrm{mm^2\,mm^{-2}}$) suggests that the behavior is friction-dominated as it overshadows the inverse contribution of increased material stresses. In contrast, the actuation temperatures increase with decreasing knit indices as the material stresses also increase. As previously discussed, the load path from the fully-martensitic to the partially-austenitic loop configuration is frictionally-favorable explaining the dominance of the material stress contribution.

Significant changes in actuation and relaxation temperatures can occur in knitted actuators of varied geometric parameters and applied loading. While the material transition temperatures can provide a good starting point for the determination of the actuation and relaxation temperatures, an exact analysis may be required for sensitive applications. The derived trends for the actuation and relaxation temperature behavior should be considered when characterizing and operating SMA knitted actuators to ensure that the full actuator performance is exploited or partial actuation is properly harnessed.

2.8 Homogenous Knit Scalability

Contractile SMA knitted actuators consist of h knitted loops in the course-wise and g knitted loops in the wale-wise directions. The effect of changing the number of loops in both directions on the contractile SMA knitted actuator performance is explored in the following sections through comparison of the actuator performance under varying

numbers of knitted loops in uniaxial force-controlled tensile experiments.

2.8.1 Homogenous Knit Length Scalability

The SMA knitted actuator knit length is geometrically determined by the height of the knitted loop (course height) and the number of loops that are aligned in the knitting direction (course-wise direction). While the course height contributes to the knit length, it is not scalable independently from other knit geometric parameters such as the loop width (wale width) and the knit index. Consequently, the %-actuation contraction is affected when scaling the knit length through adjustment of the course height. This section introduces the knit performance upon scaling the knit length through changing the number of courses. The top-left corner of Figure 2.10a graphically exemplifies the concept of course-scaling in a knitted architecture.

Contractile SMA knitted actuators of consistent ($i_k = 138\,\mathrm{mm^2\,mm^{-2}}$, $d = 0.203\,\mathrm{mm}$) knit loop parameters consisting of 15 wales were manufactured with varying numbers (h) of courses to assess the scalability of knit length performance. Four different prototypes with $h = [5, 10, 15, 20]$ were tested using the force-control strategy and compared. Figure 2.10a and b show the force-knit length plots of all for prototypes in the fully-martensitic and partially-austenitic states respectively. The force-knit length plots show their characteristic behavior with simple strain-hardening behavior in the fully-martensitic state and the trilinear behavior of initial high stiffness, plateau, and strain-hardening regimes in the partially-austenitic state. A consistent increase in knitted actuator lengths with increasing number of courses occurs in both the fully-martensitic and partially-austenitic states.

The scalability of the knit length is supported by Figures 2.10c and d, which display the force-knit length data of the prototypes scaled by their individual number of courses. The prototypes with a number of courses $h \geq 10$ show scalability while the performance of the prototype with 5 courses differs in both the fully-martensitic and partially-austenitic curves. The differences between the scaled prototypes with $h \geq 10$ and their mean are comparable to the performance variance between constant geometry SMA knitted actuators established in Section 2.5. The existence of a lower scalability bounds is caused by boundary conditions in the coursewise direction. SMA knitted actuators of critically low numbers of loops in the coursewise direction are dominated by their boundary conditions. SMA knitted actuators of $h \geq 10$ are affected by their

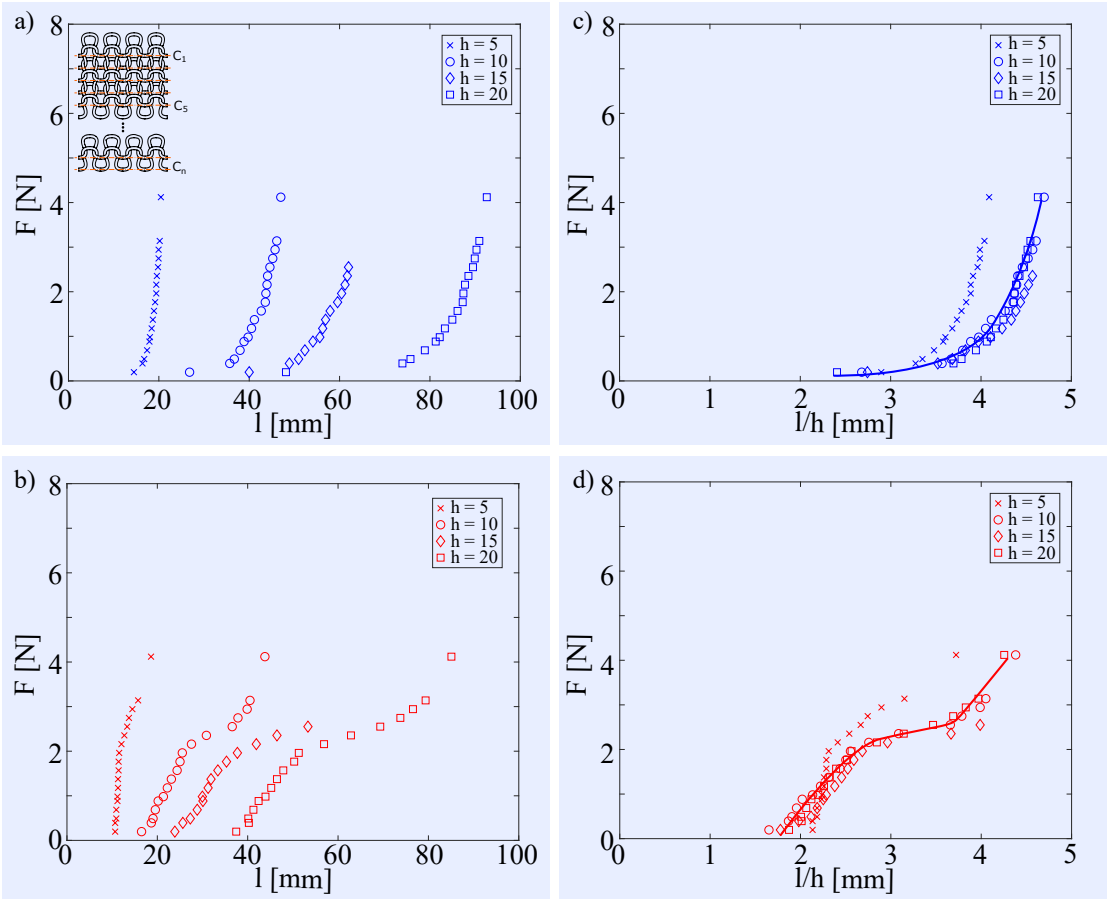

Figure 2.10: **Knit Length Scaling:** (a) Schematic coursewise scaling is shown in the upper left corner. Force-knit length profiles of the (a) fully-martensitic and (b) partially-austenitic prototypes show increasing knit lengths with increasing numbers of courses ($h = [5, 10, 15, 20]$). Scaling of the knit length by the number of courses ($\frac{l}{h}$) demonstrates the scalability of the knitted actuator performance with the number of courses for $h \geq 10$ for (c) fully-martensitic and (d) partially-austentitic profiles.

boundary conditions towards the edges, however, consistent scalable performance is accomplished in the boundary-condition-free center of the SMA knitted actuator.

Derived from the force-knit length data in the partially-austenitic and the fully-martensitic states are the %-actuation contraction plots of Figure 2.11. As the fully-martensitic and partially-austenitic force-knit length profiles are scalable for $h \geq 10$, their force-%-actuation contraction profiles overlay consistently with a maximum error of 4pp at maximum %-actuation contraction. The outlier, again, is the prototype with $h = 5$, which performs less %-actuation contraction at respective forces due to the

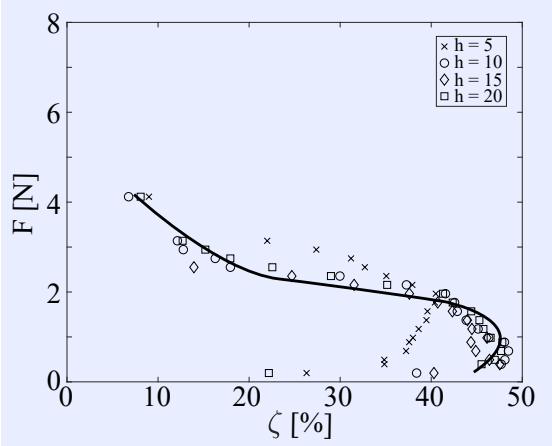

Figure 2.11: **Length Scaling Effect on Actuation Contraction:** The %-actuation contraction profiles of contractile SMA knitted actuators with $h \geq 10$ is independent of the number of courses.

dominant boundary conditions.

2.8.2 Homogenous Knit Force Scalability

SMA knitted actuator prototypes of constant ($i_k = 138\,\mathrm{mm}^2\,\mathrm{mm}^{-2}, d = 0.203\,\mathrm{mm}$) knit loop parameters were manufactured with 15 courses while varying the number g of knitted loops in the walewise direction to modify the width of the knitted actuator. Prototypes with $g = [5, 10, 15, 20, 30]$ were tested using the force-control strategy for their uniaxial tensile force-knit length response. Scaling of the number of knitted loops in the walewise direction is depicted in the upper-left corner of Figure 2.12a.

Figure 2.12a and c contain the force-knit length data of the fully-martensitic and partially-austenitic states. The data shows an increase in SMA knitted actuator stiffness with increasing numbers of loops in the walewise direction. The scalability of that stiffness increase is shown in Figure 2.12b and d, which scale the actuation forces of each prototype by their respective number of knitted loops in the walewise direction. The data suggests the scalability of actuation forces for SMA knitted actuators with $g \geq 15$ number of loops in the walewise direction within the consistency bounds discussed in Section 2.5. The SMA knitted actuator force scalability is subject to a lower boundary because of the presence of boundary conditions on the edges of the actuator. Similar to the knit length scalability, a minimum number of loops is required in the walewise

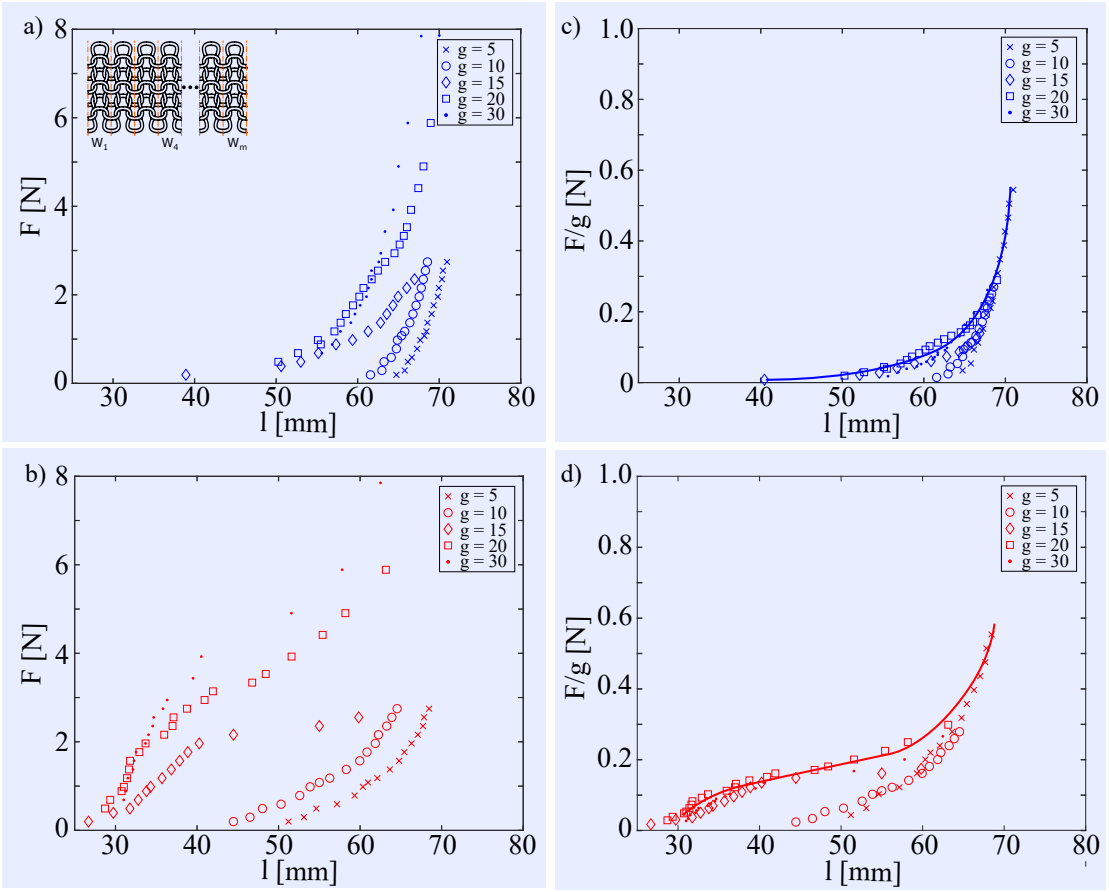

Figure 2.12: **Knit Force Scaling:** (a) Schematic walewise scaling is shown in the upper left corner. Force-knit length profiles of the (a) fully-martensitic and (b) partially-austenitic prototypes show increasing knit force with increasing numbers of wales ($g = [5, 10, 15, 20, 30]$). Scaling of the knit force by the number of wales ($\frac{F}{g}$) demonstrates the scalability of the knitted actuator performance with the number of wales for $g \geq 15$ for the (c) fully-martensitic profile and the (d) partially-austenitic profiles.

direction to prohibit a boundary-condition-dominated performance.

The resulting force-%-actuation contraction profiles (Figure 2.13) support the force scalability of the SMA knitted actuator performance. Figure 2.13a presents the unscaled data for the tested prototypes, whereas Figure 2.13b contains the same data with applied scaling of the actuation forces with the numbers of loops in the walewise direction. The scaled profiles of prototypes with $g \geq 15$ show maximum %-actuation contractions within an error margin of 2pp.

2.8.3 Homogenous Knit Scalability Discussion

Establishing the scalability of the SMA knitted actuator thermo-mechanical performance with regards to the number of courses and wales closely resembles the abstractions used in traditional spring design. Consider a homogenous knit pattern consisting of a single knitted loop geometry (knit index and wire diameter). Such a knit pattern consists of a number of knitted loops in parallel connection forming a course and a number of knitted loops in serial connection forming a wale. Every knitted loop in the knit pattern has a stiffness ($k(\varepsilon, \sigma, T)$) that depends on the material strains (ε), stresses (σ), and the temperature (T). The results of the knit length scalability supports the derivation of the serial connection rule

$$l_{knit}(T) = \sum_{i=1}^{h} l_i(T), \quad F_{knit}(T) = F_i(T) = F_h(T) \tag{2.3}$$

with the total knit length (l_{knit}) equating the sum of the height of all knitted courses (l_h) while the forces (F_h) remain constant independent of the number h of courses. Consequently, the knit stiffness (k_{knit}) is defined

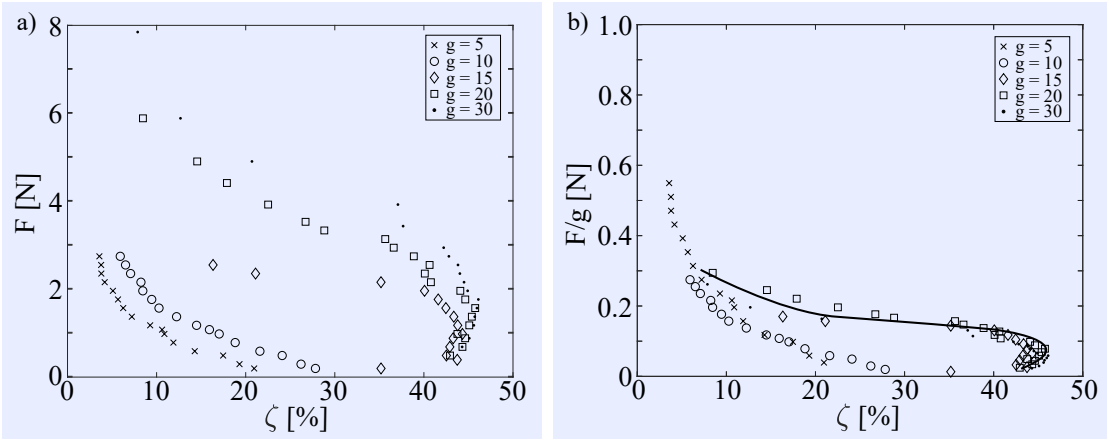

Figure 2.13: **Force Scaling Effect on Actuation Contraction:** (a) The %-actuation contraction profiles of prototypes with varying numbers g wales show an increase in forces at constant %-actuation contractions with increasing numbers of wales. (b) Scaling of the knit force by the number of wales ($\frac{F}{g}$) demonstrates the scalability of the knitted actuator performance with the number of wales for $g \geq 15$.

$$\frac{1}{k_{knit}(T)} = \sum_{i=1}^{h} \frac{1}{k_i(T)} \tag{2.4}$$

through the inverse sum of the knitted loop stiffnesses (k_h). The stiffnesses of the prototypes with 10 and 20 courses (Figure 2.10a) validate this mathematical description as the doubling of the number of courses to $h = 20$ results in a stiffness ($k_{20} = 0.12\frac{\mathrm{N}}{\mathrm{mm}}$) in a representative force region between 1 N and 2 N. This equates to the inverse sum of the stiffness ($k_{10} = 0.25\frac{\mathrm{N}}{\mathrm{mm}}$) of two $h = 10$ prototypes. Similarly, the addition of wales can be regarded as parallel connection and follows the rules

$$F_{knit}(T) = \sum_{i=1}^{g} F_i(T), \quad l_{knit}(T) = l_i(T) = l_g(T) \tag{2.5}$$

of summation of all parallel knit loop forces $F_g(T)$ to calculate the the knitted actuator force ($F_k(T)$) while the knit loop lengths are equal for all parallel knit loops. This renders the knit loop stiffness ($k_{knit}(T)$) in parallel connections to be a simple summation

$$k_{knit}(T) = \sum_{i=1}^{g} k_i(T) \tag{2.6}$$

of the individual loop stiffnesses ($k_g(T)$). The data from Figure 2.12a supports this mathematical formulation as the stiffness of the 30 wale prototype between 1 N and 2 N is ($k_{30} = 0.29\,\mathrm{N\,mm^{-1}}$) which is twice the stiffness of the 15 wale prototypes ($k_{15} = 0.14\,\mathrm{N\,mm^{-1}}$). These derived rules only apply to approximately linear regions of the knitted actuators. Additional restriction are set by the lower number of knitted loops in the walewise and coursewise directions.

The difference of the minimal required loops in the walewise and coursewise directions suggests that the boundary conditions resulting from the attachment of the knitted actuator in the uniaxial tensile tester represent a better approximation of an infinite knit structure ($h_{min} = 10$), whereas the boundaries at the horizontal edges of the knitted actuator are more inhibiting ($g_{min} = 15$) and consequently a worse approximation of an infinite, perfect knitted actuator.

2.9 Inhomogenous Knit Scalability

The serial and parallel connection equations of Section 2.8.3 were derived using homogenous contractile SMA knitted actuators that consist of knitted loops with constant knit index. The applicability of the serial and parallel connection equations for the inhomogenous knitted actuator design space was experimentally investigated in force-control uniaxial tensile experiments.

2.9.1 Inhomogenous Knit Length Scalability

A prototype made up of two sections in serial connection each containing 15 loops in the course- and walewise direction was manufactured (Figure 2.14a). Section 1 is comprised of 15 courses with knitted loops of a knit index ($i_{k,1} = 52\,\mathrm{mm}^2\,\mathrm{mm}^{-2}$), whereas section 2 consists of 15 courses with a knit index ($i_{k,2} = 138\,\mathrm{mm}^2\,\mathrm{mm}^{-2}$). The mechanical performance of this serial connection inhomogenous prototype is compared to the mechanical performance of its homogenous sections and the sum of the knit lengths of the individual sections in Figure 2.14b.

The SMA knitted actuator knit length of the serial connection aligns well with the knit length-sum of the two individual homogenous knit patterns in the fully-martensitic state. The discrepancy between the experimentally obtained serial connection and the prediction based on the sum of the individual homogenous prototypes present in the

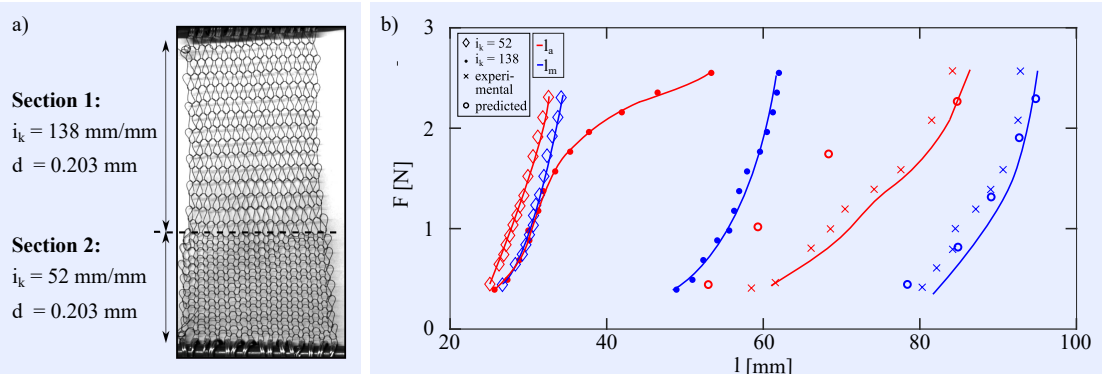

Figure 2.14: **Inhomogenous Knit Length Scalability:** (a) An inhomogenous prototype was manufactured through the serial connection of section 1 with a knit index ($i_{k,1} = 52\,\mathrm{mm}^2\,\mathrm{mm}^{-2}$) - and section 2 with a knit index ($i_{k,2} = 138\,\mathrm{mm}^2\,\mathrm{mm}^{-2}$). (b) The experimental performance of the serial connection, single sections, and the predicted knit length-sum of the single sections supports knit length scalability.

partially-austenitic state under low applied is likely caused by the introduction of a new knit-knit boundary (Figure 2.14a - dashed line) and the elimination of two tensile tester attachment boundaries. The variation in knit performance introduced by boundaries is maximized in the partially-austentitic state and under low applied loads as shown in Section 2.5. Comparison of the fully-martensitic stiffnesses of the experimental and experimental data between 1.0 N and 2.0 N supports the applicability of the knit length scalability formulae. The fully-martensitic stiffnesses of the homogenous prototypes in this load range are ($k_{i_k=138} = 0.27\,\mathrm{N\,mm^{-1}}$) and ($k_{i_k=52} = 0.3\,\mathrm{N\,mm^{-1}}$) whereas the fully-martensitic stiffness of the inhomogeneous prototypes is ($k_{serial} = 0.154\,\mathrm{N\,mm^{-1}}$).

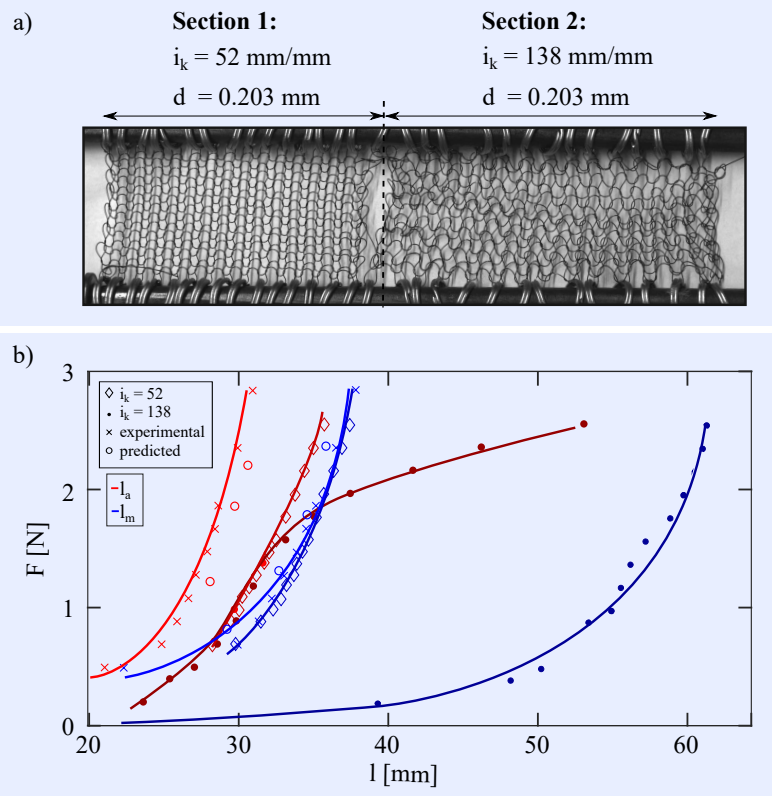

Figure 2.15: **Inhomogenous Knit Force Scalability:** (a) An inhomogenous prototype was manufactured through the parallel connection of section 1 with a knit index ($i_{k,1} = 52\,\mathrm{mm^2\,mm^{-2}}$) - and section 2 with a knit index ($i_{k,2} = 138\,\mathrm{mm^2\,mm^{-2}}$). (b) The experimental mechanical performance of the parallel connection, single sections, and the predicted force-sum of the single sections is supports force scalability.

2.9.2 Inhomogenous Knit Force Scalability

The inhomogenous knit force scalability was tested with a parallel connection prototype that contains varying knit indices in the walewise direction. Two prototypes with knit indices ($i_{k,1} = 52\,\mathrm{mm^2\,mm^{-2}}$) and ($i_{k,2} = 138\,\mathrm{mm^2\,mm^{-2}}$) with 15 wales and courses were connected in parallel in the uniaxial tensile experiment (Figure 2.15a).

Similarly to the serial connectivity, the mechanical performance of the parallel connection, the single sectionss, and the force-sum of the single sections is displayed in Figure 2.15b. Figure 2.15b supports the knit force scalability with inhomogenous knitted actuators. The force-knit length profile of the parallel connection inhomogenous knitted actuator agrees well with the force-sum of the individual prototypes. The partially-austenitic stiffnesses of the homogenous prototypes in this load range are ($k_{i_k=138} = 0.16\,\mathrm{N\,mm^{-1}}$) and ($k_{i_k=52} = 0.2\,\mathrm{N\,mm^{-1}}$) whereas the stiffness of the inhomogenous prototypes is ($k_{serial} = 0.35\,\mathrm{N\,mm^{-1}}$).

2.9.3 Inhomogenous Knit Scalability Discussion

The selection of the tested prototypes displays the intriguing capabilities of serial and parallel connection of variable knit indices. Force- and knit length-scalability can be accomplished through parallel and serial connection. Intentional selection of the parallelly and serially connected prototypes enables the manipulation of either both or just one of the fully-martensitic or partially-austenitic profiles. For example, the serial connection of Section 2.9.1 manipulates both the fully-martensitic and partially-austenitic profiles. In contrast, the parallel connection of the two prototypes in Section 2.9.2 results in a stiffening of the partially-austenitic profile as both knitted actuator sections contribute to the performance while the fully-martensitic profile remains constant at the level of the $i_k = 52\,\mathrm{mm^2\,mm^{-2}}$ prototype because of the compliance of the $i_k = 138\,\mathrm{mm^2\,mm^{-2}}$ prototype under the applied forces and knit lengths. The manipulation of just the partially-austenitic profile is a novel mode of tunability for SMA knitted actuators that can be exploited to produce larger and more tunable actuation contractions and forces.

2.10 Conclusion

This paper compiles the first experimental framework and derives widely-applicable and transferable guidelines for the design, characterization, and operation of SMA knitted actuators. SMA knitted actuators of varying geometric parameters and thermo-mechanical loading conditions were experimentally characterized to provide the fundamental data for the derivation of design, characterization, and operation guidelines for knitted actuators. In accordance with classic SMA characterization, we overview thermo-mechanical SMA knitted actuator characterization strategies, provide direction for the selection of the most appropriate characterization strategy, and point out differences between different characterization strategies, specifically with regards to the load-path dependency of SMA knitted actuators. The stability of the SMA knitted actuator performance is assessed both across constant parameter prototypes as well as for the low-cycle performance under repetitive thermo-mechanical loading. Guidelines are derived to equip experimentalists and designers with the knowledge of the thermo-mechanical loading conditions that promote thermo-mechanical architectural shakedown and result in consistent actuator performance. The effect of changing knitted loop geometries of SMA knitted actuators as well as varying external mechanical loading on the actuation and relaxation temperatures of the knitted actuator is determined experimentally. New terminology, the actuation and relaxation temperatures, is introduced to signify the onset of thermal actuation and relaxation in the SMA knitted actuator that is composed of varying volume phase fractions of austenite and martensite and is subject to architectural effects such as friction at the loop interlacing points. Higher average stresses within the SMA knitted actuator, induced by larger externally applied loads and lower knit indices, results in an increase of both the actuation and relaxation temperatures. The knowledge of these SMA knitted actuator transition temperatures is important for the characterization, operation, and design of SMA knitted actuators.

The ability to fully design SMA knitted actuator is predicated on the knowledge of the geometric parameters that effect the relationship of actuation forces, displacements, temperatures, and contractions. In combination with the correlation between the knit index and the SMA knitted actuator %-actuation contractions, which has been derived previously, [74] this publication enables the macro- and mesoscopic design of the SMA knitted actuator performance. Through experimental characterization, we identified the

correlation between the SMA knitted actuator actuation and relaxation temperatures on the knit index and external loading, as well as the linear scaling of actuation forces with the number of knitted loops in the walewise direction and actuation displacements with the number of knitted loops in the coursewise direction. The correlation of the homogenous and inhomogenous knit geometry and SMA knitted actuator performance provides the means for the simplified SMA knitted actuator design paralleling the serial and parallel connection laws of springs.

This publication elucidates the interrelations between characterization and operation strategies, SMA knitted actuator geometry, and the SMA knitted actuator performance. This first description of such interrelations enables the discussion of the language that best describes the SMA knitted actuator performance and the formulation of guidelines for characterization, operation and design. Defining the language and identifying characterization, operation, and design guidelines has broad impact for other active textile implementations as many concepts from the multiscale textile and material mechanics can be directly translated. The presented guidelines set the foundation for the advanced design of multifunctional, smart textiles.

Acknowledgements

The authors would like to thank MnDRIVE Robotics, Sensors, and Advanced Manufacturing (RSAM) and the University of Minnesota Informatics Institute Graduate Assistantship for their support of the conducted research.

Chapter 3

Performance and prediction of large deformation contractile SMA knitted actuators

K Eschen and J Abel
Department of Mechanical Engineering, University of Minnesota,
111 Church Street SE, Minneapolis, MN 55455, USA
Published in **Smart Materials & Structures**
Vol **28 2**
Pages **025014**
DOI **10.1088/1361-665X/aaf215**
Date **December 2018**

Abstract

Compliant, large deformation actuating functional fabrics are essential to next-generation wearables, aerospace structures, and medical devices as they excel at traditional mechanical performance metrics while being soft and pliable. Actuating functional fabrics have been implemented from a variety of multifunctional material systems and fabric manufacturing techniques. A specifically intriguing combination of material system and fabric manufacturing technique are contractile shape memory alloy (SMA) knitted actuators, which generate recoverable actuation deformations of up to 50%, provide actuation forces on the magnitude of 1 N-10 N*, are biocompatible, and actuate in response to thermal stimuli. However, the prediction of the knitted functional fabric actuator performance is inherently difficult due to the complex geometry of knitted architectures and the nonlinear material behavior of most multifunctional fibers. This paper presents an empirical model of the contractile SMA knitted actuator performance based on the definition of a dimensionless geometric parameter, the knit index* (i_{k})*. An experimental study of the contractile SMA knitted actuator quasi-static uniaxial thermomechanical performance validates the knit index and the wire diameter as the smallest set of performance-predicting geometric parameters. An empirical model is formulated for the prediction of the contractile SMA knitted actuator performance based on geometric inputs (forward design) and the recommendation of geometric parameters that accomplish specific performance metrics (inverse design). The process of describing and predicting the performance with dimensionless geometric parameters is a step to understanding the mechanics of contractile SMA knitted actuators, has merit for the design of other actuating functional fabrics, and propels the creation of novel wearables, medical devices, and aerospace structures with large actuation deformations.*

3.1 Introduction

Actuating functional fabrics are receiving considerable attention as they combine intriguing mechanical capabilities, e.g., large and distributed actuation deformations and variable stiffness behavior, while being naturally compliant and wearable textiles. Actuating functional fabrics integrate multifunctional fibers within traditional fabric architectures (knits, braids, weaves, etc.). Research on aerospace structures that self-deploy and morph, [86, 87, 88, 89] medical [90, 91] and rehabilitation devices, [20] as well as military and civil wearable technologies [92, 93, 94] has previously explored actuating functional fabrics. Current research, however, is limited to the implementation of actuating functional fabrics in closely defined applications as the fundamental geometric parameters that drive the actuation performance of actuating functional fabrics are complex and have not yet been thoroughly investigated.

Knitted actuating functional fabrics are a novel architectural approach of leveraging the unique material properties of multifunctional fibers to achieve large and spatially distributed actuation deformations. The design of the knitted architecture is a multiscale process that enables the tailorability of the deformation mode (planar contraction, corrugation, scrolling) as well as the magnitude of the architecture's performance metrics. [6] The geometrically simplest knitted functional fabric is the highly symmetric and planar contractile knitted architecture, which provides large actuation contractions of up to 50% and actuation forces that can range between 0.01 N and 10 N depending on the choice of multifunctional fiber. Contractile knitted actuators have been implemented by incorporating multifunctional materials such as shape memory alloys (SMA), [6] electroactive polymers, [15] and carbon nanotubes [13] as they provide actuation in response to different stimuli (electric, thermal) and excel at different performance metrics. For example, electroactive polymer knitted actuators have been investigated for medical applications because they provide forces that are safe for tissue and can achieve actuation through novel chemical mechanisms [15] and carbon nanotubes enable enhanced control-mechanisms while producing moderate actuation contractions. [13] This paper focuses on SMA knitted actuators, as they exhibit large actuation contractions (up to 50%) and generate substantial actuation forces (up to 10 N) upon thermal actuation [72] while being a lightweight and compliant architecture.

Shape memory alloys have been established as a viable solid-state actuator material through extensive research of their thermo-mechanical actuator properties. [33, 34] SMAs recover considerable material strains (up to 8%) against significant forces when thermally actuated. [35] Current research focuses on the optimization of the SMA actuator performance, which is commonly approached by improving the material itself or by incorporating it into designed geometric arrangements that amplify certain performance metrics. For example, shape memory alloys have been utilized as contractile actuators in the form of SMA bundles, [42] helical springs [43] and cables [44] resulting in significant performance improvements with regards to the ability to recover actuation strains and performing mechanical work. [45, 46] While the structural integration of SMA wire within these geometry-leveraging architectures increases the actuation performance in comparison to simple monofilament SMA wire actuators, they are still restricted to point-wise actuation. Pseudo-distributed actuation capabilities have been accomplished through structural attachment of designed SMA geometries to otherwise standalone traditional textiles. Such architectures have been designed to provide desired structural bending stiffness changes [40] and to increase the mechanical work performed by SMA springs through their parallel assembly. [41]

The benefit of the truly distributed three-dimensional actuation of SMA knitted actuators is afforded at the cost of significantly increased geometric complexity in comparison to cables or helical springs. The marriage of the highly nonlinear SMA material behavior and the knitted actuator geometry renders performance predictions based on physical models an extremely challenging task. An analytical model for the contractile SMA knitted actuator performance has been proposed, [72] however, the prescribed simplifications to achieve a closed-form solution limit the usability to specific geometric parameter combinations and require expertise in model calibration. Reliable analytical or numerical models that capture a wide range of geometric parameters, present exact results, and are accessible without extensive background knowledge, have not yet been developed.

This paper presents the derivation and experimental validation of the smallest set of geometric parameters that predict the contractile SMA knitted actuator performance and establishes an empirical model of the actuator performance. The paper expands on a prior study published in the Proceedings of the ASME Conference on Smart Materials,

Adaptive Structures, and Intelligent Systems [4] by incorporating additional experimental data, providing theoretical insight on the derivation of the knit index, and introducing and empirical model for the prediction of the SMA knitted actuator performance. The knit index is defined as a dimensionless parameter that unifies geometric measures that both describe the knitted loop geometry and affect the expected material stresses. For these reasons, the knit index is hypothesized to predict the contractile SMA knitted actuator performance. Uniaxial thermo-mechanical experiments were performed to assess the actuator performance of various wire diameter and knit index prototypes. The performed uniaxial thermo-mechanical experiments reveal a strong correlation between the knit index and actuator performance metrics (%-actuation contraction, mechanical work). An empirical model is implemented using algebraic functions that interpolate between the characterized contractile SMA knitted actuator prototypes' geometric parameters and performances. Forward and inverse design functionalities are provided in a standalone software tool. The description of the contractile SMA knitted actuator performance based on this reduced set of geometric parameters propels the understanding of the complex nonlinear contractile SMA knitted actuator mechanics. The employed process merits an adjustable procedure for other multifunctional material knitted actuators and engineering knits. The empirical model provides the means for a universal and streamlined macroscopic design of contractile knitted actuators, enabling the creation of novel wearables (e.g., self-fitting [68]) and medical (e.g., health monitoring [95]) and aerospace devices (e.g., active-compression garments [69]) using this promising functional fabric and its large actuation deformations.

3.2 Material, architecture & operation

The unique SMA material properties and the hierarchical knitted architecture enable the tailorability of the contractile SMA knitted actuator performance. This section introduces the SMA material, defines the geometry and details the operation of contractile SMA knitted actuators.

3.2.1 Shape memory alloy wire

Shape memory alloy wire is a nearly equi-atomic nickel-titanium alloy that has been implemented in many medical, rehabilitation and aerospace applications, mainly because

of its inherent superelasticity and the shape memory effect. Utilizing the shape memory effect, shape memory alloy wire accomplishes variable stiffness behavior and shape changes triggered by thermo-mechanical actuation. A martensitic solid phase transformation occurs when the wire is heated above its characteristic stress-free austenite finish temperature (A_f), which can be customized through changes in chemical composition and heat treatment. [47] The change of the lattice structure, which takes place during the solid phase transformation results in the recovery of material strains, which ultimately causes the shape memory effect. [33] The typical shape memory process begins with an undeformed wire at room temperature in its twinned martensite state. Through the application of mechanical loads above a wire-specific stress level, the detwinned martensite phase is introduced. [34] The shape memory alloy is subsequently unloaded and remains in its strained martensite state. Upon thermal actuation, achieved by heating of the wire above its austenite finish temperature, the material undergoes a solid phase transformation into the highly symmetric, stiff, austenite phase. Cooling of the shape memory alloy results in the reverse phase transformation back to the twinned martensite phase, while the shape of the alloy remains the same as in the austenite phase. Utilizing the shape memory effect, strains of up to 8% can be recovered by SMA wire, providing useful actuator capabilities. [35]

While the outlined procedure separates the mechanical and the thermal loading into distinct steps, engineering applications usually impose simultaneous thermal and mechanical loading conditions on the shape memory alloy. Shape memory alloys examine significant path-dependencies with regards to strains, stresses, and temperature. [56, 57] Complete phase transformations to the austenite lattice may not occur under applied mechanical stresses that exceed a wire-specific threshold. When the actuator temperature is above the austenite finish temperature, and mechanical stresses of such magnitudes are present, the apparent martensite phase is called stress-induced, and the complete potential actuation performance can not be leveraged. [58]

3.2.2 Contractile SMA knitted geometry

During the knit manufacturing process, a single flexible fiber is manipulated into a constrained architecture of interlacing, adjacent, and symmetrical loops to build a network of consecutive wales (columns) and courses (rows). This process creates nearly planar structures with anisotropic elastic stiffness in the textile plane. Two fundamental

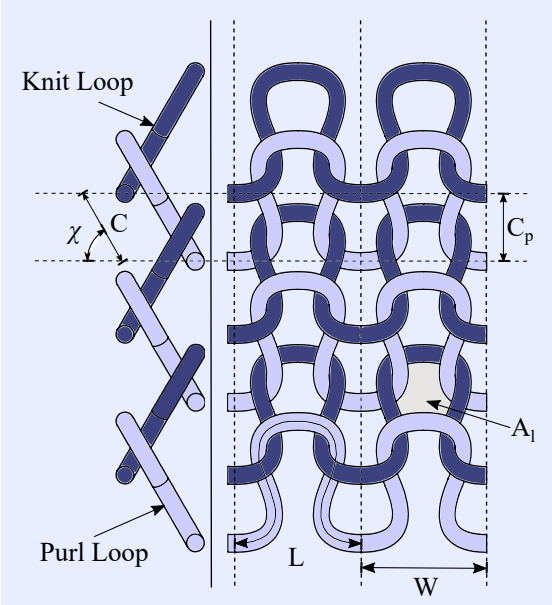

Figure 3.1: **Knitted Geometry**[†]**:** The contractile knitted architecture projected in the side-view (left) and plane-view (right) with the geometric loop parameters: course height (C), projected course height (C_p), loop angle (χ), wale width (W), loop length (L), and the loop enclosed area (A_l). [4]

repetitive units - knit and purl loops - are formed during the manufacturing process. Knit and purl loops are mirrored opposites and only differentiated by the direction in which they are passed through the interlocking loop of the previous course. Through the intentional assembly of knit and purl loops in a knitted pattern, different mechanical behaviors can be designed. [6]

Contractile SMA knitted actuators consist of horizontally aligned rows of interlacing knit and purl loops manufactured from a single strand of monofilament shape memory alloy fiber. As the knitted loops are repetitive elements, the geometry of contractile SMA knitted actuators can be described with geometric loop parameters (Figure 3.1). The course height (C) is defined as the distance between vertices of two interlacing loops. The vector between the vertices of two interlacing loops and the horizontal baseline enclose the loop angle (χ). At a loop angle of $\chi = 90°$, the course height (C) equals the projected course height (C_p). The loop length (L) is the length of the spline defining a single loop, which surrounds the loop enclosed area (A_l). The wale width (W) is defined as the horizontal distance between the vertices of two adjacent loops. The side-view

(Figure 3.1) of the contractile SMA knitted actuator illustrates the difference between a knit loop (rear vertex) and a purl loop (forward vertex), which interlock with knitted loops of the previous course in opposite direction.

3.2.3 Contractile SMA knitted actuator operation

The active behavior of contractile SMA knitted actuators is achieved through the integration of SMA wire within the constrained knitted architecture. Bending deformations are introduced to the SMA wire in the loop forming process and cause internal material stresses, even in the unloaded configuration. Upon thermal actuation of the mechanically loaded contractile SMA knitted actuator, the first-order stress-, strain- and temperature-dependent phase transformation from martensite to austenite occurs partially within the SMA wire and its stiffness increases. The partial recovery of the induced bending deformation results in straightening and relative sliding of the knitted loops and is responsible for the uniaxial structural contraction of the knitted actuator. When the contractile SMA knitted actuator is cooled below its martensite finish temperature, the stiffness of the wire decreases and the applied mechanical load causes uniaxial elongation of the contractile SMA knitted actuator into its original state. The variable stiffness of the SMA material confined within the knitted structure enables repeatable actuation of the contractile SMA knitted architecture.

3.3 Knit index derivation

The following sections discuss the simplifications applied to derive the minimal set of geometric parameters that affect the knitted loop geometry, as well as the magnitude of the material stresses, and are expected to impact the contractile SMA knitted actuator performance.

3.3.1 Knitted loop geometry

Section 3.2.2 introduces common geometric parameters utilized in the modeling of geometric, [96] passive, [97] and active [72] knit models. While these parameters are valid for their specific use cases, they do not constitute a set of independent parameters that define the knitted loop geometry. This problem caused a stalling of the design and manufacture of passive, yarn-knitted textiles in the first half of the 20th

century, [8, 98] until the elastica theory of buckled beams proposed a compelling and straightforward solution. The buckled geometry of perfectly-elastic beams resembles the geometry of knitted loops, and is entirely defined by a single parameter, the length of the buckled beam. [65] These findings were applied to passive knitted textiles, which, in their minimum energy configuration, the relaxed loop state, were consequently found to be geometrically defined by their loop length (L) (Figure 3.1). [8] More complex passive knitted architectures were mathematically described, non-dimensional geometric descriptions formulated, and the mechanical performance was correlated to these geometric parameters. [99]

The knitted loop geometry simplifications (perfectly-elastic, minimum energy configuration) applied for the derivation of the loop length as the single defining parameter are contrary to the material properties of SMA. Deformations, both plastic and thermomechanically recoverable, are induced with varying magnitude in the isothermal knit manufacturing process. These deformations can prevent the SMA knitted actuator from reaching a fully-relaxed state as described in the elastica configuration, which prohibits the general applicability of this loop dimensionality description. However, SMA knitted actuators of geometries that minimize the induced plastic deformations achieve an approximately perfectly-elastic loop shape and can be assumed to follow the models describing the dimensionality of the elastica configuration in close proximity. For SMA knitted actuators of such characteristics, it is possible to apply the elastica mathematical description and to define the dimensionality of the knitted loop using the loop length (L) as the single indicative parameter.

3.3.2 Material considerations

The material behavior of SMA is a nonlinear function of the applied stresses, strains, and temperature, all of which significantly contribute to the contractile SMA knitted actuator performance. A physically rigorous computation of the material stresses based on the geometric loop parameters of a given prototype is a complex and challenging task due to the path-dependent nonlinearities of the material behavior with regards to strains, stresses, and temperatures. The complexity of the SMA material constitutive relations exceeds the scope of this derivation of a high-level design parameter. However, it is desirable to understand the parameters that affect the stress-state of the SMA material in the contractile SMA knitted architecture.

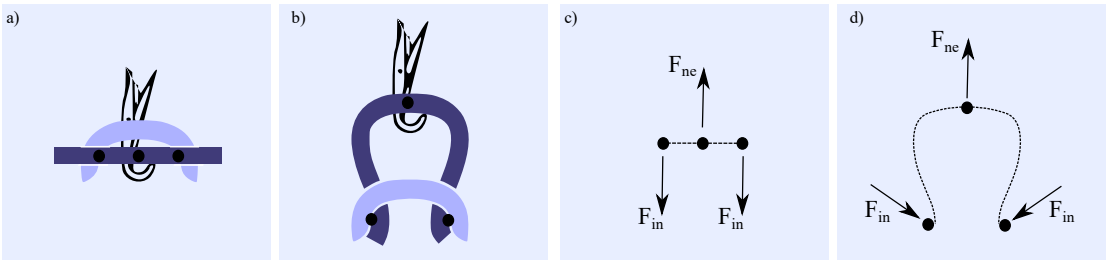

Figure 3.2: **Knit Manufacturing Process:** Three-point bending deformations are imposed on the originally straight wire in the knit manufacturing process, which results in the formation of the knitted loop.

In the knit manufacturing process, the originally straight SMA wire is subjected to three-point bending deformations, which is the main deformation mode. The bending deformations occur when the knitted loop is formed by the application of the knitting needle force (F_{ne}) on the loop vertex, which pulls the wire through its interlacing loop and creates the resultant interlacing forces (F_{in}). Figure 3.2a and 3.2c show the three-point bending condition in the knit manufacturing process and Figure 3.2b and 3.2d depicts how the bent wire is formed into a knitted loop. Through the interlocking with loops of the previous row, the formed knitted loop is constrained to its stressed geometry and cannot return to its originally straight shape. Using the assumption that Euler-Bernoulli beam bending theory (slender geometry, cross-sections perpendicular to the neutral axis, homogeneous, isotropic material) can sufficiently describe the factors that dictate the relative magnitude of bending stresses in SMA knitted actuators, the relevant geometric loop parameters can be found. The differential equation of elastic beam bending theory is known to be

$$M(x) = -w''(x) \cdot EI(x) \qquad \sigma_b(x) = \frac{M(x)}{I(x)} \cdot z \tag{3.1}$$

with the bending stresses ($\sigma_b(x)$), the bending moments ($M(x)$), the second moment of area ($I(x)$), the perpendicular distance to the neutral axis (z), the modulus of elasticity (E), and the curvature ($w''(x)$). Assuming perfectly circular cross-sections, the two defining geometric parameters of the bending stresses are the curvature and the perpendicular distance to the neutral axis.

As discussed in Section 3.3.1, the geometric analysis based on the fully-relaxed elastica configuration of the SMA knitted loop suggests that the curvature at any point

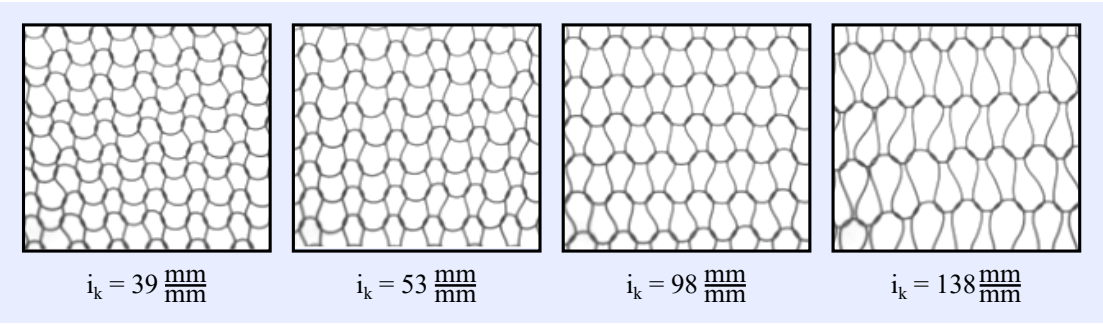

Figure 3.3: **Knit Index Comparison:** Contractile SMA knitted actuators of various knit indices with a constant wire diameter $d = 0.203\,\text{mm}$. Smaller knit index prototypes are densely knit with a high proportion of active material per unit area, whereas high knit index prototypes are open-looped architectures with a small proportion of active material per unit area.

of the knitted loop is uniquely dependent on the loop length. [8] The perpendicular distance to the neutral axis at its maximum is equal to half the SMA wire diameter ($z = d/2$). Using the stated simplifications, the geometric parameters that describe the knitted loop geometry and that affect the relative material stresses are the loop length (L) and the wire diameter (d).

3.3.3 The dimensionless knit index

A dimensionless geometric parameter, the knit index (i_k), is defined to reduce the geometric loop parameters of the knitted loop based on the knitted loop geometry and material considerations. The independent geometric parameters are the loop length (L) and the wire diameter (d).

While the loop length is an established knitted loop geometry parameter, it is difficult to measure with reasonably low errors. Measurements of the complete fiber length scaled by the number of knitted loops fail to account for the boundary loops of the knitted architecture, and therefore lead to erroneous loop lengths. Digital image measurements of the loop length are erroneous as it is not trivial to define consistent conditions that constitute the beginning and end of interlacing knitted loops. A simple, robust and error-insusceptible measure is the loop enclosed area of contractile SMA knitted actuators (A_l), which is proportional to the loop length. [65] The loop enclosed area is defined as the area enclosed by a knitted loop, depicted in Figure 3.1, and is

measured under mechanical loading conditions that realize a loop angle of $\chi \approx 90°$. The loop-enclosed area is measured post manufacturing, ergo prior to any thermal load application besides the manufacturer's preconditioning of the straight SMA wire. The measurement of the loop enclosed area of a statistically significant amount of regular, non-boundary loops is a simple image processing algorithm that can be automated with low errors and provides reliable results.

The knit index relates the loop enclosed area in the martensite ($T = 20\,°\mathrm{C}, \chi \approx 90°$) state ($A_{\mathrm{l,m}}$) to the wire diameter ($d$) by building the fraction:

$$i_k = \frac{A_{\mathrm{l,m}}}{d^2} \tag{3.2}$$

The knit index is analogous to traditional dimensionless geometric parameters that have been defined for fibers without material stiffness, while additionally considering the non-perfectly-elastic properties of the active SMA material. The knit index is an intuitive and easily obtainable parameter describing the dimensionality of contractile SMA knitted actuators. In its nature, the knit index is similar to the spring index relating geometric properties to define the overall architectural stiffness. Figure 3.3 compares contractile SMA knitted actuator prototypes of various knit indices under a constant wire diameter $d = 0.203\,\mathrm{mm}$. A low knit index corresponds to densely knitted fabrics, with a relatively high proportion of active material in a unit area, whereas open-looped structures with small proportions of active material in a unit area have a high knit index.

3.4 Experimental characterization

An experimental study was conducted to explore the potential of the knit index as a predictive dimensionless geometric parameter for the contractile SMA knitted actuator performance. This section presents the design of the prototypes, the experimental setup, and the experimental method.

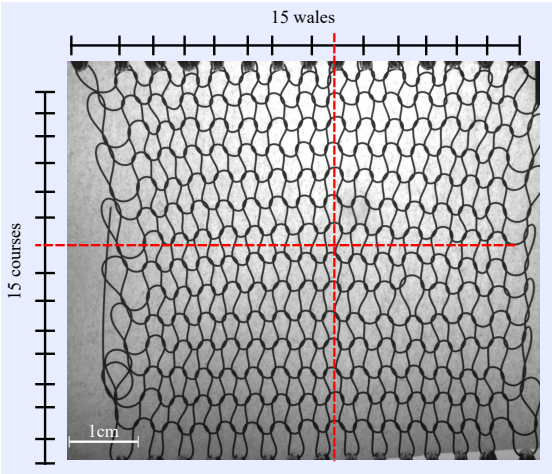

Figure 3.4: **Contractile SMA Knitted Actuator Prototype†:** The contractile SMA knitted actuator prototypes consist of 15 wales and 15 courses. The displayed prototype is manufactured with Dynalloy Flexinol® wire ($A_f = 90\,°C$, $d = 0.305\,mm$).

3.4.1 Prototypes

The empirical study was conducted using Dynalloy Flexinol® wire ($A_f = 90\,°C$) of various diameters as the multifunctional fiber of which the knitted prototypes were manufactured. Thermo-mechanical preconditioning of the SMA wire was performed by the manufacturer to overcome the majority of initial thermal-mechanical shakedown effects in the material. [82] The contractile SMA knitted actuator prototypes were manufactured on manually-driven Taitexma TH-860 and Taitexma TH-260 knitting machines of different machine gauges (g), which is the fixed distance between knitting needles. The prototypes consist of 15 wales and 15 courses, resulting in a total of 225 knitted loops (Figure 3.4). This ensures that the boundary effects of the contractile SMA knitted actuators are negligible and that a representative number of knitted loops contribute to the actuator behavior. Three different series of prototypes were investigated in the empirical study as shown in Figure 3.5: The first series, in Figure 3.5 marked by pink squares, consists of prototypes with a knit index ($i_k \cong 65\,mm^2\,mm^{-2}$), which is a relatively dense knitted architecture. The variable parameter for constant knit index prototypes in this study is the wire diameter, which ranges between $0.254\,mm \leq d \leq 0.381\,mm$. The second series consists of prototypes of constant knit indices of $i_k \cong 130\,mm^2\,mm^{-2}$ (green squares), while the wire diameter was varied similarly to the first experimental series. Prototypes of the following wire diameters were manufactured and tested throughout

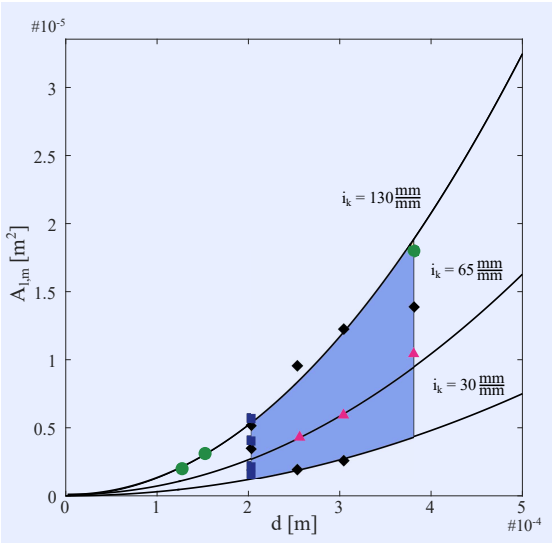

Figure 3.5: **Prototype Selection†:** The experimental study was performed with three series of prototypes - A series of nearly constant knit index prototypes $i_k \cong 65\,mm^2\,mm^{-2}$ (green circles), a series of nearly constant knit index prototypes $i_k \cong 130\,mm^2\,mm^{-2}$ (pink triangles), and a series of constant wire diameter prototypes $d = 0.2032\,mm$ (blue rectangles). Additional prototypes (black diamonds) were characterized for the empirical model building process.

the study: 0.127 mm (0.005”), 0.152 mm (0.006”), 0.203 mm (0.008”), 0.245 mm (0.01”), 0.305 mm (0.012”) and 0.381 mm (0.015”). The third series of prototypes share the constant wire diameter of $d = 0.203\,mm$, while the knit index was varied between prototypes, as depicted by the blue squares in Figure 3.5.

Additional contractile SMA knitted actuator prototypes were analyzed for the empirical model building (Section 3.7). The empirical modeling space is marked as the solid yellow area. The lower wire diameter prototypes ($d < 0.203\,mm$) are excluded from the empirical model building process as the Taitexma-series knitting machines do not allow for the manufacture of lower knit index prototypes than the ones analyzed in the second experimental series (green).

3.4.2 Experimental setup

Quasi-static thermo-mechanical experiments were performed using a custom-built uniaxial tensile testing setup (Figure 3.6) within a Cincinnati Sub Zero (CSZ) environmental chamber. The experimental setup was optimized to introduce minimal friction to the

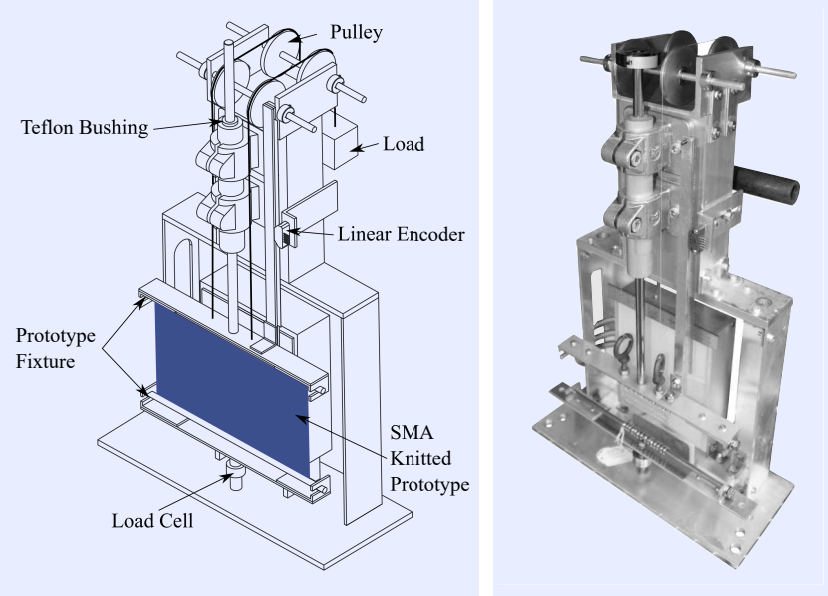

Figure 3.6: **Uniaxial Tensile Testing Setup**[†]**:** Thermo-mechanical loading conditions were imposed on the contractile SMA knitted actuators using the uniaxial tensile testing setup within an environmental chamber.

system, which is necessary for the acquisition of high-quality experimental data at low applied forces. The experimental setup consists of a bottom prototype fixture, which is immovably connected to the ground through a Honeywell M34 5lb-load cell, and a top fixture, which has a translational degree of freedom in the vertical axis allowing the knitted prototype to elongate and contract. Pulleys redirect the load of a dead weight to the top fixture, through which the mechanical load is applied to the prototype. A linear encoder setup from US Digital (200 CPI) consisting of strip and sensor is attached to the top fixture and used to measure the elongation and contraction of the SMA knitted actuator from a defined initial length.

3.4.3 Experimental procedure

The uniaxial tensile behavior of SMA actuators is most commonly characterized using either the pull-out method or the cyclic heat-cool method. [45, 70] The pull-out method is performed by applying a constant temperature below the martensite finish temperature (M_f) while incrementally increasing the mechanical load on the actuator to receive a martensite force-elongation profile. After the application of the maximum load, the

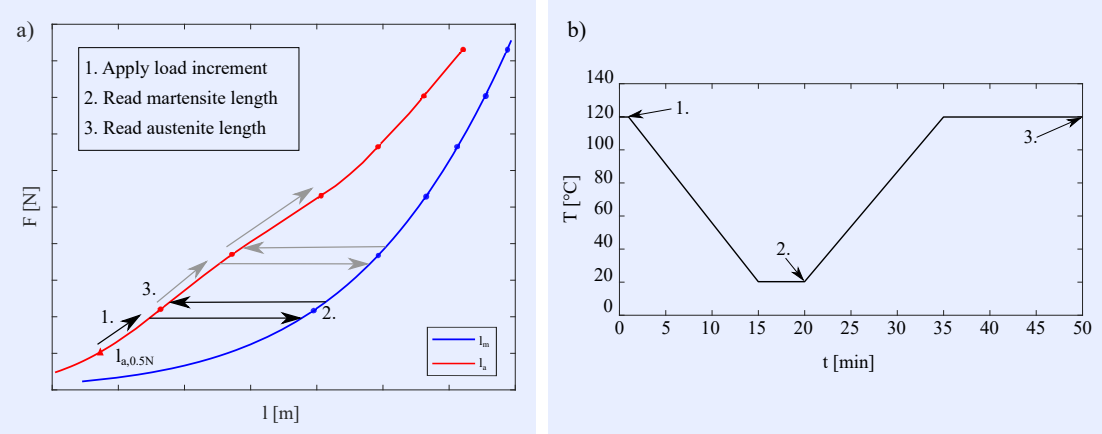

Figure 3.7: **Cyclic Heat Cool Method†:** The cyclic heat cool method was utilized with an incremental increase of the applied mechanical load: the three steps are demonstrated in the applied load over knit length profile (a) and the temperature profile is provided for a single cycle of fifty minutes (b).

SMA actuator is heated to a temperature above the austenite finish temperature (A_f), which is kept constant while incrementally decreasing the mechanical load to generate the partially-austenitic force-elongation profile. While the pull-out method can be performed very easily and provides acceptable results for plain wire and helical SMA actuators, [45] using this experimental method with contractile SMA knitted actuators leads to unreliable results of the actuation performance in comparison to cyclical actuation tests. This discrepancy can be explained by the complex hysteretic frictional behavior that occurs at the interlacing points upon actuation, [100] which is neglected when applying mechanical loads isothermally. The cyclic heat-cool method was used as it most exactly mimics the mechanical behavior of the predicted contractile SMA knitted actuator use case, which is the recommended best practice for the SMA actuator design. [77]

The thermo-mechanical loading profile of the cyclic heat-cool method resembles realistic actuation conditions, which impacts the measured actuation performance by accounting for thermally-induced frictional hysteresis of contractile SMA knitted actuators. The cyclic heat-cool method begins with the heating of the contractile SMA knitted actuator to a temperature above the austenite finish temperature ($120\,°C > A_f$) under an applied pretensioning mechanical load of 0.5 N in accordance to current testing methods for tensile properties of fabrics, [101, 102] which leads to the actuator's extension

to its reference length ($l_{\mathrm{A},0.5\,\mathrm{N}}$) (Figure 3.7). We select the temperature ($T = 120\,^{\circ}\mathrm{C}$) to be significantly above the stress-free austenite temperature to ensure phase transformation despite the presence of residual manufacturing stresses of varying magnitude. The first load increment is subsequently applied in the partially-austenitic state (Figure 3.7-1.). After the load application, the contractile SMA knitted actuator is cooled to the fully-martensitic state ($T = 20\,^{\circ}\mathrm{C}$) with the maximum martensite knit length being read out at the end of the soaking period (Figure 3.7-2.). Subsequently, the knitted actuator is reheated to the temperature $T = 120\,^{\circ}\mathrm{C}$ causing the actuator to contract to its partially-austenitic knit length (Figure 3.7-3.). These three steps define a single 50 min cycle of the cyclic heat-cool method. The next load increment is applied to the contractile SMA knitted actuator in the partially-austenitic state, and the procedure is repeated until the desired maximum mechanical load is applied.

3.5 Performance metrics

The experimentally collected data consists of information on the prototype length, the applied load, and the prototype temperature, which are the decisive physical quantities for the calculation of the knit-specific actuator performance metrics. The wide range of geometric parameters used in the experimental study and the complex force-knit length behavior of contractile SMA knitted actuators demands an efficient and descriptive method to compare their uniaxial tensile performance. While plotting the force-knit length profiles displays the entirety of the collected data, the definition of performance metrics simplifies the comparison of the tested specima. A set of performance metrics is defined to describe the actuation performance of contractile SMA knitted actuators at specific applied loads, as well as their force-knit length behavior over the complete range of applied loads.

Typical contractile actuation is thermally-induced under constant mechanical loading conditions. Therefore, the measurement of the knitted actuator contractile performance is referenced to the knit length in the fully-martensitic state (l_{M}) under constant mechanical loading conditions (Figure 3.8). The most contracted length under a defined applied load, the partially-austenitic knit length (l_{A}) is compared to the fully-martensitic knit length (l_{M}) (Figure 3.8a) at the same applied load to obtain the %-actuation contraction (ζ)

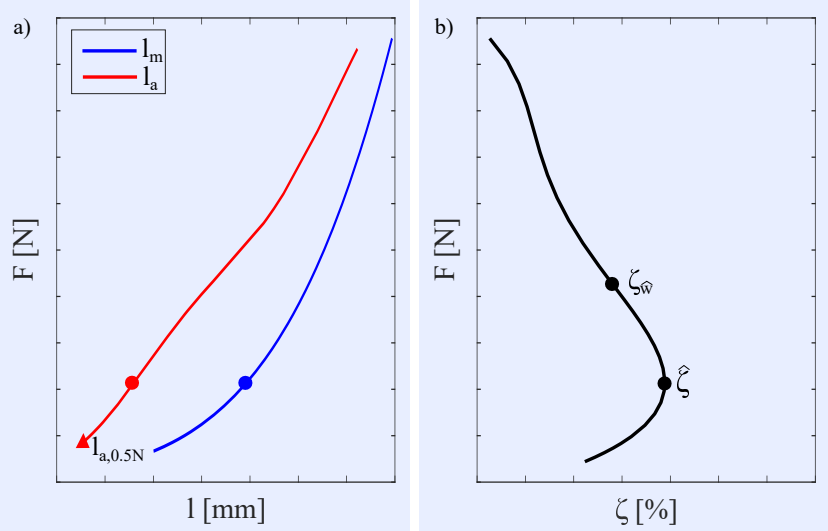

Figure 3.8: **Scalar Experimental Characterization Metrics†:** Characterization metrics were extracted from the experimental data, i.a. the partially-austenitic knit length (l_{A}), the fully-martensitic knit length (l_{M}), the maximum %-actuation contraction ($\hat{\zeta}$), and the actuation contraction at maximum work ($\zeta_{\hat{W}}$).

$$\zeta = \frac{l_{\mathrm{M}} - l_{\mathrm{A}}}{l_{\mathrm{M}}} \tag{3.3}$$

as depicted in Figure 3.8b. The maximum %-actuation contraction ($\hat{\zeta}$) denotes the peak actuation performance of a contractile SMA knitted actuators and corresponds to a single specific force at maximum %-actuation contraction ($F_{\hat{\zeta}}$). The maximum mechanical work ($\hat{W}$) is based on the traditional mechanical work definition

$$W = F_{app} \cdot \delta, \quad \delta = l_{\mathrm{M}} - l_{\mathrm{A}} \tag{3.4}$$

using the applied load (F_{app}) and the actuation displacement (δ). The mechanical work relates the ability of a knit to provide large actuation displacements to the ability to lift significant forces within a single comparative metric. Similar to the maximum %-actuation contraction metric, the %-actuation contraction at maximum mechanical work ($\zeta_{\hat{w}}$) can be calculated using Equation 3.3 at the applied load corresponding to the maximum mechanical work. This metric specifies the maximum mechanical work, as it provides insight into the components that contribute to the mechanical work, which could either lift large loads over a small distance or small loads over a large distance.

The force at which the contractile SMA knitted actuator performs the maximum mechanical work ($F_{\hat{W}}$) further specifies the maximum mechanical work metric. Figure 3.8 summarizes the performance metrics and displays them in the respective diagrams. The fully-martensitic knit length (l_{M}) and partially-austenitic knit length (l_{A}) are provided in the force-knit length profile, while the maximum %-actuation contraction ($\hat{\zeta}$) and the %-actuation contraction at maximum work ($\zeta_{\hat{W}}$) are displayed in the force-%-actuation contraction diagram. These performance metrics facilitate the discussion of the actuator performance as they can be easily compared and used for the derivation of dependencies.

3.6 Performance results

This section summarizes the experimentally obtained data on the contractile SMA knitted actuator performance from uniaxial thermo-mechanical experiments of the three series of prototypes. The comparison of the data is performed using the actuation performance metrics defined in Section 3.5, specifically, the %-actuation contraction and the mechanical work metrics. These performance metrics are correlated with the derived knit index (i_{k}) and the wire diameter (d).

3.6.1 Maximum %-actuation contraction

The maximum %-actuation contraction ($\hat{\zeta}$) is a widely used metric for the analysis of the actuation performance of uniaxial actuators. It is often referred to as structural strain or simply strains in the literature. For the purpose of contractile SMA knitted actuators, a precise definition is important to clearly distinguish the structural %-actuation contraction from the complex and variable material strains that are present within the shape memory alloy wire.

All force-%-actuation contraction profiles of contractile SMA knitted actuators share the characteristic shape with a deflection point at the maximum %-actuation contraction. Under loading conditions below the maximum %-actuation contraction ($F_{\mathrm{app}} < F_{\hat{\zeta}}$), the behavior of the knitted actuator is dominated by the variable stiffness upon phase transformation, which leverages the geometry to achieve monotonously increasing %-actuation contractions. At applied loads larger than the force at maximum %-actuation contraction ($F_{app} > F_{\hat{\zeta}}$), the knitted architecture's ability to recover the deformations decreases monotonously. [72]

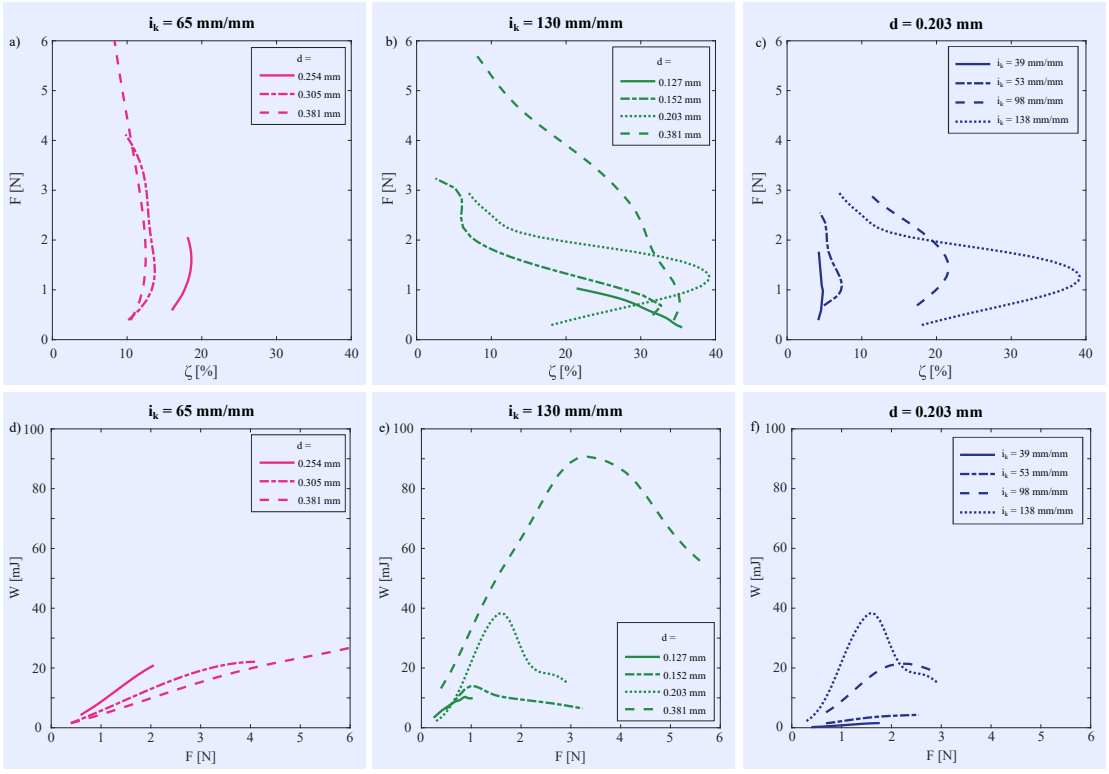

Figure 3.9: **Performance Profiles**[†]**:** The $\zeta - F_{\text{app}}$ (a-c) and the $F_{\text{app}} - W$ (d-f) profiles of the three prototype series show more distinct %-actuation contraction and mechanical work maxima for higher knit indices, as well as scaling of the actuation forces with the wire diameter.

Figures 3.9a-c display the %-actuation contraction profiles of all prototypes. In Figure 3.9a, the contractile SMA knitted actuators with a knit index of $i_{\text{k}} \cong 65\,\text{mm}^2\,\text{mm}^{-2}$ are compared to each other. Their characteristic profiles show the least distinct point of maximum %-actuation contraction as their actuator performance is relatively constant over the applied load range. The second data set, displayed in Figure 3.9b, contains the contractile SMA knitted actuators with knit indices of $i_{\text{k}} \cong 130\,\text{mm}^2\,\text{mm}^{-2}$. These profiles demonstrate a distinct maximum %-actuation contraction behavior with a quick reduction of %-actuation contraction when not operating at the force at maximum %-actuation contraction. Figure 3.9c consists of the data collected on the actuator prototypes with constant wire diameter $d = 0.203\,\text{mm}$ of varying knit indices. More distinct and higher magnitude points of maximum %-actuation contraction coincide with higher

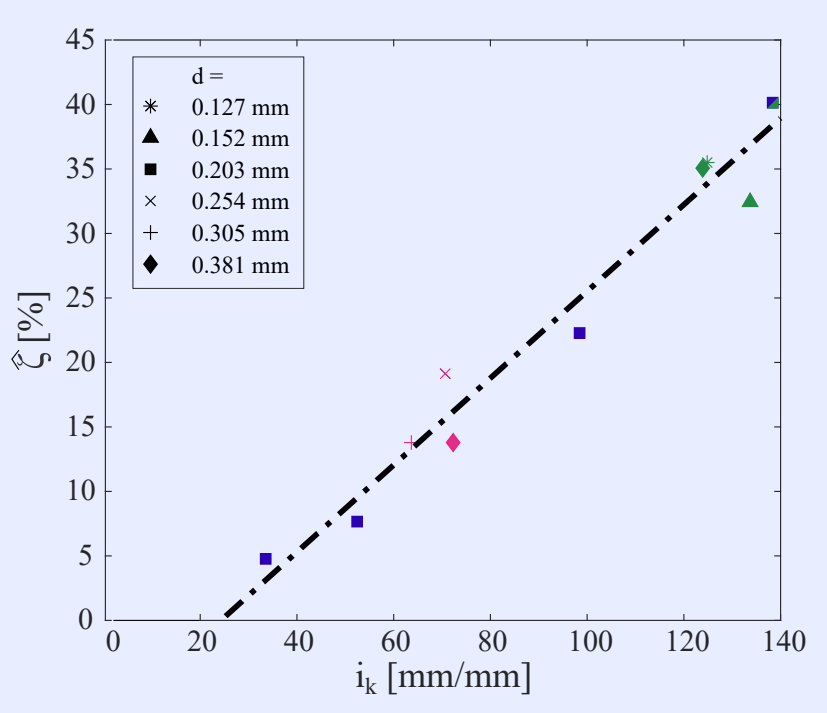

Figure 3.10: **Geometric Predictability of Maximum %-Actuation Contraction†:** The conducted experiments show that the maximum %-actuation contraction ($\hat{\zeta}$) is linear-dependent on the knit index (i_k).

knit indices, whereas lower knit indices provide lower magnitude, force-insensitive %-actuation contractions.

The maximum %-actuation contraction ($\hat{\zeta}$) is obtained by determining the global maximum of Equation 3.3 for each of the knitted prototypes. The maximum %-actuation contractions range between $\hat{\zeta}_{min} \cong 4.8\%$ at the knit index $i_k \cong 39\,\mathrm{mm}^2\,\mathrm{mm}^{-2}$ and $\hat{\zeta}_{max} \cong 40.2\%$ at the knit index $i_k \cong 138\,\mathrm{mm}^2\,\mathrm{mm}^{-2}$. The experimental data show a monotonous increase of %-actuation contraction with increasing knit indices (Figure 3.10). The slope of the fitted linear function is $m = 3/10$, i.e., the maximum %-actuation contraction increases by 3% when the knit index is raised by $10\,\mathrm{mm}^2\,\mathrm{mm}^{-2}$. Even though the dimensionless knit index simplifies the geometry parametrization of the knitted loop tremendously, a linear prediction of the maximum %-actuation contraction is supported by the experimental findings with relatively small introduced errors that consistently deviate less than 3 percent points from the fitted linear function.

3.6.2 Maximum mechanical work

The maximum %-actuation contraction is an important performance metric for uniaxial actuators, but it does not provide insight into the relationship between contractile displacements and the force that can be lifted. The mechanical work, as defined in Equation 3.4, combines the contractile displacement and applied forces within a single metric with insight for the design of contractile SMA knitted actuators. Similar to the %-actuation contraction profiles plotted in Figure 3.9a-c, every knitted actuator has a specific mechanical work profile when plotted over the applied forces. Figure 3.9d presents the mechanical work profiles for the prototypes with a low knit index of $i_\mathrm{k} \cong 65\,\mathrm{mm^2\,mm^{-2}}$. The load ranges applied in the uniaxial tensile tests were not high enough to reach a definite point of maximum mechanical work. The mechanical work profiles with the higher knit index $i_\mathrm{k} \cong 130\,\mathrm{mm^2\,mm^{-2}}$ shown in Figure 3.9e, demonstrate definite forces at which the mechanical work of the contractile SMA knitted actuators reaches a maximum. The results for the data series with the constant wire diameter $d = 0.203\,\mathrm{mm}$ is displayed in Figure 3.9f and exposes the trend of narrower, more distinct points of maximum work with increasing knit indices.

The maximum mechanical work ($\hat{W}$) is performed under the force at maximum mechanical work ($F_{\hat{\mathrm{W}}}$). The %-actuation contraction at maximum work behaves analogously to the maximum %-actuation contraction evaluated in the previous section. Contractile SMA knitted actuators with the same knit index experience the same %-actuation contraction at their points of maximum mechanical work. For example, contractile SMA knitted actuators of the knit index $i_\mathrm{k} \cong 130\,\mathrm{mm^2\,mm^{-2}}$ show a %-actuation contraction at maximum mechanical work of $\zeta_{\hat{\mathrm{W}}} \cong 26\%$.

The maximum mechanical work ($\hat{W}$) under constant knit indices increases with increasing wire diameters as displayed in Figure 3.11a. For a knit index of $i_\mathrm{k} \cong 130\,\mathrm{mm^2\,mm^{-2}}$, the maximum mechanical work ranges from $\hat{W} \cong 0.01\,\mathrm{J}$ at a wire diameter of $d = 0.127\,\mathrm{mm}$ to $\hat{W} \cong 0.09\,\mathrm{J}$ at a wire diameter of $d = 0.381\,\mathrm{mm}$. Similarly, the force at maximum mechanical work ($F_{\hat{W}}$) increases monotonously with increasing wire diameters. Figure 3.11b visualizes the linear relation between the force at maximum mechanical work and the wire diameter for at knit index of $i_\mathrm{k} \cong 130\,\mathrm{mm^2\,mm^{-2}}$. The forces at maximum mechanical work range between $F_{\hat{\mathrm{W}}} = 0.88\,\mathrm{N}$ for a wire diameter of $d = 0.127\,\mathrm{mm}$ and $F_{\hat{\mathrm{W}}} = 3.92\,\mathrm{N}$ for a wire diameter of $d = 0.381\,\mathrm{mm}$. The linear scaling of the maximum mechanical work as well as the force at maximum mechanical work

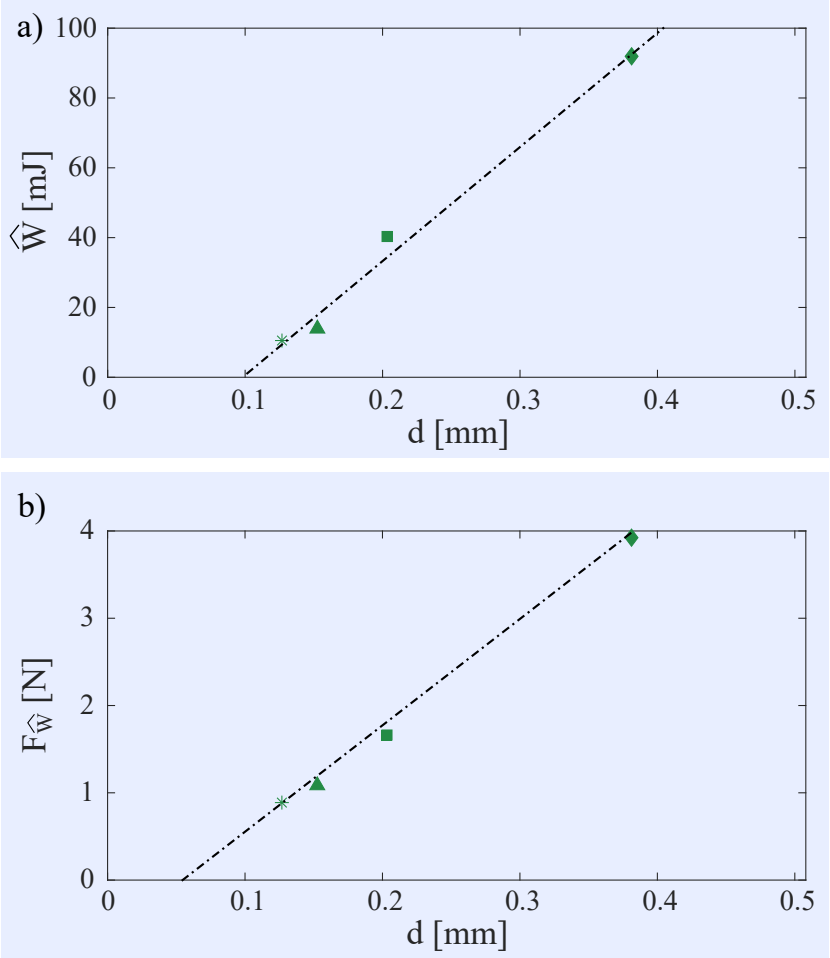

Figure 3.11: **Geometric Predictability of Work Metrics†:** Under constant knit indices ($i_k \cong 130\,mm^2\,mm^{-2}$), increasing wire diameters result in a) increased forces at maximum mechanical work ($F_{\hat{W}}$), and in b) increased maximum mechanical work ($\hat{W}$).[4]

with the prototype wire diameter under constant knit indices (Figure 3.11) is promising for the high-level design of contractile SMA knitted actuators.

3.7 Empirical model

An empirical model is formulated for the prediction of the temperature-dependent relationship between the applied load and the contractile SMA knitted actuator knit length based on the input of geometric parameters (forward design) and the calculation of

geometric knit parameters from the input of desired actuation performance metrics (inverse design). The following sections outline the algebraic functions that are employed in the model, validate the model quality, and introduce the software tool that has been implemented for the simple use of this model.

3.7.1 Modeling functions

The characteristic shape of contractile SMA knitted actuator fully-martensitic and partially-austenitic force-knit length profiles is displayed in Figure 3.8. The force-knit length profiles of the experimentally characterized contractile SMA knitted actuators are modeled with algebraic functions as the first step of the empirical model implementation. The force range for which cohesive experimental data was collected amongst all prototypes is between

$$F_{\mathrm{app}} = [1.0\,\mathrm{N}, 2.5\,\mathrm{N}] \tag{3.5}$$

which constitute the lower and upper force limits in the empirical model. The force-knit length profiles are modeled as Sigmoidal functions

$$l_{\mathrm{M,A}}\left(F_{\mathrm{app}}\right) = \frac{a_1 \cdot \left(F_{\mathrm{app}} - a_2\right)}{\sqrt{1 + a_3\left(F_{\mathrm{app}} - a_2\right)^2}} + a_4 \tag{3.6}$$

in dependency of the fitted variable F_{app} with the four fitting parameters (a_1, a_2, a_3, a_4). The fitting parameters are determined by solving the minimization problem of the nonlinear least squares formulation between the experimental data and the curve fit. The solution is obtained with the Levenberg-Marquandt algorithm, which is commonly employed in curve-fitting and readily available in Matlab. As the Levenberg-Marquandt algorithm is not guaranteed to converge at a global minimum; initial guesses are provided to increase the fitting quality.

The experimentally characterized prototypes cover a wide range of knit indices and wire diameters. The prototypes' knit indices range between $30\,\mathrm{mm^2\,mm^{-2}} \leq i_{\mathrm{k}} \leq 140\,\mathrm{mm^2\,mm^{-2}}$, while their wire diameters are within the limits $0.203\,\mathrm{mm} \leq d \leq 0.381\,\mathrm{mm}$ as shown in Figure 3.5. The proposed empirical model employs the strategy of interpolation between the characterized and modeled force-knit length profiles of defined wire diameters and knit indices. Functions are derived to interpolate between

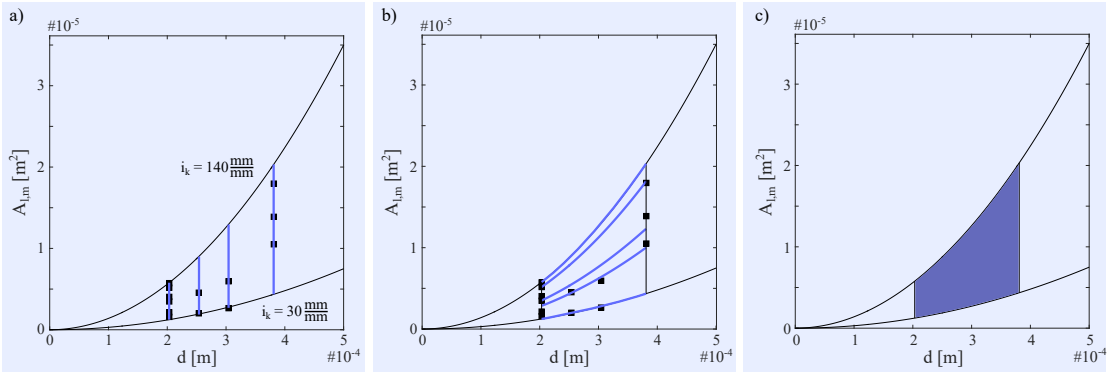

Figure 3.12: **Modeling Strategy:** The empirical model is established in a three-step procedure: modeling functions are employed for a) constant wire diameters between $0.203\,\mathrm{mm} \leq d \leq 0.381\,\mathrm{mm}$, b) constant knit indices between $30\,\mathrm{mm^2\,mm^{-2}} \leq i_\mathrm{k} \leq 140\,\mathrm{mm^2\,mm^{-2}}$ to calculate c) the contractile SMA knitted actuator performance in the defined bounds.

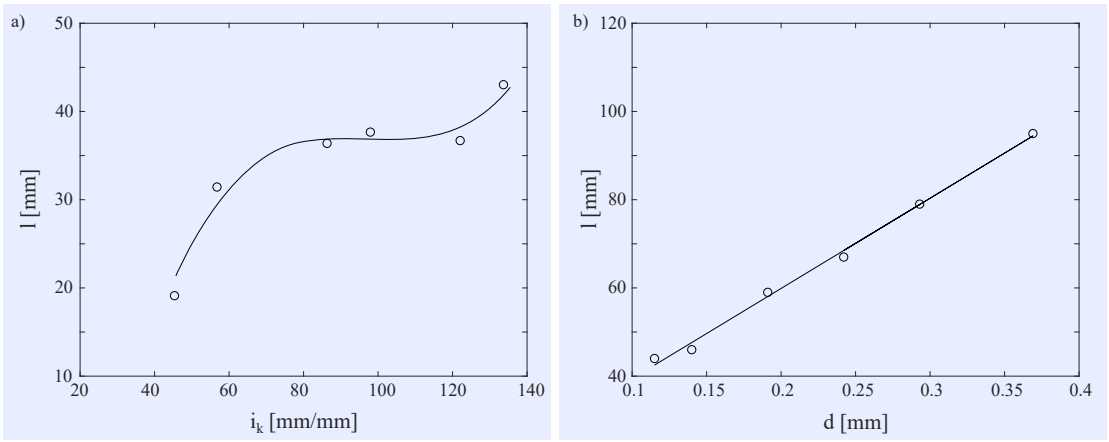

Figure 3.13: **Modeling Functions:** Exemplary experimental data (scatter) and the modeling functions (solid) of a) SMA knitted prototypes with a wire diameter $d = 0.203\,\mathrm{mm}$ under the applied load of $F_\mathrm{app} = 1.5\,\mathrm{N}$ b) and SMA knitted prototypes with a knit index of $i_\mathrm{k} = 130\,\mathrm{mm^2\,mm^{-2}}$ under the applied load of $F_\mathrm{app} = 1.0\,\mathrm{N}$

the modeled force-knit length profiles while keeping a) the wire diameter and b) the knit index at constant values (Figure 3.12).

The experimentally obtained relationship between the knit index and the knit length under constant applied loads and constant wire diameters is monotonically increasing and is best modeled as a cubic polynomial (Figure 3.13a) of the form

$$l_{\mathrm{M,A}}\left(i_{\mathrm{k}}\right) = b_1 i_{\mathrm{k}}^3 + b_2 i_{\mathrm{k}}^2 + b_3 i_{\mathrm{k}} + b_4 \tag{3.7}$$

with its fitting parameters b_1, b_2, b_3, b_4 and the physical constraint of only allowing strictly monotonic functions. Similarly, the wire diameter and knit length relate linearly under constant applied loads and constant knit indices (Figure 3.13b). The modeling function is therefore a strictly monotonous increasing function

$$l_{\mathrm{M,A}}\left(d\right) = c_1 d + c_2 \tag{3.8}$$

with the fitting parameters c_1, c_2. Figure 3.13 shows exemplary experimental data (scattered) and the employed modeling functions based on Equations 3.7 and 3.8 (solid).

3.7.2 Model validation

The quality of the empirical model is validated by comparing experimental force-knit length profiles external to the empirical model to the predicted force-knit length profile based on the modeling functions. The Euclidean error definition

$$\|e_x\| = \sqrt{\sum_{i=F_{\mathrm{app,min}}}^{F_{\mathrm{app,max}}} \left(\frac{x_{\mathrm{exp},i} - x_{\mathrm{fit},i}}{x_{\mathrm{exp},i}}\right)^2} \tag{3.9}$$

is used to assess the summed differences between the experimentally obtained and modeled performance metric (x), e.g., the %-actuation contraction (ζ) or the mechanical work (W). Table 3.1 contains the error metrics for two prototypes external to the model. The prototypes have the wire diameters ($d = 0.203\,\mathrm{mm}, 0.254\,\mathrm{mm}$) and knit indices ($i_{\mathrm{k}} = 98\,\mathrm{mm^2\,mm^{-2}}, 103\,\mathrm{mm^2\,mm^{-2}}$). Table 3.1 shows that the model is particularly successful at predicting the scalar maximum %-actuation contraction ($e_{\hat{\zeta}}$) of contractile SMA knitted actuator with normalized errors $\|e_{\hat{\zeta},norm}\| < 1\%$. The error metrics that measure vectorial quantities over the complete range of applied forces, e.g., $\|e_\zeta\|$, are also reasonably low with compound errors $\|e_\zeta\| < 10\%$. The normalized error metrics are comparably low for the entire modeled knit index and wire diameter ranges. However, the normalized error increases when the knit index is close to the lower bounds of the empirical model ($i_{\mathrm{k}} < 40\,\mathrm{mm^2\,mm^{-2}}$), which can be attributed to limited manufacturing precision resulting in higher percentual errors, which carry on

	Unit	Ext. Prototypes	
d	[mm]	0.203	0.254
$I_{k,exp}$	$[\mathrm{mm}^2\,\mathrm{mm}^{-2}]$	98	103
$I_{k,fit}$	$[\mathrm{mm}^2\,\mathrm{mm}^{-2}]$	98	103
$\|e_\zeta\|$	[pp]	1.61	0.59
$\|e_{\zeta,norm}\|$	[%]	7.75	2.20
$\|e_{\hat{\zeta}}\|$	[pp]	0.05	0.04
$\|e_{\hat{\zeta},norm}\|$	[%]	0.69	0.25
$\|e_W\|$	$[J]$	0.0018	0.0009
$\|e_{W,norm}\|$	[%]	11.99	3.58

Table 3.1: **Model Validation:** Comparison of the modeled knit index to the experimentally obtained knit index, as well as a comparison of the determined error metrics for model-external prototypes to the error metrics of model-building prototypes, validates the quality of the model as a predictive tool of the contractile SMA knitted actuator performance.

into the model.

3.7.3 Forward and inverse design

The functional modeling of the contractile SMA knitted actuator performance enables the creation of a design tool with forward and inverse capabilities. The forward design tool intuitively follows the previously described process: The inputs, knit index and wire diameter, are inserted into the empirical model, which in response outputs the knit performance metrics (knit length, %-actuation contraction, mechanical work) as a vector over the range $1.0\,\mathrm{N} \leq F_{\mathrm{app}} \leq 2.5\,\mathrm{N}$. The performance metrics are plotted in separate figures and the maximum %-actuation contraction as well as the maximum mechanical work are displayed in scalar form.

The inverse design tool requires the input of desired performance metrics in scalar or vectorial form and outputs the geometric parameters that best accomplish the desired contractile SMA knitted actuator performance. The inverse design tool minimizes the error function $\|e_x\|$ from Equation 3.9 for the performance metric (x) and provides the knit index and wire diameter of the minimum Euclidian error contractile SMA knitted actuator. The inverse design tool utilizes the same functions as the forward design tool for which reason it produces the same modeling quality as the forward design tool. A knitted actuator with an actuation performance of $\zeta = [23\ 35\ 36\ 17\ 12]\,\%$

at the respective applied loads $F_{\text{app}} = [0.5\ 1.0\ 1.5\ 2.0\ 2.5]\,\text{N}$ was identified using the inverse design tool, which recommends a $d = 0.203\,\text{mm}$ prototype with a knit index of $i_{\text{k}} = 140\,\text{mm}^2\,\text{mm}^{-2}$. This recommendation agrees with experimental results ($d = 0.203\,\text{mm}, i_{\text{k}} = 138\,\text{mm}^2\,\text{mm}^{-2}$) of such a prototype.

A graphic user interface (GUI) was developed in Matlab and compiled to be a standalone software for the convenient use of the contractile SMA knitted actuator performance empirical model (Figure 3.14). The software enables the forward and inverse design of contractile SMA knitted actuators with their respective outputs. The forward design tool functions as a plotter of contractile SMA knitted actuator performance metrics when provided with geometric input parameters. Additionally, the scalar metrics, maximum %-actuation contraction and maximum mechanical work, are output as numerical values. The inverse design tool transforms the scalar or vectorial input of applied loads and their respective performance metrics into the knit index and wire diameter combination that best accomplishes the desired actuation performance. The software is openly available for use on the University of Minnesota - Design of Active Materials & Structures website.

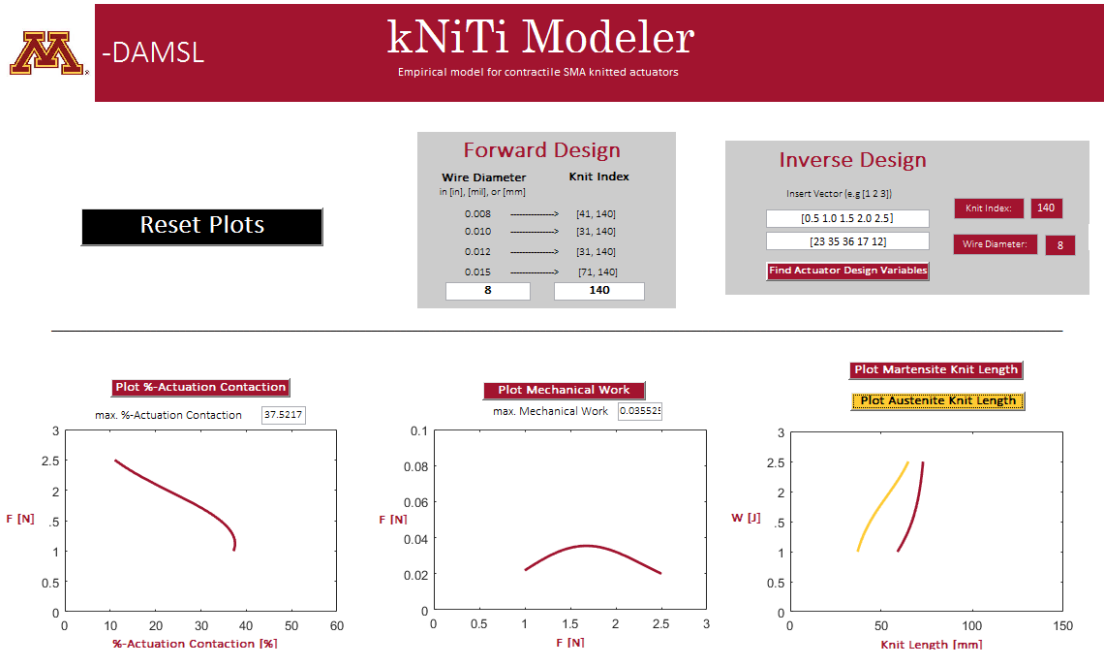

Figure 3.14: **Empirical Model Graphic User Interface (GUI):** A graphic user interface was built as a standalone software tool that enables the simple and easily accessible forward and inverse design of contractile SMA knitted actuators.

3.8 Conclusions

This paper describes the effect of geometric parameters on the contractile SMA knitted actuator performance and formulates an empirical model for the prediction of the contractile SMA knitted actuator performance. The knit index is introduced as a dimensionless geometric parameter that simplifies the complex geometric definition of contractile knitted architectures. Uniaxial thermo-mechanical tensile experiments were employed to characterize the contractile SMA knitted actuator performance: Large %-actuation contractions of up to 50% can be reported as the actuators perform against forces on the magnitude of 1 N-10 N. This size of prototype can perform mechanical work of up to 0.1 J, which can be easily increased by scaling the prototypes' number of wales and courses. The results of the experimental study reveal the strong correlation between the smallest set of independent geometric parameters, the knit index and the wire diameter, to the performance metrics. The performance metrics of the characterized prototypes are utilized to populate an empirical model. Algebraic functions interpolate

between the experimentally obtained data and build a multi-dimensional space for the design of contractile SMA knitted actuators. The empirical model accurately predicts the contractile SMA knitted actuator performance, which was validated by comparison of the model predictions to model external prototypes. Normalized scalar error metrics were found to be below 1%, whereas normalized compounded vectorial error metrics remained below 12% over the complete force range. Forward and inverse design capabilities are implemented to predict the performance based on geometric inputs and vice versa. The empirical model is coded as standalone software that is made publicly available on the University of Minnesota - Design of Active Materials and Structures Laboratory website.

The derivation of the minimal set of geometric parameters that drive the contractile SMA knitted actuator performance is a significant step to understanding the mechanics of this intriguing actuator architecture. The knowledge on the geometric trade-offs will inform physics-based models and future experimental studies on the multiscale design of SMA knitted actuators including SMA knitted actuator specific material training and lifetime performance. Preliminary studies on the SMA knit training show intriguing performance optimization capabilities, which can be better leveraged with the added understanding of this research. [73] Besides their actuation capabilities, SMA knits can also be leveraged for their sensing capabilities which stems from the temperature- and deformation-dependent electrical resistance. Despite the focus of this paper on SMA knitted actuators, this approach can be transferred and modified to simplify the description of the contractile knitted actuator performance using other multifunctional materials as the active fiber.

The expedited and informed design of contractile SMA knitted actuators provides the means for the development of promising actuation and sensing applications in the medical and rehabilitation device industries, as well as enable civil and military aerospace applications and wearable technologies.

Acknowledgements

The authors would like to thank MnDRIVE Robotics, Sensors, and Advanced Manufacturing (RSAM) for their support of the conducted research. Portions of this paper were originally published in the 2017 Proceedings of the ASME Conference on Smart

Materials, Adaptive Structures and Intelligent Systems as SMASIS2017-3926.

Chapter 4

In-Situ Strain- and Temperature-Control X-Ray Micro-Diffraction Analysis of Nickel-Titanium Knitted Architectures

K Eschen, J Garcia-Barriocanal and J Abel
Department of Mechanical Engineering, University of Minnesota,
111 Church Street SE, Minneapolis, MN 55455, USA
Published in **Materialia**
Vol **11**
Pages **100684**
DOI **10.1016/j.mtla.2020.100684**
Date **June 2020**

Abstract

The reversible phase transformation between B2 austenite phase and B19' martensite phase is the governing mechanism behind the exciting active and passive capabilities of Nickel-Titanium (NiTi) knitted architectures. NiTi knitted architectures are manufactured from a monofilament fiber of originally-straight NiTi wire that is bent into an interlocking network of adjacent loops. Depending on the thermo-mechanical load path, NiTi knitted architectures can provide excellent isothermal energy-absorption using the superelastic effect (SE) or function as large-deformation actuators that respond to thermal inputs using the shape memory effect (SME). The magnitude of NiTi knitted architecture characteristic performance metrics is dependent on the ability of the knitted architecture to undergo the reversible phase transformation, which is a function of the material stresses, strains, and temperature. This research quantifies the NiTi knitted architecture austenite phase fraction of the highly stressed filament surface in X-ray diffraction experiments as a function of the measurement position on the knitted loop and applied thermo-mechanical loading conditions. A Bruker D8 Discover 2D micro-diffractometer was equipped with a custom tensile straining- and temperature-control device. The Direct Comparison Method was employed to derive the austenite phase fraction from the X-ray diffraction patterns. This research establishes novel in-situ strain- and temperature-control X-ray micro-diffraction experiments and provides understanding of the governing deformation modes in NiTi knitted architectures.

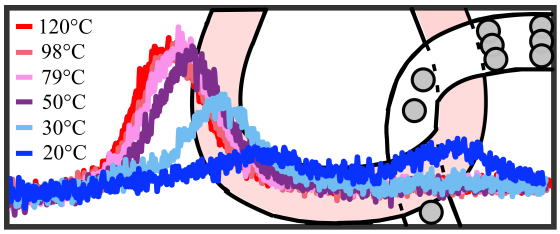

Figure 4.1: **Graphical Abstract:** The graphical abstract as published in Elsevier Materialia.

4.1 Introduction

NiTi-based shape memory alloy (SMA) knitted architectures provide large and tunable, three-dimensional actuation deformations in response to a change of the thermo-mechanical loading conditions. Due to these intriguing characteristics, NiTi knitted architectures have been implemented in medical [20, 22] and protective [103] wearables and serve as passive large deformation architectures in self-expanding stents [104] or extra-terrestrial rover tire studies. [27]

The intriguing NiTi knitted architecture characteristics are afforded by (1) the NiTi material properties and (2) the geometric assembly of NiTi filament in the knitted fabric architecture. NiTi is a binary alloy consisting of nearly equal parts nickel and titanium. NiTi exhibits a stress-, strain-, and temperature-dependent reversible martensitic phase transformation that is the underlying mechanism of its shape memory (thermally-induced) and superelastic (mechanically-induced) effects, [105] which enable the a strain recovery of up to 8% accompanied by a substantial change in material stiffness. [106] The martensitic (reversible, diffusionless, solid-to-solid) phase transformations occurs between the two dominant material phases, the B2 cubic parent austenite phase and the B19' monoclinic martensite phase. While R-phase and precipitate phases are usually also present in NiTi-based SMAs and can influence the phase transition process, they are often considered secondary to the shape memory (SME) and superelastic (SE) effects. The two effects, SME and SE, utilize different thermo-mechanical load paths that induce the phase transition (Figure 4.2).

The SME is generally started with initially unstrained NiTi (1). The material is mechanically loaded and unloaded, turning self-accommodated martensite into oriented martensite with preferred twin types (2) and residual strains present. Upon heating to the stress-free austenite start temperature (A_s), the phase transition to the high-symmetry austenite phase begins, and is completed when the temperature reaches the stress-free austenite finish temperature (A_f) (3). The oriented martensitic phase is fully-transformed into the austenitic phase which represents the memorized shape of the NiTi material and the residual thermo-elastic strains are recovered. Upon cooling to the martensite finish temperature (M_s) the reverse phase transition begins. The phase transition is completed when the martensite finish temperature is reached and self-accomodated martensite is present (1) which concludes the SME load path.

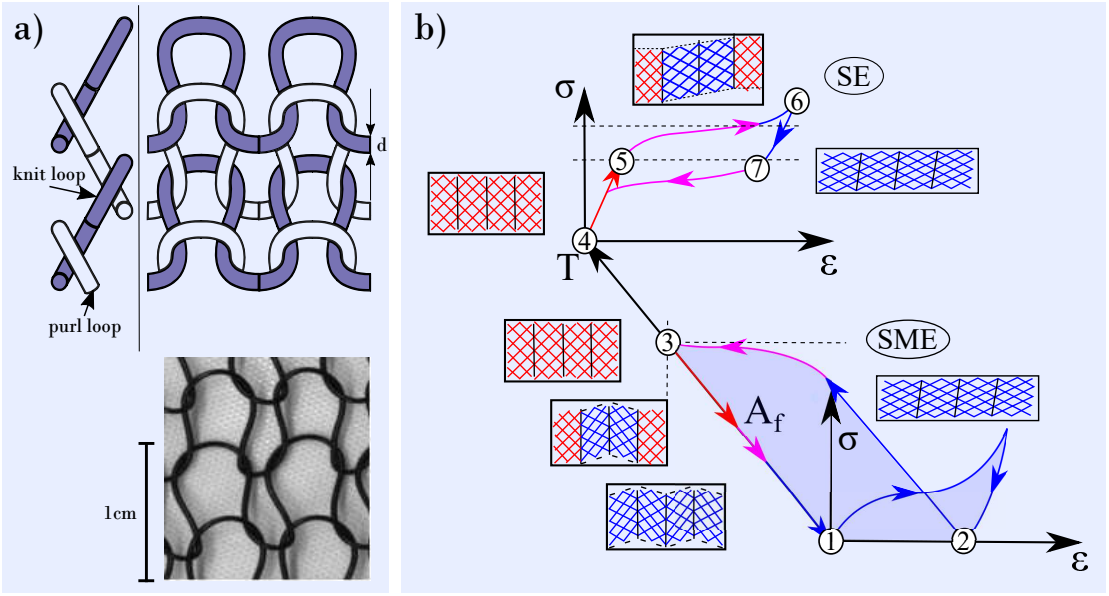

Figure 4.2: **NiTi Knitted Architecture Geometry & Material Thermo-mechanical Coupling :** (a) The active filament with the diameter (d) forms the interlocking network of knit and purl loops: Displayed are an abstracted representation and a physical prototype of the knit loop geometry and material as tested (b) NiTi undergoes stress- (σ), strain- (ε), and temperature-dependent (T) phase transitions that can be exploited in the superelastic (SE) and shape memory effects (SME).

The SE describes an isothermal mechanical load path that occurs at a temperature above the stress-free austenite finish temperature. The initially unstrained NiTi is fully-austenitic (4). Upon mechanical loading, the material elastically strains until the critical tranformation onset stress is reached (5). Upon further mechanical loading, the material transforms to oriented martensite (6) without significant increases in material stresses forming the stress-plateau. Unloading of the NiTi material results in elastic recovery of the martensitic phase (7) until a critical stress limit which marks the onset of the formation of austenite and/or other material phases (e.g., R-phase). [107] When the unloaded state (4) is regained, the material is fully-austenitic and returned into its initial condition.

Employing straight-annealed NiTi-based SMAs as the fiber in traditional knit manufacturing processes creates a fabric architecture that transforms and amplifies the ability of NiTi to recover large thermo-elastic strains. [6, 108] The knitted loop, the smallest repetitive element in knitted fabrics, is a highly bent geometry that is constrained

through the interlocking with its adjacent knitted loops. The ability to change the interlocking direction of a knitted loop with its adjacent loops enables the creation of knit patterns that exhibit varying actuation deformations (contraction, corrugation, rolling). The contractile knit pattern consists of interchanging courses of forward (knit loop) and reverse (purl loop) interlocking loops. The contractile knit pattern was selected for this research due to its relatively simple, macroscopically planar uniaxial contractions in response to the martensitic phase transformation. Current experimental analyses of the NiTi knitted architecture performance are limited to the knitted loop (meso) and knit pattern (macro) scales due to the complexity of architecture and material. [109, 74] However, when the knitted loop geometry deviates from ideal, perfectly-elastic loop geometries, [65] the NiTi knitted architecture performance is difficult to predict on the macro- and meso-scales due to the significant effect of stress- and strain-concentrations on the microstructure of NiTi. This knowledge can be obtained on the microscale.

Microstructural in-situ X-ray diffraction experiments have been performed to understand the governing micro-mechanics of NiTi, including prominent effects such a material texture, [110] shape-setting, [111] and phase transformation behavior. [112] The in-depth study of these effects is usually performed using highly-controlled, often monocrystalline, specimen. A less ideal geometry, NiTi wire, has been investigated with high resolution techniques while constraining the loading conditions to pure tension, [113, 114, 115] torsion, [116] and bending. [117] Lower fidelity micro-mechanical studies geared toward applications use materials and loading conditions that are not optimized for experimental analyses, e.g., orthodontic guidewires [118] and hard tissue implants [119] and rarely produce data that enables the study of underlying material mechanics. However, the analysis of the material microstructure in complex applications is often desirable as boundary conditions and thermo-mechanical loading paths can rarely be mimicked by idealized experiments. Limitations of current experimental equipment and techniques have been a significant burden on the in-situ X-ray diffraction analysis of NiTi within applications. While the thermo-mechanical conditions of an optimized geometry specimen can be controlled within standard X-ray diffraction equipment specimen holders, more complex geometries can currently not be analyzed for their thermo-mechanical properties in X-ray diffraction experiments.

This research presents an in-situ strain- and temperature-controlled X-ray microdiffraction (XRD) analysis to determine the phase distribution along the NiTi-based

SMA knitted architecture loop as a function of the spatial position on the knitted loop, macroscopically applied strains, and temperature. A novel experimental technique permits the in-situ control of thermo-mechanical loading conditions for complex geometries, such as NiTi knitted architecture in XRD experiments. This technique enables the derivation of the governing SMA knitted architecture mechanics in their application environment and elucidates the dominant microstructural mechanisms that enable the large macroscopic deformation recovery of NiTi knitted architectures upon the martensitic phase transition. Consequently a previously unavailable design space, the microscale, is introduced into the SMA knitted architecture design process.

4.2 Material & Prototypes

This section provides basic characterization data for the NiTi filaments utilized in the knit manufacturing process and discusses the manufacturing parameters of the knitted architecture prototypes.

4.2.1 NiTi Thermo-mechanical Characterization

NiTi filaments of varying chemical composition [120, 121] and thermo-mechanical treatment [122] are selected to realize the SME (Dynalloy Flexinol®) and SE (Fort Wayne Metals NiTi#1 filament) loading path in the knitted prototypes used for the X-ray micro-diffraction experiments. Both filaments have a diameter $d = 0.508\,\text{mm}$. The filaments' transformation temperatures were characterized using differential scanning calorimetry ($m = 50\,\text{mg}$). Fort Wayne Metals NiTi #1 is a material designed to exhibit the superelastic effect with low transformation temperatures ($M_f = -60\,°\text{C}, M_s = -40\,°\text{C}, A_s = 10\,°\text{C}, A_f = 17\,°\text{C}$) (Figure 4.3a). Dynalloy Flexinol® wire is slightly (51%) Ti-rich [123] and therefore undergoes phase transitions at relatively high temperatures ($M_f = 26\,°\text{C}, M_s = 65\,°\text{C}, A_s = 67\,°\text{C}, A_f = 87\,°\text{C}$) rendering it suitable for the exploitation of the shape memory effect as thermal loading from the referential room temperature induces the phase transformation (Figure 4.3b). Uniaxial tensile tests were performed to characterize the thermo-mechanical wire performances and provide a background for the analysis of the NiTi knitted architecture X-ray diffraction data. The Fort Wayne Metals NiTi#1 filament was strained and unstrained ($\hat{\varepsilon} = 11\%$) at room temperature while stresses were measured (Figure 4.3c). After the initial austenitic stress

increase, a plateau at $2\% \leq \varepsilon \leq 8\%$ with a plateau stress ($\sigma_p = 550\,\text{MPa}$) occurs during the martensitic, stress-induced transformation. Full transformation to martensite is marked by the end of the plateau and the subsequent martensitic stress increase. The Dynalloy Flexinol® was thermally-cycled [20 °C, 150 °C] under fixed strain conditions $\varepsilon = [2\%, 4\%, 6\%, 8\%]$ while the generated forces were measured. Thermal cycling consisted of 15min heating to 150 °C and subsequent soaking, followed by a cooling periods to 20 °C followed by 15min soaking per cycle. Under low temperatures ($T \approx 35\,°\text{C}$) the material is fully-martensitic. A high temperature plateau is present under low applied strains $[2\%, 4\%]$. The austenitic stress plateau begins at $T_{p,2\%} = 97\,°\text{C}$ at $\varepsilon = 2\%$ and $T_{p,4\%} = 123\,°\text{C}$ at $\varepsilon = 4\%$. Under larger prescribed strains, no high temperature plateau can be detected as the stresses present in the wire increase the transformation temperatures past the tested temperature range.

4.2.2 NiTi Knitted Architecture Prototypes

Two NiTi knitted architecture prototypes were manufactured, one from the Dynalloy Flexinol® filament and one Fort Wayne Metals NiTi#1 filament. The prototypes were manufactured on a Taitextma TH-260 manual flatbed knitting machine with large needle spacing ($d_n = 9.5\,\text{mm}$). The manufactured prototypes have a knit index ($i_k \approx 30\,\text{mm}^2\,\text{mm}^{-2}$) and consist of 5×6 loops. The dimensionless knit index a geometric parameter for SMA knitted loops defined as the fraction of the loop enclosed area and the squared wire diameter which enables the comparison of knitted loops of various scales. [109, 74] The relatively large wire diameter ($d = 0.508\,\text{mm}$) was selected to facilitate the use of a 0.3 mm collimator spot size and higher intensities in the x-ray diffraction procedure. A representative loop in the center of the knit prototype was selected for the microscale XRD analysis.

4.3 X-ray Diffraction Experiments

The NiTi knitted architecture prototypes were experimentally tested to determine the temperature- and macroscopic strain-dependent spatial distribution of NiTi material phases along the knitted loop.

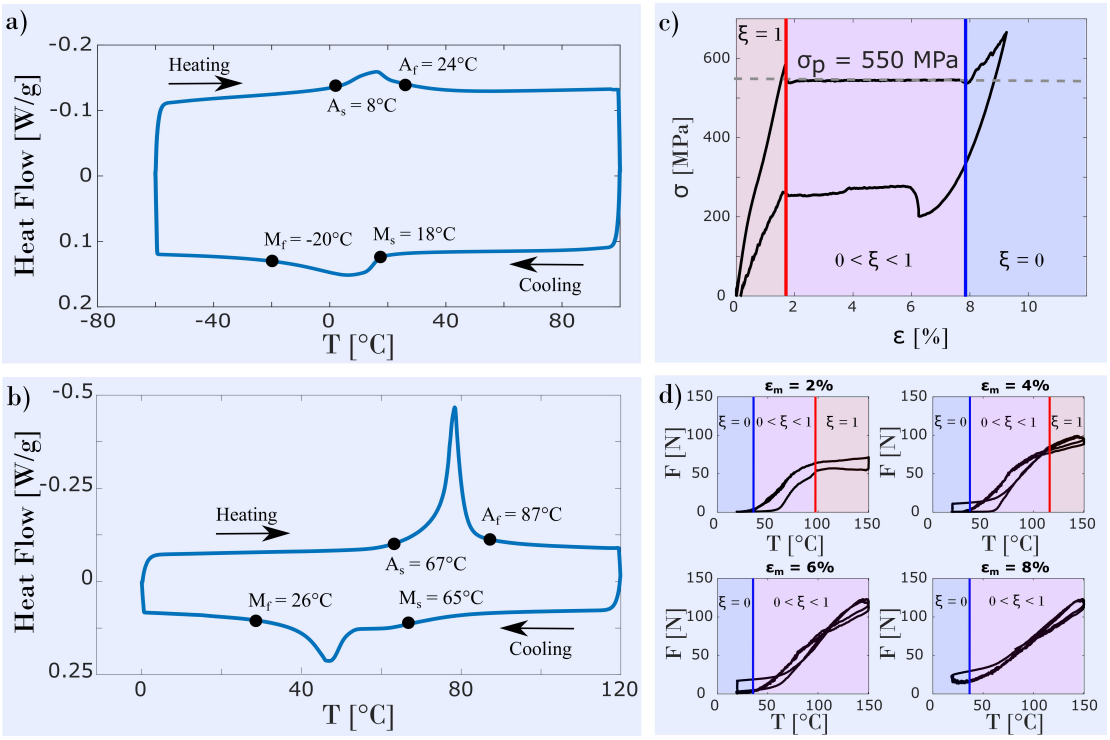

Figure 4.3: **Thermo-mechanical Characterization NiTi Wires:** Differential Scanning Calorimetry was used to identify the stress-free phase transformation temperatures of (a) the SE Fort Wayne Metals NiTi#1 and (b) the SME Dynalloy Flexinol® materials. Uniaxial tensile tests were performed on both filaments as well. The Fort Wayne Metals NiTi #1 filament was strained under constant temperatures ($T = 20\,°C$) (c), while the Dynalloy Flexinol® was subject to temperature cycling at fixed strain levels $\varepsilon = [2\%, 4\%, 6\%, 8\%]$.

4.3.1 Experimental Setup

The X-ray diffraction experiments were conducted in a Bruker D8 Discover 2D micro-diffractometer equipped with a Co-kα point radiation source (Figure 4.4a). A collimator narrowed the x-ray beam to a spot diameter $d_c = 0.3\,\text{mm}$ on the focused object. The temperature of the specimen was measured by a FLIR T-620 infrared camera with a resolution of 640×480 pixels.

A custom uniaxial knit deformation- and resistive heating device was fixed to the specimen holding stage of the micro-diffractometer (Figure 4.4b). The device consists of two parallel specimen holding rods connected by parallel shafts and a bolt to set the desired specimen. The device is designed to provide a clear path between the source

and specimen for the incident beam and the specimen and detector for the scattered beam. A maximum displacement of 60 mm can be achieved by the device. The knit specimen is resistively heated with a 0-10 V DC power supply connected via alligator clips.

4.3.2 Experimental Procedures

The two experiments, displacement-control and temperature-control, require slightly different experimental procedures. A uniaxial tensile experiment was performed on the NiTi knitted architectures as described in literature [109] to visualize the thermo-mechanical load paths employed in strain- and temperature-control procedures. Figure 4.4c displays the force-knit length profile in its fully-martensitic (blue) state and partially-austenitic (red) state. For the displacement-control experiments, performed with the Fort Wayne Metals NiTi#1 wire, the NiTi knitted architecture was displaced from its initial length $l_0 = 26\,\text{mm}$ to four macroscopic strain levels $\varepsilon_m = [5, 10, 15, 21]\%$. In the temperature-control experiment, the Dynalloy Flexinol® NiTi knitted architecture was fixed at a set displacement and the temperature was increased and decreased between $20\,^\circ\text{C} \leq T \leq 120\,^\circ\text{C}$ during the X-ray diffraction experiments. The measurement positions along the knitted loop are indicated with varying geometric symbols in Figure 4.4d while the number indicates the position along the wire diameter, (1) on the inside, (2) the midpoint, and (3) the outside. In all experiments, X-ray diffraction frames are collected at incident beam angles $\omega = [25, 35, 45]$ and detector angles $2\theta = [50, 70, 90]$ to measure X-ray diffraction peaks between 30-110 for $1000\frac{s}{\text{frame}}$. The attenuation length of the incident beam varied between $3.8\,\mu\text{m} \leq \lambda \leq 6.2\,\mu\text{m}$ depending on the incident beam angle as determined mathematically assuming a Cobalt x-ray energy $E = 6.926\,\text{keV}$ and a NiTi density $\rho = 6.45\,\text{g}\,\text{cm}^{-3}$ [124] which determined the analyzed material volume. The analyzed volume is overwhelmingly NiTi as the TiO_2 layer can be assumed to be smaller than 200 Å and consequently occupies less than 0.5% of the volume. [125] The analysis of the phase distribution on the surface of the SMA knitted actuator loop is conducted as the material stresses are assumed to be of the highest magnitude and the phase change effects to be the most extreme.

4.4 Results & Discussion

The detected scattered intensities of the in-situ displacement- and temperature-control experiments were analyzed using the Direct Comparison Method [126] and prepared to identify trends of the spatial distribution of austenitic phase in the surface wire layers as a function of the applied macroscopic strains and the temperature.

4.4.1 Data Analysis

The initial data analysis was conducted in the Bruker General Area Detector Diffraction System (GADDS) software. Intensity patterns of each frame were filtered with an octagon mask to exclude measurements points at the edges of the detector. The X-ray diffraction patterns were integrated over the goniometer angle (χ) and detector angle (2θ) and the integrated intensities were normalized using bin normalization. The resulting intensity patterns were exported to the Materials Data Inc. Jade software for further analysis. The intensity patterns of the three frames at $\omega = [25, 35, 45]/2\theta = [50, 70, 90]$ were merged for each measurement to obtain the full range between $2\theta = 30 - 110$ and a linear background fit was conducted. Literature data [127, 128, 129] provided insight into the X-ray diffraction peaks that are present in NiTi x-ray diffraction experiments. Seven of them were identified within the detected range (Table 4.1). In addition to the martensite and austenite phases, R-phase may form through direct transformation or thermal cycling in both heating and cooling load paths. Throughout this publication, R-phase was not identified at significant intensities and is lumped with monoclinic martensite phase as the quantified analysis focuses solely on the austenitic phase. [130, 131]

The austentic phase is used for the phase fraction quantification as the measured intensities can be trusted with high certainty. Drawn NiTi wire is prone to evolutionary textural effects in the martensitic phase during micromechanical mechanisms such as detwinning, variant reorientation, and stress-induced phase transition. [132] While the shape of the austenitic lattice is isotropic, and orientation therefore negligible, texture can vary the intensities of the monoclinic lattice martensite peaks significantly, and is therefore a considerable effect. [133] Correction factors ($T_{\{hkl\}}$) for preferred orientation exist based on a comparison of the preferred filament orientation direction and the reciprocal lattice vector, however, they are not suitable for texture correction when

Phase	$\{hkl\}$	$\overline{2\theta}$	F	p
A	{110}	49.5	208.97	12
A	{200}	72.36	244.92	6
A	{211}	93.08	27.15	24
M	{002}	44.97	35.58	2
M	{111}	51.27	48.11	4
M	{012}	52.56	34.75	2
M	{220}	98.83	10.31	2

Table 4.1: **List of Fitted Peaks:** The predominantly present peaks of the austenite (A) and martensite (M) phases are listed. The Miller indices {hkl}, average 2θ position ($\overline{2\theta}$), structure factor (F), and multiplicity factor (p) are also provided.

considerable preferred orientation is present. [134] Since the knitted architecture has varying local material stresses and the filament is in different orientations depending on the measurement point on the loop, martensitic peak intensities are excluded from quantitative phase fraction analyses.

Despite excluding martensitic peak intensities from the mathematical analysis, it is important to understand that an error could be introduced in the peak fitting of austenitic peaks by the presence of texture in closely neighboring martensite peaks. Such errors are expected to be maximized for the A{110} peak at $\overline{2\theta}_{A\{110\}} = 49.5$ due to the close angular proximity of the martensitic peaks M{111} ($\overline{2\theta}_{M\{111\}} = 51.27$) and M{012} ($\overline{2\theta}_{M}\{012\} = 52.56$). Figure 4.5a depicts these peaks as well as their pseudo-Voigt peak fitting functions. Despite them all showing their peak intensity between $49.5 \leq 2\theta < 52.5$, the martensite maxima fall into the shoulder of the austenite peak without affecting the quality of the independent fits. Additionally, tight constraints were selected during the peak fitting procedure for all experiments based on the shape, skew, and position of peaks in the fully-austenitic and fully-martensitic material states. The peaks were fitted as symmetrical as they occur at Bragg-angles $2\theta > 30$ with low axial divergence of the beam. The peak position was constrained to remain within close margins around the reference states throughout the experiment and ensured that peak shifting and broadening was in accordance with trends identified in literature. [135] Peak broadening from dislocations and stress-incudced defects primarily occurs in the martensite phase and does not affect the austenite phase fraction quantification. The fitting constraints have negligibly negative effects on the overall fit quality, but prevent overfitting and mitigate the introduction of errors due to the highly variable martensitic

peak intensity.

Additional mitigation of the undue influence of martensitic texture is accomplished in the experimental procedure since we use a 2D detector to collect the scattering data. This detector has an angular range of coverage of the specimen χ rotation of 45 °, which allows to properly integrate the full intensity under the diffraction poles and thus minimize the potential errors that texture could introduce and enables the analysis of partial Debye-Scherrer rings between $-70 \leq \chi \leq -110$. Further tilting of the Eulerian cradle of the diffractometer was prohibited by the experimental setup, as it would have led to collision with the incident optics of the instrument. Figure 4.5b depicts the intensity pattern for an unstrained, fully-austenitic measurement point and a strained, predominantely martensitic measurement point. Integration of the separate peak intensities and plotting against the goniometer angle χ shows texture in the martensitic peaks (Figure 4.5c).

The fitted peak areas were utilized in the direct comparison method. The direct comparison method is based on the calculation of the structure factor (F) and the multiplicity factor (p) which equate to the diffracted intensity (I),

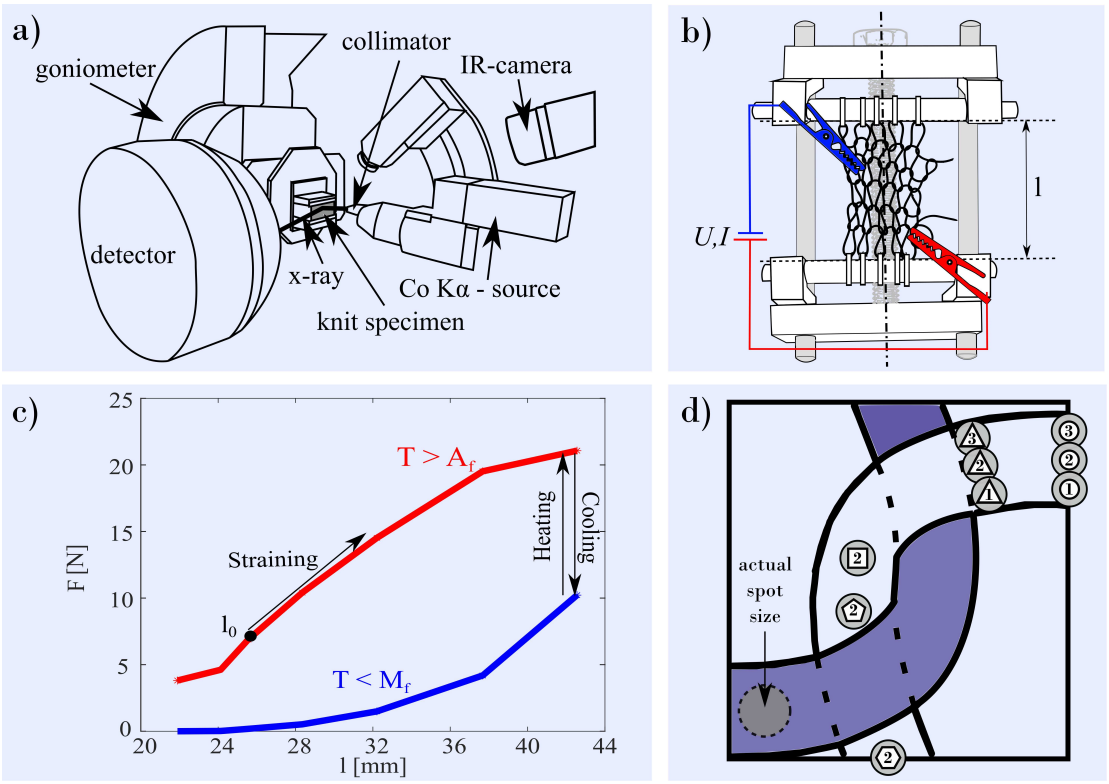

Figure 4.4: **Experimental Setup & Procedures:** (a) A Bruker D8 Discover 2D micro-diffractometer with an added FLIR T-620 infrared camera were used for the collection of X-ray diffraction patterns along the knitted loop. (b) The knitted specimen were strained, heated, and cooled in a custom straining device fixed to the diffractometer's specimen stage with resistive heating capabilities. (c) The displacement-control experiment was initiated at the knit length (l_0), from which the length was increased to the macroscopic strain levels $\varepsilon_m = [5, 10, 15, 21]\%$. (d) Measurements were conducted at the loop positions indicated by the geometric symbols (circle, triangle, rectangle, pentagon, hexagon) and their wire positions inside (1), midpoint (2), and outside (3).

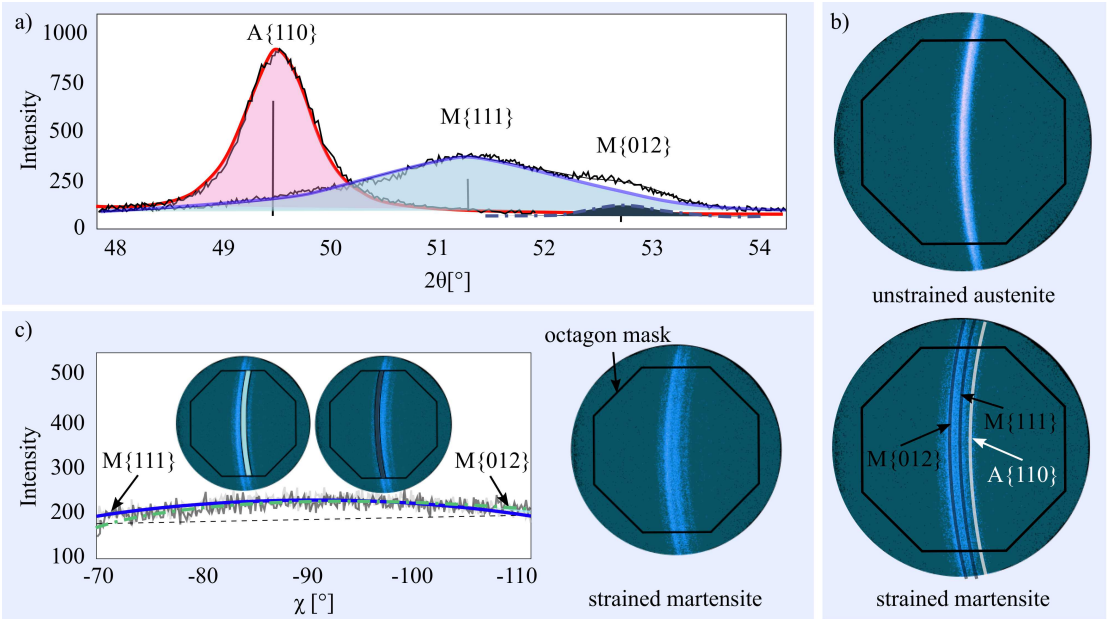

Figure 4.5: **Peak Fitting & Texture Analysis:** (a) The peaks of the most closely located reflections, A{110}, M{111}, and M{012}, are still clearly separated with overlapping shoulders. Close peak fitting constraints implemented across diffraction patterns ensure that austenitic peak intensities are largely independent of the martensite peak shape and intensities. (b) The partial Debye-Scherrer rings of a unstrained fully-austenitic measurement and a stained martensitic measurement. (c) Integration of the martensitic reflections M{111} and M{012} and plotting over (*chi*) shows texture which is accounted for in the peak integration.

$$I = |F|^2 p \left(\frac{1 + \cos^2 2\theta}{\sin^2 \theta \cos \theta} \right), \tag{4.1}$$

when multiplied with each other and the geometric function of 2θ. The structure factor was obtained from literature atomic scattering factor tables (f) for Ni and Ti, [136] which are provided as a function of $\frac{2\theta}{\lambda}$. Bragg's condition gives the relationship

$$\frac{2\theta}{\lambda} = \frac{1}{2 * d}, \tag{4.2}$$

where (d) is the atomic spacing and the Co-Kα wavelength is $\lambda_{Co-K\alpha} = 1.79\,\text{Å}$. [137] The scattering factor was derived by calculating the atomic spacing in austenite and martensite.

The atomic spacing (d_a) for austenite is

$$d_a = \frac{a_a}{\sqrt{h^2 + k^2 + l^2}}, \tag{4.3}$$

where $a_a = 3.015\,\text{Å}$ is the cubic B2 lattice constant and (h, k, l) are Miller indices. Similarly, the atomic spacing (d_m) for the B19' monoclinic lattice

$$d_m = \frac{\sin \beta_m}{\sqrt{\frac{h^2}{a_m^2} + \frac{k^2 \sin^2 \beta_m}{b_m^2} + \frac{l^2}{c_m^2} - \frac{2hl \cos \beta_m}{a_m c_m}}} \tag{4.4}$$

was calculated from the lattice constants $a_m = 2.915\,\text{Å}, b_m = 4.005\,\text{Å}, c_m = 4.754\,\text{Å}$ and $\beta_m = 100.932$. From the tabular data [136] using the calculated atomic spacings, the scattering factor (f) was obtained. The structure factor is the summation

$$F_{\{hkl\}} = \sum_{j=1}^{n} f \exp\left[2\pi i \left(hx_j + ky_j + lz_j\right)\right] \tag{4.5}$$

over the product of atomic scattering factor and the lattice geometry parameters where n is the number of atoms in the lattice and (x_j, y_j, z_j) are the fractional coordinates of nickel and titanium. The multiplicity factor is a count of all symmetry-equivalent planes (e.g., B2 $\{100\}$ = (100), (010), (001), (-100), (0-10), (00-1)). Each measured area intensity (I_m) of a fitted peak was corrected by the calculated intensities (I) of Equation 4.1

$$S_{\{hkl\}} = \frac{I_m}{I} \tag{4.6}$$

to obtain the scaled intensity $S_{\{hkl\}}$. To account for slight variations of the x-ray penetrated volumes due to the circular geometry of the NiTi wire, the scaled intensities ($S_{\{hkl\}}$) of the fitted peaks for each of the m diffracting lattices planes in a single measurement were summed

$$\tilde{S}_{\{hkl\}} = \sum_{i=1}^{m} S_{\{hkl\},i} \tag{4.7}$$

to quantify the total number of counts in a single experiment. Since the number of counts detected should remain constant unless the refracting volume changes, the scaled intensities ($S_{\{hkl\}}$) were corrected

$$V_{\{hkl\}} = \frac{S_{\{hkl\}}}{\tilde{S}_{\{hkl\}}} \tag{4.8}$$

by the intensity count sum over all diffracting lattice planes $\tilde{S}_{(hkl)}$ of the X-ray diffraction experiment, which we name the volume-corrected intensity ($V_{\{hkl\}}$).

The relative austenite phase fraction (ξ) was identified by comparison of the calculated austenitic volume-corrected intensities of each measurement ($V_{\{hkl\}}$) to volume-corrected intensities ($V_{\{hkl\},ref}$) of a reference pattern that was collected under reliably austenitic conditions ($\sigma = 0\,\text{MPa},\ T > A_f$).

$$\xi = \frac{T_{A\{110\}} + T_{A\{200\}} + T_{A\{211\}}}{T_{A\{110\},ref} + T_{A\{200\},ref} + T_{A\{211\},ref}} \tag{4.9}$$

4.4.2 Displacement-control Results

This section presents the results from the in-situ displacement-control experiments on the NiTi knitted architecture manufactured from the Fort Wayne Metals NiTi#1 material. X-ray diffraction experiments were conducted at various measurement positions spatially distributed over the knitted loop repetitive unit cell. These measurement positions are indicated in Figure 4.6a by the various geometric shapes and numbering. The number (1) is assigned to measurements on the inside, (2) measurement on the centerline, and (3) on the outside of the knitted loop. The measurements were performed at

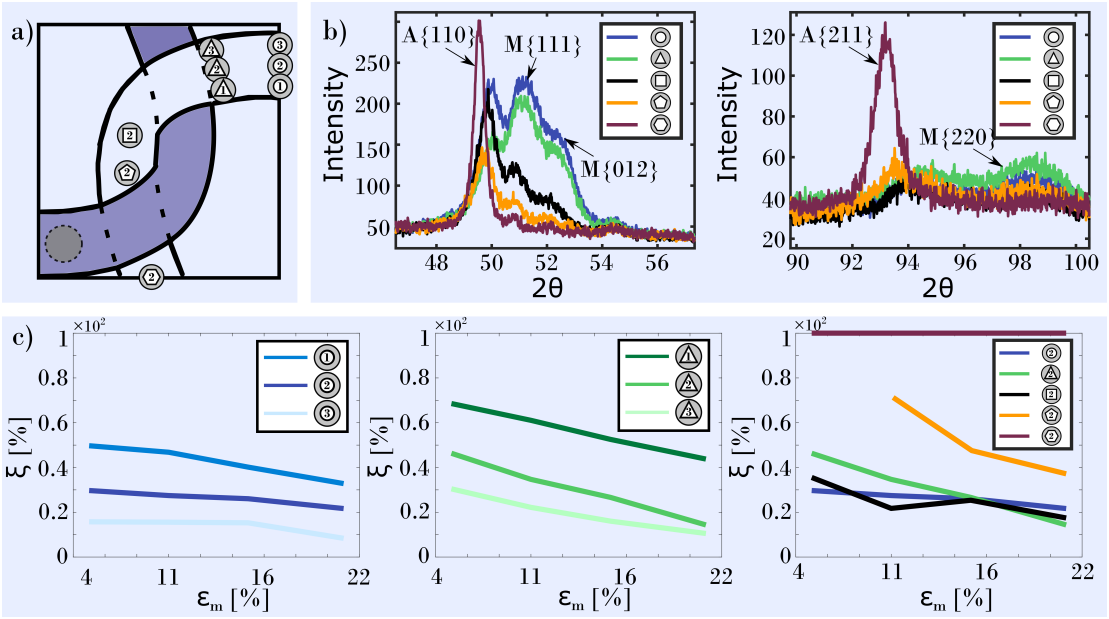

Figure 4.6: **Displacement-Control Results:** (a) The measurement positions circle, rectangle, triangle, pentagon and hexagon are indicated on the knitted loop repetitive unit cell. (b) 2θ-Intensity patterns are provided for all midpoint measurement positions at applied macroscopic strains $\varepsilon_m = 21\%$ around the austenitic peaks A{110} and A{211}. (c) The derived austenite phase fractions (ξ) are plotted over the macroscopic strain (ε_m). The phase transition occurs at measurement positions under bending and contact stresses, while the tension-loaded hexagon measurement position remains fully-austenitic throughout the experiment.

different macroscopic strain levels $\varepsilon_m = [5, 10, 15, 21]\%$. Exemplary X-ray diffraction patterns of the center-line measurements at $\varepsilon_m = 21\%$ are shown in Figure 4.6b. The 2θ-Intensity plots focus on the 2θ ranges around the austenitic A{110} and A{211} peaks which are in close angular proximity to the martensite peaks M{111}, M{012}, and M{220}, which necessitates the peak decomposition strategy.

Figure 4.6c provides the austenite phase fraction (ξ_A) in relation to the applied macroscopic strain (ε_m) on the NiTi knitted architecture for each measurement position. The subscripts are defined so that the first letter indicates the measurement position along the knitted loop (c-circle, t-triangle, r-rectangle, p-pentagon and h-hexagon) and the second letter the measurement position along the wire diameter (1-inside, 2-midpoint, 3-outside). These two letters are followed by the macroscopic strain applied during the measurement.

Measurement position "circle" shows the overall smallest austenite phase fractions in the NiTi knitted architecture. On the inside of the wire diameter (1), the austenite phase fraction decreases from $\xi_{c,1,5\%} = 49.7\%$ at the lowest macroscopic strain level to $\xi_{c,1,21\%} = 32.8\%$ at the highest macroscopic strain level. On the midpoint (2) and outside (3), a decrease of austenite volume fraction from the inside to the outside can similarly be observed. On the midpoint, the austenite phase fraction declines from $\xi_{c,2,5\%} = 29.7\%$ to $\xi_{c,2,21\%} = 21.7\%$ and on the outside, it declines from $\xi_{c,3,5\%} = 15.7\%$ to $\xi_{c,3,21\%} = 8.3\%$. This progression of decreasing austenite phase fraction from the inside to the outside of the NiTi wire is caused by an asymmetry of required tensile and compressive stresses to induce the phase transition in NiTi. [138, 139] NiTi under compressive stresses may not form stress plateaus that are as clear as those formed under tensile stresses (compare Figure 4.3c), however, compressive transformation occurs at elevated stress levels of approximately 1.3× magnitude of tensile transformation stresses. Consequently, the neutral bending axis of NiTi is asymmetrically located on the inside of the wire diameter in contrast to classic Euler-Bernoulli theory. [140] This behavior can also be observed in the loop contact measurement position close to the loop vertex indicated by the "triangle" (t), which resembles the behavior of vertex measurement position "circle" while the austenite phase fractions are slightly increased due to the decreased bending moment of this cross-section. The austenite phase fraction decreases from $\xi_{t,1,5\%} = 68.5\%$ to $\xi_{t,1,21\%} = 43.7\%$ on the inside, from $\xi_{r,2,5\%} = 46.3\%$ to $\xi_{t,2,21\%} = 14.3\%$ on the center, and from $\xi_{t,3,5\%} = 30.5\%$ to $\xi_{t,3,21\%} = 10.5\%$ on the outside when the macroscopic strain is increased in the experiment.

The third ε_m-ξ plot compares all center-line measurements to each other. Measurement position "hexagon" at the loop inflection point remains fully-austenitic throughout all applied macroscopic stress levels, suggesting that the stresses induced in this mostly tension-loaded knitted loop position remain below the transformation onset stresses. A large change in austenite phase fraction occurs in loop contact measurement position closest to the inflection point "pentagon", where the phase fraction decreases from $\xi_{p,2,10\%} = 72.4\%$ to $\xi_{p,2,21\%} = 37.2\%$. A X-ray diffraction experiment in this position could not be performed at macroscopic strain levels lower than $\varepsilon_m = 10\%$ as the interlocking wire cast a shadow until it sled past this measurement point with increased prescribed displacements. This measurement position is subject to tensile, bending, and contact stresses that superpose and contribute to the large change in austenite phase

fraction. Contact measurement position "rectangle" is under similar loading conditions as "pentagon", however, the decreased bending radius and large bending stresses at this position cause a low austenite phase fraction even at small applied macroscopic strain. Additionally, this measurement position is normal to the center of the loop contact point which is assumed to carry the largest contact stresses. Therefore, the austenite phase fraction reaches magnitudes similar to loop vertex measurement position "circle" and the contact measurement position closest to the loop vertex "triangle" and decreases from $\xi_{r,2,5\%} = 35.5\%$ to $\xi_{r,2,21\%} = 17.4\%$ under increasing macroscopic strains.

The largest variation in austenite volume fraction occurs in loop contact measurement position "pentagon" where the loop is initially mainly austenitic and subject to steadily increasing bending, tensile and contact stresses. Here, the NiTi material is stressed from its cubic austenite phase into its monoclinic martensite phase along the superelasic load path and undergoes large deformations and a significant change in material stiffness. While the superposition of bending, tensile and contact stresses induces the largest variation in austenite volume fraction, the loop vertex measurement position "circle", which is uniquely loading under bending stresses, suggests that the bending loading mode has the largest impact of all superimposed loading modes. This is supported by the large decrease of austenite volume fraction when comparing the inside loop vertex measurement position which is under compressive bending stresses to the outside loop vertex measurement position which is under tensile bending stresses. We therefore conclude that the dominant and simplest to control deformation mode of NiTi knitted architectures is bending deformation. In order to optimize the NiTi knitted architecture performance, it is advisable to tune the bending moments so that a large portion of the NiTi stress-pleateau is utilized. While the loop inflection point (hexagon), which is primarily loaded under tension, is expected to transition from austenite to martensite under sufficiently high macroscopically applied strains, the bending deformations induced in the manufacturing process pre-strain the wire into varying strain-conditions along the plateau and enable deformations with minimal macroscopic loading.

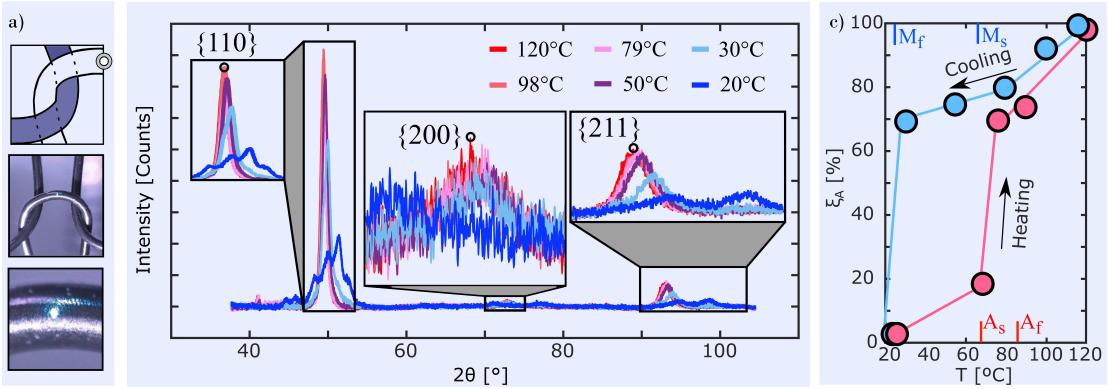

Figure 4.7: **Temperature-Control Results:** (a) Temperature-control experiments were conducted at the center-line loop vertex measurement position. (b) The 2θ-Intensity patterns of the cooling experiment are provided and qualitatively display the decline of austenitic phase with decreasing applied temperatures (c) NiTi characteristic temperature path-dependent austenite phase fractions are derived from the X-ray diffraction data. The transformation temperatures at the measurement position are elevated compared to stress-free transition temperatures due to the presence of bending stresses at the loop vertex.

4.4.3 Temperature-control Results

The temperature-control experiments were performed at the center-line loop vertex position indicated by the white circle in Figure 4.7a. The austenite peaks reported in Table 4.1 can be observed in Figure 4.7b. This figure displays the complete X-ray diffraction profiles between $2\theta = 30 - 110$ for the tested temperatures $T = [120, 98, 79, 50, 30, 20]$°C where the first experiment was conducted at $T = 120\,°\text{C}$ with subsequent cooling to the smaller temperatures until $T = 20\,°\text{C}$ was reached. The austenite peaks A{110}, A{200}, A{211} are highlighted specifically as they qualitatively portray the decline of austenitic peak intensities with the decrease of the applied temperature. The data from austenite volume fraction analysis of the cooling and heating X-ray diffraction experiments are displayed in Figure 4.7c. The martensite finish (M_f), martensite start (M_s), austenite start (A_s) and austenite finish (A_f) temperatures obtained from DSC of the stress-free wire (Section 4.2.1) are also provided for comparison. The austenite phase fraction of the cooling experiment steadily decreases from the reference state $T = 120\,°\text{C}$ at $\xi_{c,2,120\,°\text{C}} = 100\%$ to $T = 30\,°\text{C}$ where the austenite volume fraction is $\xi = 70\%$. The decline of the austenite volume fraction at temperatures above the martensite start

temperature is caused by the variable stresses induced in the material during the knitting process. A rapid drop of the austenite volume fraction occurs between $T = 30\,^{\circ}\mathrm{C}$ and $T = 20\,^{\circ}\mathrm{C}$ where the material transitions to a fully-martensitic phase due to the combination of the lowering temperature and the manufacturing stresses. Regardless of the induced manufacturing stresses, the knitted actuator is in its martensitic state at temperatures below the martensite finish temperature (M_f).

The same analysis was conducted for a heating experiment with multiple data points between $T = 20\,^{\circ}\mathrm{C}$ and $T = 120\,^{\circ}\mathrm{C}$. At $T = 70\,^{\circ}\mathrm{C}$, the austenite volume fraction increased to $\xi_{c,2,70\,^{\circ}\mathrm{C}} = 18\%$. A rapid increase occurs until A_f is reached at $T = 87\,^{\circ}\mathrm{C}$ where $\xi_{c,2,87\,^{\circ}\mathrm{C}} = 74\%$. However, due to the stresses induced in the manufacturing process, the material is not fully-austenitic at this temperature. Upon further heating, more austenitic phase forms and the material is fully-austenitic at loop vertex measurement position at $T = 120\,^{\circ}\mathrm{C}$.

These results are consistent with previously published NiTi material behavior and the findings from Section 4.4.2. The superposition of tensile, bending, and torsional deformations lead to a stress-state that increases the transition temperatures above the temperatures obtained in the stress-free state. While the NiTi characteristic temperature path-dependence based on the different transition temperatures for the austenite and martensite formation is clearly visible from the data, these temperatures are shifted to higher magnitudes by the presence of material stresses. Through connection with the results of Section 4.4.2, it can be concluded that the full NiTi knitted architecture performance can only be exploited when the applied temperature overcomes the required temperatures for transformation of the highly-stressed knitted loop portions in the contact area and the areas of large tensile bending stresses.

4.4.4 Limitations and Future Work

The presented study investigates the austenite volume fraction in the surface layers of a SMA knitted actuator loop. Future studies could provide additional information by overcoming some of the current limitations introduced by the experimental equipment, knit geometry, and prototypes.

The experimental equipment, the Bruker D8 Discover 2D x-ray microdiffractometer, enables this first quantitative analysis of the knitted architecture microstructure, however, overcoming some of its limitations will provide additional insight. A higher energy

beam would penetrate a larger volume and increase the scattering intensities within the same testing time. This could increase the understanding of the micro-mechanics beyond the surface layer and better resolve the individual reflections. Consequently, advanced diffraction pattern analysis, e.g., Rietveld refinement, could be used to quantify additional phases (martensite, R-phase), lattice strains, and stresses. While the utilized 2D detector can detect texture within the range of analyzed angles, a full texture analysis through specimen rotation would further increase the understanding of the microstructure.

Additional limitations are introduced by the geometry of the knitted architecture. The knitted loops interlace, which produces a shadow at the loop contact point that cannot be analyzed. This geometric limitation could be overcome through rotation of the specimen and increased penetration. Due to the circular geometry of the wire, the originally circular beam measures an elliptical shape and the the beam is less in focus with increasing distance from the center point of the beam. Higher energy x-rays and smaller collimator sizes would further reduce this error and enable a better spatial resolution along the wire diameter.

Lastly, transfer between different knitted loop geometries with varying bending radii, contact areas, and filament diameters, as well as the variation of additional shape memory material compositions will require a larger study and the analysis of systematically designed prototypes.

4.5 Conclusion

The NiTi knitted architecture microstructure was analyzed in in-situ strain- and temperature-control experiments to identify the predominant deformation mechanisms of this complex architecture. The Direct Comparison Method was employed to derive the austenite phase fraction from the X-ray diffraction patterns. Through comparison of the austenite phase fraction at spatially distributed measurement positions on the knitted loop under varying macroscopically applied strains and temperatures, the following conclusions could be drawn:

1. Under the predominantly axial loading conditions of the loop inflection point, no martensitic phase transition occurs and deformations, if present, are purely

austenitic-elastic. The NiTi knitted architecture undergoes the largest deformations and phase transitions under bending loads.

2. The smallest austenite volume fraction is present in the tensile bending stress area on the outer diameter of the loop vertex. The compression-tension asymmetry of NiTi martensitic phase transition results in a shift of the neutral bending axis towards the inner diameter. The location and magnitude of the maximum stress volume is an important NiTi knitted architecture design criterion relevant for the NiTi material selection.

3. The largest change in austenite volume fraction occurs in the contact area, which is subject to axial, bending, and contact stresses.

4. The phase transition within SMA knitted architectures is elevated to higher temperatures than the stress free transition temperatures due to the material stresses induced in the knit manufacturing process. The full NiTi knitted actuator performance, i.e. the full exploitation of thermally-recoverable deformations, requires the increase of the applied temperature to a magnitude that induces phase transition at the maximum stress volume.

In order to accomplish this analysis, novel experimental techniques were developed. In-situ strain- and temperature-control X-ray micro-diffraction experiments on a complex knitted geometry have been realized for the first time within a Bruker D8 Discover 2D micro-diffractometer, closely replicating the in-application conditions. A custom straining device and resistive temperature-control setup was developed and can be utilized for various straining applications and electroactive/resistive heating materials. The performed experiments are a significant step towards in-situ, in-operando, and in-application microstructure X-ray diffraction analysis that can elucidate the micro- and macro-mechanics of complex material architectures.

Acknowledgments

The authors thank Minnesota's Discovery, Research, and InnoVation Economoy (MnDRIVE) for the generous support and funding of the MnDRIVE Informatics PhD Graduate Assistantship. Parts of this work were carried out in the Characterization Facility,

University of Minnesota, which receives partial support from NSF through the MRSEC program. Ashley Bucsek is greatly appreciated for her support and teaching during the initiation of this research. Rachael Granberry and Charles Weinberg aided in the differential scanning calorimetry and uniaxial tensile data collection.

Chapter 5

A Finite Beam Element Model of the SMA Knitted Actuator Performance

K Eschen, C Weinberg and J Abel
Department of Mechanical Engineering, University of Minnesota,
111 Church Street SE, Minneapolis, MN 55455, USA
In preparation for submission to **Smart Materials & Structures**

Abstract

Multifunctional textiles have gained recent attention due their inherently intrinsic properties that provide actuator, energy dampening, or sensory capabilities within small form factor textiles without external attachments. Such technologies are specifically appealing for medical and aerospace wearables, where active compression, haptic feedback, or the tracking of bodily functions are important tasks that are ideally conducted in a minimally-intrusive fashion. Current design capabilities of multifunctional textile are limited as present predictive tools lack accuracy and universality. This paper presents a finite beam element modeling tool for shape memory alloy (SMA) knitted architectures. The temperature-dependent variation of material properties within the SMA knitted loop affects the macroscopic force-extension behavior of SMA knitted architectures leading to an actuated and a relaxed knitted architecture response. This difference is exploited as the active property in SMA knitted architectures. The modeling architecture defines interfaces between sub-models organized in modules, specifically the material constitutive module, repetitive unit cell module, manufacturing module, contact module, and a boundary condition module. The SMA knitted architecture is modeled utilizing a 1D SMA constitutive model, quarter loop knit unit cell, a differential geometry-based manufacturing model, while assuming 3D Coulomb friction conditions. Kinematically-suitable boundary conditions are applied and the simulation predictions are compared quantitatively to macroscopic tensile experimental results, as well as qualitatively to microscopic x-ray diffraction phase analysis. The verification against experimental data supports the ability of the modeling tool to accurately predict the SMA knitted architecture thermo-mechanical performance with mean force-extension errors of less than 5%. The modeling tool provides the basis to understand, design, and optimize the lightweight, large force and deformation SMA knitted actuator textiles for novel applications. Additionally, the multifunctional textile modeling tool is implemented based on highly interchangeable sub-models to create synergies and propel the modeling of any multifunctional textile.

5.1 Introduction

Wearable technologies have received tremendous attention in the past years and recent wearable computing and medical wearable market projections suggest compound annual growth rates of up to 28% and a growth to a global market size of $82 billion until 2023. [18, 19] The applications of wearable technologies range from consumer products such as haptic feedback devices [141] or fitness trackers [142] to medical, [20] rehabilitative, [143] health monitoring, [144] and defense applications. [71]

Early wearable technologies have equipped traditional wearable items, such as clothing and watches, with additional sensors, [145] actuators, [41, 146] and electronics. [147] The recent wearable technologies focus has been on fully-integrated, intrinsically-smart fabrics, which accomplish their advanced functionality through novel fiber- and material-systems. [17] The resulting smart fabric is inherently hierarchical and spans the nano- and micro-scales (material level), the meso- (unit cell level) and macro-scales (fabric level) up to the application scale with full system integration. In contrast to attached sensor and actuator devices, this approach enables unique smart behaviors that are afforded by the textile itself without compromising desirable fabric qualities such as flexibility, form factor, and softness.

Smart fabrics of various textile architecture and multifunctional fiber combinations have generated recent attention. Smart fabrics provide enhanced actuation, sensing, and energy storage capabilities through the integration of multifunctional fibers within spatial fabric architectures. Such multifunctional fibers include, among others, shape memory alloys (SMA), [148] shape memory polymers (SMP), [149] and carbon nanotubes (CNT), [150] which, in response to a thermo-mechanical or electro-mechanical input, reversibly transform between states of varying fiber geometry and stiffness. Through the integration of fibers in spatial fabrics – e.g., knitted, [96, 151, 152, 153]woven, [154, 155, 156] braided [157] – the 1D change of fiber geometry and stiffness can be transformed and amplified in two-/three dimensions. [6] For example, blended yarn-based fabrics with electro-conductive filaments provide excellent strain-, [158, 159] humidity-, [160] or pressure-sensing capabilities [161] for health monitoring and artificial skin applications. Textile antennae enable integrated wearable communication [71, 94] and can be tuned to operate at various frequencies through designed deformations while being robust and lightweight. Actuator textiles made of shape memory alloys produce large

3D displacements and forces in response to thermo-mechanical inputs, [6] shape memory polymers can exhibit smart properties based on thermal or electrical impulses, [15] and carbon nanotubes textiles have been proposed for simultaneous strain-sensing and actuation artificial muscle applications. [13]

Current multifunctional fabric designs are largely based on empirical findings and isolated, specialized, and highly-confined models. Due to the novelty of smart fabrics, most published research is concerned with empirically showcasing the gained capabilities of assembling the selected multifunctional filament in a textile architecture. These experiments highlight the smart fabric capabilities, e.g., through quasi-static tensile tests, [13] conductivity measurements, [71] or dynamic analysis, [15] and set up the stage for the derivation of universal design rules.

Multifunctional fabric modeling is an emerging discipline that could provide the means for universal design rules. However, multifunctional fabric models are currently limited by the high specialization and complexity of spanning multiple modeling scales [162] and thus far only exist with reduced dimensionality for SMA knitted architectures. SMA knitted architectures have been modeled empirically, [163] analytically, [72] and numerically, [164] but do not permit the simple variation of material and textile unit cell, while also being limited to a small range of thermo-mechanical loading cases. Most generally, fabric modeling architectures connect microscale multifunctional material constitutive models to mesoscopic unit cell models, and impose macroscopic constraints and boundaries for the specific system. While the connection of multiscalar sub-models in a multifunctional fabric approach has not been researched previously, many sub-models, i.e., multifunctional material models, fabric unit cell geometry models, and model solving methods exist and can be employed in an overarching modeling architecture. Microscale multifunctional material constitutive models exist phenomenologically and atomistic/lattice-based, and are implemented in varying dimensionality for shape memory alloys, [165, 166, 167] piezoelectric materials, [168] shape memory polymers, [169] and carbon-nanotubes. [170] Similarly, geometric mesoscopic textile unit cell models have already been proposed for plain [96] and garter [72] knitted fabrics, plain weave fabrics [154] and braided fabrics. [157] A compilation of textile geometry models is provided in the WiseTEX Suite, which can export geometry models suited for finite element computations. [171] A multifunctional fabric modeling tool that connects material and textile models, enables the application of complex loading states, produces

multifunctional fabric performance predictions, and will further propel multifunctional fabrics as a viable technology for fully-integrated, smart wearables.

This paper presents a multiscale modeling architecture for multifunctional fabrics. This architecture connects models on all scales in interchangeable modules, enables the exploitation of modeling synergies to reduce modeling effort, provides cross-comparison between modeling approaches, and presents a universal tool for multifunctional fabric modeling. We introduce a modular multifunctional fabric modeling architecture and populate it with an initial set of multiscale sub-models that interact through clearly defined sub-model in- and outputs. The modeling architecture is initially focused on SMA knitted fabrics and contains microscale material models, three-dimensional mesoscopic mathematical function-based and nodal input geometry models of the fabric unit cell, and a finite element solving algorithm based on beam elements arbitrarily oriented in space with comprehensive load-bearing complexity (bending, shear, tension/compression, torsion). Through assembly of the modeled fabric unit cell elements, macroscopic models are generated with imposed boundary conditions and constraints. Optimization and calibration to multiscale experimental inputs (e.g., macroscale displacements and forces, microscale phase-volume fraction) can be employed to expand modeling accuracy and study parameter uncertainties. The proposed modeling architecture is a highly flexible and expandable basis for improved multifunctional fabric analysis. Through this research, future multifunctional fabric models can employ the implemented sub-models through standardized in- and output scripts and significantly reduce the modeling effort through synergy effects. Potential future sub-models include a variety of material models, contact models, boundary models, and 2D/3D model solution approaches, as well as optimization routines on objective functions that identify parameters based on the comparison of experimental and modeled data. This research presents and verifies the first three-dimensional model of the contractile SMA knitted architecture and sets up a multifunctional fabric modeling architecture that can be adapted to a variety of material and textile geometry combinations.

5.2 Finite Beam Element Framework

Fabrics are flexible architectures that consist of a network of interlacing fibers. [172] The fiber, the element common to all fabrics, is a long and slender geometry that is

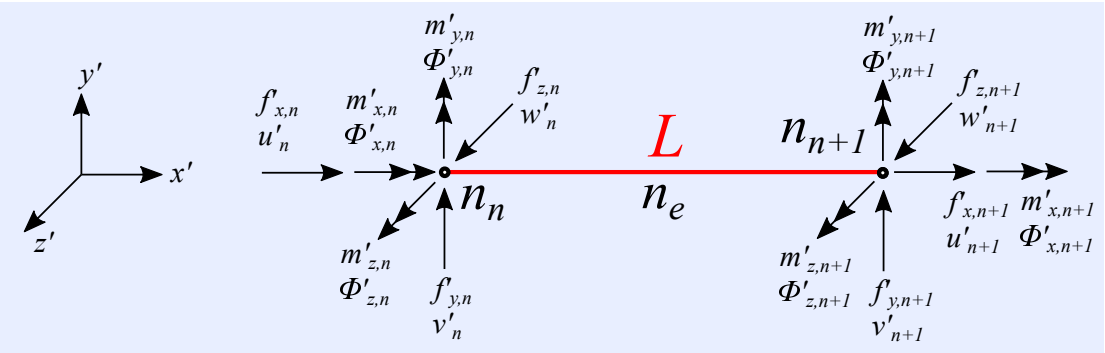

Figure 5.1: **Finite Beam Element:** The basic finite beam element between the nodes n and $n+1$ supports tensile forces $(f'_{x,n}, f'_{x,n+1})$ and displacements (u'_n, u'_{n+1}), torsional moments $(m'_{x,n}, m'_{x,n+1})$ and displacements $(\Phi'_{x,n}, \Phi'_{x,n+1})$, shear forces $(f'_{y,n}, f'_{y,n+1}, f'_{z,n}, f'_{z,n+1})$ and displacements $(v'_n, v'_{n+1}, w'_n, w'_{n+1})$, as well as bending moments $(m'_{y,n}, m'_{y,n+1}, m'_{z,n}, m'_{z,n+1})$ and displacements $(\Phi'_{y,n}, \Phi'_{y,n+1}, \Phi'_{z,n}, \Phi'_{z,n+1})$ around the y'- and z'-axes with respect to the local coordinate system $(x', y'z')$.

bent, twisted, buckled, or elongated to create the various types of fabrics. [173]
Finite element methods (FEM) have been developed and optimized for a variety of geometric modeling requirements. Most generally, fully three-dimensional formulations can be used to solve complex geometries. When permitted by the geometry, significant reductions in the model complexity can be accomplished through simplifications such as plane stress, plane strain, frame, or grid formulations. [174] The finite beam element arbitrarily oriented in space formulation can be a very elegant solution for the modeling of long and slender 3D objects that can support fully three-dimensional loads (Figure 5.1) with a substantial reduction of the computational cost in comparison to fully three-dimensional FEM. As fabrics are constructed from long and slender fibers, the finite beam element arbitrarily oriented in space formulation is utilized as the framework for the multifunctional fabric modeling architecture. Using this method, the fabric geometry is discretized into a defined number of nodes (n_n) and elements $(n_e = n_n - 1)$. Discretization can be performed linearly in a selected coordinate, with the goal of constant element lengths, or customized with higher node densities in areas of interest as prescribed by a function. The finite element framework is the centerpiece of the presented modeling architecture and conducts the tasks of discretization, assembly of stiffness matrices, and solution of force-displacement equations (Figure 5.2) while taking inputs from a variety of modeling modules. The modeling architecture operates

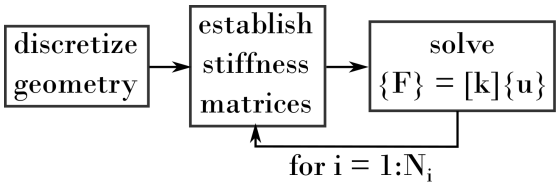

Figure 5.2: **Finite Element Flowchart:** The finite element method performs the tasks of discretizing the geometry, generating the stiffness matrix, and solving the linear system of equations. A for loop iterates the procedure until the range of desired thermo-, electro-, or magneto-mechanical inputs are covered.

iteratively (i) for (N_i) increments of small changes in applied forces or displacements. This approach is chosen to address the nonlinear behavior that is introduced by the geometry, contact conditions, and material constitutive relations while performing this simple and fast finite element routine that can be solved without numerical techniques. These nonlinear behaviors are introduced in the sub-models that are part of the multiple modules that interact with the modeling framework.

5.3 Modules

Modules are defined to interact with the multifunctional modeling architecture finite beam element framework to simplify the variation of the fabric architecture and multifunctional material. Additionally, sub-models of varying complexity can also be compared to each other for the identification of limitations and assessment of possible complexity-reductions. The modules accomplish specific modeling tasks and interface with the framework through standardized in- and outputs to enable their seamless interchangeability. The initial set of modules is: constitutive material module, representative volume element module, contact module, manufacturing module, and boundary condition module.

5.3.1 Constitutive Material Module

This module contains the constitutive multifunctional material model that predicts the change of material properties based on the thermo-, electro-, or magneto-mechanical inputs. To maintain the simplicity of the model, the material constitutive module is not added as a non-linear constraint during the solution of the finite beam element method,

which assumes linear material parameters. Instead, the constitutive material module receives relevant environmental inputs, such as the temperature, as well the calculated displacements and forces from the linear finite element method, and calculates the new material properties and the material stress state for the next iteration of the modeling algorithm.

Constitutive multifunctional material models have been developed for most commonly used multifunctional materials. Regardless of the multifunctional material, these models can be most broadly grouped as phenomenological, energy-based, or atomistic / lattice-based. [175, 176, 177] While atomistic and lattice-based models can provide superior micro-mechanical insight, such models are often highly complex and geared towards understanding the material response itself rather than being implemented in a design context. In contrast, phenomenological models compromise the insight into the physics of the multifunctional material microstructure, but model functionally the material properties such as phase diagrams, plasticity, or hysteresis. Due to their ability to accurately capture the multifunctional material behavior, their relative modeling simplicity, and low computational cost, this modeling architecture focuses on phenomenological constitutive material models. While such material models also exist for piezoelectric materials, [168] shape memory polymers, [169, 178] and many other multifunctional materials, a set of existing SMA phenomenological material models is introduced here in detail due to the modeling architecture validation using the intriguing contractile SMA knitted architecture.

Shape memory alloys are metallic compounds that commonly are based on nickel-titanium in its binary form or with additional alloyed elements. [105] They exhibit a strain-, stress-, and temperature-dependent transition between an austenitic and a martensitic material phase which demonstrate varying material properties (e.g., Young's modulus, shear modulus, etc.). The most prominent shape memory alloy behaviors, superelasticity and the shape memory effect, are introduced through mechanically- (superelasticity) and thermally-induced (shape memory effect) phase transition. Significant material strains of up to 8% can be recovered thermo-elastically through this phase transition. [35] The degree of transition is measured by the martensite volume fraction (ξ), which is equal to one for a fully-martensitic material and zero for a fully-austenitic material. As the martensite phase can be induced mechanically and thermally, the martensite volume fraction can be split into a stress-induced martensite volume fraction (ξ_s) and

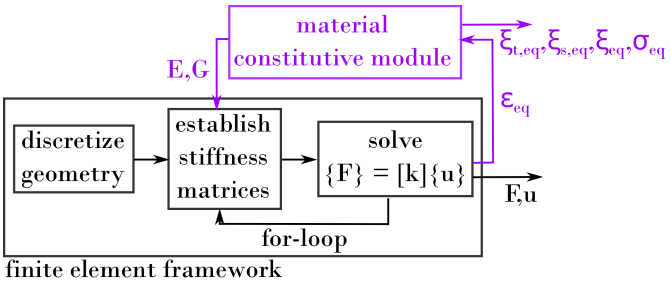

Figure 5.3: **Material Constitutive Module:** The material constitutive model receives inputs from the solution of the finite element procedure, updates material properties for the next model iteration, and outputs the material state. In case of SMA material, the inputs are material strains (ε) and initial conditions, updated material properties are the elasticity (E) and shear (G) moduli, and outputs are the material phase fraction (ξ), stress-induced martensite fraction (ξ_s), temperature-induced martensite fraction (ξ_t) and material stresses (σ).

a temperature-induced martensite volume fraction (ξ_t), for which $\xi_t + \xi_s \leq 1$ must be true. [179] The stress-induced transformation occurs at critical transformation stresses which may depend on the stress-state, [180, 138, 139] and can be defined by the detwinning start stress (σ_s) and the detwinning finish stress (σ_f) under tensile, compressive, or shear loading conditions. The critical transformation temperatures are the martensite start (M_s), austenite start (A_s), martensite finish (M_f), and austenite finish (A_f) temperatures.

Material constitutive relations try to capture this behavior with varying accuracy and complexity. A binary elasticity and shear moduli approach that distinguishes austenitic moduli (E_A, G_A) at a temperature above the stress-free austenite finish temperature (A_f) from martensitic moduli (E_M, G_M) at temperatures below the stress-free martensite finish temperature (M_f) can present a valid simplification for stiffness-dominated systems [72] (Figure 5.4a - binary modulus model). An extension of this approach models the behavior above the austenite finish temperature as a tri-linear curve with austenitic moduli (E_A, G_A) at stresses below the detwinning start stresses, plateau moduli (E_P, G_P) in the detwinning region and martensitic moduli (E_M, G_M) at stresses above the detwinning finish stress (Figure 5.4b - simple superelastic model). In contrast, the material behavior below the martensite finish temperature remains constant (E_M, G_M) regardless of the applied stress. Free-energy and thermodynamic approaches were pursued to increase the capabilities of macroscopic, phenomenological

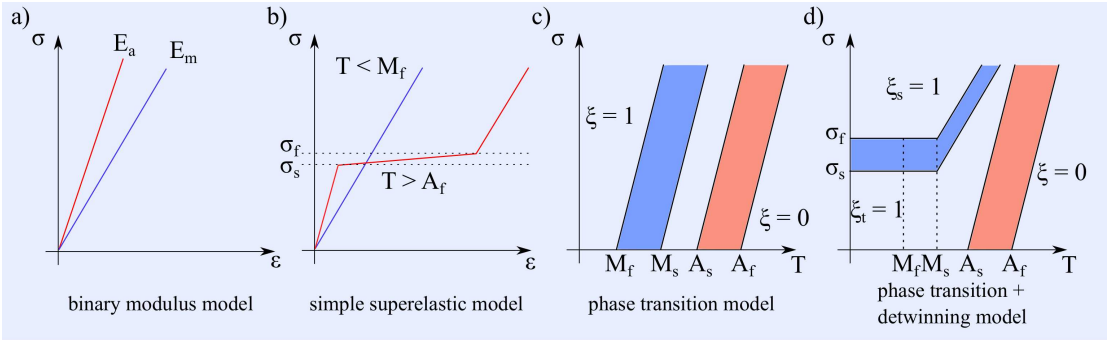

Figure 5.4: **1D Shape Memory Alloy Phenomenological Material Constitutive Models:** Shape memory alloy material constitutive models of varying complexity have been proposed in literature and implemented in the modeling architecture's constitutive model module. A simple binary moduli approach (a) and an extension that models the behavior above the austenite finish temperature as trilinear (b) are computationally inexpensive and can be appropriate approximations of the material behavior. Published models describe the thermodynamics of the phase transition through a internal variable, the martensite phase fraction (ξ) and have been proposed to model the transition between austenite and martensite (c), or even distinguish between stress- and temperature-induced martensitic phase (d).

shape memory alloy material models. Such models developed from capturing superelasticity [181] to capturing transformation temperature-related phase changes [182] (Figure 5.4c - phase transition model). A prominent model that phenomenologically captures the temperature- and stress-induced phase transitions is the Brinson shape memory material model, [165] which was initially proposed in pure tension (Figure 5.4d - phase transition and detwinning model), but has been adapted to also capture compressive scenarios. [183] The four approaches introduced in this section and Figure 5.4 are implemented in the modular modeling architecture.

The implemented constitutive material models are all one-dimensional and are incapable of simultaneously processing multi-axial strain states without pre-processing. The reduction of the 3D strain state obtained from the beam element finite element method to a 1D input suitable for the constitutive material model is accomplished through an equivalent strain formulation

$$\varepsilon_{eq} = \sqrt{(\varepsilon_{b,y} + \varepsilon_{b,z} + \varepsilon_{t,x})^2 + \left(\frac{\gamma}{C^E}\right)^2}, \tag{5.1}$$

where ($\varepsilon_{b,y}$) and ($\varepsilon_{b,z}$) are bending strains, ($\varepsilon_{t,x}$) are tensile strains, and (γ) are shear

strains from torquing and bending (if Timoshenko beam theory is applied, compare supplemental materials). While tensile normal strains from bending and normal loading are assumed to induce transition at an equivalent stress level, shear strains are scaled by the empirical coefficient (C^E) to accommodate for the generally lower transition stresses of this loading mode. [184, 183] Consequently the stresses and phase fractions that are output by the constitutive model are also equivalent stresses (σ_{eq}) and phase fractions (ξ_{eq}).

5.3.2 Repetitive Volume Element Module

Textiles are inherently hierarchical, which means that textiles are arranged out of repeating elements on multiple levels or scales. [185] In a traditional textiles, such levels could be composed of a repetitive filament/yarn geometry, a textile unit cell such as a knit loop, a braid unit, or a weave unit, the textile pattern composed of multiple unit cells, and grid patterns composed of multiple textile patterns. [6] This decomposition of textiles into hierarchical levels stems from the introduction of minimum energy principles for the description of textile properties. [186, 187] Minimum energy models exist for yarns [188, 189] on the filament scale, weave unit cells, [154, 155, 156] braid unit cells, [157] and knit unit cells such as plain, [96], garter [151, 152] and rib [153] knit unit cells. Based on these geometry models, the forces and deformations of the fabric unit cells can be computed analytically or numerically and the textile pattern performance can be predicted by assembly of multiple unit cells. The general interaction of the repetitive volume element module with the finite element framework is displayed in Figure 5.5. Input parameters specific to the repetitive volume element, typically element width, height, diameter, etc. are provided to define the function ($f(x, y, z)$) that resembles the repetitive volume element. This function serves as the input for the discretization algorithm which turns the continuous function into discrete data points.

The repetitive volume element is not necessarily tied to a certain textile scale. However, repetitive volume elements are typically defined on the microscale filament/yarn level or the mesoscale. Figure 5.6 shows a set of filament/yarn geometries, monofilament, single-ply, and multi-ply yarns which all can serve as the filament that is used for the manufacture of the textile unit cell. Figure 5.6 presents three simple textile unit cells for garter knits, plain weaves, and plain braids. Through the assembly of repetitive volume elements, a complete textile pattern can be generated. The garter knit geometry

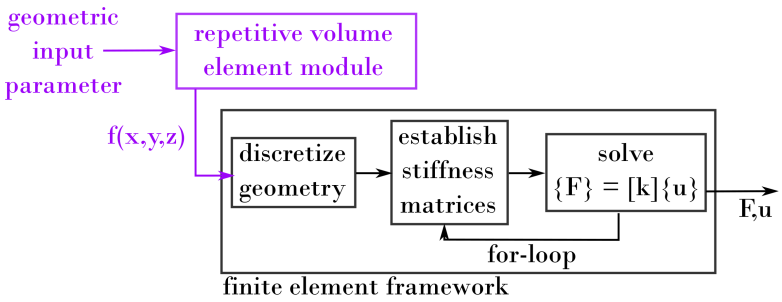

Figure 5.5: **Repetitive Volume Element Module:** The repetitive volume element model receives geometric inputs depending on the specific implementation of the textile unit cell. These inputs are turned into a geometry function ($f(x, y, z)$) in Cartesian coordinates.

is discussed in detail as it is used for the validation of this modeling architecture. The bold and dotted outlines of Figure 5.6 surrounding the monofilament fiber, the garter knit repetitive volume element, and the garter textile pattern indicate the combination of geometry selections in this publication. When used with multifunctional materials, garter knitted textiles produce linear contractile deformations upon changing the material properties through thermo-mechanical loading. [163] Garter knitted textiles are manufactured from a single flexible fiber that forms a network of interlacing knitted loops. The knitted loops of adjacent, horizontally-aligned rows are mirrored opposites (knit and purl loops) that only differ in the direction in which they are pulled through the previous row. The garter knit unit cell is defined by the wale width (W), course height (C), projected course height (C_p), loop angle (χ), loop length (L), ridge height (r), and loop enclosed area (A_l). The fraction of the loop enclosed area (A_l) and the squared wire diameter (d) is called the knit index (i_k). An additional, free-geometry definition tool is implemented based on Bezier curves, which can be defined reproduce experimentally-obtained unit cell geometries. The number of defining Bezier points can be chosen freely to accomplish sufficient approximation of the unit cell geometry. This tool is utilized in the validation of the SMA knitted architecture in this publication. Experimentally-derived initial geometries based on 2D imaging of knitted loops and the measurement of the ridge height (r) generate the initial geometry of the SMA knitted architecture prototype unit cells. The knit pattern is defined by the number of loops in the wale-/column- (m) and course-/row-wise (n) directions. [109]

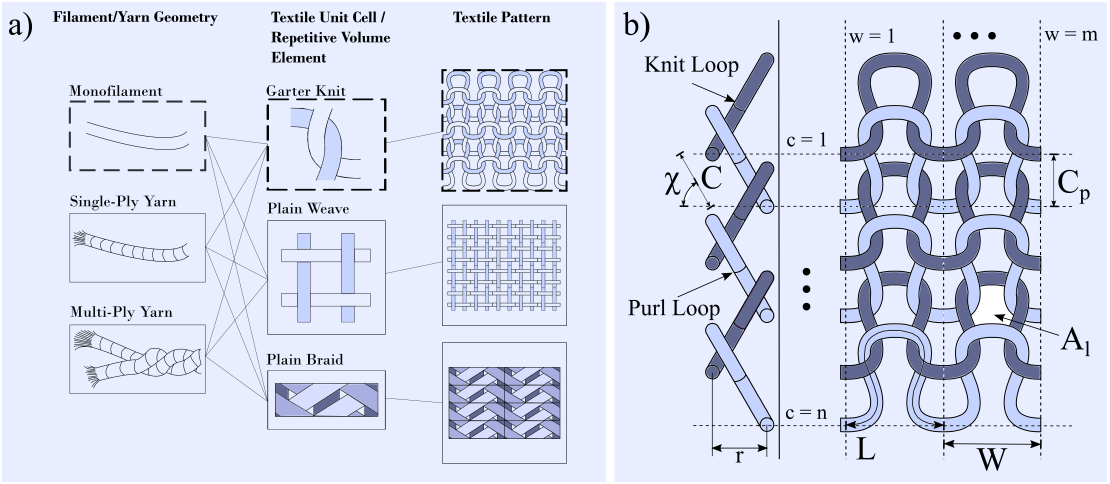

Figure 5.6: **Repetitive Volume Element Models:** a) Repetitive volume elements can be defined on the fiber/yarn level, the textile unit cell level, and the textile pattern level. The specific geometry selected for the validation of this modeling architecture is the monofilament garter knit geometry highlighted by the bold, dotted outlines. b) The geometric parameters that describe the garter knitted unit cell are the wale width (W), course height (C), projected course height (C_p), loop angle (χ), loop length (L), the ridge height (r), and loop enclosed area (A_l), whereas the knit pattern is defined by the number of loops in the wale-/column- (m) and course-/row-wise (n) directions.

5.3.3 Manufacturing Module

The manufacturing module provides the initial stress-strain filament conditions for the modeling architecture. The initial filament stress-strain state of shape memory alloys can be affected by post-manufacturing annealing, also referred to as shape-setting. Annealing of the SMA textile leads to zero-stress and -strain initial conditions and SMA material phase according to the stress-free transition temperatures. If no post-manufacturing annealing is performed, the stresses and strains introduced to the originally-straight filament during the manufacturing procedure - yarn spinning, knitting, weaving, or braiding - need to be accounted for. Manufacturing and process models have been published for knitting, [190, 191, 192, 193] weaving and weave preforming, [194, 195] spinning, [196, 197] and braiding [198] processes and can provide insight into the forces and deformations applied in the manufacturing process and their resultant material stresses and strains.

A simple and universally applicable method that avoids the implementation of specific manufacturing models to compute strains is provided by the differential geometry

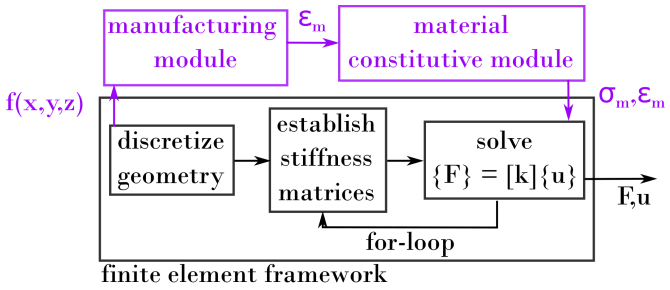

Figure 5.7: **Manufacturing Module:** In the first iteration of the finite element framework, the discretized geometry is fed to the manufacturing module which computes the manufacturing strains based on the Frenet-Serret formulae. The manufacturing strains are inserted into the material constitutive module to fully-define the initial stress-strain state of the textile geometry, which resembles the initial condition for the first iteration of the finite element routine.

Frenet-Serret formulae. [199, 200]

$$\frac{\mathrm{d}T}{\mathrm{d}s} = \kappa N, \quad \frac{\mathrm{d}N}{\mathrm{d}s} = -\kappa T + \tau B, \quad \frac{\mathrm{d}B}{\mathrm{d}s} = -\tau N \tag{5.2}$$

These formulae describe the derivatives of the tangent (T), normal (N), and binormal (B) unit vectors with respect to the arc length (s) through which the curvature (κ) and torsion (τ) of the curve can be defined. While the Frenet-Serret formulae do not account for tensile strains, they are suitable for the prediction of bending and torsional strains and therefore able to provide approximations of the post-manufacturing strain state in bending-/torsion-dominated manufacturing processes. In contrast to more complex manufacturing models, this differential geometry approach also assumes a simple manufacturing path as it only compares the start and end geometries. Sequential manufacturing processes or possible manufacturing steps that temporarily cause stresses and strains exceeding those in the final geometry can not be modeled with this simplified approach. The strains calculated from the curvature and torsion of the geometry are inputs to the material constitutive model to compute the initial stress-strain and phase volume fraction distribution of the textile architecture.

5.3.4 Contact Module

One of the most complex features of textiles is the relative motion, slipping, and sticking of interlocking fibers which renders the textile stiffness a combination of macroscopic

architectural stiffness, mesoscopic unit cell geometry stiffness, and microscopic material stiffness. Direct numerical finite element simulations have been performed to specifically investigate appropriate fiber interactions including tied contact [97] and contact with friction [201] in passive knitted textiles. Mechanical unit cell-based models commonly model the fiber interaction as applied forces that resemble tied contact at a defined interlacing point. [151, 72] While the most broadly applicable finite element contact analyses enable the simulation of textile interactions before and after the establishment of contact through tracking of gap functions, impenetrability conditions, and defined friction conditions, the fact that contact boundaries are a priori unknown and the discontinuity, i.e., the step increase of applied forces upon contact, in the force profile are significant numerical challenges. On the other hand, tied contact reduces the textile stiffness to the material and unit cell stiffness while neglecting the architectural, relative motion of unit cells.

As a part of this multifunctional fabric modeling architecture, a contact area identification and force application model is implemented that utilizes the simplification of repetitive unit cells and kinematic loop constraints to accomplish accurate contact modeling. The model is based on the assumption that contact between interlacing fibers is always established and that interlacing knitted loops are point reflections around a loop alignment point, which changes based on kinematic constraints.

The original geometry defined by the unit cell geometry and discretized in the finite element framework is the starting point for the contact module routine (Figure 5.8a). A tube is defined around the original knitted loop geometry with the specified filament diameter (d) and number of cross-sectional points (n_t) on the tube (Figure 5.8b). A second knit geometry, called the contacting knitted loop is defined to interlace with the original knitted loop geometry. Alignment is accomplished by defining an alignment node and calculating the interlacing point between the two volumetric knitted loops. The interlacing point has the coordinates $(x_i = x_n - r\sin(\alpha), y_i = y_n - r\cos(\alpha), z_i = z_n)$, where (x_n, y_n, z_n) are the coordinates of the alignment node and the angle (α) is the angle of the contacting element in the x,y plane with respect to the global coordinate system. This knitted loop interlacing point is the point around which the point reflection of the original geometry is performed to create the contacting geometry. The reflection

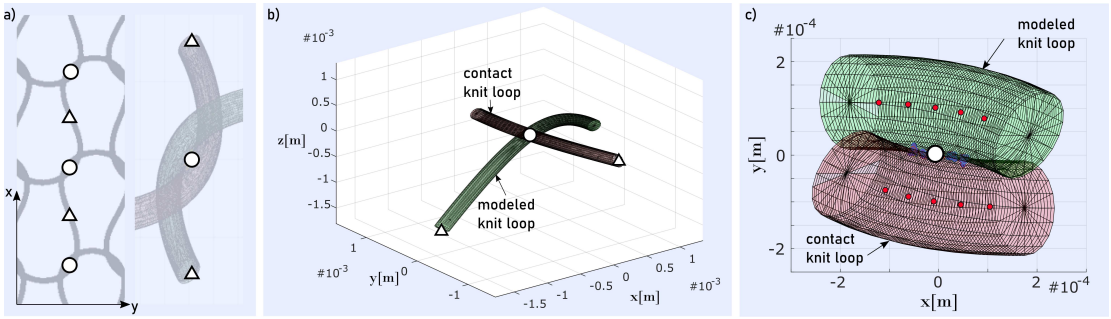

Figure 5.8: **Contact Module:** a) Kinematic constraints and continuity conditions are applied to model sliding. Interlacing point y-coordinates (circle) align with the inflection point y-coordinates (triangle) independent of the applied load for geometric continuity in the symmetric knitted loop unit cells. b) A contacting knitted loop is reflected around the original knitted loop geometry around the interlacing point. c) Euclidean distances between nodes along the original and contacting knitted loops are calculated and compared to a contact limit distance. If the Euclidean distances are smaller than the limit, contact is established and loads are applied on the nodes in contact.

matrix

$$R = \begin{bmatrix} \cos(\theta) & -\sin(\theta) \\ \sin(\theta) & \cos(\theta) \end{bmatrix} \tag{5.3}$$

produces the contacting knitted loop through point reflection by the angle $\theta = \pi$. The alignment node is defined by kinematic constraints. In repetitive, unit cell based knitted textiles, continuity of the knitted geometry requires

$$x_i - x_{in} = 0 \tag{5.4}$$

that the distance between the x-coordinates of the interlacing point (x_i) and the inflection point (x_{in}) of the knitted loop is zero. Consequently, sliding occurs to fulfill the condition of equation 5.4 based on the deformations of the knitted loop and translation of the loop inflection point.

The original and contacting tubes can be locally refined in the area of potential contact to increase the accuracy of contact predictions (Figure 5.8c). The Euclidean distances ($E_{o\to c}$) between all defined points the original knitted loop surface and contacting knitted loop surface in the area of potential contact are calculated and compared

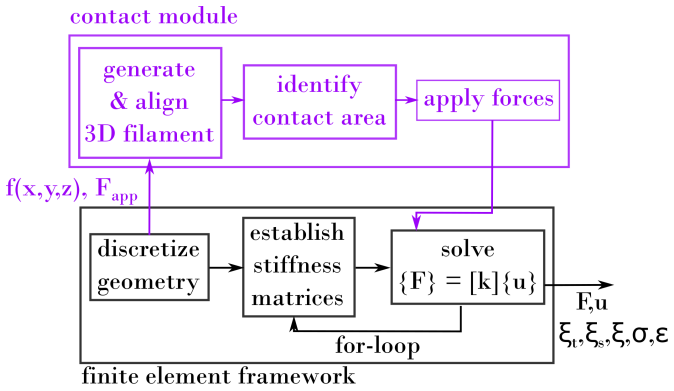

Figure 5.9: **Contact Module:** The contact module generates tubes around the spline geometry and the rotated contacting geometry which is aligned through kinematic periodicity constraints. The contact area at the loop interaction is identified and forces are applied in the contact point.

to a limiting distance, the minimum separation distance (d_{ms}), which defines the minimum distance of original and contacting tube points not to be in contact. Consequently,

$$\begin{aligned} &\text{if} \quad E_{o\to c} > d_{ms} \quad \to \quad \text{no contact} \\ &\text{if} \quad E_{o\to c} \leq d_{ms} \quad \to \quad \text{contact} \end{aligned} \tag{5.5}$$

provides the condition that identifies whether two nodes on the original and contacting tubes are in contact. Forces that are applied to the contacting geometry are defined in Section 5.3.5 and are transmitted to the original geometry through the nodes in contact. The model interaction chart (Figure 5.9) shows the contact module as it interacts with the finite element framework.

5.3.5 Boundary Conditions Module

The modeled system has $6 \times n_n$ degrees of freedom (DOF), as there are three DOFs in both rotation and translation for every node (n_n) in the system. Degrees of freedom must be constrained to ensure periodicity of the repetitive volume element throughout the entire simulation and to represent the boundary conditions in the textile geometry.

Figure 5.10a displays the constraints placed on the translational and rotational nodal displacements of the modeled repetitive volume element. Constrained displacements are presented in red. In the loop inflection point (triangle), all translational displacements

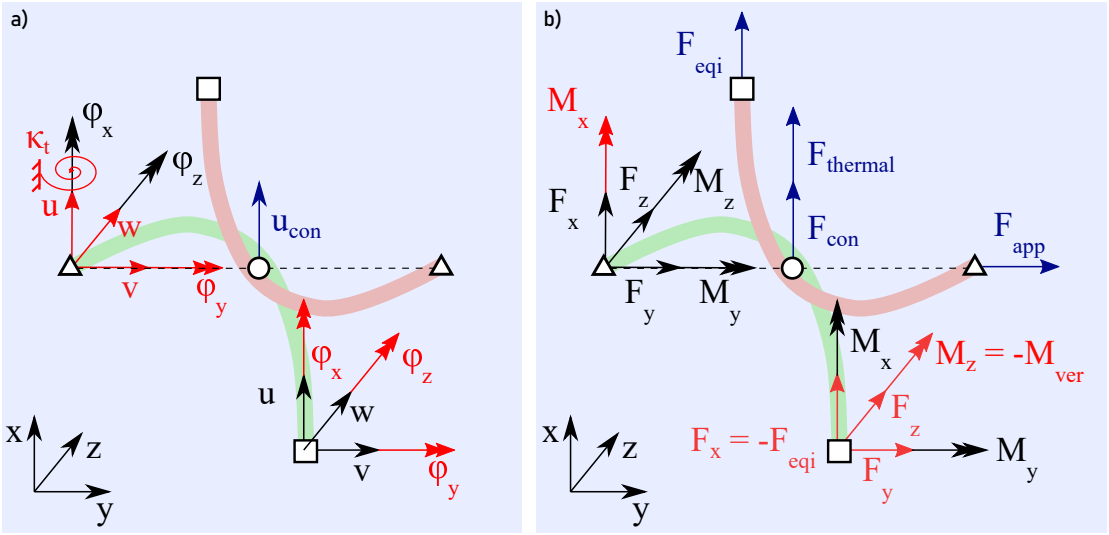

Figure 5.10: **Boundary Conditions:** Prescribed forces and displacements are applied in the loop inflection, contact, and vertex points. a) The constrained translational and rotational displacement DOFs are represented in red, a rotational spring of spring stiffness (κ_t) governs the flattening of the loop ridges. b) displays the prescribed forces in red. The equilibrium force (F_{eqi}) in the loop vertex and the applied external load (F_{app}) are transferred into the loop contact point along with the resulting moments from that transfer.

(u, v, w) are constrained as this coordinate is chosen as the fixed point in the computation. Rotation around the y-axis (ϕ_y) does not occur in knitted loops and is consequently prohibited in both the inflection and loop vertex (rectangle) points. For periodicity, rotations in the loop vertex point as well as translation in the x- and z-coordinate of the inflection point are constrained.

The conditions identified in the contact module are realized as kinematic constraints in the boundary condition module. The kinematic periodicity constraint ensures that the inflection point and interlacing point x-coordinates coincide. Three contact conditions are implemented: slipping, sticking, and jamming, which is a special sticking case. The geometric jamming condition

$$(\max(x_{con}) + r) - x_{mod,vertex} \leq 0 \tag{5.6}$$

is true when the model loop vertex x-coordinate ($x_{mod,vertex}$) is larger than the sum of its maximum x-coordinate ($\max(x_{con})$) of the contacting geometry and filament radius

(r). This condition is called the jamming condition as the legs of a single loop touch each other and prevent sliding. If the jamming condition is true, x-translation of the contact point is constrained in addition to the previously applied constraints. Similarly, this constraint is also applied upon normal sticking, which is detected by comparing the contact forces (F_{con}) with their normally-oriented applied load (F_{app}). The contact forces are inversely solved from the macroscopically applied forces and displacements between two simulation increments. An additional contribution called the thermally-recoverable contact force ($F_{thermal}$) is added as a temperature-dependent element to the contact force. The originally-straight SMA filament is deformed in its martensite state into the knitted loop geometry during manufacturing after which the knitted loops are in contact without significant normal contact forces in the macroscopically unloaded state ($F_{thermal} = 0$). Upon heating of this geometry, thermally-recoverable material phases lead to a recovery-force generation [50, 51] in an assumed geometrically-constrained state. This force is approximated as a constant offset force in the contact point at temperatures above the austenite finish temperature ($F_{thermal}$). If the Coulomb condition

$$F_{app} \leq \mu(F_{con} + F_{thermal}) \tag{5.7}$$

is true, x-axis translation of the contact point is constraint in the boundary condition module to prevent the kinematically-governed sliding. Otherwise, the x-axis translation of the contact point is enabled and the loop displaces, resulting in a new alignment, ergo sliding, of the contacting geometry. The collapsing of the garter knit ridges under applied loads is modeled by the addition of a torsional spring with stiffness (κ_t) around the x-axis of the loop inflection point.

The prescribed forces and moments are displayed in Figure 5.10b. A moment around the x-axis (M_x) is prescribed in the loop inflection point of same magnitude as the resulting moment from the force application on the quarter loop geometry to account for the symmetric loading of the loop. In the loop vertex, the equilibrium force (F_{eqi}) is applied in the negative y-direction, whereas forces in the x- and z-directions are set to be zero. A moment exists at the loop vertex around the z-axis, the magnitude of which equals the moment required to bend the knitted loop from a straight configuration into the bent configuration defined by the loop contact point. In the loop contact point, the forces (F_{eqi}) and (F_{app}) are transferred into the loop contact point and the resulting moments around the x-,y-, and z-axes are from the transfer are applied.

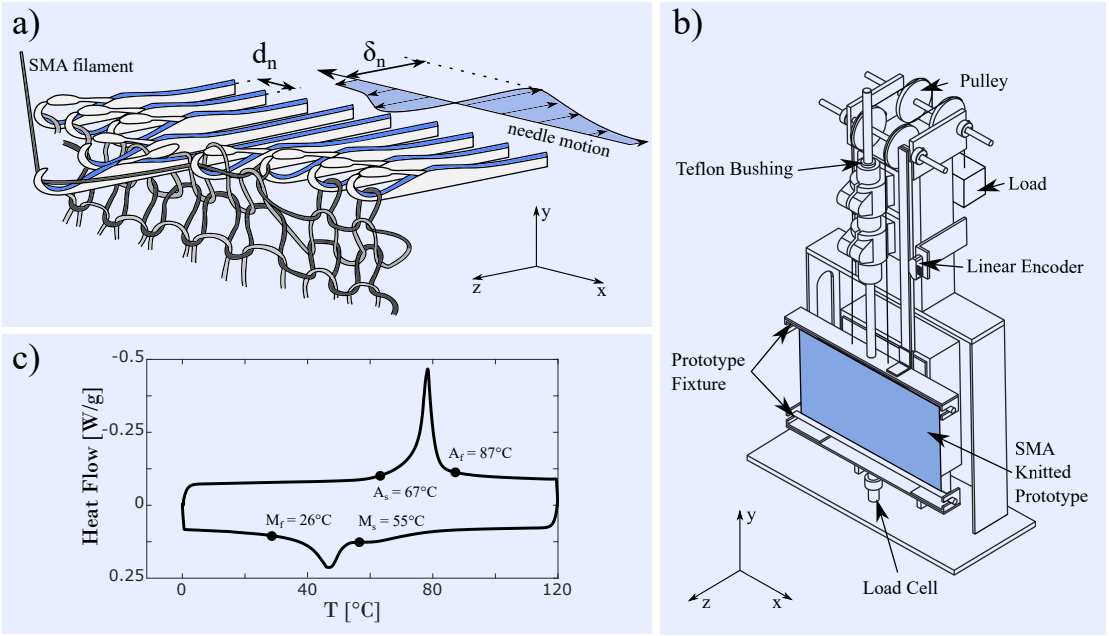

Figure 5.11: **Manufacturing, Experiment & Material Parameters:** a) SMA knitted prototypes were manufactured from originally-straight SMA filament on flatbed knitting machines at room temperature. b) A custom textile tensile machine within an environmental chamber was utilized to characterize the the force-extension behavior of SMA knitted textiles in the relaxed and actuated states. c) Differential scanning calorimetry was used to identify the stress-free transition temperatures of the SMA filament for use in the SMA material model.

5.4 Model Validation

Tensile experiments were conducted to evaluate the predictive capabilities of the multifunctional textile modeling architecture. The contractile SMA knitted architecture was chosen to verify the thermo-mechanical force-extension model accuracy because of its intriguing performance for applications ranging from wearable compression garments [202] to large non-pneumatic rover tires. [203] This section introduces the prototype selection, manufacturing, and experimental characterization, and discusses the material parameter selection. The experimental and simulated results are compared macroscopically and microscopically in detail for a single knitted prototype, followed by a parameter study presenting error data between simulation and experiment for various knitted prototypes.

5.4.1 Prototypes

SMA knitted architectures were manufactured on Taitexma TH-series flatbed knitting machines (Figure 5.11a). The martensitic SMA filament is continuously pulled through the loops of the previous course through coordinated motion of latch needles at room temperature. Two parameters, the needle spacing (d_n) and the needle displacement (δ_n) can be controlled in the knit manufacturing process to determine the loop geometry and consequently the knit index (i_k). [74] The SMA knitted architectures were manufactured from originally-straight Dynalloy Flexinol® filament without thermal post-processing after the knitting process. Prototypes of ($n = m = 15$) loops ensured that the performance was not dominated by the boundary conditions of the knitted architecture. [109] Prototypes of varying knit indices were manufactured, experimentally tested, and modeled for the validation procedure.

5.4.2 Experimental Design

Thermo-mechanical testing was conducted in a custom tensile testing setup housed inside an environmental chamber for temperature-control (Figure 5.11b). The setup enables the measurement of the linear knitted architecture displacement through a US Digital linear encoder strip and sensor resolving 200 counts per inch (CPI). Loads were incrementally applied in a force-control experimental procedure and continuously measured with a Honeywell M34 miniature load cell. Temperatures were varied between ($T = [20, 120]\,°\text{C}$) to characterize the actuated and relaxed states of the knitted architecture at each load increment.

5.4.3 Material Parameters

Dynalloy Flexinol® filaments with a rated austenite finish temperature ($A_{f,r} = 90\,°\text{C}$) was utilized in the creation of the knitted architectures. The stress-free transition temperatures were obtained through differential scanning calorimetry (Figure 5.11c) and are listed among other material parameters in Table 5.1. Additional material parameters that serve as inputs for the utilized material model [165] were estimated based on literature recommendations. [204, 205]

5.4.4 Comparison of Simulated and Experimental SMA Knitted Architecture Thermo-Mechanical Behavior

This section discusses the results of a temperature-dependent, force-extension simulation for a single SMA knitted prototype and compares them to experimentally obtained results. Results are compared by extracting quantitative data on the macroscale and discussing qualitatively the trends between simulation and experiment on the microscale. A prototype with an experimentally-measured knit index ($i_{k_{exp}} = 125\,\mathrm{mm^2\,mm^{-2}}$), a wire diameter ($d = 0.203\,\mathrm{mm}$), and 15 loops in each the course- and wale-wise directions was experimentally-tested and the geometric loop parameters were extracted ($W = 4.6\,\mathrm{mm},\ r = 1.9\,\mathrm{mm},\ C_p = 2.1\,\mathrm{mm}$). The simulation utilizes the material input parameters described in Section 5.4.3. Force-extension was modeled matching the temperatures used to induce the relaxed ($T = 20\,^{\circ}\mathrm{C}$) and actuated ($T = 120\,^{\circ}\mathrm{C}$) states in the experiments. The thermally-recoverable force was approximated as a constant force ($F_{thermal} = 0.06\,\mathrm{N}$) applied in simulation for temperatures above the austenite finish temperature.

The macroscopic thermo-mechanical behavior of the SMA knitted architecture is displayed in Figure 5.12. Figure 5.12a compares the actuated (red) and relaxed (blue) force-extension profiles of the experiment and the simulation. The theory and experiment both show an approximately tri-linear profile in the actuated state with an initial high-stiffness regime, a plateau, and the knitted textile-characteristic strain-hardening behavior at larger extensions. [109] The initial high-stiffness regime in the actuator profile ($T = 120\,^{\circ}\mathrm{C}$) is caused by a normal loop contact force ($F_{con} + F_{thermal}$) generated through the thermal recovery of bending deformations which opposes relative sliding of the interlocking knitted loops. As the externally-applied load increases the forces tangential to the contact normal increase causing the onset of stick-slip behavior. This behavior is dominant in the plateau regime which is governed by large relative loop motion accompanied by the flattening of loop ridges through loop rotation. As the loop legs slide relative to one another, the geometric conditions change prohibiting further sliding and the stiffness starts to increase again. Once the x-coordinate of the loop leg approaches the x-coordinate of the loop vertex point, jamming occurs, which prohibits further sliding of the knitted loops. At this point, additional elongation of the knitted loop is purely a function of loop rotation, i.e., the flattening of loop ridges, and filament deformations without relative translation of knitted loops. Consequently, the stiffness

of the knitted architecture significantly increases.

Figure 5.12b portrays the knit architecture and knitted loop deformations at ($T = 120\,°\text{C}$) at three extension levels representing the initial stiffness regime ($F = 0.6\,\text{N}$), the plateau ($F = 3.0\,\text{N}$), and the fully-extended, high-stiffness regime ($F = 6.0\,\text{N}$). As the knitted architecture elongates along the y-axis, the x-axis coordinate, the width, decreases. The resulting knitted architecture Poisson's ratio at ($\text{F} = 6\,\text{N}$) is ($\nu = 0.35$). The 3D view of the knitted loops shows how the ridges of the knitted loops collapse with increasing applied loads. The relaxed force-extension profiles, both in experiment and simulation, exhibit a j-shape strain-hardening behavior (Figure 5.12a). The initial stiffness regime of the relaxed force-extension profile is missing as no thermally-recoverable force is present at this lower temperature ($T < M_f$). Consequently, knitted loops slide relative to one another at lower applied forces and the plateau occurs nearly immediately upon loading. The strain-hardening of the relaxed profile occurs due to the same effects described in the actuated force-extension profile, including stick-slip and jamming. The mean percent extension error (η) between the simulated and measured force-extension profiles is ($\eta_a = 1.48\%$) for the actuated profile and ($\eta_r = 4.4\%$) for the relaxed profile at forces above ($F = 1\,\text{N}$). The discrepancy between the simulation and experiment in the relaxed state is maximized at lower forces, at which frictional non-linearities have a significant effect on the experimental results and the model results. Specifically the simplifying model assumption that contact is always established, which is a good assumption at low forces in the actuated state but may not always reflect the contact state at low forces the relaxed state, contributes to an over-prediction of the relaxed SMA knitted architecture stiffness at lower forces.

Variable	Name	Used Value	Literature
Moduli			
E_m	*Young's modulus mart.*	40 GPa	$24.8 - 50$ GPa [106, 180]
E_a	*Young's modulus aust.*	70 GPa	$50 - 90$ GPa [204, 106, 180]
Θ	*Thermal modulus*	$0.55\,\mathrm{MPa\,°C^{-1}}$	$0.55\,\mathrm{MPa\,°C^{-1}}$ [165]
General Properties			
ν	*Poisson's ratio*	0.33	0.33 - 0.42 [205, 206]
μ	*static friction coeff.*	0.13	0.025-0.26 [207]
ε_L	*maximum residual strain*	0.067	0.067 [165]
C^E	*empirical coefficient*	1.8	2 [184]
Transition Properties			
C_m	*material constant mart.*	$13\,\mathrm{MPa\,°C^{-1}}$	$8 - 8.5\,\mathrm{MPa\,°C^{-1}}$ [208, 165]
C_a	*material constant aust.*	$13\,\mathrm{MPa\,°C^{-1}}$	$3.5 - 13.8\,\mathrm{MPa\,°C^{-1}}$ [208, 165]
σ_s	*crit. trans. start stress*	200 MPa	50-400 MPa [209]
σ_f	*crit. trans. finish stress*	250 MPa	200-800 MPa [209]
Transition Temperatures			
A_s	*austenite start temp.*	67 °C	-150 - 100 °C [209]
A_f	*austenite finish temp.*	87 °C	in range of A_s
M_s	*martensite start temp.*	23 °C	-140 - 160 °C [209]
M_f	*martensite finish temp.*	55 °C	in range of M_s

Table 5.1: **Material parameters:** The transition temperatures - austenite finish (A_f), austenite start (A_s), martensite start (M_s), and martensite finish (M_f) temperatures, the transition properties - material constants (C_a) and (C_m) which describe the increase of critical transformation stresses as the temperature increases for the austenite transition boundary and martensite transition boundary and the critical transformation start (σ_s) and finish (σ_f) stresses, the general properties - Poisson's ration (ν), static friction coefficient (μ), maximum residual strain (ε_L), the equivalent strain empirical coefficient (C^E), and the moduli - austenite elastic modulus (E_a), martensite elastic modulus (E_m), and thermal modulus (Θ).

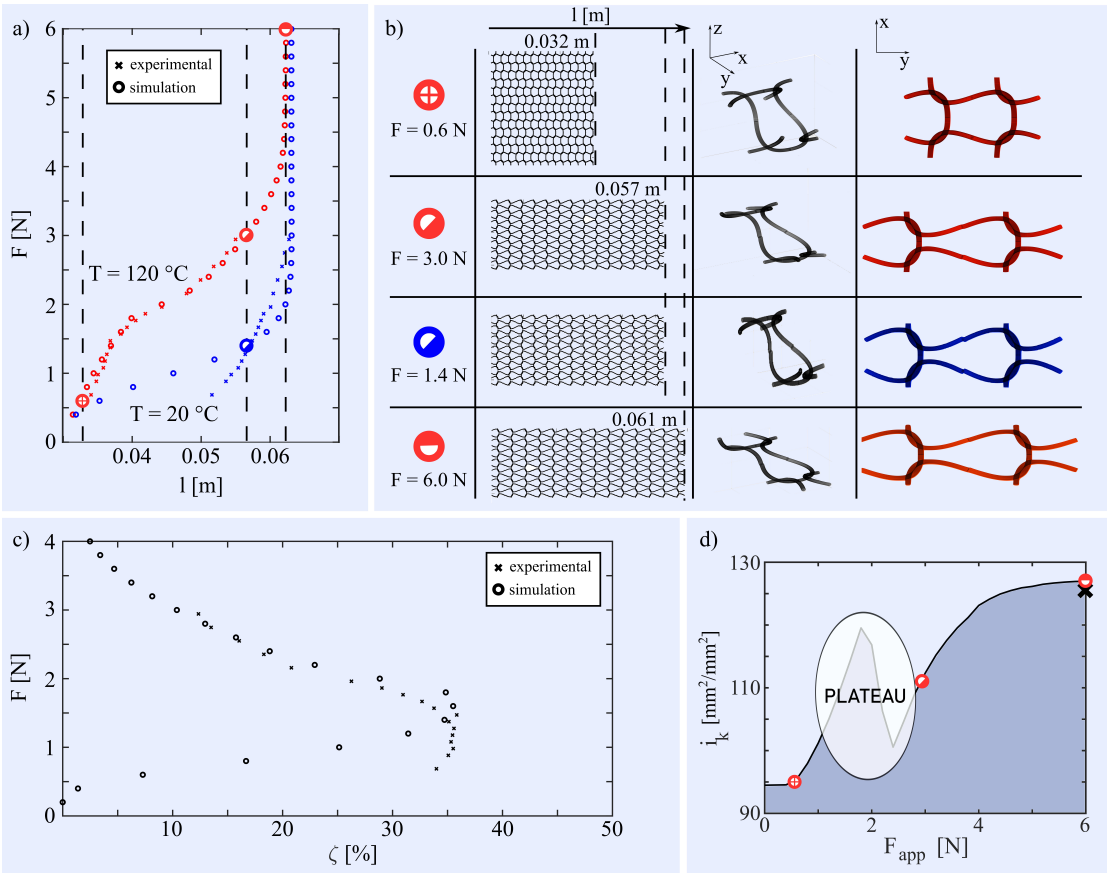

Figure 5.12: **Detailed Macroscopic Results:** (a) The experimental SMA knitted architecture exhibits a temperature-dependent force-extension behavior which is well-matched by the simulated results. (b) Geometric features of the SMA knitted architecture thermo-mechanical behavior are visualized. The complete knitted architecture as well as knitted loops are presented at different force levels ($F = 0.6\,\mathrm{N}, F = 3.0\,\mathrm{N}, F = 6.0\,\mathrm{N}$) showing the length-wise extension and width-wise contraction, as well as loop-level collapsing of ridges and relative sliding. (c) The %-actuation contraction simulation output matches the experimental results. (d) The knit index measurement and simulation match with a small (η_{i_k}1.3%) error.

The %-actuation contraction (ζ) is defined as the normalized difference

$$\zeta = \frac{l_r - l_a}{l_r} \tag{5.8}$$

between the relaxed, fully-martensitic, and the actuated, partially-austenitic SMA knitted architecture lengths at defined force levels. Figure 5.12c displays the good fit between experimental and simulated %-actuation contraction profiles of the SMA knitted architecture. The maximum %-actuation contraction ($\hat{\zeta}_{exp} = 35.84\%$) of the measured prototype occurs at the force ($F_{\hat{\zeta},exp} = 1.472\,\mathrm{N}$), which is matched by the simulated maximum %-actuation contraction ($\hat{\zeta}_{sim} = 35.51\%$) at the force ($F_{\hat{\zeta},sim} = 1.6\,\mathrm{N}$) with a small error ($\eta_{\hat{\zeta}} = 0.9\%$ and $\eta_{F_{\hat{\zeta}}} = 8\%$). A useful way to verify the correctness of the measured geometric properties used as the input in the simulation is the comparison of the experimentally measured and simulated knit index at large applied forces (Figure 5.12d). The measured knit index of the utilized knitted architecture is ($i_{k_{exp}} = 125\,\mathrm{mm^2\,mm^{-2}}$). Measurements were conducted when the geometric condition of loop jamming and loop ridge collapse was accomplished at large applied forces. In the simulation, the knit index is calculated for every applied load increment. Figure 5.12d shows the knit index simulation plotted over the applied load, as well as the experimentally-obtained knit index. Because the knit index contains the measure of the loop area in the 2D knitted loop projection, which changes significantly as the ridges of the knitted loops collapse, an increase of the knit index with increasing applied loads occurs. The knit index asymptotes at large applied forces at ($i_{k_{sim}} = 126.9\,\mathrm{mm^2\,mm^{-2}}$) with a small percent error ($\eta_{i_k} = 1.3\%$) supporting the utility of the knit index as a geometric predictive measure of the maximum %-actuation contraction. [163]

The microstructure was evaluated experimentally for qualitative comparison to the simulated results. X-ray diffraction experiments have been conducted for SMA knitted architectures to understand the distribution of material phases as a function of the spatial loop coordinate. [5] A Bruker D8 Discover 2D x-ray diffraction experiment was equipped with a knit sample holder for structural strain and resistive heat control (Figure 5.13a). The temperature was monitored with an IR camera. Measurements were taken by focusing the collimated ($d_c = 0.3\,\mathrm{mm}$) Co-Kα beam onto measurement points along the spline of the knitted loop. The raw intensity data was processed using the direct comparison method to extract the phase distribution information. The

experimental results are displayed in Figure 5.13b. Austenitic material phase can be observed in the loop inflection point for both experimentally characterized structural strain levels ($\varepsilon = 4\%$ and 21%). The highest martensite volume fraction is present in the measured loop contact point. The shadow from the interlacing loop prohibited the measurement of the second loop contact point. Predominantly martensitic phase is also present between the loop contact points and in the loop vertex, however, more austenitic phase is still present at the observed strain levels. An increase of martensitic phase is observable in every measurement point when increasing the structural strain from 4% to 21%.

The simulated phase fraction results confirm the experimental observations. Data was extracted at the structural strain levels tested in the experiment as well as at maximum extension at ($\varepsilon = 200\%$). Largely austenitic phase is present in the loop inflection point regardless of the structural strain. All other trends are supported by the experimental results, martensite is most prominent in the loop contact areas, and largely martensitic, mixed phase occurs between the contact points and in the loop vertex. The second contact point, which could not be measured in the experiment due to the shadowing interlacing loop, is also largely martensitic.

Figure 5.13c displays the thermo-mechanical path of three loop locations, the inflection point (triangle), between the contact areas (circle), and close to the loop vertex (rectangle). Stresses are plotted against the temperature along with the relevant transformation temperatures (A_f, A_s, M_s, M_f) and transformation stresses (σ_s, σ_f) of the 1D shape memory constitutive model. The entire thermo-mechanical loading path, from initial manufacturing at ($T = 20\,^{\circ}\mathrm{C}$) to the heating of the knitted loop into the actuated state ($T = 20\,^{\circ}\mathrm{C} \rightarrow T = 120\,^{\circ}\mathrm{C}$), and mechanical loading of the actuated knitted architecture, is displayed. It is apparent that the initial manufacturing procedure induces complete de-twinning in the contact region, partial de-twinning in the loop vertex, and no de-twinning in the loop inflection point. Thermo-elastic stresses ($\Theta = 0.55\,\mathrm{MPa}\,^{\circ}\mathrm{C}^{-1}$) lead to a constant increase of the stresses in each location during heating to the actuated state. As the loop locations reach the austenite transformation regime, additional stresses are created due to the phase transformation from martensite to austenite. While the loop inflection point fully-transforms to austenite, the loop contact and loop vertex point remain in a mixed material phase condition when ($T = 120\,^{\circ}\mathrm{C}$) is reached. Loading of the actuated knitted architecture loads to a further

increase of stresses in each loop segment. The loop contact point reaches stresses that cause de-twinning even at such elevated temperatures, whereas the loop inflection and loop vertex point remain at the same material phase fraction during the loading process.

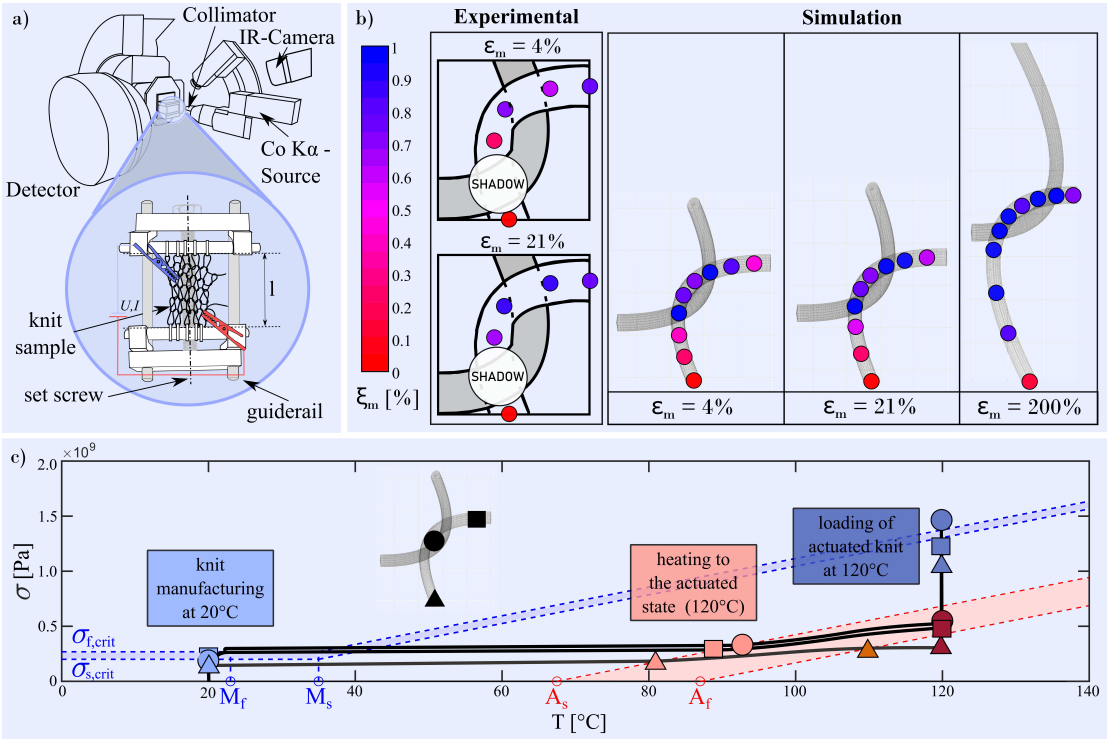

Figure 5.13: **Detailed Microscopic Results:** (a) Temperature- and strain-controlled SMA knitted architecture x-ray diffraction experiments were conducted in a Bruker D8 Discover 2D diffractometer equipped with a custom knit holder to understand the phase distribution along the knitted loop geometry. [5] (b) The phase distribution was evaluated using the Direct Comparison Method and is displayed for ($\varepsilon = 4\%$ and 21%). Austenitic phase is observed at the highest proportion in the loop leg, whereas martensitic phase is most prominent in the loop contact point. The simulated results match the trends observed in the experiment. [5] (c) The exact path of three finite elements (circle, rectangle, triangle) is displayed from the knit manufacturing at ($T = 20\,°\mathrm{C}$) to the heating into the actuated state ($20\,°\mathrm{C} \rightarrow 120\,°\mathrm{C}$) and subsequent loading of the knitted architecture ($T = 120\,°\mathrm{C}$).

5.4.5 Simulation Parameter Study

Additional experiments and simulations were conducted to verify the modeling approach for knitted architectures of varying wire diameters and knit indices. The simulations and experiments followed the same setup and analysis procedures as outlined in detail previously. The geometric loop input parameters for the simulation, and a comparison of the output parameters from experiment and simulation are detailed Table 5.2

Experiment			Loop Geometry			Simulation Output			
d [mm]	$i_{k_{exp}}$	$\hat{\zeta}_{exp}$	W [mm]	C_p [mm]	r [mm]	η_r	η_a	$\hat{\zeta}_{sim}$	$i_{k_{sim}}$
0.203	75	19.46%	4.0	2.28	2.7	2.3%	2.2%	21.2%	77
0.203	98	22.28%	4.14	2.35	3.2	4.33%	3.29%	25.1%	101
0.203	125	35.82%	4.5	2.18	3.8	4.4%	1.48%	35.51%	126
0.203	138	42.12%	3.6	2.35	4.8	3.85%	5.32%	43.2%	141
0.127	145	34.76%	3.0	1.64	2.6	5.44%	8.26%	30.63%	149
0.381	137	35.09%	9.9	3.8	7.0	5.52%	2.66%	36.29%	142

Table 5.2: **Simulation Parameter Study:** Multiple knitted architectures were modeled after the two defining experimental SMA knitted architecture design parameters, the filament diameter (d) and the experimentally-measured knit index ($i_{k_{exp}}$). The initial loop geometry input parameters for the simulation were approximated from imaging of the prototypes including the wale width (W), projected course height (C_p), and ridge height (r). Error measurements of the relaxed (η_r) and actuated (η_a) knit length, as well as the maximum %-actuation contraction ($\hat{\zeta}$), and the simulation maximum load knit index ($i_{k_{sim}}$) are displayed in the simulation output columns. The relatively small errors between simulated and experimentally-obtained force-extension profiles, which are consistently below 5.5% except for the small diameter prototype, support the predictive capability of this modeling tool across knitted architectures.

The simulation parameter study supports the utility of the multifunctional fabric modeling architecture as a predictive tool of SMA knitted architectures (Table 5.2). The study of varying knit indices while keeping the SMA filament diameter constant ($d = 0.203\,\text{mm}$), as well as keeping the experimentally-obtained knit index constant ($i_{k_{exp}} \approx 140\,\text{mm}^2\,\text{mm}^{-2}$) while changing the filament diameter indicates that the modeling tool is capable of predicting the performance of a wide range of SMA knitted architectures. Error values remained below 8.5% for actuated and below 5.5% for relaxed

force-extension profiles. The largest errors occur in the small diameter ($d = 0.127\,\mathrm{mm}$) prototype. These larger errors are at least partially caused by the higher uncertainty in the experimental characterization as the forces applied to the small diameter architecture are significantly lower (maximum applied force $\hat{F} = 1\,\mathrm{N}$) than for the other prototypes. As the force-extention profiles are well-predicted by the model, the maximum %-actuation contraction of SMA knitted architectures could also be predicted successfully with errors ranging between $0.9 \leq \eta_{\hat{\zeta}} < 11.5\%$. The simulated knit index agrees with the experimentally-obtained knit indices which serves as a cross-check for the performance and geometric results. Microscopic simulation outputs also agree with the trends obtained in x-ray diffraction experiments opening opportunities for the microstructural design of SMA knitted architectures.

5.5 Conclusion

In this paper, we develop a modular multifunctional textile modeling tool based on finite beam element theory which is verified along the example of the SMA knitted architecture. The modeling tool is capable of predicting the thermo-mechanical performance of SMA knitted architectures and produces insight on the macro-, meso-, and microscale. Modules that contain sub-models interact with the finite beam element framework through defined interfaces which enables the simple adaption to a variety of multifunctional textile model implementations. These modules are: material constitutive module, repetitive volume element module, manufacturing module, contact module, and the boundary condition module. The SMA knitted architecture was modeled using a 1D-SMA constitutive model while modeling the repetitive quarter loop unit cell. The SMA knitted architecture manufacturing deformations were approximated through differential geometry considerations without stress-relieving post-manufacturing procedures. Contact was modeled in three dimensions using Coulomb friction with prominent stick-slip behavior and considering the jamming conditions characteristic for highly-loaded knitted textiles. The simulated SMA knitted architecture performance in the actuated and relaxed states were verified against experimental data on the macro- and micro-scales. This modeling approach captures the majority of super-positioned material and architectural mechanisms present in SMA knitted architectures, specifically the initial high-stiffness regime of actuated knitted architectures due to thermo-elastically

recoverable deformations post-manufacturing, the collapsing of ridges between knitted loops upon mechanical loading, and the variable deformation from distributed stress-strain conditions leading to local martensitic phase transformation of material volumina.

Limitations and potential for future improvements exist specifically regarding the simplification of the 3D stress-strain state to utilize a 1D material constitutive model. The validity of this approach has been empirically shown elsewhere, however, the dimensional reduction to obtain an equivalent strain limits the ability to decouple phase transformation initiated by tensile, compressive, bending, and shear deformations which would provide additional insight into potential geometric and material design options.

This modeling architecture provides significant improvements towards understanding the mechanics of SMA knitted architectures. The study of performance trade-offs in numerical experiments will enhance the design of SMA knitted architectures and enable the exploitation of their desirable lightweight multifunctional knit properties in applications. Through the modular design of the modeling tool, simple variation of sub-models can be implemented to translate findings to other multifunctional textile implementations and increase the broader understanding of multifunctional textiles in general.

Acknowledgements

The authors thank Minnesota's Discovery, Research, and InnoVation Economoy (Mn-DRIVE) for the generous support and funding of the Mn-DRIVE Informatics PhD Graduate Assistantship under which the authors conducted this research.

Chapter 6

Functionally Graded Knitted Actuators with NiTi-based Shape Memory Alloys for Topographically Self-Fitting Wearables

K Eschen*, R Granberry*, B Holschuh and J Abel
Department of Mechanical Engineering, University of Minnesota,
111 Church Street SE, Minneapolis, MN 55455, USA
Department of Design, Housing, and Apparel, University of Minnesota,
1985 Buford Avenue, Saint Paul, MN 55018, USA
Published in **Advanced Materials Technologies**
Vol **4 11**
Pages **1900548**
DOI **10.1002/admt.201900548**
Date **November 2019**
* Rachael Granberry and Kevin Eschen contributed equally to this collaborative work.

Detailed description of specific contributions to be found in the acknowledgements.

Abstract

Advances in actuating fabrics could enable a paradigm shift in the field of smart wearables by dynamically fitting themselves to the unique topography of the human body. Applications including soft wearable robotics, continuous health monitoring, and body-mounted haptic feedback systems are dependent upon simultaneous body proximity and garment stiffness for functionality. Passive fabrics and fitting mechanisms are unable to conform around surface concavities and require either high elasticity or a multiplicity of closure devices to achieve garment fit. The design, manufacture, and validation of the first circumferentially-contractile and topographic self-fitting garments composed of NiTi-based shape memory alloy (SMA) knitted actuators that dynamically conform to the unique shape and size of the wearer's body in response to a change of the garment's temperature is introduced. Advanced materials and systems innovations (1) enable novel garment manufacturing and application strategies, (2) facilitate topographical fitting (spatial actuation) through garment architectural design, and (3) provide tunable NiTi-based SMA actuation temperatures to enable actuation on the surface of human skin. This research represents a paradigm shift for wearable applications by redefining garment fit to fully-topographical conformation to the wearer through advanced materials and structures design.

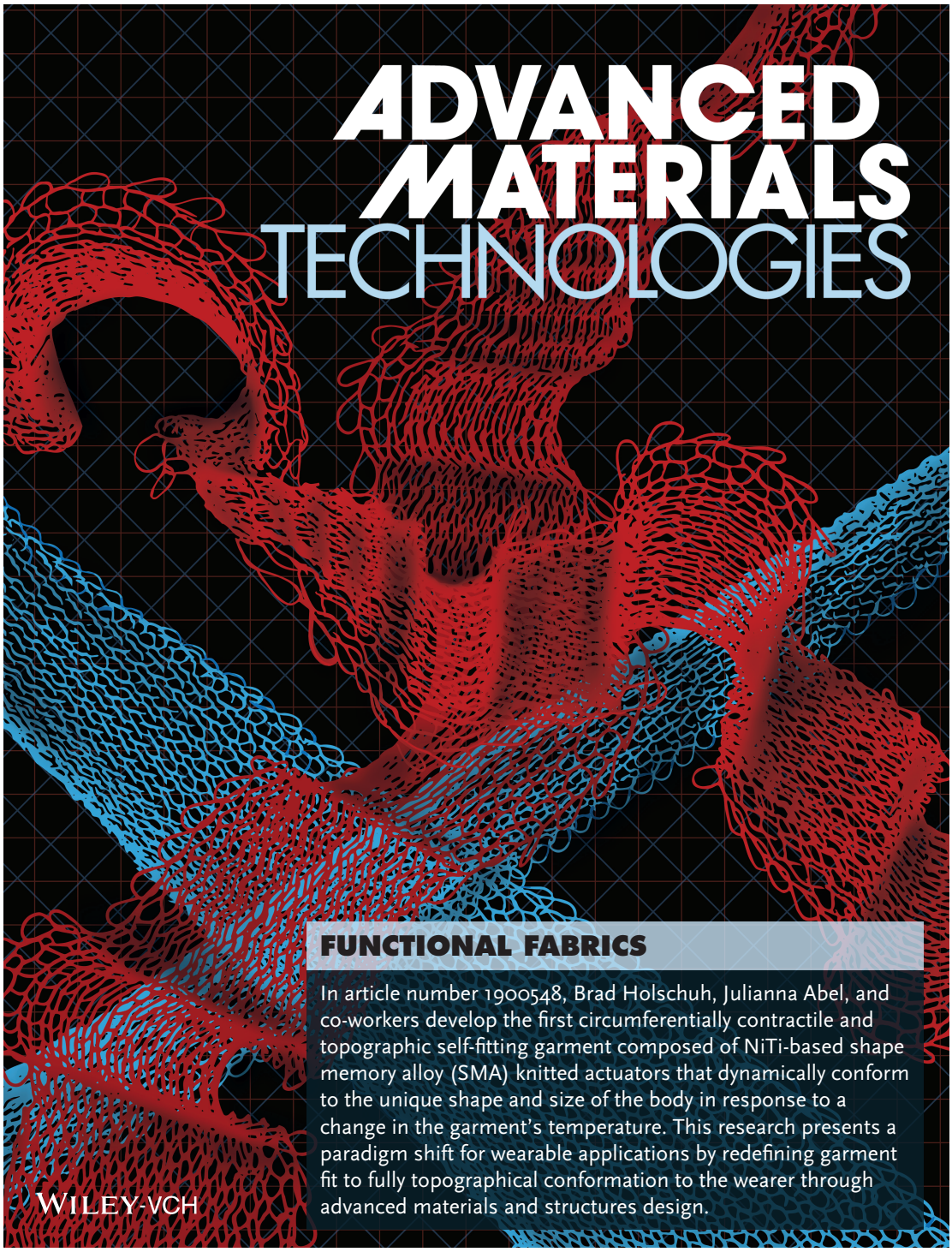
ADVANCED MATERIALS TECHNOLOGIES
FUNCTIONAL FABRICS
In article number 1900548, Brad Holschuh, Julianna Abel, and co-workers develop the first circumferentially contractile and topographic self-fitting garment composed of NiTi-based shape memory alloy (SMA) knitted actuators that dynamically conform to the unique shape and size of the body in response to a change in the garment's temperature. This research presents a paradigm shift for wearable applications by redefining garment fit to fully topographical conformation to the wearer through advanced materials and structures design.
WILEY-VCH

6.1 Introduction

Wearables, spanning consumer clothing to smart body-mounted devices, are plagued with fit and sizing challenges due to vast population anthropometric variability. [210, 211] Accurate fit around a range of body shapes and sizes is a necessity for functional wearables, specifically those with integrated sensors and actuators that require stiffness of sufficient magnitude to enable structural anchoring at precise anatomical locations. [212] While polyether-polyurea copolymer (elastane) fabrics are capable of accomplishing accurate fit through undersized garment design, highly-compliant garments fail to anchor functional components to the body. To achieve garment-body proximity and appropriate stiffness, designers compose sizing systems (S, M, L) and mount hardware to less compliant materials that are fitted to the body with adjustable closures (e.g., laces, Velcro®). [143, 213] Despite the combination of fitting approaches, wearable device functionality remains highly variable due to garment fit inconsistencies between users, a limitation that ultimately inhibits usability. [214] Multifunctional fabrics integrate advanced materials such as NiTi-based shape memory alloys (SMA), shape memory polymers (SMP) or carbon-nanotubes (CNT) and present a novel approach to the fit and sizing challenges of smart wearables that eliminate the bulk, complexity, and 1D nature of current approaches. Actuating multifunctional fabrics provide spatially- and functionally-distributed, tunable mechanical behavior that enables self-fitting and -stiffening around the variable topography of the human body. Prior work on actuating fabric structures has focused on traditional actuators (e.g., pneumatics, hydraulics, motor-driven bowden cables) attached to or layered with passive fabrics. [215] Other research has attached 1D multifunctional actuator geometries (e.g., wire, springs) to traditional textile structures. [40, 216, 41] These approaches are bulky, complex, and exhibit limited surface deformation. Prior work on spatially (3D) actuating multifunctional fabrics found that sophisticated shape-changing soft-robotic tasks such as translatory motion (length variability), rotational motion (rolling) and their superposition (wrinkle release), as well as significant volume changes can be accomplished. [6, 60, 217, 13, 15, 218] The most promising active material system for actuating fabrics is NiTi-based SMA, which offers a unique combination of high energy density, and large actuation displacements and forces. SMAs are advanced engineering materials

that exhibit path-dependent thermo-mechanically-induced martensitic phase transformations that enable the unique superelastic and shape memory effects. The phase transformations are introduced as a function of the applied materials stress, strain, and temperature, and depend on the thermo-mechanical loading history of the material. The reversible transformation between the cubic austenite and the monoclinic martensite lattices enables variable stiffness, as well as the ability to undergo and recover large deformations of up to 8% (Figure 6.1a). [219] This specific self-fitting application leverages the shape memory effect of NiTi-based SMAs. Sufficient mechanical straining and stressing of the NiTi-based SMA wire results in a detwinning of the initially twinned monoclinic martensite at temperatures below the martensite finish temperature ($T < M_f$). Upon heating above the material-specific austenite finish temperature ($T > A_f$) the martensitic transformation to the cubic austenite lattices occurs and the imposed strains and stresses are recovered. The initial state of the wire is recovered through subsequent cooling ($T < M_f$) which forces the reverse phase transformation to the original unstructured twinned martensite lattice. The phase transformation temperatures of NiTi-based SMA are highly programmable and can be tailored for a given application according to chemical composition and metallurgical heat treatment. Spanning martensite start (M_s) temperatures between -100 °C and -400 °C while preserving the shape memory effect, NiTi-based SMA renders the potential for a wide array of applications. [120, 121] For binary NiTi alloys, manipulation of the Ni-volume fraction results in drastic variation of the transformation temperatures (A_f, A_s, M_s, M_f) and thermal hysteresis. Slight Ni-richness ($c_{Ni} \approx 51.5\text{at} - \%$) produces approximately 200 °C lower transformation temperatures compared to marginally Ti-rich (c_{Ni} 49%) NiTi-based SMAs. [120] The partial replacement of Ni or Ti with ternary alloying agents modifies the transformation temperatures as a function of the concentration and number of valence electrons. [121] Heat treatment, specifically aging under defined times and thermo-mechanical loads, can cause the formation of precipitates (e.g., Ni_4Ti_3) and a consequential increase of the phase transformation temperatures through a decrease of the Ni-content in the matrix. [122] Contractile SMA knitted actuators are actuating multifunctional fabrics composed of a single filament of SMA deformed and constrained into a traditional weft knit structure that can accomplish tunable actuation contractions between 4-50%. [163] As shown in Figure 6.1b, weft knits are composed of interlocking networks of geometrically identical loops organized in wales (columns)

and courses (rows) forming knit patterns. Actuation contraction (ζ) is defined by the relation between the fully-martensitic knit length (blue) ($T < M_f$) and the contracted partially-austenitic knit length (red) ($T > A_f$) at constant macroscopically applied mechanical loading (Figure 6.1c). Tunable %-actuation contraction of contractile SMA knitted actuators is a function of two geometric design parameters, the wire diameter (d) and the knit index (i_k). [163] The knit index is a linear predictor of actuation contraction and non-dimensional geometric number defined as the fraction of the loop enclosed area and the squared wire diameter (Figure 6.1b). While the maximum %-actuation contraction can reach up to 50% at the specific peak actuation-contraction loading, for self-fitting wearables, the actuation contraction occurs in a near-zero load state. In compliance with ISO standards, the prototypes were designed with respect to the %-actuation contraction at $F = 0.5\,\mathrm{N}$ which represents the minimum load at which knitted textiles produce consistent performance. [101] Under such loads, %-actuation contractions within the range of 4-40% are attainable. Figure 6.1d depicts a multiplicity of knitted courses laid flat (left) and connected circumferentially to form a sleeve that translates uniaxial into circumferential contraction for circumferential fitting. This work presents the design and validation of functionally graded knitted actuators with NiTi-based SMAs for topographically self-fitting wearables, highlighting the flexibility and universality of the design process for a variety of fitting and actuation applications. Prototypes designed for multiple body regions using varying NiTi alloy compositions and thermo-mechanical properties were designed for leg and wrist showing topographical and self-fitting. The garment for the leg, a large and geometrically complex region of the body was implemented using commercially available, high-temperature NiTi (Dynalloy, Flexinol®, $A_f = 90\,^{\circ}\mathrm{C}$) and validated for contractile ability and conformity to the leg topography using 3D marker tracking. Improved topographical conformity and body-temperature actuation are presented in a wrist sleeve manufactured from custom, small batch, Ni-rich NiTi material with novel transformation properties engineered by Fort Wayne Metals.

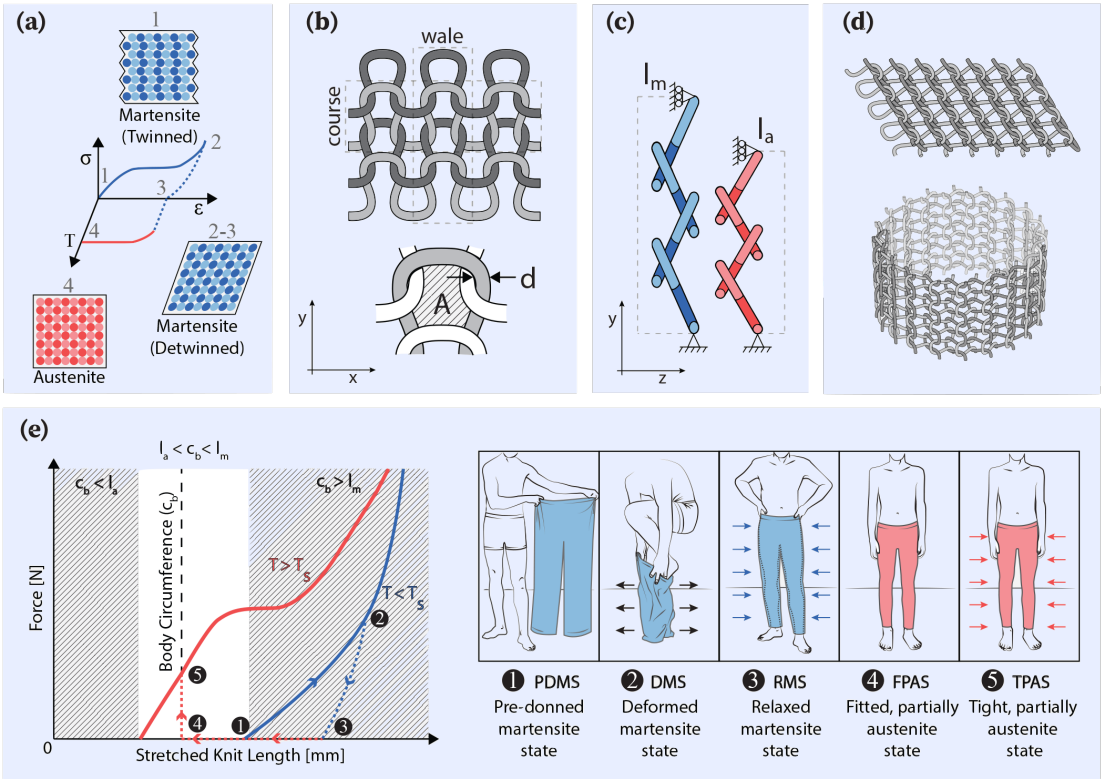

Figure 6.1: **SMA Introduction & Self-Fitting Operation:** a) Shape memory alloys are characterized by recoverable strain achieved through changes in material crystalline structure. Applied stresses turn twinned martensite 1) into detwinned martensite 2,3). Application of thermal loads recovers the mechanically imposed strains and stresses as the material returns to an austenite state 4). b) Knit geometry and geometric design parameters, including SMA wire diameter (d) and loop enclosed area (A). A column of knitted loops forms a wale and row of knitted loops form a course. c) Knit architectures (i.e., garter knit) can produce planar contractions between martensite (blue) and austenite (red) material phases, producing a distinct martensite length (l_m) and austenite length (l_a) per applied load. d) Knit fabrics are constructed through successively added courses. To achieve circumferential contraction, fabrics are wrapped with courses parallel and wales perpendicular to the length of the body. e) Self-fitting garments designed with knitted SMA experience the following stages through use; 1) Pre-donned martensite state (PDMS): The garment begins oversized, compliant, and fully marten-sitic. 2) Deformed martensite state (DMS): Outward forces are exerted that partially detwin the martensitic garment as it is pulled over the body. 3) Relaxed martensite state (RMS): Martensite relaxation occurs once the garment is on the body. 4) Fitted, partially austenite state (FPAS): The garment contracts when actuated to recover its austenite length, achieving the dimensions of the body and 5) tight, partially austenite state (TPAS): tightens around that form.

6.2 Results and Discussion

The thermo-mechanical behavior of SMA knitted actuators guides the operation for self-fitting wearable, detailed in Figure 6.1e. (1) In its initial state, the pre-donned martensite state (PDMS), the self-fitting garment begins oversized and compliant (Figure 6.1e-1). In this state, the SMA material is composed of twinned and detwinned martensite, determined by the strains and stresses imposed during the knit manufacturing process. The knitted loops allow for relative translatory and rotational displacements to enable structural compliance. (2) Subsequent to the PDMS, the garment is subject to don forces as it is pulled over the leg and reaches the deformed martensite state (DMS), Figure 1e-2. As the knitted actuator is strained macroscopically, both the twinned and detwinned martensite are elastically deformed and a partial transition from twinned to detwinned martensite occurs at the lattices that are subject to sufficiently high stresses. Translation and rotation of knitted loops also contribute to extension. (3) Post don, the external forces are released and the self-fitting garment relaxes from Figure 6.1e-2 to -3 into the donned relaxing martensite state (DRMS). The residual displacements between points 1 and 3 of Figure 6.1e are caused by material and knit architectural effects. Elastic deformations are recovered in both the twinned and detwinned martensite; however, no reverse transformation from detwinned to twinned martensite occurs. Additionally, frictional forces at the contact points of interlacing knitted loops resist full-recovery of the imposed donning displacements. (4) Self-fitting and self-stiffening are initiated by an increase in thermal load above the austenite finish temperature of the self-fitting garment. The garment recovers thermo-elastic deformations and the garment circumference dimensions decrease as the garment enters into the fitting partially-austenitic state (FPAS). The SMA material transitions from twinned and detwinned martensite to detwinned martensite and austenite, a state that is referred to as partially-austenitic. The change of lattice structure from martensite to austenite causes both material stiffening as well as garment circumference reduction due to partial recovery of knitted loop bending deformations imposed in the manufacturing process. At point 4, the body and garment dimensions are equal, therefore, further phase transition from martensite to austenite does not provide additional displacements. (5) Because thermal loading continues to transition twinned and detwinned martensite to austenite, the knitted loops interlock into a higher friction configuration into the tight

partially-austenitic state (TPAS). The reconfiguration (architectural stiffening) generates circumferential forces (Figure 6.1e-5) which are translated to the wearer's body as compressive pressures.

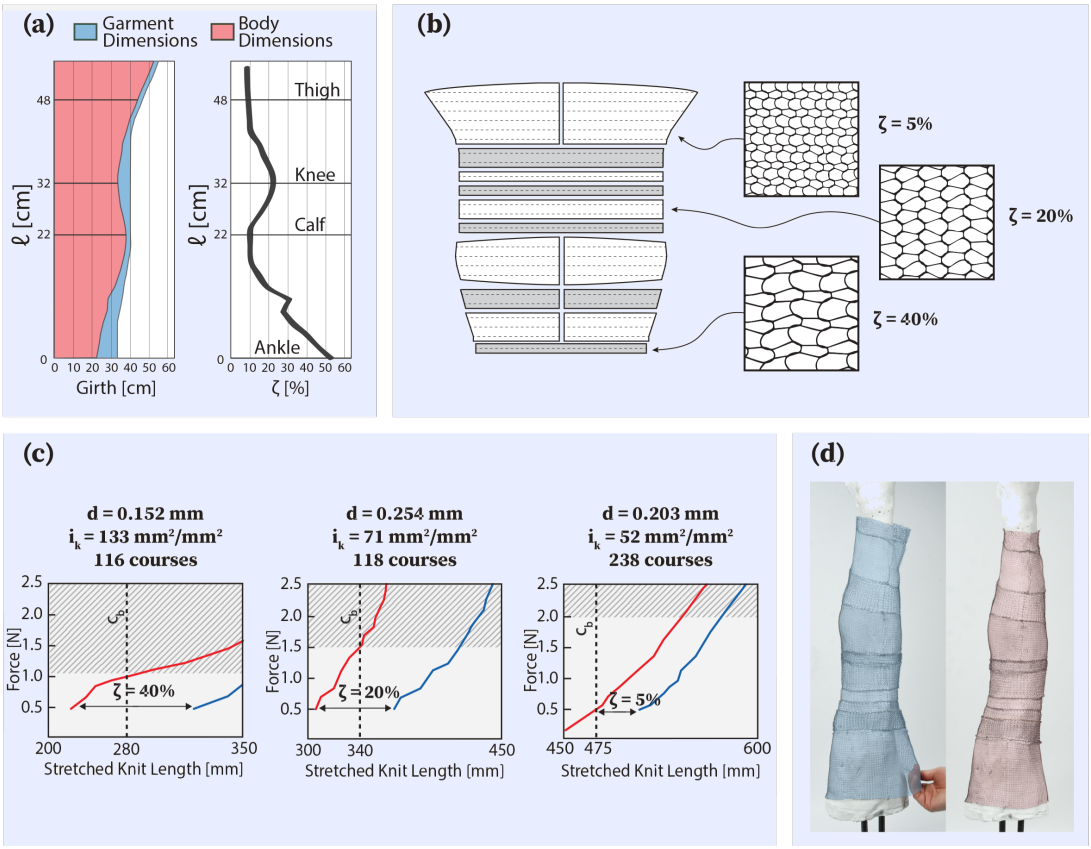

Figure 6.2: **Self-Fitting Garment Design:** a) Required self-fitting garment actuation contraction [%] determined through anthropometric analysis. Functionally graded garment per-formance is required to produce even pressures on the body. b) Garment pattern derived from anthropometric analysis. Ten segmented panels make up the garment, each with unique dimensions and actuation contraction performance mirroring the body. Panels with non-rectangular forms are split at center front so that all shaped edge conditions can be manufactured identically. c) Garment pattern dimensions were determined by pairing body circumference (c_b) measurements with the appropriate SMA knitted actuator force-displacement curves. Knitted courses were added or subtracted to position the body circumference (c_b) between the austenite knit length (l_a) and martensite knit length (l_m) to keep forces below 10 mmHg. d) The completed self-fitting garment is depicted in unactuated (left) and actuated (right) states.

The design process for self-fitting wearables was grounded in anthropometric analysis and guided by performance (i.e., %-actuation contraction), comfort (i.e., pressure), manufacturability, tactile acuity, weight, and cost requirements. Figure 6.2a depicts the methodology for defining garment actuation contraction performance using anthropometry and minimum garment dimensions based on donning logistics. [220] Uniaxial contraction is accomplished upon heating above the austenite finish temperature through the recovery of bending deformations and formation of ridges between alternating courses of knit and purl loops, which are mirrored opposites. The %-actuation contraction (ζ) of SMA knitted actuators is defined as

$$\zeta = \frac{(l_m - l_a)}{l_m} \tag{6.1}$$

the normalized difference between the fabric's martensite length (l_m) and austenite length (l_a) at a given load and, while following the engineering strain definition, named in clear distinction to material strains. [163] The complex thermo-mechanical loading state of SMA knitted actuators with variable strains and stresses inhibits the assumption of full austenitic transformation at A_f, which is defined as a stress-free transformation temperature. The dimensions of a participant's leg collected for the initial prototype (Figure 6.2a - red) are plotted along with the minimum garment dimensions (Figure 6.2a - blue) to enable don/doff, specifically to pull the garment over the heel. Similarly, the design requirements for a wrist sleeve were determined by plotting the body dimensions along with the minimum garment dimensions to enable the sleeve to be pulled over the maximum hand circumference (further described in supplemental materials). The %-actuation contraction requirements for self-fitting garments are thus defined by the percent difference between the garment dimensions and the body dimensions at each circumferential cross-section. Assuming the austenitic fabric length (l_a) equals the circumference of the body (c_b) when fitted ($l_a = c_b$) and the martensitic fabric length (l_m) equals the circumference of the garment (c_g) when oversized ($l_m = c_g$), analysis in Figure 6.2a reveals that self-fitting garments should have a functionally graded design to prevent over-constricting certain areas of the body (e.g., thigh) and under-fitting others (e.g., ankle). Comfort requirements were established to retain garment pressures below that of medical compression garments. [221] The critical force (F_{crit}) at which the critical pressure is reached ($p_{crit} = 1300\,\mathrm{Pa}$) was determined for the variable limb

cross-sectional radius (r) per standard cross-sectional fabric width ($w = 0.02\,\mathrm{m}$), assuming rigid cylinders. [220, 221] The 11 panels that make up the self-fitting leg sleeve are depicted in Figure 6.2b. The SMA knitted actuator performance was compared to body dimensions for the determination of the required number of courses to accomplish the desired actuation displacements (Figure 6.2c) with additional detail provided in the supplemental materials. Each panel was knit on a manual weft knitting machine (Taitexma TH-860) with pre-conditioned SMA wire (Dynalloy, Flexinol®, $A_f = 90\,^{\circ}\mathrm{C}$). The final prototype is depicted in Figure 6.2d in a compliant, oversized martensitic state (left) and in a stiff, fitted austenitic state (right). An innovative approach towards a quantitative measure of fit (traditionally a qualitative process) was developed through three-dimensional, non-contact displacement and strain measurements from 3D marker tracking. The experimental validation methods were designed to measure the success of the self-fitting design by (1) assessing the fit quality through comparison of the fitted garment dimensions in relation to the dimensions of the participant's leg geometry, and by (2) characterizing the accomplished %-actuation contractions in the fitting process.

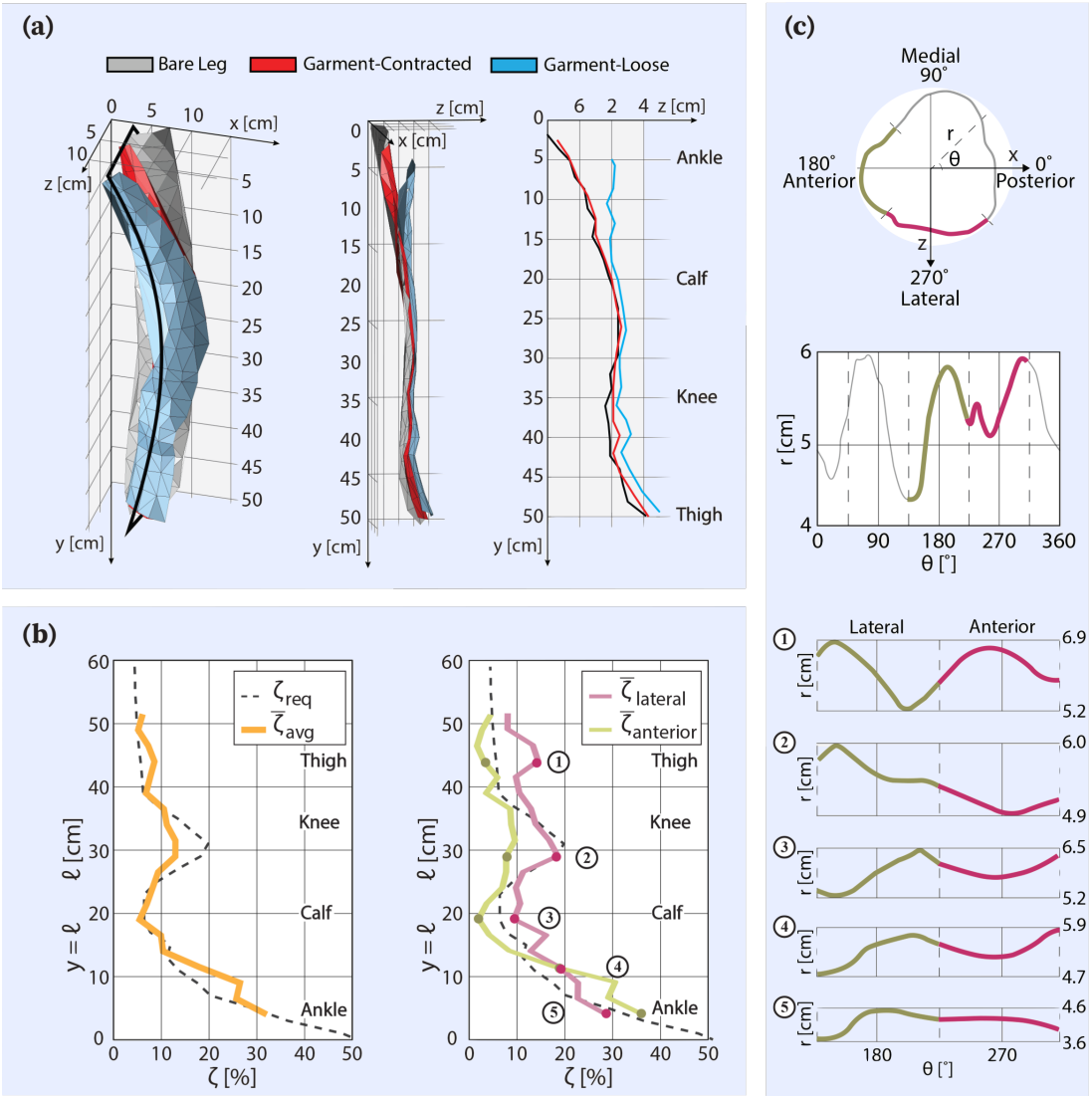

Figure 6.3: **Self-Fitting Garment Performance Analysis:** a) The bare leg replica (gray), the unactuated garment surface (blue), and the actuated garment surface (red) were interpolated. A 2D slice was extracted to evaluate fit in terms of garment proximity to the body. b) (left) Measured actuation contraction was averaged from 10 anterior marker tracking trials and 10 lateral marker tracking trials (right). Anterior and lateral marker tracking trails were split to evaluate differences in performance based on area of the body. c) Cross-sections were gathered from the leg replica through 3D scanning. Deviation from perfectly cylindrical geometries was analyzed for each cross-section by plotting the radial coordinate against the angular coordinate. The anterior and lateral derived radial magnitudes were extracted and evaluated for their convexity or concavity. Plots 1–5 depict examples of regions with adequate actuation contraction as well as inadequate actuation contraction (anterior 1, 2, and 3), characterized by sharp, convex peaks.

The interpolated surfaces of the leg replica (gray), the fitted garment (red), and the oversized garment (blue) (Figure 6.3a) demonstrate successful self-fitting performance; however, suggest improvements could be made at the interface of the knee and lower thigh ($y = 39\,\text{cm}$). To enable quantitative analysis of the non-planar anatomy, a curved slice that follows the largest z-dimensions of the leg replica was extracted. As shown in Figure 6.3a center and right, while the mean dimensional difference between the leg replica and the fitted garment was 1.6 mm, the minimum garment thickness of 0.4 mm reduces the difference to 1.2 mm. The maximum dimensional difference between the leg replica and the fitted garment (5.2 mm) occurs at the transition from thigh to knee ($y = 39\,\text{cm}$), an area of complex geometry that exhibits large concavities and convexities.). In addition to garment-body proximity, 3D marker tracking data was used to evaluate garment actuation contraction and shows garment over-contraction in some areas of the body and under-contraction in others. Figure 3b displays the average %-actuation contractions ($\overline{\zeta}_{avg}$) derived from the normalized difference of Euclidean distances between neighboring markers aligned in the x-directions from the oversized and fitted garment analyses of both the anterior and lateral views. Measurements towards the ankle ($y = 5 - 15\,\text{cm}$) depict average overperformance caused by a larger than predicted martensite garment dimension. In contrast, measurements at the knee ($y = 31\,\text{cm}$) depict average under-contraction of up to 7 percentage points. Figure 6.3b right splits the anterior and lateral views to show that,while the self-fitting marker measurements above the ankle ($y = 11 - 46\,\text{cm}$) show under-contraction in the anterior view, over-contraction occurs in the lateral view. Only lower calf cross-sectional areas ($y = 10.2\,\text{cm}$), which are approximately cylindrical, show identical %-actuation contraction in both lateral and anterior views, suggesting performance is dependent on the surface topography upon which contractile SMA knitted actuator fabrics actuate. The consistent under-contraction of the self-fitting garment around the knee, specifically at $y = 32\,\text{cm}$ where both lateral and anterior views under-contract, motivates further investigation of body surface conditions. A self-fitting garment can contract fully and not be proximal to body concavities just as the garment can be proximal to the body and not fully contracted across body convexities; therefore, the quantitative analysis was supplemented with a topographical analysis to demonstrate the effect of non-cylindrical body shape on purely contractile SMA knitted actuators. As depicted in Figure 6.3c, each cross-section was divided into medial, lateral, anterior, and posterior quadrants.

The equivalent radial coordinate (r) of each cross-section was analyzed with respect to the angular coordinate (θ). Five spliced lateral and anterior radial coordinate plots chosen as extreme examples were then matched with the %-actuation contraction performance plots in Figure 6.3c. Comparing Figure 6.3b and 6.3c numbers 1-5, areas of topographical concavity or relatively mild convexity contracted adequately, while garment under-contraction occurred at angles of extreme topographical convexity. Here concavity and convexity are defined analogous to convex functions; If a line segment between any two $r(\theta_1)$ and $r(\theta_2)$ is consistently equal or greater than the values of $r(\theta)$ between θ_1 and θ_2, the topography is called concave. Extreme concavities are those concavities that maximize the area enclosed by the line segment and $r(\theta)$. Topographical convexities follow the same definition for $-r(\theta)$.

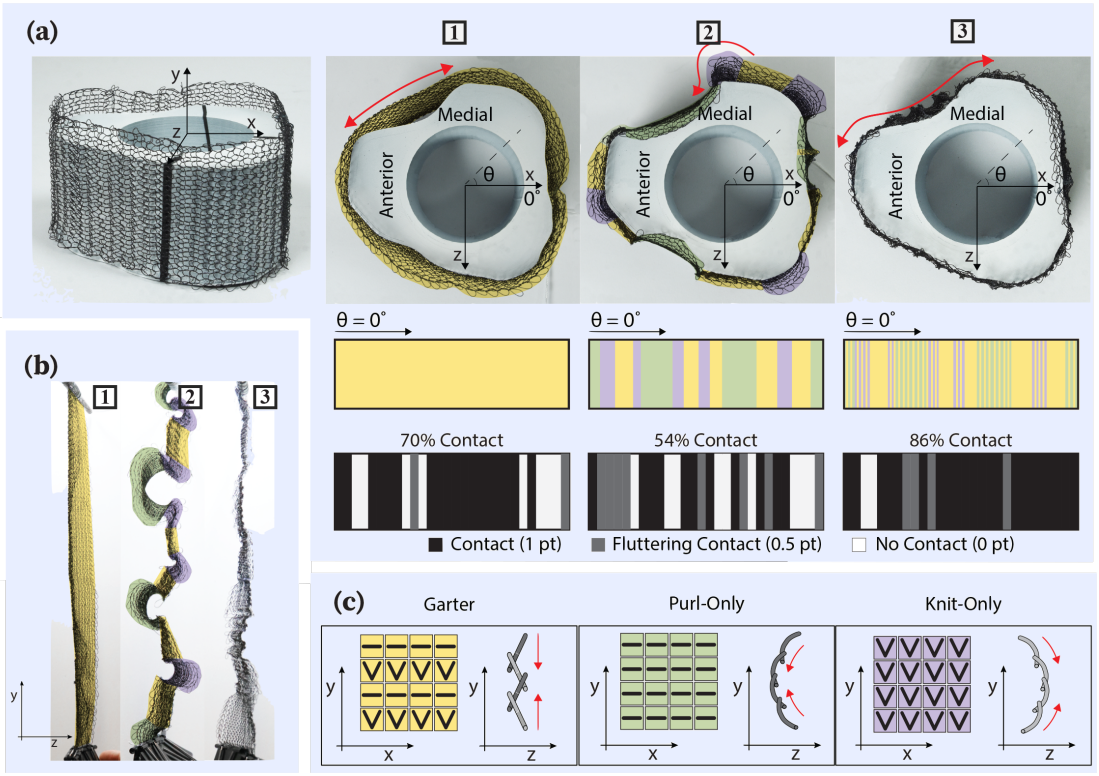

Figure 6.4: **Topographical Self-Fitting:** a) A 3D printed leg cross-section was used to evaluate the fit of contractile SMA knitted actuators around complex body topography. Contact sensing at 28 discrete points around the circumference of the cross-section was used to evaluate fit (i.e., contact) between samples 1–3 of varying knitted architectures. 1) A garter knit panel replicating the geometry used in the self-fitting garment prototype shows bridging over concave surfaces and results in approximately 70% contact with sensing points. 2) A second panel constructed with modified knit geometries, specifically alternating garter, knit-only, and purl-only architectures, shows improved fit around concave and convex surfaces; however, the transitions between the three different architectures produce areas that lift off the surface, which resulted in poor contact performance of 54%. 3) A third panel constructed with blended garter, knit-only, and purl-only architectures produces improved fit around concave and convex surfaces with 86% contact with sensing points. b) Actua-tion contraction of panels a) 1–3 depicted under planar loading. 1) The garter knit panel remains planar upon actuation. 2) The alternating garter, knit-only, and purl-only panel take sharp, non-planar shape change. 3) The blended garter, knit-only, and purl-only panel produces gradated, non-planar shape change more appropriate for leg topography. c) Knit patterns are an organized grid of knitted loops combined in series and in parallel. [6] Garter knit patterns are formed by alternating knit courses and purl courses while purl-only and knit-only are formed by repeating stitches throughout the grid.

To improve the fit of SMA knitted actuators, specifically to conform around body topography, we created modified grid patterns to achieve fully spatial actuation for one body cross-section between the knee and thigh ($y = 32\,\text{cm}$, Figure 6.3b), chosen for its complex geometry. The cross-section was 3D printed and three variable grid pattern prototypes were manufactured. Figure 6.4a and Figure 6.4b present the SMA knitted actuator panels in their actuated states both around the body cross-section (a) and under uniaxial loading (b). The first contractile SMA knitted actuator panel was fabricated according to the original self-fitting garment design at the region of the leg from which the cross-section was extracted ($d = 0.3\,\text{mm}, i_k = 72\,\text{mm}^2\,\text{mm}^{-2}$) (Figure 6.4a-1 isometric, 6.4a-2 cross-section, and 6.4b-1 linear). Fit was evaluated through a novel contact sensing method that measured garment-cross-section contact through resistant at 28 discrete points. While the results of the 3D marker tracking show adequate fabric actuation contraction at concave body contours, the contact sensing investigation confirms that the fabric does not conform around concavities, but rather bridges the surface. Consequently, a second prototype sleeve (Figure 6.4a-2 and 6.4b-2) was designed with purl-only regions placed at concave areas of the body to force the fabric to curve inward and knit-only regions placed at convex areas of the body to force the fabric to curve outward. Figure 6.4c, depicts the actuation behavior of the three knitted architectures: (1) garter, (2) purl-only, and (3) knit-only. While the prototype sleeve (Figure 6.4a-2 and 6.4b-2) does accomplish non-planar actuation and curls in directions appropriate for body topography, the juncures between the two knit patterns are discontinuous and the fabric lifts off the surface. Contact sensing of sleeve 2 shows diminished contact ($54\% < 70\%$) in relation to sleeve 1 due to abrupt changes in knit pattern. A third prototype sleeve (Figure 6.4a-3 and 6.4b-3) includes transitions between architecture types to soften the curling actuation of non-planar architectures. Figure 6.4a-3 depict increased fit (i.e., 86% contact), or proximity to the body, through gradient transitions between garter, purl-only, and knit-only knitted architectures.

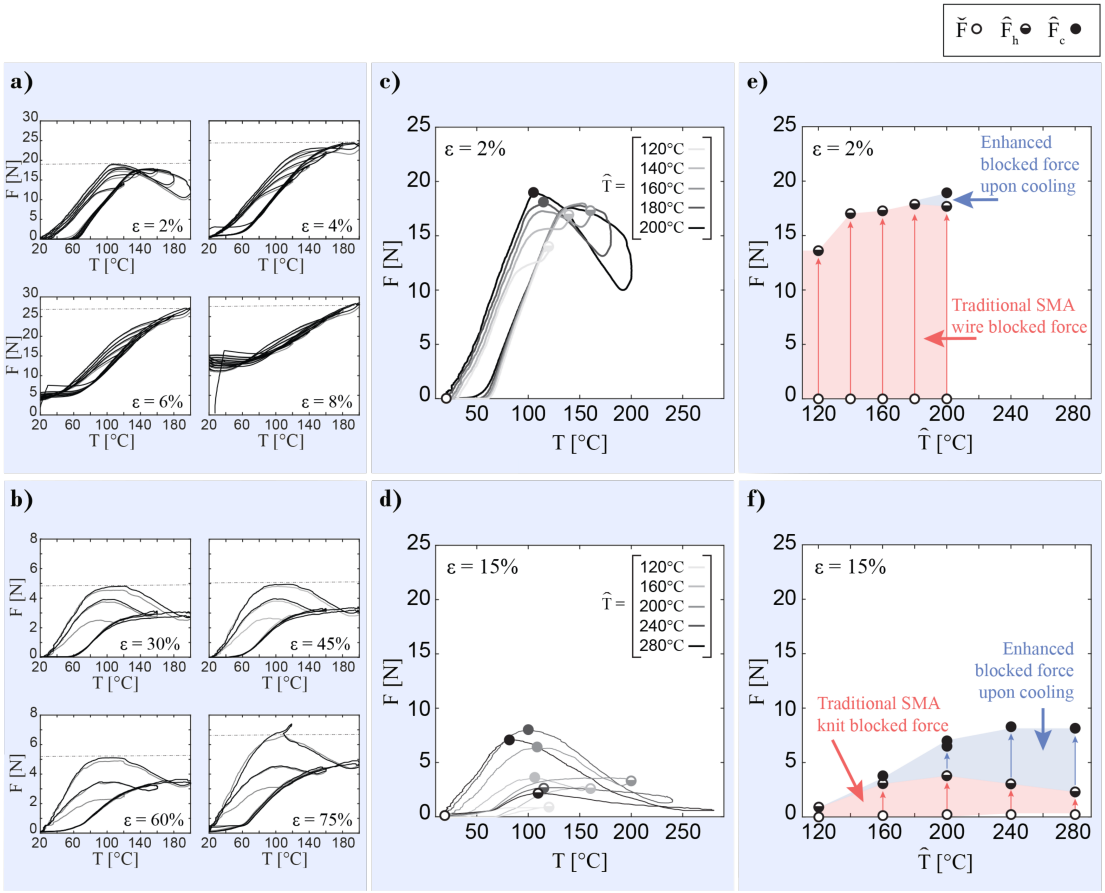

Figure 6.5: **Body Heat Actuation Material Design:** a) DSC curves to compare 90 °C Flexinol® manufactured by Dynalloy and the custom material designed by Fort Wayne Metals to actuate on the surface of human skin. b) Microstructure characterization of custom Fort Wayne Metals material through X-ray diffraction shows the thermally-induced austenite and martensite material states. c) Stress–strain data for custom Fort Wayne Metals material at varying temperatures ($T = [45, 34, 25,$ and$-73\,°\mathrm{C}]$, $l = 0.000{,}04\,\mathrm{s}^{-1}$, $d = 0.076\,\mathrm{mm}$) shows the characteristic NiTi temperature-dependent plateau. d) Cyclic stress–strain data for one sample ($T = 70\,°\mathrm{C}$, $l = 0.000{,}08\,\mathrm{s}^{-1}$, $d = 0.127\,\mathrm{mm}$) shows material performance degradation and stabilization after 7 loading and unloading cycles.

The design and manufacturing procedures for a topographically fitting garment was applied to a self-fitting wrist sleeve designed to slide over the hand and conform to the anatomy of the wrist solely powered by the participant's body heat. The final prototype was designed with a small batch of custom, Ni-rich NiTi manufactured by Fort Wayne Metals and composed of 54.5-57.0% Ni with ternary elements O,N, C, Co, Cu, Cr, Fe, and Nb (0.010 - 0.050% maximum per additive). The material was cold-worked into a 0.142 mm diameter wire and straight-annealed. DSC testing (depicted in Figure 6.5a) was completed to ascertain thermal transition temperatures ($A_f = 36.5\,^{\circ}\text{C},\ A_s = 23.5\,^{\circ}\text{C},\ M_s = -50.5\,^{\circ}\text{C},\ M_f = 73.5\,^{\circ}\text{C}$). While the austenite finish temperature ($A_f = 36.5\,^{\circ}\text{C}$) is higher than mean skin temperature in thermally comfortable environments ($T_s \approx 35\,^{\circ}\text{C};\ T_{amb} \approx 32\,^{\circ}\text{C}$), the thermal transition temperatures were low enough to demonstrate actuation on the human body with minimal applied heat. X-ray diffraction (XRD) informs about the microstructural composition of the Fort Wayne Metals material at $T = -85\,^{\circ}\text{C}$ (martensite) and $T = 45\,^{\circ}\text{C}$ (austenite) (Figure 6.5b). Stress-strain data was collected to demonstrate the material behavior at temperatures around the application use-case ($T = [25\,^{\circ}\text{C}, 35\,^{\circ}\text{C}, 45\,^{\circ}\text{C}]$) as well as below the martensite finish temperature ($T = -73\,^{\circ}\text{C}$) (straight wire, d = 0.076 mm, Figure 6.5c). Figure 6.5c highlights the temperature-dependence of the material upper plateau stress. Cyclic stress-strain data for the material ($d = 0.127\,\text{mm}$) is depicted in Figure 6.5d. The first self-fitting, self-stiffening prototype made for direct contact with the human body is depicted in Figure 6.6. The prototype was designed to stretch over the subject's largest hand circumference (20 cm) and contract to achieve the dimensions of the subject's wrist (15 cm). To achieve the required actuation contraction ($\zeta_{req} = 25\%$), a large knit index ($i_k = 124\,\text{mm}^2\,\text{mm}^{-2}, d = 0.142\,\text{mm}$) was selected to accomplish actuation contraction up to 36% (Figure 6.6a). Garter and knit-only patterns were used within the knitted architecture to mirror the topography of the wrist (Figure 6.6b). Specifically, a knit-only knit architecture was used around curved surfaces (i.e., proximal, medial surfaces, and over the ulna head). A garter knit architecture was used distal and proximal to the ulna head to conform around the cylindrical protrusion. Consistent with garment operations outlined in Figure 6.1e, Figure 6.6c depicts topographical self-fitting: (1) PDMS - The prototype is initially exposed to temperatures below the martensite finish temperature ($M_f = -73.5\,^{\circ}\text{C}$) and brought back to room temperature ($RT = 20\,^{\circ}\text{C}$), which is below the austenite start temperature ($A_s = 23.5\,^{\circ}\text{C}$) (Figure

6.6c-1). (2) DMS - The compliant, martensitic sleeve is pulled over the largest part of the hand (Figure 6.6c-2). (3) RMS - The prototype is positioned on the subject's wrist while remaining slightly oversized (Figure 6.6c-3). (4) FPAS - The prototype is warmed by body heat, both the adjacent skin and the palm of the other hand (Figure 6.6c-4). (5) TPAS - The stiff and fitted prototype conforms around the curvature of the wrist bones after warming (Figure 6.6c-5). While the thermal transition temperatures of the material require future adjustment, the prototype confirms the feasibility of a self-fitting, self-stiffening wearable designed for direct contact with the human body.

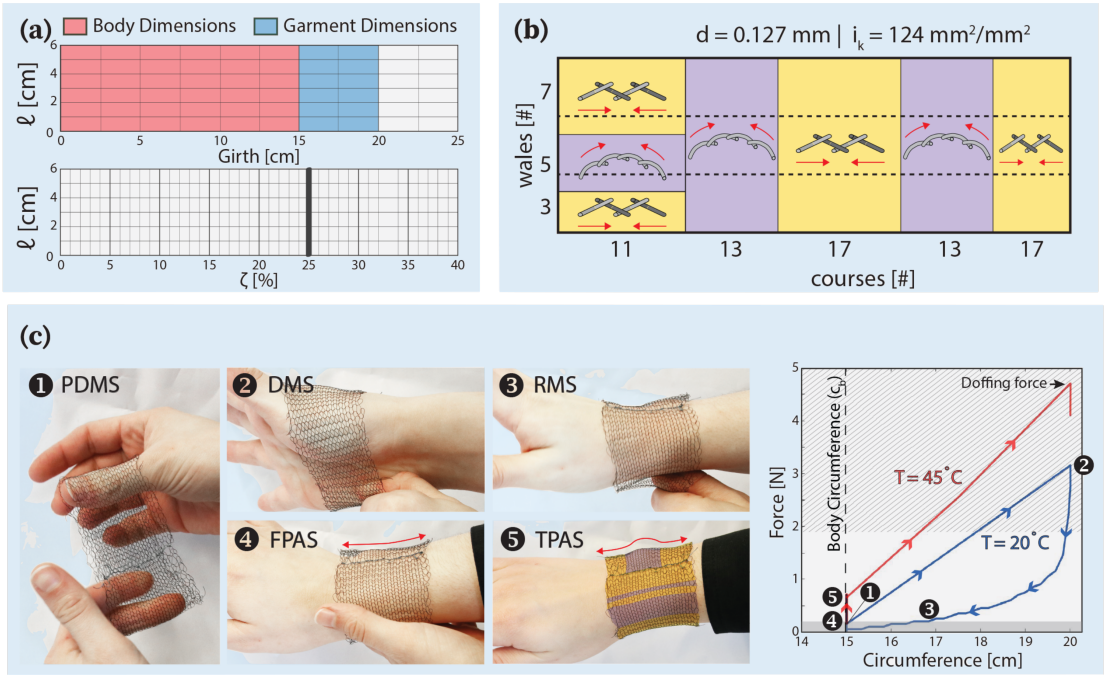

Figure 6.6: **Topographically Self-Fitting Wrist Sleeve:** a) Garment actuation contraction requirements ($\zeta_{req} = 25\%$) were defined by comparing the body dimension (i.e., wrist circumference) to the required garment dimensions to enable don/don (i.e., hand circumference). b) A wrist sleeve was designed using a SMA knitted actuator architecture that contracts up to 36% under low load (i.e., $F = 0.05\,\text{kg}$). Multiple knitted architectures (i.e., garter knit and knit-only) were incorporated into the design to improve fit around the curves of the wrist bone. c) A topographically conforming wrist sleeve prototype was designed with a small batch of custom NiTi fabricated by Fort Wayne Metals to implement unpowered, self-fitting with body heat. The sleeve performance was validated through thermome-chanical testing to observe force-displacement behavior and evaluate implementation of the designed garment operation. 1) Pre-donned martensite state (PDMS): The martensitic wrist sleeve begins in room temperature under no load ($T = 20\,°\text{C}, F = 0\,\text{N}$). 2) Donned martensite state (DMS): The martensitic wrist sleeve is pulled over the largest part of the hand ($T = 20\,°\text{C}, F = 3.2\,\text{N}$). 3) Relaxed martensite state (RMS): Martensite relaxation causes the sleeve to contract slightly around the body; however, the sleeve remains oversized ($T = 20\,°\text{C}, F = 0\,\text{N}$). 4) Fitted, partially austenite state (FPAS): The palm is used to assist the material in warming to skin temperature ($T = 45\,°\text{C}, F > 0\,\text{N}$). 5) Tight, partially austenite state (TPAS): The warmed sleeve self-fits around the curvature of the wrist ($T = 45\,°\text{C}, F = 0.7\,\text{N}$), exerting low forces under 10 mmHg ($F_{crit} = 1.9\,\text{N}$). To doff the garment, the warmed, fitted sleeve is manually pulled off the body with low forces ($T = 45\,°\text{C}, F = 4.7\,\text{N}$). The grey box ($F = 0$–$0.2\,\text{N}$) represents the area of the 25 lb load cell that cannot be resolved.

6.3 Conclusion

NiTi-based SMA knitted actuators present a paradigm shift for smart wearables, spanning consumer, medical, and aerospace spheres, by enabling no-power, topographically-conforming garments through innovations in NiTi-based material systems and garment design processes. The presented work surpasses traditional apparel methodologies and will enable unpowered, automated fit through the exact setting of material transformation temperatures to accommodate a wide range of user dimensions. Design and manufacturing processes implemented with multiple prototypes highlight the flexibility and applicability of the approach to any body region and garment size. Multiple NiTi-based SMA materials with distinct thermo-mechanical properties are used to fabricate prototypes that demonstrate the adaptability of the material system. Because garment tightening and garment-body conformity are inequivalent, novel spatial actuation contraction is leveraged to achieve topographical conformity, a quality that is unachievable with passive fabrics or uniaxial actuators. The resulting topographically self-fitting wrist sleeve demonstrates the functionality and feasibility of a NiTi-based SMA knitted actuators in the design of a new class of smart wearables.

6.4 Experimental Section

6.4.1 Materials

NiTi-based 90 °C Flexinol® actuator wire was purchased from Dynalloy, Inc. in 0.152 mm, 0.203 mm, 0.254 mm, and 0.305 mm diameters and used without any material modifications. The custom NiTi-based actuator wire used in the self-fitting wrist sleeve was provided by Fort Wayne Metals in a 0.152 mm diameter only. The custom material was composed of 54.5-57.0% Ni and contained tertiary elements O, N, C, Co, Cu, Cr, Fe, and Nb (0.010 - 0.050% maximum per additive). The custom material was heat treated during the manufacturing process and was not modified after the material was received.

6.4.2 Calculation for Garment Dimensions

To calculate the number of knitted courses and wales required to achieve the dimensions and shape of each of the 11 knit panels depicted in Figure 6.2b, fabric force-length data collected was scaled so that any given leg circumference was positioned between

its paired fabric's austenite and martensite lengths at low load (0.05 kg), as shown in Figure 6.1e and 6.2c. The number of knit courses (fabric length) was decreased if the body circumference (c_b) was less than or equal to the austenite fabric length (l_a) so that the garment does not have to use maximum %-actuation contraction potential to successfully self-fit (Figure 6.1e, $c_b < l_a$). Conversely, the number of knit courses was increased if the body circumference (c_b) exceeded the martensite fabric length (l_m) because in this scenario the unactuated garment would already fit (Figure 6.1e, $c_b > l_m$). Additionally, the number of knit courses was increased if the force at the body circumference (c_b) and austenite fabric length (l_a) intersection (Figure 6.1e-4) exceeded the critical force (F_{crit}). The number of wales was determined through traditional, passive knit scaling methodologies by counting the number of wales per predetermined dimensions (here 2 cm) and scaling per panel width specifications.

6.4.3 SMA Knit Actuator Thermomechanical Architectural Shakedown

Once knit, each panel was thermally loaded between 20 °C and 120 °C under constant mechanical loading (F = 0.5 N) for 50 cycles to enable the material to settle into its new knitted configuration. [222, 99]

6.4.4 3D Marker Tracking Setup

An experimental test stand replicating the shape and dimensions of the participant's leg was cast from Densite® K-5 plaster for testing the active fitting garment, which was manufactured with 90 °C Flexinol® wire. The garment was donned and doffed over the foot and external heat was applied with heat guns. Bow-tie markers were sewn to the garment in the anterior and lateral-views using a 4×20 marker pattern to capture the circumferential contraction of the garment along its length. Two CMOS cameras with frame rates of 20 f/s tracked the markers to produce a 3D point cloud for each frame during the fitting procedure. 3D Marker Tracking Procedure: The garment was donned on the experimental test stand and thermo-mechanically loaded following the load path displayed in Figure 6.1e. The experimental procedure was repeated ten times for both the front and side views. Repeated measures and statistical analysis were

required due to variable oversized reference configurations post donning in the martensite state. The oversized garment, similar to traditional clothing, can fall into a nearly infinite number of equilibrium states due to low architectural stiffness (e.g., wrinkle formation). Because the %-actuation contraction (ζ) is dependent on the initial garment dimensions, oversized garment variability affects the measured %-actuation contraction. Stereo digital imaging for 3D marker tracking has a limited field of view because both cameras are required to continuously capture every marker. Rather than capturing a cumulative 360iew of the garment, we sampled actuation contraction performance at the anterior and lateral leg views. Capturing 180rovided a representative sample of concave and convex topographies and contractile performances of SMA knitted actuator fabrics around the human body. 3D Marker Tracking Analysis: The 3D marker tracking algorithm (Correlated Solutions VIC3D) outputs a Cartesian coordinate point cloud for each frame captured during the thermo-mechanical loading of the self-fitting garment. Despite the approximately circular leg geometry which would be most efficiently described with polar coordinates, we conducted this analysis in the Cartesian system to comply with the standard anatomical terms of directional description (x-axis = transverse axis, y-axis = vertical axis, z-axis = sagittal axis), depicted in Figure 6.3a. The Euclidean distance (E) was calculated between adjacent markers of each circumferential marker quadruplet (a,b,c,d) and the %-actuation contraction (ζ) was determined for in the oversized, fully-martensitic and the fitted partially-austenitic garment. 3D surface plots were created from the point clouds of the leg replica, the fitted garment, and the oversized garment for the fit quality analysis. Delauney triangulation was used to interpolate between the discrete points and generate the continuous surface. Potential sources of measurement error stem from marker thickness, garment thickness, and the marker attachment method, as well as errors introduced in the marker tracking calibration, imaging process, and the interpolation process for the generation of the analyzed surfaces. Contact Sensing Procedure: A custom setup was designed to experimentally collect contact information between the 3D printed knee cross-section and the SMA knitted actuator sleeve prototypes (Figure 6.4a-1-3) to observe the influence of knitted architecture on garment fit (i.e., conformity) around body topography. Resistance measurements were used to identify contact. An electrode was permanently connected to the sleeve and electrically conductive materials (copper tape) were placed

around the knee cross-section at 28 discrete locations (see supplemental materials, Figure A.1). Upon contact, the measured resistance settles to values below $3\,\Omega$ whereas it is unpredictable but of significantly higher magnitude without established contact. A data acquisition device (NI-6341) enabled 8 simultaneous resistance measurements and four contact measurement runs were performed for each of the sleeve samples 1-3. The resistance data was processed to identify the upper envelope signal (Hilbert transform) and avoid faulty contact information stemming from sign-changes in resistance while no contact was established (Figure A.2). The contact cut-off resistance ($3\,\Omega$) was defined as the maximum in-contact resistance measurement error to accurately identify the in-contact ($R > 3\,\Omega$) / no-contact ($R < 3\,\Omega$) signals. Additional details are provided in the supplemental materials. A semi-quantitative evaluation method was established to compare sleeves 1-3. For each sleeve, the contact condition at measurement points 1-28 was identified as a "contact", "flutter", and "no contact" condition based on resistance data (Figure A.3). The value 1 was assigned for "contact", 0.5 for "flutter", and 0 for "no contact". 86% of contact measurements were identified to be in-contact for sleeve 3 compared to 70% for sleeve 1 and 54% for sleeve 2.

6.4.5 X-Ray Diffraction Procedure

Microstructural characterization of the custom Fort Wayne Metals NiTi material was performed on a Bruker D8 Advance Cu-source, theta-theta diffractometer. The diffractometer enables the characterization of thermally-induced martensite and austenite states at respective material phase transition finish temperatures ($M_f = -73.5\,°\text{C}$, $A_f = 36.5\,°\text{C}$) through cooling/heating between -190 °C and 300 °C. The NiTi wire was cut into innumerable pieces and randomly distributed on the measurement stage to recreate conditions resembling powder to enable the measurement of all diffraction peaks despite the 1D detector limitation. This is a necessary step to avoid missing peaks that could only be resolved in higher dimension detectors because of the known presence of texture in the wire. Experiments were performed in a nitrogen environment to avoid the formation of crystals upon cooling. Figure 6.5b presents the 2θ-intensity plots of the austenitic state and the martensitic state with potential R-phase and precipitate peaks.

6.4.6 NiTi Tensile Characterization Setup

Characterization of Fort Wayne Metals custom NiTi wire samples and the fabricated wrist sleeve were conducted on an Instron machine (model #3365) housed in a thermal chamber (calibration, -80 °C to 150 °C) and equipped with a 25-lb load cell (±1% of force reading from 0.6 N-0.2 N). Pneumatic side-action grips pressurized to 345 kPa were used to grip straight wire samples. A mechanical couple (see supplemental material, Figure A.4) was used to hold the wrist sleeve in place during testing.

6.4.7 NiTi Thermal Response Characterization Procedure

Multiple FWM NiTi samples from the same sample batch (0.076 mm diameter) were exposed to the transition temperatures and mechanically strained to observe resulting material stresses. Each sample was strained at a rate of $0.0004\,\mathrm{s}^{-1}$ and subsequently unloaded at each fixed temperature (Figure 6.5c).

6.4.8 NiTi Cyclic Characterization Procedure

Cyclic stress-strain behavior was observed by repeated loading and unloading one FWM NiTi sample ($d = 0.127\,\mathrm{mm}$) at a temperature above the austenite finish temperature ($T = 70\,^{\circ}\mathrm{C}$) at a rate of $0.000{,}08\,\mathrm{s}^{-1}$ (Figure 6.5d). Wrist Band Tensile Characterization Procedure: The experimental, self-fitting wrist band designed with custom FWM NiTi material was evaluated through force-displacement testing to validate the garment operation and forces throughout the donning process. The testing setup, detailed in supplemental materials (Figure A.4), shows that the circular wrist band was tested at half scale (i.e., body circumference ($c_b = 15\,\mathrm{cm}$), equivalent length in testing setup ($l = \frac{c_b}{2} = 7.5\,\mathrm{cm}$) and scaled up in Figure 6.6c. The wrist band was cooled below the martensite finish temperature ($T = -73\,^{\circ}\mathrm{C}$) before beginning the test procedure. (1) The thermal chamber temperature was raised to room temperature ($T = 20\,^{\circ}\mathrm{C}$). (2) Holding the temperature at room temperature, the circular sleeve was extended ($0.01\,\mathrm{mm\,s}^{-1}$) to a length that would enable donning over the circumference of the hand ($l = 10\,\mathrm{cm}$) and held for 5 minutes. (3) The garment was then mechanically unloaded ($0.01\,\mathrm{mm\,s}^{-1}$) and (4) returned to the length of the wrist ($l = 7.5\,\mathrm{cm}$), followed by another 5 minute hold. Because the test was conducted through displacement-control, the

recovery from a relaxed martensite length to the wrist circumference length was accomplished by the testing instrument rather than through garment actuation contraction. Here, actuation contraction is represented by the distance between the length at which martensite forces are no longer legible by the load cell ($F = 0.2\,\mathrm{N},\ l = 8.4\,\mathrm{cm}$) and the length representing the wrist circumference ($l = 7.5\,\mathrm{cm}$). (5) The chamber was then heated above body skin temperature ($T = 45\,^{\circ}\mathrm{C}$) and held for 15 minutes to observe an increase in blocked force ($l = 7.5\,\mathrm{cm}$). After the 15 minute hold, the wrist sleeve displacement was increased again to observe the forces required to doff the garment while still warm ($T = 45\,^{\circ}\mathrm{C}$).

Acknowledgements

K.E. and R.G. contributed equally to this work. R.G., K.E., and J.A. developed the self-fitting garment operation. K.E. and R.G. collaborated in the design process of the self-fitting garment. K.E. led the garment 3D marker tracking data collection and analysis procedures, developed the topographical investigation method, conducted XRD analysis of the custom NiTi material, and developed the setup used to gather and analyze contact sensing data for which the method was suggested for use by B.H.. R.G. took lead on the motivating framework, designed the anthropometric analysis procedure, system requirements, and technical specifications of wearables, developed the custom NiTi material requirements in collaboration with FWM, led the development of the knitted garment patterns and manufacturing procedures, characterization of the self-fitting wrist sleeve, and conducted thermomechanical performance analysis of the custom material. J.A. and B.H. guided the direction, motivation, and methods for the work. This work was supported in part by a NASA Space Technology Research Fellowship (Grant #80NSSC17K0158), Minnesota's Discovery, Research, and InnoVation Economy Robotics, Sensors, and Advanced Manufacturing (MnDRIVE RSAM) Initiative, and the University of Minnesota Office of the Vice President for Research UMII MnDRIVE Graduate Assistantship. Thank you to Fort Wayne Metals for supplying the nickel-rich NiTi material. Thank you to the University of Minnesota Polymer Characterization Facility and Charles Weinberg from the University of Minnesota Design of Active Materials and Structures Lab for assisting with DSC testing. Thank you for support from the University of Minnesota's Wearable Technology Lab, specifically Heidi

Woelfe, for coordinating time on the Instron machine.

Chapter 7

Manipulating and magnifying generated force upon heating and cooling in SMA knitted actuators

K Eschen*, R Granberry*, B Holschuh and J Abel
Department of Mechanical Engineering, University of Minnesota,
111 Church Street SE, Minneapolis, MN 55455, USA
Department of Design, Housing, and Apparel, University of Minnesota,
1985 Buford Avenue, Saint Paul, MN 55018, USA
In preparation for submission to **Materials & Design**
* Rachael Granberry and Kevin Eschen contributed equally to this collaborative work.

Detailed description of specific contributions to be found in the acknowledgements.

Abstract

This work reexamines traditional shape memory alloy (SMA) loading paths commonly used in SMA-based actuator applications and presents a novel, superimposed condition in which SMA generates substantial forces upon heating and cooling. This atypical effect was found to be prominent at the completion of material phase transformation, at which point thermal expansion/contraction became the dominant force-generating mechanism. We demonstrate both manipulation and magnification of generated forces can be accomplished by varying the applied thermal load, actuator strain, as well as actuator architecture. Specifically, we present SMA knitted actuators as an actuator architecture that increases the effect by aggregating SMA wires within a complex strain profile – effectively providing a larger operational window for the effect to propagate. By incorporating a generated force upon cooling within an actuator operational sequence, we detail methods that enable future SMA-based applications to enhance traditional blocked force through active cooling or use generated force upon cooling alone.

7.1 Introduction

The choice of a mechanical actuator for a given application starts with a comparison of macroscopic performance metrics, such as stress and strain, in relation to the application requirements. [223] Smart materials, such as shape memory alloys (SMA), piezoelectrics (PE), dielectric elastomers (DEA), or carbon nanotubes (CNT), have expanded the pool of traditional mechanical actuators, providing the opportunity to miniaturize actuation and diversify trade-offs in mechanical performance; however, the type of stimulus that produces an actuation response, such as temperature, light, pH, or magnetic field, as well as the required magnitude of stimulus variation must be considered carefully within the framework of the application. This work focuses on shape memory alloys (SMA), a group of metallic materials that can recover a memorized shape after undergoing substantial deformations (up to 8%). [33, 209]

NiTi is a widely used SMA that exhibits two predominant solid phases, the parent austenite phase and the low-symmetry martensite phase, each presenting different material properties such as stiffness, thermal expansion, or conductivity. This solid-to-solid phase transformation is the underlying mechanism behind SMA material behaviors, the most well-known of which are the shape memory effect (SME) and superelastic effect (SE), explored extensively in prior work (Figure 7.1a). [35, 75, 70, 224]

Here, we investigate non-traditional SMA loading paths – beyond the SME and SE – to present a novel, superimposed condition in which SMA generates traditional blocked forces upon heating, followed by substantial forces upon cooling, an effect that has not been exploited before in actuator design.

This work builds off prior SMA material research that has examined recovery stress generation (RSG), a behavior that is produced by deforming and constraining an SMA specimen in its martensite phase and subsequently thermal loading and unloading (Figure 7.1b). [50, 51, 52, 225] Increasing material strain produces increasingly greater SMA recovery stresses; however, higher thermal loads are required to fully transform SMA into an austenitic state as tensile strains increase. [50, 51] Some applications, such as rock-splitters and socket fittings, have leveraged this material behavior with an SMA material that exhibits enlarged hysteresis (i.e., the difference between A_f and M_s) to sustain an austenite material state without sustaining an elevated temperature; [226, 227, 228, 229] however, these applications are not dependent on enlarging forces

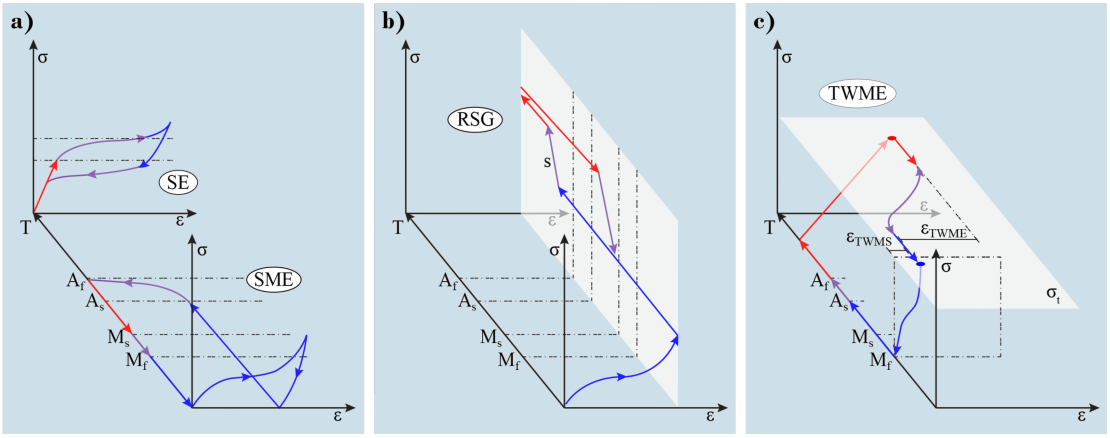

Figure 7.1: **Shape memory alloy (SMA) thermo-mechanical loading paths:** (a) The shape memory effect (SME) and the superelastic effect (SE) and commonly used thermo-mechanical paths. (b) Recovery stress generation (RSG) is a hybrid loading path produced when an SMA specimen in held at a fixed strain. (c) The two-way memory effect (TWME) is another hybrid loading path produced through material training.

upon cooling - only sustaining the maximum force generated upon heating. Observation of generated force upon cooling in these prior studies - beyond what was achieved upon heating - has been attributed to thermal expansion/contraction as well as to the two-way memory effect (TWME). [54, 50, 51] The TWME, another hybrid thermal and mechanical load path depicted in Figure 7.1c, is known to produce a third, stable state – in addition to the self-accommodated martensite state and the austenite state - through crystal orientation training under a fixed training stress (σ_t). [53] The TWME, which produces a recoverable TWME strain (ε_{TWME}), has been shown to accomplish stress recovery up to 100 MPa; [54, 55] however, these stresses are substantially lower than those observed in RSG characterization. [50, 51]

By investigating the intersection of smart materials and actuator design, we present hybrid combinations of the SE and SME that enable SMA knitted actuators to accomplish an enhanced blocked force upon cooling, beyond what is achievable with a traditional SMA blocked force, by exploiting thermal contraction throughout SMA phase transformation. We illustrate that this effect is most prominent at the interface of material phase transformation, where traditional thermal contraction/expansion assumes a larger role in force/stress generation. Additionally, we present an actuator architecture – a SMA knitted actuator – that is shown to both manipulate and magnify the effect.

Experimental data reveals that SMA knitted actuators enlarge the generated force upon cooling effect compared to a standard SMA wire actuators due to their knitted architecture, which aggregates SMA wires and produces complex and highly variable material stresses/strains within the structure. In this work, we demonstrate that (1) generated stresses upon cooling observed in isostrain conditions can be exploited in actuator design to produce substantial generated forces (not just sustained forces) and (2) SMA knitted actuator architectures can be used to both manipulate and magnify generated forces upon cooling.

By exploiting generated force upon heating through active cooling in SMA knitted actuators, we encourage a reexamination of thermal loading paths commonly used in SMA actuator applications and offer new opportunities to use SMA-based actuator in applications spaces that have previously been challenging for SMA, such as those that are intolerant of sustained, elevated temperatures and/or require increased stiffness (actuation) upon a decrease in temperature rather than an increase in temperature. In addition to translating a subtle material effect to usable actuation paths, we present two novel actuation sequences that illustrate (i) a method of using active cooling to generate useful forces in an SMA-based actuator application and (ii) a method of using active heating before SMA actuator use to pre-program a target generated force upon cooling. This work broadens the types of applications in which SMA actuators can operate and provides new design tools for those developing mechanical actuators for complex applications.

7.2 Materials & methods

The SMA material and chosen actuator architecture are detailed here, followed by a summary of experimental methods designed to investigate generated force upon cooling.

7.2.1 Materials & actuator design

We used NiTi actuator wire (90 °C Flexinol®, Dynalloy, Inc.) with a diameter (d) of 0.203 mm in all experimental procedures. The stress-free material transformation temperatures were obtained through differential scanning calorimetry: $M_f = 26\,^{\circ}\mathrm{C}$, $M_s = 65\,^{\circ}\mathrm{C}$, $A_s = 67\,^{\circ}\mathrm{C}$, $A_f = 87\,^{\circ}\mathrm{C}$. [109] Additionally, we characterized knitted architectures manufactured from SMA filament made of the NiTi actuator wire material.

SMA knitted actuators are inherently soft and compliant textiles that provide large, distributed, three-dimensional and recoverable actuation deformations in response to controlled changes in temperature. During the manufacturing process, a single, straight-annealed SMA filament is bent into a constrained architecture of interlacing, adjacent, and symmetrical loops to build a network of consecutive wales (columns) and courses (rows) (Figure 7.2a). This process creates nearly planar structures with anisotropic elastic stiffness in the textile plane. The fundamental unit of knitted architectures is the knitted loop, which is defined by the filament diameter (d) and the loop enclosed area (A_l). These loops can be scaled by a number of course-wise loops (n) and wale-wise loops (m) (Figure 7.2a). The knitted loop can be pulled through its previous, interlacing loop either from the front or the back, resulting in two variations of knitted loops called knit (front) and purl (back) loops. Contractile SMA knitted actuators, explored here, consist of interchanging courses entirely made of knit or purl loops, called a garter knit pattern.

The specific prototype used throughout this publication has a filament diameter ($d = 0.203\,\mathrm{mm}$) and knit index ($i_k = 138\,\mathrm{mm^2\,mm^{-2}}$) depicted in Figure 7.2a. The SMA knitted actuator has been previously characterized through two fundamental paths that demonstrate variable force-extension behavior: (1) force-control and (2) displacement-control (Figure 7.2b). The force-control path mechanically loads the macroscopic actuator while enabling free-displacement. Upon heating, the knitted actuator, whose architecture produces mixed material stresses and strains, recovers macroscopic displacements as it contracts from its fully-martensitic, relaxed profile length (l_M) to its partially-austenitic, actuated, profile length (l_A). The %-actuation contraction (ζ) is defined as the engineering strain between the relaxed profile length (l_M) and the actuated profile length (l_A). [109] This performance metric can be tuned through the knit index (i_k), defined as the fraction of the loop enclosed area (A_l) and the squared wire diameter (d^2). [74] The prototype actuator displayed in Figure 7.2a provides a maximum %-actuation contraction ($\hat{\zeta} = 48\,\%$) at ($F_{\hat{\zeta}} = 1\,\mathrm{N}$). Alternatively, the displacement-control path constrains the actuator to a defined length while enabling generated force in response to heating and cooling. The prototype actuator displayed in Figure 7.2a accomplishes a maximum austenite force per unit width ($\hat{t}_A$) of $135\,\mathrm{N\,m^{-1}}$ and a generated unit force, defined as the difference between austenite and martensite unit forces, of $89\,\mathrm{N\,m^{-1}}$. [230] All SMA knitted actuator samples underwent a thermo-mechanical

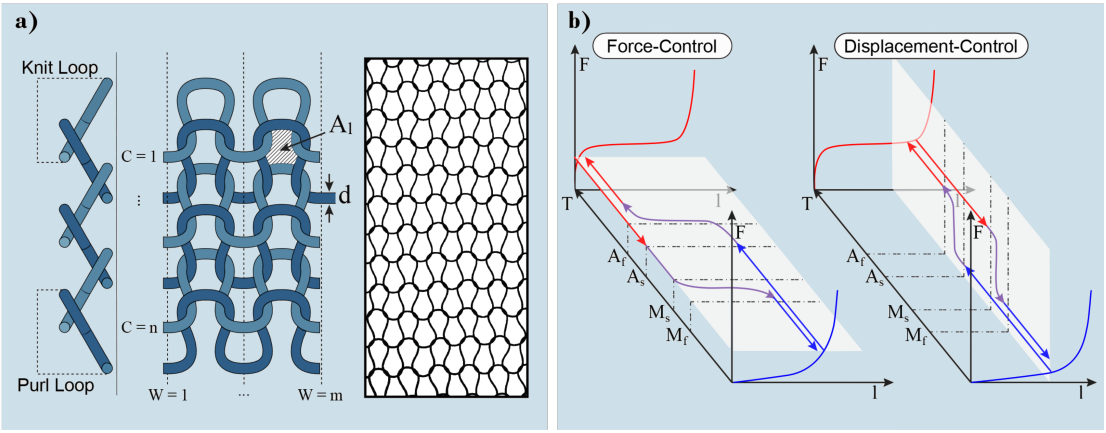

Figure 7.2: **SMA Knitted Architecture Fundamentals & Prototypes:** a) Contractile SMA knitted architectures are manufactured of interlacing courses of knit and purl loops. The loop geometry is defined by the filament diameter (d) and the loop enclosed area (A_l), which define the knit index. A prototype as used throughout this publication is displayed. b) Force-control and displacement-control characterization strategies can be utilized for SMA knitted architectures.

training procedure, which is detailed in the Supplemental Materials, before characterization. Both thermo-mechanical paths demonstrate that contractile SMA knitted actuators can accomplish large actuation contractions, work, and generated forces while being lightweight architectures.

7.2.2 Experimental procedure

The experimental investigation was designed to observe a generated force upon cooling in SMA knitted actuators and identify the mechanisms that induce and/or magnify this behavior. Straight SMA actuator wire was characterized alongside SMA knitted actuators manufactured with the same wire to decouple material and architectural contributions to the effect. The magnitude of the resulting cooling recovery force was evaluating through constrained thermal cycling, or displacement-control testing. Here, a displacement-control testing procedure is conducted by either applying tensile force to a sample as the sample is exposed to cyclic temperature profiles that induce material phase transformation. While isostrain testing, a procedure which maintains consistent material strain throughout thermal cycling, is a preferred material characterization procedure, SMA knitted actuator architectures produce mixed materials strains

throughout the structure, making the procedure incompatible with our actuator samples. Sample characterization was conducted in tension with a tensile testing machine (Instron, model #3365) housed in an environmental chamber (Instron #3119 − 609) with an added coolant inlet hose connected to a liquid nitrogen tank. The setup was equipped with a 50-N load cell (±0.5 % accuracy to 1/200 of reading, ±0.1 % accuracy from 1/200 to 1/500 of reading, Instron 3540 series) and pneumatic side-action grips (Instron #2732−009). Straight wire specimen were gripped directly with the pneumatic grips, which were pressurized between 350 kPa-415 kPa (50-60 Psi). SMA knitted actuators required a custom-built couple that was held by the pneumatic grips and enabled each knitted wale to be pulled uniformly. The pneumatic grips grasped a u-bar that positioned a zinc-plated carbon steel rod perpendicular to the test specimen to enable a threaded connection via zinc-plated split rings, which terminated each knitted wale.

Wire	20 °C ↔ 120 °C	20 °C ↔ 140 °C	20 °C ↔ 160 °C
$\varepsilon = [2, 4, 6, 8]\%$	Cycles 1-2	Cycles 3-4	Cycles 5-6
Actuator	20 °C ↔ 120 °C	20 °C ↔ 160 °C	20 °C ↔ 200 °C
$\varepsilon = [15, 30, 45, 60, 75]\%$	Cycles 1-2	Cycles 3-4	Cycles 5-6
Wire	20 °C ↔ 180 °C	20 °C ↔ 200 °C	
$\varepsilon = [2, 4, 6, 8]\%$	Cycles 7-8	Cycles 9-10	
Actuator	20 °C ↔ 240 °C	20 °C ↔ 280 °C	
$\varepsilon = [15, 30, 45, 60, 75]\%$	Cycles 7-8	Cycles 9-10	

Table 7.1: **Displacement-Control Experimental Procedure:** Straight SMA wire (Flexinol®, $d = 0.203$ mm, $A_f = 87$ °C) and SMA knitted actuators were investigated through methods designed to induce a generated force upon cooling. Five successively increasing temperature profiles were applied repeatedly to each sample.

Straight SMA actuator wire (Flexinol®, $d = 0.203\,\text{mm}$, $A_f = 87\,^\circ\text{C}$) was evaluated at at 2%, 4%, 6%, and 8% structural strain in relation to an austenine free reference length. Four prototypes of equivalent manufacturing parameters were created with Dynalloy Flexinol® filament from a single production batch ($d = 0.203\,\text{mm}$) to ensure consistent material performance. The four prototypes were structurally-strained ranging from ($15\% \leq \varepsilon < 82\%$) in reference to the austenite free length.

At each fixed strained length, the sample was exposed to a thermal cycling profile summarized in Table 7.1 to observe generated force. The sample was (1) heated from room temperature ($T = 20\,^\circ\text{C}$) to a maximum temperature $\hat{T}$, (2) held for a 10-minute soak, (3) cooled back to room temperature, and (4) held for a 5-minute soak. The maximum temperature ($\hat{T}$) was gradually increased throughout thermal cycling to observe temperature-dependent changes in generated force. These maximum temperature are outlined in Table 7.1.

To investigate the ability of SMA knitted actuators to reversibly and cyclically generate force upon cooling and decrease force upon reheating, additional testing was conducted to observe thermal cycling between a maximum temperature ($\hat{T}$) at which the sample is presumably fully austenitic and a lower temperature at which higher forces are observed. The procedure was conducted with a standard SMA knitted actuator sample (15×15 loops) as well as with a SMA knitted actuator sleeve (32×15 loops) designed to mimic systems that contract around volumes. The actuator sleeve, which was made by joining the beginning and the end of each knitted course with a zinc-plated slit ring, was placed around the custom-built mechanical couple. The SMA knitted actuator was strained to 75 % while the actuator sleeve was strained to 15 %, both in relation to the sample-specific austenite free reference length. Table 7.2 depicts the testing procedure for both the SMA knitted actuator and the SMA knitted actuator sleeve. The SMA knitted actuator was exposed to two complete thermal cycles between 20 °C and 200 °C with 5-minute and 10-minute holds, respectively. After two thermal cycles, the actuator was heated back to 200 °C and cycled between lower temperatures ranging from 160 °C to 100 °C to observe generated force upon cooling. Each thermal cycle was repeated twice. The actuator sleeve was exposed to two complete thermal cycles between 20 °C and 240 °C with 5-minute and 10-minute temperature holds, respectively. After two thermal cycles, the sleeve was cycled between a maximum temperature of 240 °C and a lower temperature of 110 °C to observe generated force upon cooling. This thermal

cycle was repeated six times to observe repeatability.

Actuator	20 °C ↔ 200 °C	200 °C ↔ 160 °C	200 °C ↔ 140 °C
$\varepsilon = 75\,\%$	Cycles 1-2	Cycles 3-4	Cycles 5-6
Sleeve	20 °C ↔ 240 °C	240 °C ↔ 110 °C	
$\varepsilon = 15\,\%$	Cycles 1-2	Cycles 3-8	
Actuator	200 °C ↔ 120 °C	200 °C ↔ 100 °C	
$\varepsilon = 75\,\%$	Cycles 7-8	Cycles 9-10	

Table 7.2: **Thermal Cycling Along the Cool-Down Path:** A SMA knitted actuator (15×15) was thermally cycled while constrained at 15 % structural strain to investigate cool-down force recovery. Repeated thermal cycles were performed between a maximum temperature and a lower temperature at which higher force were observed. The procedure was also conducted with a SMA knitted actuator sleeve (32×15) to observe implications for certain applications.

7.3 Results & Discussion

This section provides the experimental results, analysis, and a discussion of the governing mechanisms. Firstly, a set of performance metrics is introduced to ensure appropriate nomenclature throughout the section. The architectural influence on the generated force response and the key design variables are discussed. The utility of the generated force response in applications is highlighted for an active-cooling and an active-heating application.

7.3.1 Performance Metrics

Before proceeding with the experimental results, the RSG thermo-mechanical path is revisited and discussed in terms of a SMA wire and SMA knitted actuators. We develop additional definitions and nomenclature for specific points along these paths for clarity. Figure 7.3 depicts a thermo-mechanical path for the SMA wire specimen held at a defined actuator strain. Point 1 is called the minimum martensite force, $\check{F}$. Upon increasing temperature, the maximum force upon heating ($\hat{F}_h$) occurs at the temperature, $T_{\hat{F},h}$ (point 2). The generated force upon heating (ΔF_h), also known as a traditional blocked force, is defined as the difference between the maximum force upon heating ($\hat{F}_h$) and

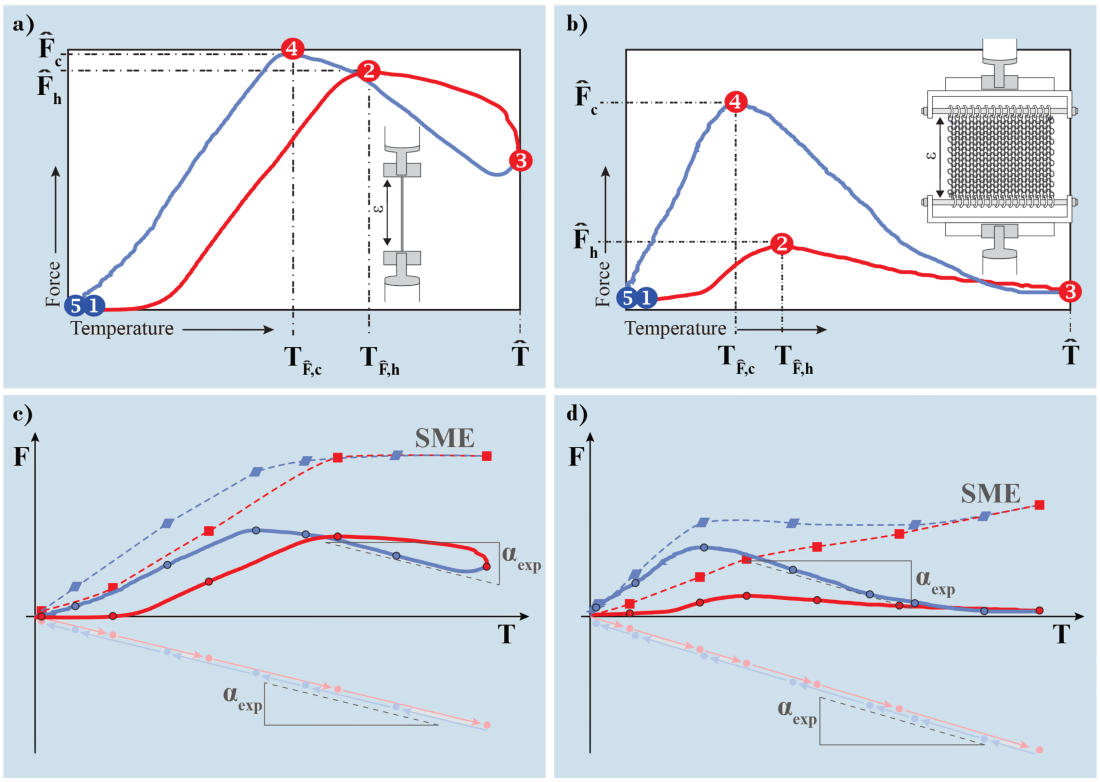

Figure 7.3: **Generated force path for different SMA actuator geometries:** The force-temperature behavior for SMA wire (a) and SMA knitted architectures (b) display similar thermo-mechanical behavior defined by points 1-5. Thermal expansion/contraction and SME contributions to the SMA actuator wire (c) and knitted actuator (d) thermo-mechanical path are separated to explain the generated force behavior.

the minimum martensite force ($\check{F}$). Subsequent force-relaxation to point 3 is initiated by further increasing the temperature to the maximum temperature ($\hat{T}$). Cooling from point 3 to point 4 results in an increase in force. Generated force upon cooling (ΔF_c), a non-traditional blocked force, is defined as the difference between the maximum force upon cooling, which is also the maximum force ($\hat{F}_c = \hat{F}$), and the maximum force upon heating ($T_{\hat{F}} < \hat{T}$). Once the maximum force upon cooling (point 4) is reached at a temperature below the maximum temperature, forces relax to point 5. Figure 7.3b shows the same counterclockwise thermo-mechanical path for a displacement-constrained SMA knitted actuator. While the order of operations remains constant between the wire and knitted actuator samples, the relative magnitude of the maximum force ($\hat{F} = \hat{F}_c$) and

the maximum force upon heating ($\hat{F}_h$) are heavily manipulated by the knitted geometry.

7.3.2 Architectural influence of generated force response

The results demonstrate that generated force response can be manipulated through actuator architecture. Starting with the SMA wire actuator, thermo-mechanical displacement-control behavior in Figure 7.4a is consistent with prior work which has shown (i) increased material strain produces increased generated force and (ii) increased temperature is required to accomplish a complete phase transformation at higher strains. [51, 50, 231] Due to the limiting upper temperature of the experiment ($\hat{T} = 200\,°\text{C}$), a generated force upon cooling could not be observed for most structural strains tested ($\varepsilon = [4\,\%, 6\,\%, 8\,\%]$). At $T = 20\,°\text{C}$, the minimum martensite forces ($\check{F}$) were $\check{F}_{4\,\%} = 0\,\text{N}$, $\check{F}_{6\,\%} = 5\,\text{N}$, $\check{F}_{8\,\%} = 12\,\text{N}$ at the respective structural strain levels. The maximum force ($\hat{F}$) was observed at the maximum temperature ($\hat{T}$), which was not sufficient to accomplish the maximum attainable recovery of austenitic phase. The maximum forces upon heating were $\hat{F}_{h,4\,\%} = 24\,\text{N}$, $\hat{F}_{h,6\,\%} = 27\,\text{N}$, $\hat{F}_{h,8\,\%} = 28\,\text{N}$ and occur when the maximum temperature was $\hat{T} = 200\,°\text{C}$.

Generated force upon cooling was observed in the SMA wire at lower structural strain levels ($\varepsilon = 2\,\%$) shown in detail in Figure 7.4b, in agreement with the literature. The maximum force upon heating occurred in thermo-mechanical cycles with maximum temperatures of $\hat{T} = 160\,°\text{C}, 180\,°\text{C}$, and $200\,°\text{C}$. These thermal cycles reached a maximum force upon heating of $17.5\,\text{N}$ ($\hat{F}_{h,2\,\%}$) before stresses relaxed with further increasing temperatures. The maximum generated force upon cooling ($\Delta\hat{F}_c$) was $1.32\,\text{N}$, which occurred when the maximum temperature was $\hat{T} = 200\,°\text{C}$ at ($T_{\Delta\hat{F}_c} = 107\,°\text{C}$). This generated force upon cooling increased the total generated force by $7.5\,\%$ over the generated force upon heating. This maximum force, observed during cooling, was $\hat{F} = 18.89\,\text{N}$. The initial heating path for each structural strain value investigated was offset from the subsequent thermal cycle until internal stresses partially relaxed upon cyclic loading. Figure 7.4c compares the generated force upon cooling and the traditionally utilized generated force upon heating in SMA actuators as a function of the final temperature to which the SMA wire was heated. While an additional $7.5\,\%$ generated force could be gained, the results demonstrate that the effect of utilizing this thermo-mechanical load path in SMA wire actuators is relatively small.

The ability of the SMA wire to generate force throughout both heating and cooling

is caused by the temperature path-dependent material phase transformation which is super-positioned with the actuator's thermal contraction/expansion properties. [51, 50] Figure 7.3c separates these super-positioned effects graphically. The thermal expansion coefficient (α_{exp}) was experimentally determined when force relaxation and generation occurred at temperatures outside the phase transition regime in the SMA wire. Assuming linear thermal expansion/contraction, the SME contribution to the generated force can be extracted. The super-positioned temperature path-dependency, which is utilized to generate additional force upon cooling, is caused by the varying magnitudes of the transformation temperatures, specifically utilizing the Class I thermo-elastic transformation with a lower martensite start temperature (M_s) compared to the austenite finish temperature (A_f). This leads to a phase transition regime between ($M_s \leq T < A_f$) in which phase transition occurs upon heating but does not occur upon cooling. Returning to Figure 7.3a, generated force during heating from point 1 to point 2 was caused by the solid phase transformation of wire volumes from martensite to austenite which dominated the thermal force relaxation from heating. When those two effects reached equilibrium at point 2, the maximum force upon heating ($\hat{F}_h$) was reached. Further heating resulted in a decrease of the generated force upon heating as thermal expansion was the predominant material behavior. Reversion of the temperature gradient caused the thermal expansion to be recovered by thermal contraction, which is generally assumed to be a linear effect in both heating and cooling driven by the coefficient of thermal expansion. Due to the Class I thermo-elastic transformation, cooling below the stress-adjusted austenite finish temperature did not result in the loss of generated force from the solid phase transition until the stress-adjusted martensite start temperature was reached. Consequently, the thermal contraction upon cooling dominated the behavior until the maximum force ($\hat{F}$) was reached in point 4. This maximum force occured at lower temperatures than the maximum force upon heating. As the temperature was further decreased, the reverse transition from austenitic volumes to martensitic volumes occurred and overshadowed the thermal contraction upon cooling until point 5 was reached. Other effects that may play a role in this behavior have also been discussed. Microstructural effects such as dislocation arrays, retained martensite, and aligned precipitates could play a role in the path-dependent behavior. [51] For lower stress levels, the TWME has also been discussed as a potential contributor to the additional generated force. [54] While it can be expected that a generated force will

occur in the highly structurally strained SMA wire samples if higher temperatures were tested, the relative force increase has been shown to be largest at lower strain levels. [51]

ε	$\hat{F}_{h,200\,^{\circ}\mathrm{C}}$	$\hat{F}$	$T_{\Delta\hat{F},c}$	$\Delta\hat{F}_c$
15 %	1.8 N	4.0 N	119 °C	2.2 N
30 %	2.5 N	4.52 N	119 °C	2.02 N
45 %	2.9 N	4.81 N	115 °C	1.91 N
60 %	3.4 N	5.07 N	110 °C	1.67 N
75 %	4.7 N	6.59 N	103 °C	1.89 N

Table 7.3: **SMA Knitted Actuator Generated Force of Prototype 4:** The SMA knitted actuator generated force varies as a function of the applied structural strain (ε).

The results of the displacement-control experiment with SMA knitted actuators, displayed in Figure 7.4d, depict an enlarged generated force upon cooling compared to SMA wire data. Unlike the SMA wire experiment, force relaxation did not occur upon heating to ($\hat{T} = 200\,^{\circ}\mathrm{C}$) because of variable strains present in the knitted loop, which are known to locally shift transformation temperatures. As shown in Figure 7.4d, all generated forces (heating and cooling) were dependent on the structural strain imposed on the knitted actuator and the maximum temperature to which the actuator was heated. Table 7.3 provides a summary of all results. For the thermo-mechanical cycle with a maximum temperature of 200 °C ($C_{\hat{T}=200\,^{\circ}\mathrm{C}}$), the maximum force upon heating ($\hat{F}_{h,200\,^{\circ}\mathrm{C}}$) increased from 1.8 N at the lowest structural strain level ($\varepsilon = 15\,\%$) to 4.7 N at the highest structural strain level ($\varepsilon = 75\,\%$). Despite the fact that force relaxation did not occur by the maximum temperature, cooling resulted in an additional generated force, which was not observed in the SMA wire experiment. The maximum forces upon cooling and heating ranged from $\hat{F}_{15\,\%} = 4.0\,\mathrm{N}$ at the temperature $T_{\hat{F},15\,\%} = 119\,^{\circ}\mathrm{C}$ to $\hat{F}_{75\,\%} = 6.59\,\mathrm{N}$ at the temperature $T_{\hat{F},75\,\%} = 103\,^{\circ}\mathrm{C}$. These data suggest that the temperature at which the maximum force upon cooling occurred ($T_{\hat{F},c}$) decreased as generated forces upon cooling increased (ΔF_c). The maximum generated force upon cooling ($\hat{F}_c = 2.2\,\mathrm{N}$) was present at ($\varepsilon = 15\,\%$) structural strain, a value that dropped to to $\approx 1.89\,\mathrm{N}$ at ($\varepsilon = 75\,\%$) strain.

The temperature range explored in Figure 7.4d was not sufficient to induce force relaxation upon heating, which was a defining feature of the low-strain SMA wire test. Consequently, another SMA knitted actuator prototype was manufactured and tested up to ($\hat{T} = 280\,^{\circ}\mathrm{C}$) ($\varepsilon = 15\,\%$) structural strain (Figure 7.4e).

When heating to a maximum temperature of ($\hat{T} = 280\,^{\circ}\mathrm{C}$), force relaxation was observed after the maximum force upon heating ($\hat{F}_{h,15\,\%} = 2.2\,\mathrm{N}$), which occurred at $T_{\hat{F},h,15\,\%} = 115\,^{\circ}\mathrm{C}$. However, force relaxation occurred significantly slower than in the wire experiment. While the force-relaxation rate in the SMA wire was ($q_{wire} = -0.097\frac{\mathrm{N}}{^{\circ}\mathrm{C}}$), the SMA knitted actuator presents a plateau with a force-relaxation rate of only ($q_{knit} = -0.0094\frac{\mathrm{N}}{^{\circ}\mathrm{C}}$). Upon reversing the temperature gradient, a maximum force of ($\hat{F}_{15\,\%} = 7.11\,\mathrm{N}$) was measured, resulting in a maximum generated force upon cooling of ($\Delta\hat{F}_c = 4.9\,\mathrm{N}$). This enhanced blocked force upon cooling represented a 222 % increase in generated force compared to the traditional blocked force with heating alone. Figure 7.4f compares the traditionally utilized generated force upon heating in SMA knitted architectures with the additionally-gained generated force upon cooling of the novel loading path. As the maximum temperatures were increased, a significant portion of the total generated force was caused by the subsequent cooling. The variable strains of the knitted loop geometry, which prevent the relaxation of forces as larger temperatures are reached, allowed for the utilization of the path-dependent, additionally generated force upon cooling due to thermal contraction.

Returning to Figure 7.3b, the thermo-mechanical path of SMA knitted actuators is governed by both phase transition and thermal contraction/expansion. The SMA knitted loop is a pre-strained geometry that is largely dependent on the recovery of bending deformations introduced in the manufacturing process. Within the knitted loop, various bending radii lead to highly variable strain states within the loop segment. This geometric reality limits the magnitude of the maximum force upon heating, as the recovery of bending deformations produces smaller forces than the recovery of normal deformations. Despite limiting the maximum force upon heating, the dependence on variable bending strain recovery produces desirable thermo-mechanical behaviors. Figure 7.3d parallels the decomposition of thermal expansion/contraction and phase transition contributions to the generated force of the wire observations. When assuming a linear coefficient of thermal expansion/contraction, the graphical decomposition shows that

the heating SME path does not reach a plateau behavior as is present in the wire decomposition. Due to the continuous variation of strains within the knitted actuator, different segments of the loops achieve transition from martensite to austenite at different temperatures. As the loop relaxes due to thermal expansion, a segment of the knitted loop with larger bending strains undergoes more austenitic transformation, increasing the phase transition force contribution, and resulting in a force equilibrium of the knitted actuator over a large, temperature-insensitive force plateau. When the knitted actuator is cooled, immediate generated force due to thermal contraction occurs without the reverse, force-relaxing phase transition of austenitic to martensitic volumes. If a knitted actuator is heated sufficiently, fully utilizing the force plateau upon heating, a large generated force upon cooling can be accomplished as thermal contraction can occur over the widest temperature window. When the maximum force upon cooling is reached, the phase transition from austenite to martensite starts to dominate the architecture again and the generated forces are released. A coupled rod-beam model was implemented to investigate the theoretical magnitudes of the generated force upon cooling in an abstracted knitted loop geometry. The model, which is further discussed in the supplemental materials, suggests that the magnitudes observed experimentally can be accomplished from thermal contractile effects.

7.3.3 Analysis of key design variables

The thermo-mechanical design variables that affect the magnitude of the generated force and temperatures at which the maximum force occurs are discussed. The maximum temperatures and applied structural strains are the factors that are highlighted specifically.

Between all prototypes and structural strain levels, increasing of the maximum temperature led to an increase of the total generated force. Figure 7.5a displays the generated force upon heating and cooling of SMA knitted actuators of all utilized prototypes with the characteristic points of maximum generated force upon heating ($\hat{F}_h$ - half-filled) maximum generated force upon cooling ($\hat{F}_c$ - filled), and fully-martensitic force (F_m - unfilled) for a single prototype. Figure 7.5b compares the maximum generated force ($\hat{F}$) between all prototypes as a function of the maximum temperature ($\hat{T}$) for the various controlled structural strain levels. Different prototypes are indicated by the variation of the geometric shape and strain levels are coded to follow the color spectrum

from red - ($\varepsilon = 15\%$) to black ($\varepsilon = 82\%$) structural strain. This behavior occurs as the variable strains in the SMA knitted loops are further transitioned toward a fully-austenitic state as the temperature increases without sacrificing force upon heating due to thermal expansion. As the prototype is cooled from the maximum temperature, the force generated by the phase transition remains constant whereas thermal contraction further generates forces upon cooling. The smallest maximum force ($\hat{F}_{120\,^\circ\mathrm{C}} = 0.6\,\mathrm{N}$) occurs at the structural strain level ($\varepsilon = 15\%$) of prototype 2 when heating to the maximum temperature ($\hat{T} = 120\,^\circ\mathrm{C}$). The maximum generated force of this prototype and structural strain level increase to ($\hat{F}_{160\,^\circ\mathrm{C}} = 2.53\,\mathrm{N}$) and ($\hat{F}_{200\,^\circ\mathrm{C}} = 4.0\,\mathrm{N}$) with increasing maximum temperatures. Within a single prototype, higher structural strain levels and higher maximum temperatures lead to a larger maximum force. For example the maximum force of prototype 2 at ($\hat{T} = 120\,^\circ\mathrm{C}$) progresses from ($\hat{F}_{15\%} = 0.6\,\mathrm{N}$) to ($\hat{F}_{75\%} = 3.4\,\mathrm{N}$), whereas the total forces range from ($\hat{F}_{15\%} = 4.0\,\mathrm{N}$) to ($\hat{F}_{75\%} = 6.59\,\mathrm{N}$) at $\hat{T} = 200\,^\circ\mathrm{C}$.

While the maximum forces follow this pattern within a prototype data set, it is difficult to compare the data between data sets without processing. Despite the small differences in SMA knitted prototype length post manufacturing and thermo-mechanical training, relatively large differences in the actuator performance upon displacement-controlled subsequent heating and cooling can be reported. The manufacturing consistency between prototypes was evaluated through the measurement of the zero-load knit length under austenitic temperatures ($T = 120\,^\circ\mathrm{C}$) which ranged between $l_{A,ref} = [41.29\,\mathrm{mm}, 41.4\,\mathrm{mm}]$. Prototype 3 only reaches a maximum force ($\hat{F}_{82\%} = 5.77\,\mathrm{N}$) when heated to the maximum temperature ($\hat{T} = 200\,^\circ\mathrm{C}$) despite being structurally-strained to ($\varepsilon = 82\%$). Such discrepancies between prototypes occur regularly (e.g., comparing prototype 1, $\varepsilon = 32\%$ and prototype 3, $\varepsilon = 49\%$) due to manufacturing inconsistencies which have the potential to trigger large force variation. While most prototypes were only heated to a maximum temperature ($\hat{T} = 200\,^\circ\mathrm{C}$), regardless if the various structural strain levels, a single prototype was heated to the maximum temperature ($\hat{T} = 280\,^\circ\mathrm{C}$) while being strained to ($\varepsilon = 15\%$). In contrast to the prototypes only heated to ($\hat{T} = 200\,^\circ\mathrm{C}$), which continually show increasing forces with rising maximum temperatures, this prototype reaches asymptotic behavior of the maximum force ($\hat{F} \approx 8\,\mathrm{N}$) with increasing temperatures. This suggests that the full-potential to generate forces has not been utilized in the prototypes that do not show asymptotic maximum

forces and heating to higher temperatures is recommended.

Another prevalent effect is the increase in generated force upon cooling when selecting larger maximum temperatures in the thermo-mechanical load cycle (Figure 7.5c). However, in contrast to the total generated force, larger structural strains lead to a decrease of the generated force upon cooling. For example, prototype 3 strained to ($\varepsilon = 82\%$) provides no generated force upon cooling when the maximum temperature is below ($\hat{T} < 140\,^{\circ}\mathrm{C}$) and is maximized at ($\Delta\hat{F}_{c,200\,^{\circ}\mathrm{C}} = 1.47\,\mathrm{N}$) at the maximum temperature ($\hat{T} = 200\,^{\circ}\mathrm{C}$). Prototype 1, however, tested at $\varepsilon = 16\%$ provides a significantly larger maximum generated force upon cooling of ($\Delta\hat{F}_{c,200\,^{\circ}\mathrm{C}} = 3.25\,\mathrm{N}$) at the same temperature. As the generated force upon cooling is defined as the difference of maximum force and generated force upon heating, the asymptotic behavior of the maximum forces carries into the maximum generated force upon cooling. As the maximum temperature is increased, prototype 4, which was tested to the highest temperatures ($\hat{T} = 280\,^{\circ}\mathrm{C}$) at the structural strain $\varepsilon = 15\%$, asymptotes at the maximum generated force upon cooling ($\Delta\hat{F}_c = 5\,\mathrm{N}$). Similarly to the maximum forces described in Figure 7.5b, slight differences between prototype lengths and manufacturing render the quantitative comparison of forces difficult without processing.

A normalization strategy was applied to provide better comparability between the prototypes. Every thermo-mechanical cycle of differing maximum temperatures and structural strain levels was normalized by division through its maximum force upon heating ($\hat{F}_h$). Figure 7.5d shows the thermo-mechanical force-temperature prototype 4 normalized by the maximum force upon heating. Consequently, the normalized force (F_n) is a dimensionless quantity with the value 1 at the maximum normalized force upon heating. All other normalized force magnitudes are to be understood as a multiple of the maximum force upon heating. Figure 7.5e compares the normalized maximum forces ($\hat{F}_n$) of the four prototypes at the various applied strain levels plotted against the maximum temperature ($\hat{T}$). It is apparent that the normalization causes a sorting of the normalized maximum forces by the applied strain levels. Across prototypes, lower strain levels result in larger maximum normalized forces, whereas large applied strains cause lower maximum normalized forces. Under largest applied strains ($\varepsilon = 82\%$), prototype 3 does not generate any force upon cooling resulting in a maximum normalized force ($F_n = 0.87\,\mathrm{N\,N^{-1}}$) at $\hat{T} = 120\,^{\circ}\mathrm{C}$. Prototype 1, strained to ($\varepsilon = 16\%$) produces a maximum normalized force ($F_n = 1.08\,\mathrm{N\,N^{-1}}$) at $\hat{T} = 120\,^{\circ}\mathrm{C}$, with every other strain

level falling in between those to normalized forces. At ($\hat{T} = 200\,°\text{C}$), the ($\varepsilon = 16\%$) and the ($\varepsilon = 82\%$) strain levels remain the bounding strain levels with maximum normalized forces of ($F_n = 2.18\,\text{N}\,\text{N}^{-1}$) and ($F_n = 1.34\,\text{N}\,\text{N}^{-1}$), respectively. Prototype 4, which has been strained to ($\varepsilon = 15\%$) and heated to the largest maximum temperatures exhibits the same asymptotic behavior after normalization as in the original data. At $\hat{T} = 280\,°\text{C}$, the normalized force is ($F_n = 3.21\,\text{N}\,\text{N}^{-1}$). Figure 7.5f provides the same information as Figure 7.5e shifted from the starting point ($F_n = 1\,\text{N}\,\text{N}^{-1}$) to ($F_n = 0\,\text{N}\,\text{N}^{-1}$). This occurs as the maximum generated force upon cooling ($\Delta\hat{F}_c$) is defined as the difference between the maximum force ($\hat{F}$) and the force upon heating ($\hat{F}_h$). Upon normalization, the maximum normalized force is transformed to the values shown in Figure 7.5e and the maximum normalized force upon heating returns the value 1.

7.3.4 Manipulating generated force within applications

Repeated thermal cycling along the cooling path demonstrated a repeatable increase in force with cooling and decrease in force with heating. As shown in Fig. 7.6a, upon heating the SMA knitted actuator ($\varepsilon = 75\,\%$) from point 1 ($T = 20\,°\text{C}$) to point 2 ($T = 200\,°\text{C}$), force increased from 0.5 N to 5.0 N. This maximum force at point 2 was stable for the 10-minute hold. Upon cooling between point 2 ($T = 200\,°\text{C}$) and 3a ($T = 160\,°\text{C}$), force increased from 5.0 N to 8.2 N, an elevated force that was also stable for a 10-minute hold. Force returned to 5.0 N with a return to $T = 200\,°\text{C}$ (points 3a to 4), completing a clockwise thermo-mechanical path. Likewise, cooling from point 2 ($T = 200\,°\text{C}$) to point 3b ($T = 140\,°\text{C}$) produced a stable increase in force from 5.0 N to 9.3 N. Force returned to 5.0 N between points 3b and 4 when temperature was increased again to 200 °C. The clockwise thermo-mechanical cycle was continued ($2 \rightarrow 3 \rightarrow 4$) through points 3c and 3d, reaching maximum forces of 9.8 N and 9.7 N, respectively. The decline in maximum cooling force from the cycle that contained point 3c to the cycle that contained point 3d indicated that the maximum force increase upon cooling, 4.8 N, had been reached. By including the maximum force increase upon cooling within the operation, traditional blocked force achieved by heating only was nearly doubled. After thermomechanically cycling along the cooling path, temperature was decreased from $T = 200\,°\text{C}$ (point 4) to $T = 20\,°\text{C}$ (point 5) producing a decrease in force from 5.0 N to 0.5 N and completing a counterclockwise loop ($1 \rightarrow 2 \rightarrow 5$).

The experimental data depicted in Fig. 7.6a suggests new heat/cool operations

can enable novel SMA actuation strategies for complex applications. Fig 7.6b-c depict an example application that utilizes active cooling to leverage an enhanced blocked upon cooling. The example application is a wearable, lower body compression garment (CG) for astronauts made of SMA knitted actuators that requires customized stress-free material transformation temperatures (A_s, A_f, M_s, M_f) for tactile comfort (Fig. 7.6b). CGs are worn by astronauts during Earth reentry, landing, and egress to support the cardiovascular system upon reintroduction to gravitational forces. The CG is worn several hours before reentry is initiation, a time when compressive pressure is not needed. Maximum compressive pressure (i.e., 40-80 mmHg) is required during the landing sequence while the body experiences maximum downward gravitational forces. After egress, compression is needed several days to a week as the body readjust to the gravity environment.

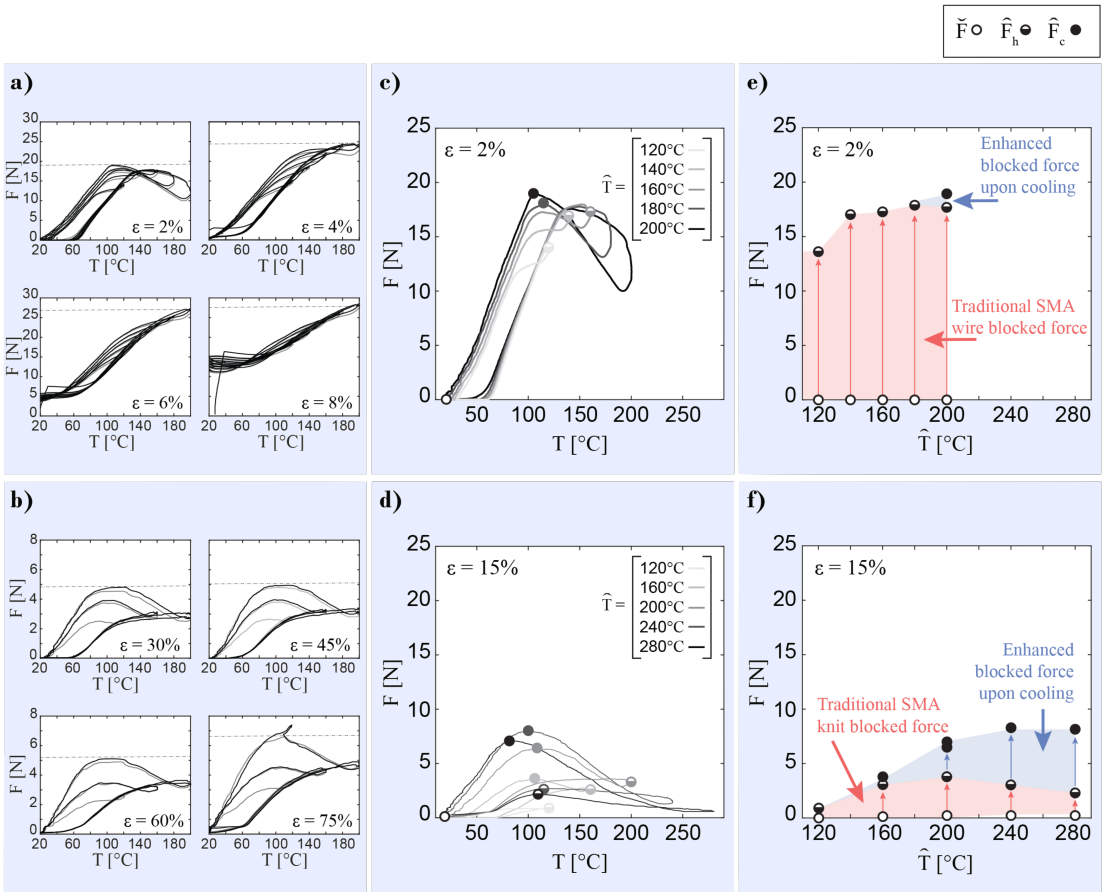

Figure 7.4: **Influence of Knit/Wire Geometry on Performance:** a) and b) display the set of wire and SMA knitted architecture force-control results of single respective prototypes. c) and d) show the highest performing structural strain levels of the wire ($\varepsilon = 2\%$) and knit prototype ($\varepsilon = 15\%$). e) and f) compare the generated force upon heating to the generated force upon cooling, which is significantly larger, relatively and absolutely, in SMA knitted architectures.

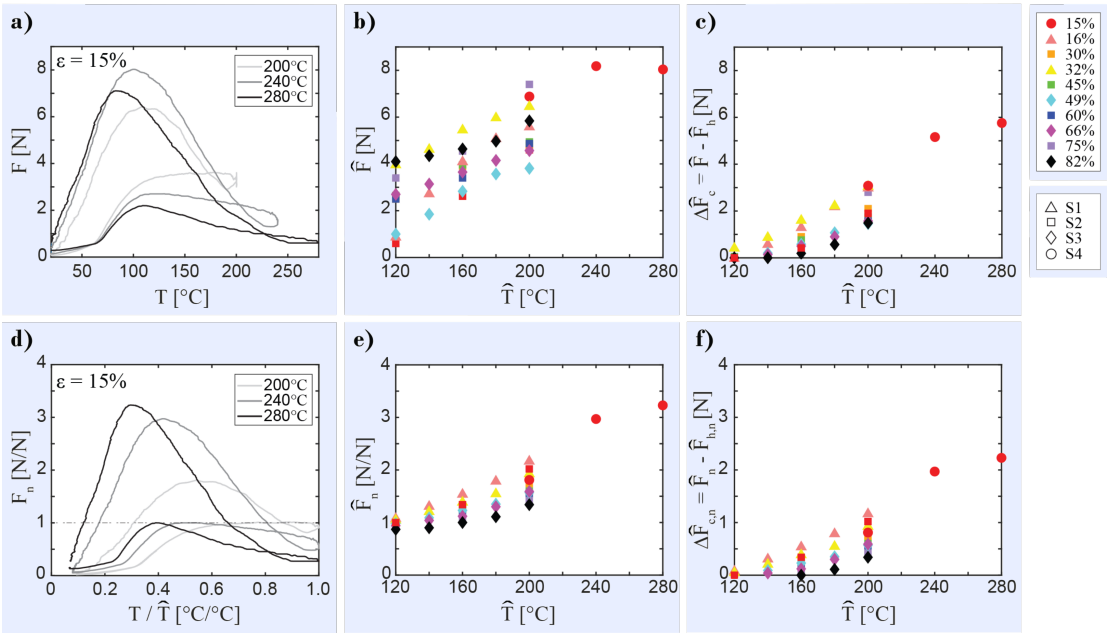

Figure 7.5: **Normalization Highlights Key Design Variables:** a) displays the temperature-force relationship of the high-temperature experiment at ($\varepsilon = 15\%$). b) and c) highlight the dependency of the generated force upon cooling and the maximum force of this prototype as functions of the maximum temperature. No clear trends of the applied strains can be detected in this representation. d) elucidates the normalization strategy based on division by the maximum force upon heating. e) and f) display the normalized generated force upon cooling and normalized maximum force. Normalization of the data results in a sorting that reveals the trends of larger generated forces upon cooling and maximum forces when strain levels are lowered.

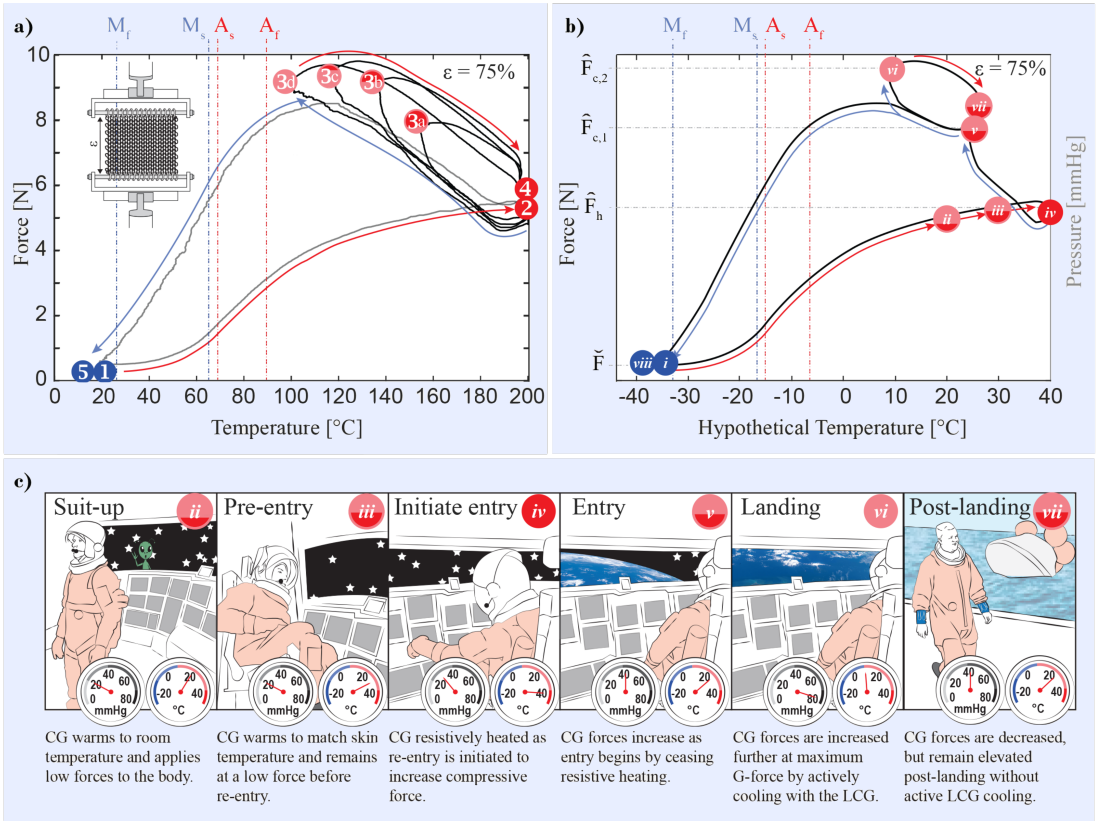

Figure 7.6: **Proposed application exploiting enhanced blocked force upon cooling by actively cooling during use:** a) Experimental data collected for an SMA knitted actuator. b) Proposed actuation operation for an application, mimicking the thermomechanical performance observed in experimental data. c) Proposed application, corresponding the actuation operation.

The proposed actuation operation for the astronaut CG application is depicted in Fig. 7.6b and applications-specific details are depicted in Fig. 7.6c. Here, the astronaut CG starts in a fully martensitic state in an industrial freezer (*i*, $T = -35\,^{\circ}\mathrm{C}$). As the astronaut begins to suit-up in preparation for Earth landing activities, the CG is removed from the freezer and pulled over the body, producing an actuator strain of 75 % (*ii*, $T = 20\,^{\circ}\mathrm{C}$). Heating the CG from $-35\,^{\circ}\mathrm{C}$ to $20\,^{\circ}\mathrm{C}$ produces an increase in force, which translates to an increase in compressive pressure on the body (*ii,* $P = 20\,\mathrm{mmHg}$). The CG is layered with additional garments, including a liquid cooling garment (LCG) that provides controllable cooling across the body, and a pressurized launch and entry suit, shown in orange in Fig. 7.6c. The crew wear all suit layers during a pre-entry phase that can last for 24-48 hours. During this time, the astronaut assumes a seated posture and the CG warms to match the body's skin temperature (*iii*, $P = 20\,\mathrm{mmHg}$, $T = 30\,^{\circ}\mathrm{C}$). Here, compressive pressure should be kept low to reduce physical discomfort while compression is not needed. Once Earth entry activities are initiated, the CG is momentarily heated to the maximum allowable touch temperature to initiate maximum CG compression (*iv*,$P = 35\,\mathrm{mmHg}$, $T = 40\,^{\circ}\mathrm{C}$). This maximum force upon heating ($\hat{F}_h$) is represented in Fig. 7.6b at point *iv*. Once heat input has ceased, CG forces increase as the garment cools back to match the body's skin temperature, producing a maximum force upon cooling, $\hat{F}_{c,1}$ (*v*, $P = 40\,\mathrm{mmHg}$, $T = 30\,^{\circ}\mathrm{C}$). This additional compressive pressure can be further increased during the landing sequence by increasing the active cooling provided by the LCG. Here, the LCG reduces the temperature of the CG to $10\,^{\circ}\mathrm{C}$, which produces a maximum force upon cooling ($\hat{F}_{c,2}$) and a maximum compressive pressure of 80 mmHg as the body is experiencing a spike in gravitational forces (*vi*,$P = 80\,\mathrm{mmHg}$, $T = 10\,^{\circ}\mathrm{C}$). Once the crew have successfully landed on Earth, the LCG is no longer in use and the astronaut may need compressive support several hours or days post-landing. As shown in Fig. 7.6b, upon removing the added cooling and settling back to $30\,^{\circ}\mathrm{C}$, which is approximately human skin temperature, the CG remains at an elevated force ($\hat{F}_{c,1}$).

Results of a SMA knitted actuator sleeve characterization, shown in Fig. 7.7, demonstrate the stability of repeated thermal cycling along the cooling path. When heated from $20\,^{\circ}\mathrm{C}$ (point 1) to $240\,^{\circ}\mathrm{C}$ (point 2), force increased from 0.1 N to 0.3 N, passing through a maximum heating force of 1.25 N. This maximum force was stable through the 10-minute temperature hold. Upon cooling from point 2 ($T = 240\,^{\circ}\mathrm{C}$) to point 3a

($T = 110\,°\text{C}$), force increased from 0.3 N to 2.5 N. The maximum force upon cooling was also stable throughout the 10-minute temperature hold. The force decreased back to 0.3 N upon a return to 240 °C (point 3a to 4). This clockwise thermo-mechanical cycle was repeated five additional times to observe repeatability. Cooling from T = 240 °C (point 4) back to T = 110 °C (point 3b) produced a force increase from 0.3 N to 2.8 N. The subsequent cycle, which passed through point 3c, produced a maximum cooling force of 2.9 N. The maximum force upon cooling continued to increase and reached 3.2 N by the sixth thermal cycle (point 3f). All six clockwise thermo-mechanical cycles started and ended with a force of 0.3 N at $T = 240\,°\text{C}$.

While the previous application demonstration depicts utilizing enhanced blocked force upon cooling through an active cooling method, other applications (Fig. 7.7b-c) can utilize active heating to 'program' a desired maximum force upon cooling ($\hat{F}_c$) before use. For simplicity, we provide another CG example composed of SMA knitted actuators for terrestrial medical use. As with the previous application, SMA materials used in this type of system require customized stress-free material transformation temperatures (A_s, A_f, M_s, M_f) for tactile comfort (Fig. 7.6b). Here, the required compressive pressure value is much lower (i.e., 0-35 mmHg) and the only requirement is that the initial force upon donning the CG be lower then the final force while wearing the CG. Medical compression garments are notoriously difficult to don, especially for elder populations with limited dexterity and strength.

The proposed actuation operation for the terrestrial medical CG application is depicted in Fig. 7.7b and applications-specific details are depicted in Fig. 7.7c. Here again, the CG begins martensitic in a freezer. In many settings, an industrial freezer may not be available and a fully martensitic phase may be achieved by applying pull forces to the garment while below the stress-free martensite start temperature (M_s) to reach martensite finish (*i*, $T = -18\,°\text{C}$). CG compressive pressures are 'programmed' by stretching the CG around a form so that garment strain is held at 15 % and placing the CG in the dryer. While some home dryers have explicit temperature-control, other dryers have garment settings that utilize different drying temperature (e.g., 'normal/cotton' = 135 °C, 'permanent press' = 125 °C, 'delicate/low-heat' = 110 °C). Here, the CG is initially programmed for a low-compression setting using a low-heat setting (*ii*, $T = 110\,°\text{C}$). Once heated to the target temperature, the garment is removed immediately from the dryer and pulled over the body while the garment is still warm.

As shown by the path *ii*→*iii* in Fig. 7.7b, the sooner the garment is pulled over the body, the lower the donning forces will be. The CG reaches maximum force upon cooling ($\hat{F}_{c,1}$) once the CG fully reaches equilibrium with skin temperature (*iii*, P = 20 mmHg,$T = 30\,^{\circ}$C). This maximum force is stable and the CG can be worn throughout the day. If more compressive pressure is required, the CG can be re-programmed by removing the garment from the body with a zipper-release, puling the garment back around the form to maintain a garment strain of 15 %, and placing the CG back in the dryer. To increase the compression class, a higher dryer temperature is utilized (*iv*,$T = 135\,^{\circ}$C). After the dryer cycle, the garment is again pulled quickly onto the body before it has cooled completely. Upon cooling to match the skin temperature, the CG reaches its new maximum force upon cooling ($\hat{F}_{c,2}$), which produces an increased compressive pressure (*v*,P = 35 mmHg, $T = 30\,^{\circ}$C). This elevated compression can be sustained indefinietly throughout wear. When the CG is no longer needed, the garment can be removed through a zipper-release and placed back in the freezer (*vi*).

7.4 Conclusion

While traditional SMA blocked force produced by heating is well understood and a commonly used actuation condition, we demonstrate that (1) actuator forces can also be generated after heating and upon cooling and (2) these added generated forces upon cooling can be manipulated and magnified by actuator geometry. This novel thermo-mechanical loading path can be used both to significantly increase the traditional blocked force, otherwise accomplished by heating SMA, and/or to produce a generated force upon cooling alone, which was shown in some cases to be of similar magnitude to a traditional generated force upon heating. Experimental data suggests that the governing material mechanism behind the effect is a superposition of thermal expansion/contraction and the SME in a Class I thermo-elastic transformation. We investigated the effect in SMA wire as well as SMA knitted actuators to illustrate that SMA knitted actuators are highly-suitable for this novel loading path due to their complex strain profile. Specifically, the SMA knitted actuator architecture was shown to produce a temperature-insensitive force plateau upon heating in addition to enhanced hysteresis between a fully austenite state and the onset of the reverse transition to martensite. This combination of characteristics produces an enlarged generated force

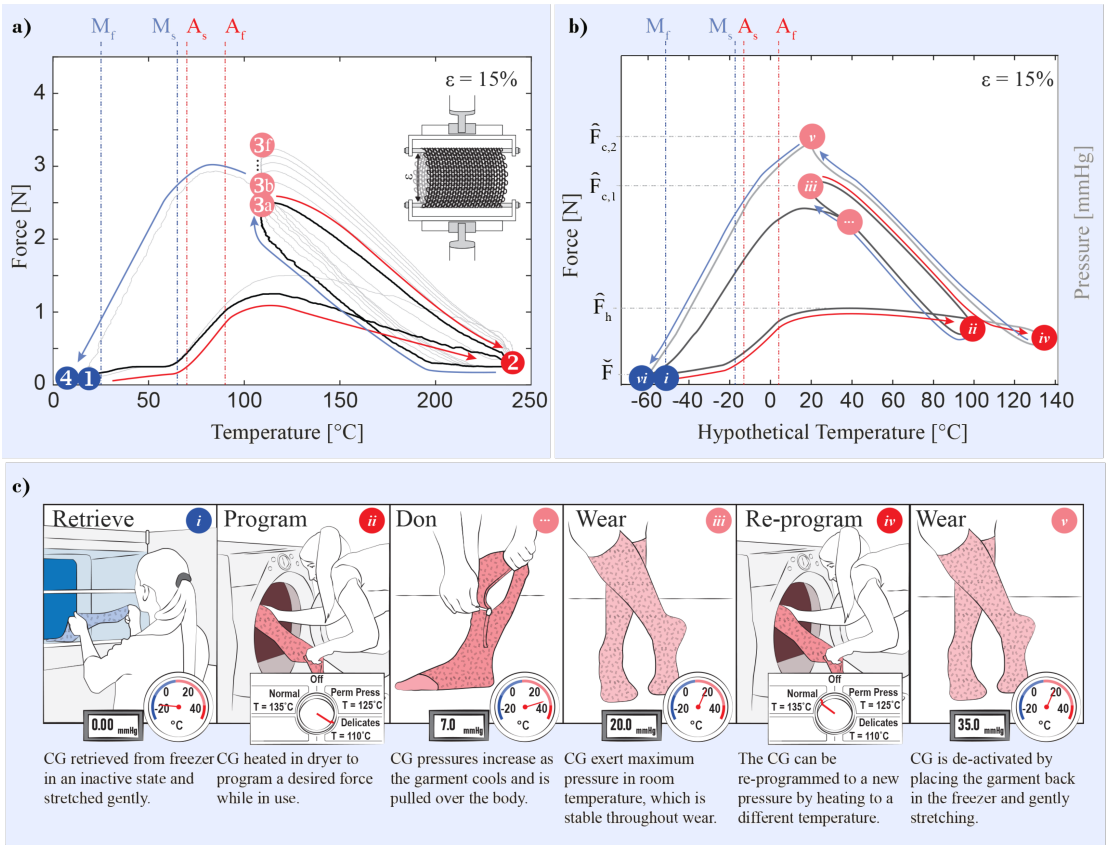

Figure 7.7: **Proposed application exploiting enhanced blocked force upon cooling by actively heating before use:** a) Experimental data collected for an SMA knitted actuator sleeve. b) Proposed actuation operation for an application, mimicking the thermomechanical performance observed in experimental data. c) Proposed application, corresponding the actuation operation.

upon cooling compared to SMA wire samples and this generated force is shown to be manipulated through applied structural strain and temperature.

Exploiting generated force upon heating through active cooling within SMA knitted actuators reexamines the way we think about using SMA in actuator applications. We present two novel actuation sequences that demonstrate (i) useful forces can be generated in applications with available active cooling and (ii) large forces can be 'programmed' by actively heating to a target temperature before use in a lower-temperature environment. Both applications utilize generated force upon cooling after heating to manipulate blocked force magnitudes without requiring continuous thermal loading. This

research inspires reconsideration of common SMA operation design points by introducing alternative heating/cooling regimes that enable generated forces at lower final temperatures as well as by introducing an exciting actuator geometry that exploits these novel effects.

Acknowledgements

R.G. and K.E. contributed equally. R.G., K.E., B.H., and J.A. developed the performance metrics in group discussion. R.G. and K.E. collaborated on developing the experimental procedure under the guidance of J.A., analyzed the experimental data collaboratively under the guidance of J.A. and B.H., except for the normalization procedure, which was developed by K.E. with feedback from R.G., B.H., and J.A.. R.G. led the motivating framework, led the development of thermo-mechanical load paths for use in wearable systems, and developed the specific applications (active heating and active cooling) using experimental load paths (found in Chapters 7.1 & 7.2.2 & 7.3.4) with feedback from K.E., B.H. and J.A.. K.E. led the description of SMA material effects in general, the derivation of contributing material effects to the generated force upon heating and cooling, and the normalization strategy for enhanced comparison of experimental data (found in Chapters 7.2.1 & 7.3.2 & 7.3.3) with feedback from R.G., B.H., and J.A.. J.A. and B.H. guided the direction, motivation, and methods for the work. This work was supported in part by a NASA Space Technology Research Fellowship (Grant #80NSSC17K0158), Minnesota's Discovery, Research, and InnoVation Economy Robotics, Sensors, and Advanced Manufacturing (MnDRIVE RSAM) Initiative, and the University of Minnesota Office of the Vice President for Research UMII MnDRIVE Graduate Assistantship. Thank you to Kirstyn Johnson from NASA Johnson Space Center's Crew Survival Lab as well as Amy Ross and Shane McFarland from the Advanced Spacesuit Lab for guidance on the astronaut compression garment concept and operation. Thank you for support from the University of Minnesota's Wearable Technology Lab, specifically Heidi Woelfe, for coordinating time on the Instron machine. The authors thank Othmane Benafan and Santo Padula II from NASA Glenn Research Center for discussions related to the SMA material effects that may contribute to the behaviors described in this publication.

Chapter 8

Conclusion

This chapter summarizes the contributions from the research findings on the multi-scale mechanics of shape memory alloy knitted architectures. The contribution section specifies the accomplishment of the research objectives defined in Section 1.5. Ideas for future research directions to further improve the understanding of these highly nonlinear architecture are also presented.

8.1 Contributions

This work provides an increased understanding of the multiscale mechanics of shape memory alloy knitted architectures through the derivation of design guidelines based on fundamental experimental findings, provides predictive capabilities through the development of an empirical and a high-fidelity model, and demonstrates the new design capabilities in medical/aerospace design applications. Chapters 2 and 3 describe the experimental derivation of guidelines for the design, operation and characterization of contractile SMA knitted architectures on the macro- and meso-scales. The specific major contributions of these chapters are the following:

- SMA knitted architectures were established as a technology with repeatable performance and design rules regarding low-cycle lifetime performance, functional dependence of actuation and relaxation temperature on the SMA knitted architecture geometry and external loading, and homogeneous/inhomogeneous knitted architecture design were defined.

- Performance variations based on the utilized operation- or characterization-strategy were discussed and the frictional effects that cause the variations were described.
- Knit-geometry based performance-predictive capabilities were provided through the translation of parallel and serial spring design methodologies to SMA knitted architectures.
- Loop-geometry based performance-predictive capabilities were provided through the definition and experimental verification of the knit index, a dimensionless geometric parameter derived from perfectly-elastic knit theory and Euler-Bernoulli beam theory considerations.

An additional layer of SMA knitted architecture mechanistic understanding and design capabilities was introduced in Chapter 4, which investigates the micro-scale mechanics of SMA knitted architectures. An in-situ strain- and temperature-control SMA knitted architecture x-ray diffraction experiment gave a first insight into the mirco-structural mechanics of SMA knitted architectures. The main contributions of this research were the following:

- The contractile SMA knitted architecture performance is primarily dependent on the recovery of bending deformations.
- The contact area is the highest stressed area and area that undergoes the largest phase transitions in the SMA knitted architecture with superposed bending and contact stresses.
- Phase transition temperatures are elevated to higher temperatures due to the presence of manufacturing stresses and applied loads as a function of the spatial position on the knitted loop.

The conclusions drawn from the experimental research have inspired and informed efforts to provide mathematical predictive tools. As a first step, an algebraic empirical model was formulated based on the large experimental data set as presented in Chapter 3. High-fidelity predictive capabilities for multifunctional textiles were provided through the implementation of a multifunctional textile modeling architecture based on finite beam element theory. The modeling architecture was verified for the contractile SMA

knitted architecture, which is detailed in Chapter 5. The specific contributions of the modeling efforts are the following:

- A quick and simple-to-use empirical model was implemented to predict the SMA knitted actuator performance of Dynalloy Flexinol® contractile SMA knitted architectures from the inputs filament diameter and knit index.
- A finite beam element modeling architecture was implemented in Matlab with multifunctional textile-specific tools. The specific tools include a manufacturing model, SMA material models, and contact models.
- The contractile SMA knitted architecture model was verified against experimental data on the micro- and macroscale.

The experimentally-derived guidelines and predictive tools have enabled the design of meaningful applications with contractile SMA knitted architectures. A contractile topographically self-fitting SMA knitted sleeve was designed with utility for health monitoring and haptic feedback application, and as a precursor for compression applications. Additionally, operation strategies that magnify the generated force and provide a temperature-insensitive force-plateau by exploiting the knitted loop geometry have been developed. Chapters 6 and 7 describe the design of the self-fitting SMA knitted actuator sleeve and discuss novel operational design procedures that can lead to increased blocked force performance in SMA knitted architectures. The major contributions are summarized in the following:

- On-body operational strategies for SMA knitted architectures that utilize body heat to accomplish contractile topographical fitting and pressure-generation were developed.
- Two functional SMA knitted architecture self-fitting prototypes were designed, manufactured, and verified with novel optical and resistive fit evaluation techniques.
- New SMA knitted architecture operational procedures were developed to increase the generated force through subsequent heating and cooling by exploiting the variable strain profile of knitted architectures.

- Active heating and active cooling applications were identified utilizing the novel generated force operation.

8.2 Future Work

The findings of this thesis research can be translated to expand the breadth of knowledge of multifunctional textiles composed of different materials or textile structures, and to provide deeper insight into the contractile SMA knitted architecture. The depth of understanding gathered for the contractile SMA knitted architecture is currently unmatched by other multifunctional textile implementations: Methods, design guidelines, and modeling tools developed throughout this research can therefore be applied as a starting point to the research of various other multifunctional textile architectures of differing active filaments or knit patterns. Some specific recommendations for future work are laid out for the scales on which contractile SMA knitted architectures have been studied in this work.

Microscale - High-energy diffraction experiments: While design parameters that can be controlled on the macro- and meso-scales are now well-understood, design options on the micro-scale of the contractile SMA knitted architecture have not yet been fully-understood and exploited. The x-ray diffraction study detailed in Chapter 4 has scratched the surface of possibilities by providing details on the predominant deformation modes and phase fraction distributions. Higher energy beams can be produced by different x-ray sources, neutron diffraction experiments, or synchrotron experiments and can lead to improvements of the penetration depth, angular resolution, and reduce the relative noise levels. The collection of experimental diffraction data of improved quality would enable the use of Rietveld refinement to characterize the micro-structure of the SMA knitted architecture prototype and resolve strains, stresses, plasticity, and details on the martensitic grains. Further development of the experimental setup could enable the rotation of the prototype and reveal interesting details on preferential orientation of grains within the knitted architecture. Understanding the micro-mechanical context and the factors that reduce and increase the macroscopic performance can lead to a variety of SMA knitted architecture optimization strategies. Theoretical ideas for such strategies are geometric optimization, manufacturing strategy optimizations, global and localized annealing of the knitted architecture, and material chemistry optimizations to

tailor the thermo-mechanical hysteresis.

Micro-/Mesoscale - Equivalent SMA material stress-strain state: At the intersection of textile geometric modeling and nonlinear material modeling, the development of SMA textile models presents challenges that quickly increase the complexity to undesirable levels. Many textile geometries have been modeled for passive architectures and reduced material states that consider 1D stress-strain states or operate with equivalent stress definitions. Due to the complexity of the SMA material, e.g., the variation of the phase transitions stresses for compression, tension, bending, and torsion, such reductions are commonly inappropriate and lead to inaccurate predictions of the material behavior. A formulation that reduces the 3D stress-strain state to a single equivalent stress value compatible with existing analytical textile models and 1D material models while considering the variation of material properties by the underlying loading conditions would significantly improve the ability to build upon the existing understanding of textile architectures. Such a formulation could be conducted in the stress-strain domain or be translated into the energy-domain.

Meso-/Macroscale - Manufacturing Model: The manufacturing model utilized in the finite element multifunctional textile modeling tool is based on a differential geometry analysis of the post-manufacturing geometry, which presents a significant simplification of the complex deformation- and load-path inflicted on the SMA filament in the manufacturing process. Firstly, the differential geometry analysis neglects normal strains entirely as it only detects bending (deviation from straight geometry) and torsional (deviation from planar geometry) strains. Additionally, the differential geometry approach neglects the loading path of the manufacturing process without considering where loads and deformations were applied. A flatbed knitting machine knit manufacturing model could be based on a three-point bending flexural analysis of straight SMA filament with a cantilevered and a tensioned end while varying the distances of the bending points (needle spacing, d_n) and the centrally-applied deformation (needle motion, δ_n). Figure 8.1a displays the manufacturing process in 3D, while Figure 8.1b shows a potential manufacturing model setup in 2D.

Application Scale - Comfort Improvements: The current contractile SMA knitted architecture consists of single filament SMA wire of approximately similar diameters as commercially available yarns. However, traditional textile yarns are made of hundreds or thousands of individual filaments and have significantly lower stiffness

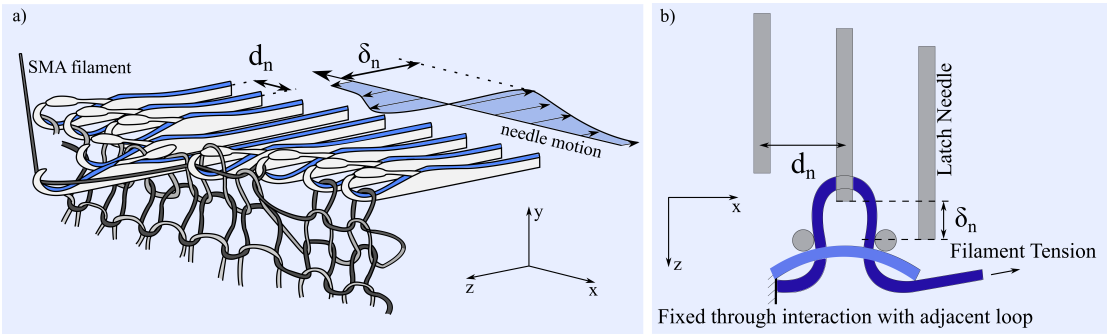

Figure 8.1: **Sketch of Potential Manufacturing Model Approach:** A three-point bending flexural analysis of SMA filament could be a potential approach to gain insight into manufacturing strains and stresses.

which contributes to the comfortable haptic experience in wearables. The development of SMA yarns or combinations of SMA and traditional yarns in a textile will significantly improve the haptic experience of contractile SMA knitted architectures in wearable applications.

8.3 Closing

While SMA knitted textiles were highlighted as intriguing multifunctional fabrics previously, they were not yet understood well enough to reliably utilize them in applications. The geometric and material design parameters on the macro-, meso-, and microscale were have not yet been conclusively related to the thermo-mechanical performance, significantly limiting the ability to predict and optimize the force-extension behavior.

In this dissertation, the multiscale mechanics of SMA knitted architectures were researched to propel the textile to a technology that can be implemented in applications. The knowledge that was generated in this work has produced design guidelines for the SMA knitted architecture specifically, and serves as a foundation for the experimental and numerical exploration of other multifunctional textile architecture and material combinations.

References

[1] J. E. Huber, N. A. Fleck, and M. F. Ashby. The Selection of Mechanical Actuators Based on Performance Indices. *Proceedings: Mathematical, Physical and Engineering Sciences*, 453(1965):2185–2205, 1997.

[2] E. M. Lauridsen, S. Schmidt, R. M. Suter, and H. F. Poulsen. Tracking: a method for structural characterization of grains in powders or polycrystals. *Journal of Applied Crystallography*, 34(6):744–750, December 2001.

[3] Ashwin Rao. *Design of shape memory alloy (SMA) actuators*. SpringerBriefs in applied sciences and technology. Computational mechanics. Springer, Cham, 2015.

[4] Kevin Eschen and Julianna Abel. Effect of Geometric Design Parameters on Contractile SMA Knitted Actuator Performance. *Proceedings of the ASME 2017 Conference on Smart Materials, Adaptive Structures and Intelligent Systems*, page V002T04A018, September 2017.

[5] Kevin Eschen, Javier Garcia-Barriocanal, and Julianna Abel. In-situ strain- and temperature-control X-ray micro-diffraction analysis of nickel–titanium knitted architectures. *Materialia*, 11:100684, June 2020.

[6] Julianna Abel, Jonathan Luntz, and Diann Brei. Hierarchical architecture of active knits. *Smart Materials and Structures*, 22(12):125001, 2013.

[7] Mary Mccabe, Elliott Potter, Cory Simon, Elliott Potter, and Clint Baggerman. Smart Fabrics Technology Development, 2010.

[8] D. L. Munden. The Geometry and Dimensional Properties of Plain-Knit Fabrics. *Journal of the Textile Institute Transactions*, 50(7):T448–T471, July 1959.

[9] J. A. Smirfitt. 24—Worsted 1 x 1 Rib Fabrics Part Ii. Some Physical Properties. *Journal of the Textile Institute Transactions*, 56(6):T298–T313, June 1965.

[10] E.R. Post and M. Orth. Smart fabric, or "wearable clothing". In *Digest of Papers. First International Symposium on Wearable Computers*, pages 167–168, October 1997. ISSN: null.

[11] E. R. Post, M. Orth, P. R. Russo, and N. Gershenfeld. E-broidery: Design and fabrication of textile-based computing. *IBM Systems Journal*, 39(3.4):840–860, 2000. Conference Name: IBM Systems Journal.

[12] Yan Liu, Aggie Chung, JinLian Hu, and Jing Lv. Shape memory behavior of SMPU knitted fabric. *Journal of Zhejiang University-SCIENCE A*, 8(5):830–834, April 2007.

[13] Javad Foroughi, Geoffrey M. Spinks, Shazed Aziz, Azadeh Mirabedini, Ali Jeiranikhameneh, Gordon G. Wallace, Mikhail E. Kozlov, and Ray H. Baughman. Knitted Carbon-Nanotube-Sheath/Spandex-Core Elastomeric Yarns for Artificial Muscles and Strain Sensing. *ACS Nano*, 2016.

[14] E. Lemaire, C. J. Borsa, and D. Briand. Green piezoelectric for autonomous smart textile. *Journal of Physics: Conference Series*, 660(1):012082, 2015.

[15] Ali Maziz, Alexandre Concas, Alexandre Khaldi, Jonas Stålhand, Nils-Krister Persson, and Edwin Jager. Knitting and weaving artificial muscles. *Science Advances*, 3(1), 2017.

[16] Ayman F. Abouraddy, Ofer Shapira, Mehmet Bayindir, Jerimy Arnold, John D. Joannopoulos, and Yoel Fink. Fabrics that. *Optics and Photonics News*, 17(12):21–21, December 2006.

[17] Wanasinghe Arachchige Dumith Madushanka Jayathilaka, Kun Qi, Yanli Qin, Amutha Chinnappan, William Serrano-García, Chinnappan Baskar, Hongbo Wang, Jianxin He, Shizhong Cui, Sylvia W. Thomas, and Seeram Ramakrishna. Significance of Nanomaterials in Wearables: A Review on Wearable Actuators and Sensors. *Advanced Materials*, 31(7):1805921, 2019.

[18] BCC Research. Wearable Computing: Technologies, Applications and Global Markets (IFT107C), 2018.

[19] BCC Research. Medical Wearables: Beyond FitBit (HLC240A), 2019.

[20] Rachael Granberry, Julianna Abel, and Bradley Holschuh. Active Knit Compression Stockings for the Treatment of Orthostatic Hypotension. *SIGCHI Symposium on Wearable Computers*, September 2017.

[21] Omid Dehzangi, Omar Iftikhar, Bhavani Anantapur Bache, Jeffrey Wensman, and Ying Li. Force and activity monitoring system for scoliosis patients wearing back braces. In *2018 IEEE International Conference on Consumer Electronics (ICCE)*, pages 1–4, January 2018. ISSN: 2158-4001.

[22] Rachael Granberry, Kevin Eschen, Brad Holschuh, and Julianna Abel. Functionally Graded Knitted Actuators with NiTi-Based Shape Memory Alloys for Topographically Self-Fitting Wearables. *Advanced Materials Technologies*, 0(0):1900548.

[23] Shaowei Lu, Shuai Wang, Gongdong Wang, Junchi Ma, Xiaoqiang Wang, Hailong Tang, and Xiangdong Yang. Wearable graphene film strain sensors encapsulated with nylon fabric for human motion monitoring. *Sensors and Actuators A: Physical*, 295:200–209, August 2019.

[24] Samriddhi Mathur Narayanan, Bhandare Rupika, and Priyanka Nair Geetha. Smart Air Mattress: A Prevention to Pressure Ulcers | Our Heritage. Library Catalog: archives.ourheritagejournal.com.

[25] E. Hornbogen. Shape memory alloys: New materials for future engineering. July 1988.

[26] Stephen V. DellaCorte Pepper. Nitinol 60 as a Material For Spacecraft Triboelements. Vienna, Austria, September 2009.

[27] Henry Koon, Julianna Abel, Jeremy Schaeffer, and Santo Padula II. Design of knitted superelastic tire treads for next generation non-pneumatic rover tires. *Conference Proceedings from International Conference on Shape Memory and Superelastic Technologies*, pages 238–239, 2019.

[28] Daniel T. Grant, Mujahid Abdulrahim, and Rick Lind. Flight Dynamics of a Morphing Aircraft Utilizing Independent Multiple-Joint Wing Sweep. *International Journal of Micro Air Vehicles*, 2(2):91–106, June 2010. Publisher: SAGE Publications Ltd STM.

[29] Natasha R. Jones, Jeremy P. Eastwood, and Jerome P. Jarrett. Adapting Three-Dimensional Shock Control Bumps for Swept Flows. *AIAA Journal*, 55(3):861–873, 2017. Publisher: American Institute of Aeronautics and Astronautics _eprint: https://doi.org/10.2514/1.J055169.

[30] S. Jacobs, C. Coconnier, D. DiMaio, F. Scarpa, M. Toso, and J. Martinez. Deployable auxetic shape memory alloy cellular antenna demonstrator: design, manufacturing and modal testing. *Smart Materials and Structures*, 21(7):075013, June 2012. Publisher: IOP Publishing.

[31] Allen T. Benafan Guzik. Design and Development of CubeSat Solar Array Deployment Mechanisms Using Shape Memory Alloys. Technical report, June 2018.

[32] Daniel D. Shin, Kotekar P. Mohanchandra, and Gregory P. Carman. High frequency actuation of thin film NiTi. *Sensors and Actuators A: Physical*, 111(2):166–171, March 2004.

[33] K. Otsuka, T. Sawamura, and K. Shimizu. Crystal structure and internal defects of equiatomic TiNi martensite. *physica status solidi (a)*, 5(2):457–470, 1971.

[34] A. S. Sastri, M. J. Marcinkowski, and D. Koskimaki. Nature of the NiTi martensite transformation. *physica status solidi (b)*, 25(2):K67–K69, 1968.

[35] John A. Shaw and Stelios Kyriakides. Thermomechanical aspects of NiTi. *Journal of the Mechanics and Physics of Solids*, 43(8):1243–1281, August 1995.

[36] Brent Utter, Jonathan Luntz, Diann Brei, Daniel Teitelbaum, Manabu Okawada, and Eiichi Miyasaka. Design and operation of a fully implantable SMA actuated implant for correcting short bowel syndrome. In Mehdi Ahmadian and Mehrdad N. Ghasemi-Nejhad, editors, *Active and Passive Smart Structures and Integrated Systems 2009*, volume 7288, pages 480 – 492. International Society for Optics and Photonics, SPIE, 2009.

[37] *Vacuum Gripper System Based on Bistable SMA Actuation*, volume Volume 1: Development and Characterization of Multifunctional Materials; Modeling, Simulation, and Control of Adaptive Systems; Integrated System Design and Implementation of *Smart Materials, Adaptive Structures and Intelligent Systems*, 09 2018, https://asmedigitalcollection.asme.org/SMASIS/proceedings-pdf/SMASIS2018/51944/V001T04A014/2568266/v001t04a014-smasis2018-7980.pdf. V001T04A014.

[38] A. Emiliavaca, C. J. de Araújo, C. R. Souto, and A. Ries. Characterization of shape memory alloy micro-springs for application in morphing wings. *Smart Materials and Structures*, 28(1):015010, November 2018. Publisher: IOP Publishing.

[39] Alexander Czechowicz, Sven Langbein, and Jan Pollmann. Benefits of standardization illustrated by shape memory actuators in industrial applications. In *Innovative Small Drives and Micro-Motor Systems; 9. GMM/ETG Symposium*, pages 1–6, September 2013.

[40] T. P. Chenal, J. C. Case, J. Paik, and R. K. Kramer. Variable stiffness fabrics with embedded shape memory materials for wearable applications. In *2014 IEEE/RSJ International Conference on Intelligent Robots and Systems*, pages 2827–2831, September 2014.

[41] Bradley T. Holschuh and Dava J. Newman. Morphing Compression Garments for Space Medicine and Extravehicular Activity Using Active Materials. *Aerospace Medicine and Human Performance*, 87(2):84–92, February 2016.

[42] K. J. De Laurentis, A. Fisch, J. Nikitczuk, and C. Mavroidis. Optimal design of shape memory alloy wire bundle actuators. In *Proceedings 2002 IEEE International Conference on Robotics and Automation (Cat. No.02CH37292)*, volume 3, May 2002.

[43] Brad Holschuh and Dava Newman. Low spring index, large displacement Shape Memory Alloy (SMA) coil actuators for use in macro- and micro-systems. *Proc. SPIE MOEMS-MEMS*, 8975:897505–897505–11, 2014.

[44] Benjamin Reedlunn and John A. Shaw. Shape Memory Alloy Cables. *Proc. SPIE 6929, Behavior and Mechanics of Multifunctional and Composite Materials 2008*, 6929:69291G–69291G–11, 2008.

[45] Isabel Czarnocki, Wonhee Kim, Brent Utter, Jonathan Luntz, Diann Brei, and Paul Alexander. Design of SMA Helical Actuators: An Experimental Study. *Proc. ASME 2013 Conference on Smart Materials, Adaptive Structures and Intelligent Systems*, page V001T04A017, 2013.

[46] Daniel B. Biggs and John A. Shaw. Experimental characterization of shape memory alloy actuator cables. *Proc. SPIE 9800, Behavior and Mechanics of Multifunctional Materials and Composites 2016; 98000D (2016)*, pages 98000D–98000D–12, 2016.

[47] K. H. Eckelmeyer. The effect of alloying on the shape memory phenomenon in nitinol. *Scripta Metallurgica*, 10:667–672, August 1976.

[48] O. Benafan, R. D. Noebe, T. J. Halsmer, S. A. Padula, G. S. Bigelow, D. J. Gaydosh, and A. Garg. Constant-Strain Thermal Cycling of a Ni50.3Ti29.7Hf20 High-Temperature Shape Memory Alloy. *Shape Memory and Superelasticity*, 2(2):218–227, June 2016.

[49] P. Šittner, D. Vokoun, G. N. Dayananda, and R. Stalmans. Recovery stress generation in shape memory Ti50Ni45Cu5 thin wires. *Materials Science and Engineering: A*, 286(2):298–311, July 2000.

[50] O. Benafan, S. A. Padula, R. D. Noebe, D. W. Brown, B. Clausen, and R. Vaidyanathan. An in situ neutron diffraction study of shape setting shape memory NiTi. *Acta Materialia*, 61(10):3585–3599, 2013.

[51] O. Benafan, R. D. Noebe, T. J. Halsmer, S. A. Padula, G. S. Bigelow, D. J. Gaydosh, and A. Garg. Constant-Strain Thermal Cycling of a Ni50.3Ti29.7Hf20 High-Temperature Shape Memory Alloy. *Shape Memory and Superelasticity*, 2(2):218–227, 2016.

[52] H. C. Tong and C. M. Wayman. Some stress-temperature-energy relationships for thermoelastic martensitic transformations. *Scripta Metallurgica*, 8(2):93–100, 1974.

[53] H. Tas, L. Delaey, and A. Deruyttere. Stress-induced transformations and the shape-memory effect. *Journal of the Less Common Metals*, 28(1):141–151, July 1972.

[54] R. Stalmans, J. Van Humbeeck, and L. Delaey. Effects of Training on the Shape Memory Behaviour of Cu-Zn-Al Alloys, 1992.

[55] Takashi Fukuda, Akiyocji Deguchi, Tomoyuki Kakeshita, and Toshio Saburi. Stress Induced R - B2 Transformation and Pseudoelasticity Associated with Twinning in a Ni-Ti Alloy Including Aligned Particles of Ti3Ni4. *Marterials Transactions*, 38(12):1057–1062, 1997.

[56] S. A. Padula, D. Gaydosh, A. Saleeb, and B. Dhakal. Transients and Evolution in NiTi. *Experimental Mechanics*, 54(5):709–715, June 2014.

[57] O. Benafan, R. D. Noebe, S. A. Padula, A. Garg, B. Clausen, S. Vogel, and R. Vaidyanathan. Temperature dependent deformation of the B2 austenite phase of a NiTi shape memory alloy. *International Journal of Plasticity*, 51(Supplement C):103–121, December 2013.

[58] M. A. Iadicola and J. A. Shaw. An experimental method to measure initiation events during unstable stress-induced martensitic transformation in a shape memory alloy wire. *Smart Materials and Structures*, 16(1):S155, 2007.

[59] Julianna Abel, Poorna Mane, Benjamin Pascoe, Jonathan Luntz, and Diann Brei. Experimental investigation of active rib stitch knitted architecture for flow control applications. In *Proc. SPIE 7643, Active and Passive Smart Structures and Integrated Systems 2010, 76430H (April 09, 2010); doi:10.1117/12.847699*, volume 7643. SPIE, April 2010.

[60] Min-Woo Han and Sung-Hoon Ahn. Blooming Knit Flowers: Loop-Linked Soft Morphing Structures for Soft Robotics. *Advanced Materials*, 29(13):1606580, April 2017.

[61] Hui Zhang, Xiaoming Tao, Shanyuan Wang, and Tongxi Yu. Electro-Mechanical Properties of Knitted Fabric Made From Conductive Multi-Filament Yarn Under Unidirectional Extension. *Textile Research Journal*, 75(8):598–606, August 2005.

[62] T. S. Nutting and G. A. V. Leaf. Generalized Geometry of Weft-Knitted Fabrics. *Journal of the Textile Institute Transactions*, 55(1):T45–T53, January 1964. Publisher: Taylor & Francis _eprint: https://doi.org/10.1080/19447026408660207.

[63] Kentaro Kawasaki and Takayuki Ono. Stretch Properties of Weft Knitted Fabrics. *Journal of the Textile Machinery Society of Japan*, 14(3-4):122–127, 1968.

[64] Julianna Abel, Jonathan Luntz, and Diann Brei. A two-dimensional analytical model and experimental validation of garter stitch knitted shape memory alloy actuator architecture. *Smart Materials and Structures*, 21(8):085011, 2012.

[65] G. A. V. Leaf. A property of a buckled elastic rod. *British Journal of Applied Physics*, 9(2):71, 1958.

[66] Santo Padula. Utilizing Shape Memory Alloys for Novel, Non-Pneumatic Tire Design - Designing for the Best of Both Worlds, April 2019.

[67] Henry Koon, Julianna Abel, Jeremy E. Schaffer, and Santo Padula. Design of knitted superelastic tire treads for next generation non-pneumatic rover tires. In *ASM International - International Conference on Shape Memory and Superelastic Technologies, SMST 2019*, ASM International - International Conference on Shape Memory and Superelastic Technologies, SMST 2019, pages 238–239, United States, January 2019. ASM International. International Conference on Shape Memory and Superelastic Technologies 2019, SMST 2019 ; Conference date: 13-05-2019 Through 17-05-2019.

[68] Kevin Eschen, Rachael Granberry, Brad Holschuh, and Julianna Abel. Active-contracting variable-stiffness fabrics
for self-fitting wearables. *Proceedings of the ASME 2018 Conference on Smart Materials, Adaptive Structures and Intelligent Systems*, 2018.

[69] Bradley T Holschuh and Dava J Newman. Morphing Compression Garments for Space Medicine and Extravehicular Activity Using Active Materials. *Aerosp. Med. Hum. Perform.*, 87(2):84–92, 2016.

[70] C.b. Churchill, J.a. Shaw, and M.a. Iadicola. Tips and Tricks for Characterizing Shape Memory Alloy Wire: Part 2—Fundamental Isothermal Responses. *Experimental Techniques*, 33(1):51–62, January 2009.

[71] A. Kiourti and J. L. Volakis. High-Geometrical-Accuracy Embroidery Process for Textile Antennas With Fine Details. *IEEE Antennas and Wireless Propagation Letters*, 14:1474–1477, 2015.

[72] Julianna Abel, Jonathan Luntz, and Diann Brei. A Two-Dimensional Analytical Model and Experimental Validation of Garter Stitch Knitted Shape Memory Alloy Actuator Architecture. *Smart Materials and Structures*, 21(8):085011, 2012.

[73] Shiping Yi, Charles Weinberg, Kevin Eschen, and Julianna Abel. Preliminary Experimental Study of the Effect of Shape Setting on Knitted SMA Structures. *Proceedings of the ASME 2017 Conference on Smart Materials, Adaptive Structures and Intelligent Systems*, page V001T02A011, September 2017.

[74] Kevin Eschen and Julianna Abel. Performance and prediction of large deformation contractile shape memory alloy knitted actuators. *Smart Materials and Structures*, 2018.

[75] J. A. Shaw, C. B. Churchill, and M. A. Iadicola. Tips and Tricks for Characterizing Shape Memory Alloy Wire: Part 1—Differential Scanning Calorimetry and Basic Phenomena. *Experimental Techniques*, 32(5):55–62, 2008.

[76] M. J. O'Neill. Measurement of Specific Heat Functions by Differential Scanning Calorimetry. *Analytical Chemistry*, 38(10):1331–1336, September 1966.

[77] O. Benafan, J. Brown, F. T. Calkins, P. Kumar, A. P. Stebner, T. L. Turner, R. Vaidyanathan, J. Webster, and M. L. Young. Shape memory alloy actuator design: CASMART collaborative best practices and case studies. *International Journal of Mechanics and Materials in Design*, 10(1):1–42, March 2014.

[78] H. J. Pfaeffle, Dimitris C. Lagoudas, Iradj G. Tadjbakhsh, and Kevin C. Craig. Design of flexible rods with embedded SMA actuators. *Proceedings of SPIE*, 1917(1):762–773, 1993.

[79] Glen S. Bigelow, Santo A. Padula, Anita Garg, Darrell Gaydosh, and Ronald D. Noebe. Characterization of Ternary NiTiPd High-Temperature Shape-Memory Alloys under Load-Biased Thermal Cycling. *Metallurgical and Materials Transactions A*, 41(12):3065–3079, December 2010.

[80] G. S. Bigelow, A. Garg, S. A. Padula, D. J. Gaydosh, and R. D. Noebe. Load-biased shape-memory and superelastic properties of a precipitation strengthened high-temperature Ni50.3ti29.7hf20 alloy. *Scripta Materialia*, 64(8):725–728, April 2011.

[81] Helen Sun, Anupam Pathak, Jonathan Luntz, Diann Brei, Paul W. Alexander, and Nancy L. Johnson. Stabilizing Shape Memory Alloy Actuator Performance through Cyclic Shakedown: An Empirical Study. volume 6930, pages 69300Q–69300Q–11, 2008. bibtex: sun_stabilizing_2008-1 bibtex[editora=Davis, L. Porter and Henderson, Benjamin K. and McMickell, M. Brett;editoratype=collaborator].

[82] Christopher B. Churchill and John A. Shaw. Shakedown Response of Conditioned Shape Memory Alloy Wire. *Proc. SPIE 6929, Behavior and Mechanics of Multifunctional and Composite Materials 2008; 69291F (2008)*, pages 69291F–69291F–12, 2008. bibtex: churchill_shakedown_2008-1.

[83] H. R. Sanjari, D. Semnani, and M. Sheikhzadeh. Investigating the Performance of Various Relaxation Processes on the Surface Regularity and Dimensional Properties of Plain Knitted Fabrics Using the Image Processing Technique. *Fibres & Textiles in Eastern Europe*, Nr 2 (85):36–42, 2011.

[84] J Uchil, K. K Mahesh, and K. Ganesh Kumara. Electrical resistivity and strain recovery studies on the effect of thermal cycling under constant stress on R-phase in NiTi shape memory alloy. *Physica B: Condensed Matter*, 324(1):419–428, November 2002.

[85] F04 Committee. Test Method for Determination of Transformation Temperature of Nickel-Titanium Shape Memory Alloys by Bend and Free Recovery. Technical report, ASTM International.

[86] Cees Bil, Kevin Massey, and Ermira J Abdullah. Wing morphing control with shape memory alloy actuators. *Journal of Intelligent Material Systems and Structures*, 24(7):879–898, May 2013.

[87] Geoffrey Mcknight, Robert Doty, Andrew Keefe, Guillermo Herrera, and Chris Henry. Segmented Reinforcement Variable Stiffness Materials for Reconfigurable

Surfaces. *Journal of Intelligent Material Systems and Structures*, 21(17):1783–1793, November 2010.

[88] Akira Todoroki, Keisuke Kumagai, and Ryosuke Matsuzaki. Self-deployable Space Structure using Partially Flexible CFRP with SMA Wires. *Journal of Intelligent Material Systems and Structures*, 20(12):1415–1424, August 2009.

[89] A. Y. N. Sofla, D. M. Elzey, and H. N. G. Wadley. A rotational joint for shape morphing space truss structures. *Smart Materials and Structures*, 16(4):1277, 2007.

[90] Gang Li, Yi Li, Ping Lan, Xiaowen He, and Hong Hu. Polydioxanone weft-knitted intestinal stents: fabrication and mechanics optimization. *Textile Research Journal*, 83(20):2129–2141, December 2013.

[91] Mark Ransley, Peter Smitham, and Mark Miodownik. Active chainmail fabrics for soft robotic applications. *Smart Materials and Structures*, 26(8):08LT02, 2017.

[92] M. Yuen, A. Cherian, J. C. Case, J. Seipel, and R. K. Kramer. Conformable actuation and sensing with robotic fabric. In *2014 IEEE/RSJ International Conference on Intelligent Robots and Systems*, pages 580–586, September 2014.

[93] Hochung Ryu, Sangki Park, Jong-Jin Park, and Jihyun Bae. A knitted glove sensing system with compression strain for finger movements. *Smart Materials and Structures*, 27(5):055016, 2018.

[94] Hasan Shahariar, Henry Soewardiman, Clifford A. Muchler, Jacob J. Adams, and Jesse S. Jur. Porous textile antenna designs for improved wearability. *Smart Materials and Structures*, 27(4):045008, 2018.

[95] Y. K. Kim, H. Wang, and M. S. Mahmud. *Wearable body sensor network for health care applications*. Elsevier Ltd, 2016.

[96] K.F. Choi and T.Y. Lo. An Energy Model of Plain Knitted Fabric. *Textile Research Journal*, 73(8):739–748, August 2003.

[97] Dani Liu, Daniel Christe, Bahareh Shakibajahromi, Chelsea Knittel, Nestor Castaneda, David Breen, Genevieve Dion, and Antonios Kontsos. On the role of

material architecture in the mechanical behavior of knitted textiles. *International Journal of Solids and Structures*, 109:101–111, March 2017.

[98] Ernest Tompkins. *The Science of Knitting*. Wiley, 1914.

[99] J. A. Smirfitt. 19—Worsted 1 x 1 Rib Fabrics Part I. Dimensional Properties. *Journal of the Textile Institute Transactions*, 56(5):T248–T259, May 1965.

[100] Arif Kurbak. Geometrical and mechanical modelings of dry relaxed slack plain knitted fabrics for the benefit of technical textile applications part II: Mechanical modeling induced by friction. *Textile Research Journal*, 87(7):853–864, May 2017.

[101] ISO 13934-1:2013 - Textiles – Tensile properties of fabrics – Part 1: Determination of maximum force and elongation at maximum force using the strip method.

[102] ISO 13934-2:2014 - Textiles – Tensile properties of fabrics – Part 2: Determination of maximum force using the grab method.

[103] Alenka Salej Lah, Peter Fajfer, Goran Kugler, and Tatjana Rijavec. A NiTi Alloy Weft Knitted Fabric for Smart Firefighting Clothing. *Smart Materials and Structures*, 2019.

[104] Dieter Stoeckel, Alan Pelton, and Tom Duerig. Self-expanding nitinol stents: material and design considerations. *European Radiology*, 14(2):292–301, February 2004.

[105] Frederick E. Wang, William J. Buehler, and Stanley J. Pickart. Crystal Structure and a Unique "Martensitic" Transition of TiNi. *Journal of Applied Physics*, 36(10):3232–3239, October 1965.

[106] Petr Šittner, Ludek Heller, Jan Pilch, Caroline Curfs, Thiery Alonso, and Denis Favier. Young's Modulus of Austenite and Martensite Phases in Superelastic NiTi Wires. *Journal of Materials Engineering and Performance*, 23(7):2303–2314, July 2014.

[107] Ali Shamimi, Behnam Amin-Ahmadi, Aaron Stebner, and Tom Duerig. The Effect of Low Temperature Aging and the Evolution of R-Phase in Ni-Rich NiTi. *Shape Memory and Superelasticity*, 4(4):417–427, December 2018.

[108] Luděk Heller, K. Janouchová, P. Šittner, and D. Vokoun. Functional textiles driven by transforming NiTi wires. *MATEC Web of Conferences*, 33:03010, 2015. Publisher: EDP Sciences.

[109] Kevin Eschen, Rachael Granberry, and Julianna Abel. Guidelines on the design, characterization, and operation of shape memory alloy knitted actuators. *Smart Materials and Structures*, 2020.

[110] R. Vaidyanathan, M. A. M. Bourke, and D. C. Dunand. Phase fraction, texture and strain evolution in superelastic NiTi and NiTi–TiC composites investigated by neutron diffraction. *Acta Materialia*, 47(12):3353–3366, September 1999.

[111] O. Benafan, S. A. Padula, R. D. Noebe, D. W. Brown, B. Clausen, and R. Vaidyanathan. An in situ neutron diffraction study of shape setting shape memory NiTi. *Acta Materialia*, 61(10):3585–3599, June 2013.

[112] A. N. Bucsek, L. Casalena, D. C. Pagan, P. P. Paul, Y. Chumlyakov, M. J. Mills, and A. P. Stebner. Three-dimensional in situ characterization of phase transformation induced austenite grain refinement in nickel-titanium. *Scripta Materialia*, 162:361–366, March 2019.

[113] W. W. Schmahl, J. Khalil-Allafi, B. Hasse, M. Wagner, A. Heckmann, and Ch. Somsen. Investigation of the phase evolution in a super-elastic NiTi shape memory alloy (50.7at.%Ni) under extensional load with synchrotron radiation. *Materials Science and Engineering: A*, 378(1):81–85, July 2004.

[114] M. Hasan, W. W. Schmahl, K. Hackl, R. Heinen, J. Frenzel, S. Gollerthan, G. Eggeler, M. Wagner, J. Khalil-Allafi, and A. Baruj. Hard X-ray studies of stress-induced phase transformations of superelastic NiTi shape memory alloys under uniaxial load. *Materials Science and Engineering: A*, 481-482:414–419, May 2008.

[115] M. L. Young, M. F. X. Wagner, J. Frenzel, W. W. Schmahl, and G. Eggeler. Phase volume fractions and strain measurements in an ultrafine-grained NiTi shape-memory alloy during tensile loading. *Acta Materialia*, 58(7):2344–2354, April 2010.

[116] Satish B. Alapati, William A. Brantley, Masahiro Iijima, Scott R. Schricker, John M. Nusstein, Uei-Ming Li, and Timothy A. Svec. Micro-XRD and temperature-modulated DSC investigation of nickel–titanium rotary endodontic instruments. *Dental Materials*, 25(10):1221–1229, October 2009.

[117] Matthew Carl, Baozhuo Zhang, and Marcus L. Young. Texture and Strain Measurements from Bending of NiTi Shape Memory Alloy Wires. *Shape Memory and Superelasticity*, 2(3):254–263, September 2016.

[118] M. Iijima, W. A. Brantley, W. H. Guo, W. A. T. Clark, T. Yuasa, and I. Mizoguchi. X-ray diffraction study of low-temperature phase transformations in nickel–titanium orthodontic wires. *Dental Materials*, 24(11):1454–1460, November 2008.

[119] C. L Chu, C. Y Chung, P. H Lin, and S. D Wang. Fabrication of porous NiTi shape memory alloy for hard tissue implants by combustion synthesis. *Materials Science and Engineering: A*, 366(1):114–119, February 2004.

[120] J. Frenzel, E. P. George, A. Dlouhy, Ch. Somsen, M. F. X. Wagner, and G. Eggeler. Influence of Ni on martensitic phase transformations in NiTi shape memory alloys. *Acta Materialia*, 58(9):3444–3458, May 2010.

[121] Mehrdad Zarinejad and Yong Liu. Dependence of Transformation Temperatures of NiTi-based Shape-Memory Alloys on the Number and Concentration of Valence Electrons. *Advanced Functional Materials*, 18(18):2789–2794, 2008.

[122] Jafar Khalil-Allafi, Antonin Dlouhy, and Gunther Eggeler. Ni4ti3-precipitation during aging of NiTi shape memory alloys and its influence on martensitic phase transformations. *Acta Materialia*, 50(17):4255–4274, October 2002.

[123] Raffaella Aversa, Francesco Tamburrino, Relly Victoria Petrescu, Florian Ion Petrescu, Mateus Artur, Guanying Chen, and Antonio Apicella. Biomechanically Inspired Shape Memory Effect Machines Driven by Muscle Like Acting Niti Alloys. SSRN Scholarly Paper ID 3075373, Social Science Research Network, Rochester, NY, November 2016.

[124] B. L. Henke, E. M. Gullikson, and J. C. Davis. X-Ray Interactions: Photoabsorption, Scattering, Transmission, and Reflection at E = 50-30,000 eV, Z = 1-92. *Atomic Data and Nuclear Data Tables*, 54(2):181–342, July 1993.

[125] Sanjay Shrivastava. *Medical Device Materials: Proceedings from the Materials & Processes for Medical Devices Conference 2003, 8-10 September 2003, Anaheim, California*. ASM International, January 2004. Google-Books-ID: Jv1Wysf1jv8C.

[126] B.D. Cullity. Addison-Wesley Publishing Company, 1956.

[127] P. Šittner, P. Lukáš, V. Novák, M. R. Daymond, and G. M. Swallowe. In situ neutron diffraction studies of martensitic transformations in NiTi polycrystals under tension and compression stress. *Materials Science and Engineering: A*, 378(1):97 – 104, 2004.

[128] Husin Sitepu. Structural refinement of neutron powder diffraction data of two-stage martensitic phase transformations in ti50.75ni47.75fe1.50 shape memory alloy. *Powder Diffraction*, 22(3):209–218, 2007.

[129] Y. Kudoh, M. Tokonami, S. Miyazaki, and K. Otsuka. Crystal structure of the martensite in Ti-49.2 at.%Ni alloy analyzed by the single crystal X-ray diffraction method. *Acta Metallurgica*, 33(11):2049 – 2056, 1985.

[130] T. W. Duerig and K. Bhattacharya. The Influence of the R-Phase on the Superelastic Behavior of NiTi. *Shape Memory and Superelasticity*, 1(2):153–161, June 2015.

[131] P. Šittner, M. Landa, P. Lukáš, and V. Novák. R-phase transformation phenomena in thermomechanically loaded NiTi polycrystals. *Mechanics of Materials*, 38(5):475–492, May 2006.

[132] S. Cai, J. E. Schaffer, Y. Ren, and C. Yu. Texture evolution during nitinol martensite detwinning and phase transformation. *Applied Physics Letters*, 103(24):241909, December 2013. Publisher: American Institute of Physics.

[133] Vitalij K. Pecharsky and Peter Y. Zavalij. *Fundamentals of Powder Diffraction and Structural Characterization of Materials*. Springer US, Boston, MA, 2005. Pages: 1-713.

[134] W. A. Dollase. Correction of intensities for preferred orientation in powder diffractometry: application of the March model. *Journal of Applied Crystallography*, 19(4):267–272, August 1986.

[135] T Ungár. Microstructural parameters from X-ray diffraction peak broadening. *Scripta Materialia*, 51(8):777–781, October 2004.

[136] H. P. Hanson, F. Herman, J. E. Lea, and S. Skillman. HFS atomic scattering factors. *Acta Crystallographica*, 17(8):1040–1044, August 1964.

[137] X-ray energy - GISAXS.

[138] K. Gall, H. Sehitoglu, Y. I. Chumlyakov, and I. V. Kireeva. Tension–compression asymmetry of the stress–strain response in aged single crystal and polycrystalline NiTi. *Acta Materialia*, 47(4):1203–1217, March 1999.

[139] Yong Liu, Z Xie, J Van Humbeeck, and L Delaey. Asymmetry of stress–strain curves under tension and compression for NiTi shape memory alloys. *Acta Materialia*, 46(12):4325–4338, July 1998.

[140] S. De la Flor, C. Urbina, and F. Ferrando. Asymmetrical Bending Model for NiTi Shape Memory Wires: Numerical Simulations and Experimental Analysis. *Strain*, 47(3):255–267, 2011.

[141] Max Pfeiffer and Michael Rohs. Haptic Feedback for Wearables and Textiles Based on Electrical Muscle Stimulation. In Stefan Schneegass and Oliver Amft, editors, *Smart Textiles: Fundamentals, Design, and Interaction*, Human–Computer Interaction Series, pages 103–137. Springer International Publishing, Cham, 2017.

[142] Heike Leutheuser, Nadine R. Lang, Stefan Gradl, Matthias Struck, Andreas Tobola, Christian Hofmann, Lars Anneken, and Bjoern M. Eskofier. Textile Integrated Wearable Technologies for Sports and Medical Applications. In Stefan Schneegass and Oliver Amft, editors, *Smart Textiles: Fundamentals, Design, and Interaction*, Human–Computer Interaction Series, pages 359–382. Springer International Publishing, Cham, 2017.

[143] Leonardo Cappello, Jan T. Meyer, Kevin C. Galloway, Jeffrey D. Peisner, Rachael Granberry, Diana A. Wagner, Sven Engelhardt, Sabrina Paganoni, and Conor J.

Walsh. Assisting hand function after spinal cord injury with a fabric-based soft robotic glove. *Journal of NeuroEngineering and Rehabilitation*, 15(1):59, June 2018.

[144] Preeti Kumari, Lini Mathew, and Poonam Syal. Increasing trend of wearables and multimodal interface for human activity monitoring: A review. *Biosensors and Bioelectronics*, 90:298–307, April 2017.

[145] Jan Meyer, Bert Arnrich, Johannes Schumm, and Gerhard Troster. Design and Modeling of a Textile Pressure Sensor for Sitting Posture Classification. *IEEE Sensors Journal*, 10(8):1391–1398, August 2010.

[146] Ye Ding, Myunghee Kim, Scott Kuindersma, and Conor J. Walsh. Human-in-the-loop optimization of hip assistance with a soft exosuit during walking. *Science Robotics*, 3(15), February 2018.

[147] M. M. Bait-Suwailam, I. I. Labiano, and A. Alomainy. Effect of textile properties on a low-profile wearable loop antenna for healthcare applications. In *2019 13th European Conference on Antennas and Propagation (EuCAP)*, pages 1–4, March 2019.

[148] Zhixiang Rao, Xiaojun Yan, Xiaoyong Zhang, Bin Zhang, Jun Jiang, Shuqing Zhang, Chaoyong Guo, Dawei Huang, and Mingjing Qi. Experimental and numerical studies on a novel shape-memory alloy wire–woven trusses capable of undergoing large deformation. *Journal of Intelligent Material Systems and Structures*, 30(15):2283–2298, September 2019. Publisher: SAGE Publications Ltd STM.

[149] Xiaobin Su, Yingyu Wang, and Xiongqi Peng. An anisotropic visco-hyperelastic model for thermally-actuated shape memory polymer-based woven fabric-reinforced composites. *International Journal of Plasticity*, 129:102697, June 2020.

[150] Jaegeun Lee, Dong-Myeong Lee, Yeonsu Jung, Junbeom Park, Hun Su Lee, Young-Kwan Kim, Chong Rae Park, Hyeon Su Jeong, and Seung Min Kim. Direct spinning and densification method for high-performance carbon nanotube fibers. *Nature Communications*, 10(1):2962, July 2019. Number: 1 Publisher: Nature Publishing Group.

[151] W. J. Shanahan and R. Postle. A Theoretical Analysis of the Plain-Knitted Structure. *Textile Research Journal*, 40(7), January 1970.

[152] H. Hong, M.D. De Araujo, R. Fangueiro, and O. Ciobanu. Theoretical Analysis of Load-Extension Properties of Plain Weft Knits Made from High Performance Yarns for Composite Reinforcement. *Textile Research Journal*, 72(11):991–996, November 2002. Publisher: SAGE Publications Ltd STM.

[153] Zheng-Ming Huang, S. Ramakrishna, and Aye Aye Thwe. Modeling and Characterization of Fatigue Strength of Laminated Composites with Knitted Fabric Reinforcement. *Journal of Composite Materials*, 36(15), January 2002.

[154] J. L. Kuhn and P. G. Charalambides. Modeling of Plain Weave Fabric Composite Geometry. *Journal of Composite Materials*, 33(3):188–220, February 1999.

[155] S. D. Green, M. Y. Matveev, A. C. Long, D. Ivanov, and S. R. Hallett. Mechanical modelling of 3D woven composites considering realistic unit cell geometry. *Composite Structures*, 118:284–293, December 2014.

[156] T. M. McBride and Julie Chen. Unit-cell geometry in plain-weave fabrics during shear deformations. *Composites Science and Technology*, 57(3):345–351, January 1997.

[157] Guang-Wu Du and Frank K. Ko. Unit Cell Geometry of 3-D Braided Structures. *Journal of Reinforced Plastics and Composites*, 12(7):752–768, July 1993.

[158] Zhihua Ma, Rui Xu, Wei Wang, and Dan Yu. A wearable, anti-bacterial strain sensor prepared by silver plated cotton/spandex blended fabric for human motion monitoring. *Colloids and Surfaces A: Physicochemical and Engineering Aspects*, 582:123918, December 2019.

[159] Nan Nan, Jianxin He, Xiaolu You, Xianqiang Sun, Yuman Zhou, Kun Qi, Weili Shao, Fan Liu, Yanyan Chu, and Bin Ding. A Stretchable, Highly Sensitive, and Multimodal Mechanical Fabric Sensor Based on Electrospun Conductive Nanofiber Yarn for Wearable Electronics. *Advanced Materials Technologies*, 4(3):1800338, 2019.

[160] Liyun Ma, Ronghui Wu, Aniruddha Patil, Shuihong Zhu, Zhaohui Meng, Haiqiang Meng, Chen Hou, Yifan Zhang, Qiang Liu, Rui Yu, Jun Wang, Naibo Lin, and Xiang Yang Liu. Full-Textile Wireless Flexible Humidity Sensor for Human Physiological Monitoring. *Advanced Functional Materials*, 29(43):1904549, 2019.

[161] Juan Xie, Yongtang Jia, and Menghe Miao. High sensitivity knitted fabric bidirectional pressure sensor based on conductive blended yarn. *Smart Materials and Structures*, 28(3):035017, February 2019.

[162] Lina M. Castano and Alison B. Flatau. Smart fabric sensors and e-textile technologies: a review. *Smart Materials and Structures*, 23(5):053001, 2014.

[163] K Eschen and J Abel. Performance and prediction of large deformation contractile shape memory alloy knitted actuators. *Smart Materials and Structures*, 28(2):025014, 2019.

[164] Stepan V. Lomov, Maarten Moesen, Rudy Stalmans, Gosia Trzcinski, Jan Van Humbeeck, and Ignaas Verpoest. Finite element modelling of SMA textiles: superelastic behaviour. *The Journal of The Textile Institute*, 102(3):232–247, March 2011.

[165] L.C. Brinson. One-Dimensional Constitutive Behavior of Shape Memory Alloys: Thermomechanical Derivation with Non-Constant Material Functions and Redefined Martensite Internal Variable. *Journal of Intelligent Material Systems and Structures*, 4(2):229–242, April 1993.

[166] J. G. Boyd and D. C. Lagoudas. A thermodynamical constitutive model for shape memory materials. Part I. The monolithic shape memory alloy. *International Journal of Plasticity*, 12(6):805–842, January 1996.

[167] A. F. Saleeb, S. A. Padula II, and A. Kumar. A multi-axial, multimechanism based constitutive model for the comprehensive representation of the evolutionary response of SMAs under general thermomechanical loading conditions. *International Journal of Plasticity*, 27(5):655–687, May 2011.

[168] J. e. Huber, N. a. Fleck, C. M. Landis, and R. M. McMeeking. A constitutive model for ferroelectric polycrystals. *Journal of the Mechanics and Physics of Solids*, 47(8):1663–1697, August 1999.

[169] Hisaaki Tobushi, Kayo Okumura, Shunichi Hayashi, and Norimitsu Ito. Thermomechanical constitutive model of shape memory polymer. *Mechanics of Materials*, 33(10):545–554, October 2001.

[170] Q. Wang and C. M. Wang. The constitutive relation and small scale parameter of nonlocal continuum mechanics for modelling carbon nanotubes. *Nanotechnology*, 18(7):075702, January 2007.

[171] S. Lomov. *WiseTex software suit*. 2010.

[172] Jenny Udale. *Basics Fashion Design 02: Textiles and Fashion*. AVA Publishing, August 2008. Google-Books-ID: mcaXCYVz8ikC.

[173] R. Alagirusamy and A. Das. 2 - Yarns: Production, processability and properties. In R. Fangueiro, editor, *Fibrous and Composite Materials for Civil Engineering Applications*, Woodhead Publishing Series in Textiles, pages 29–61. Woodhead Publishing, January 2011.

[174] Daryl L. Logan. *A First Course in the Finite Element Method*. Cengage Learning, January 2011. Google-Books-ID: KptPymzHa_gC.

[175] Ashish Khandelwal and Vidyashankar Buravalla. Models for Shape Memory Alloy Behavior: An overview of modeling approaches. *The International Journal of Structural Changes in Solids*, 1(1):111–148, 2009.

[176] Thao D. Nguyen, Christopher M. Yakacki, Parth D. Brahmbhatt, and Matthew L. Chambers. Modeling the Relaxation Mechanisms of Amorphous Shape Memory Polymers. *Advanced Materials*, 22(31):3411–3423, 2010.

[177] D. H. Wang and W. H. Liao. Magnetorheological fluid dampers: a review of parametric modelling. *Smart Materials and Structures*, 20(2):023001, January 2011.

[178] Hao Zeng, Jianhua Liu, Zhimin Xie, and Huiyu Sun. Modeling the shape memory and strength properties of fiber-reinforced shape memory polymer composite laminates. *Smart Materials and Structures*, 28(10):105011, August 2019.

[179] G. B. Stachowiak and P. G. McCormick. Shape memory behaviour associated with the R and martensitic transformations in a NiTi alloy. *Acta Metallurgica*, 36(2):291–297, February 1988.

[180] Ashley N. Bucsek, Harshad M. Paranjape, and Aaron P. Stebner. Myths and Truths of Nitinol Mechanics: Elasticity and Tension–Compression Asymmetry. *Shape Memory and Superelasticity*, 2(3):264–271, September 2016.

[181] K. Tanaka and R. Iwasaki. A phenomenological theory of transformation superplasticity. *Engineering Fracture Mechanics*, 21(4):709–720, January 1985.

[182] C. Liang and C. A. Rogers. One-Dimensional Thermomechanical Constitutive Relations for Shape Memory Materials. *Journal of Intelligent Material Systems and Structures*, 8(4):285–302, April 1997.

[183] Reza Mehrabi, Mahmoud Kadkhodaei, and Mohammad Elahinia. Constitutive modeling of tension-torsion coupling and tension-compression asymmetry in NiTi shape memory alloys. *Smart Materials and Structures*, 23(7):075021, June 2014.

[184] Petr Sittner, Yasuhiro Hara, and Masataka Tokuda. Experimental study on the thermoelastic martensitic transformation in shape memory alloy polycrystal induced by combined external forces. *Metallurgical and Materials Transactions A*, 26(11):2923–2935, November 1995.

[185] S. V. Lomov, G. Huysmans, and I. Verpoest. Hierarchy of Textile Structures and Architecture of Fabric Geometric Models. *Textile Research Journal*, 71(6):534–543, June 2001.

[186] J. W. S. Hearle and W. J. Shanahan. An Energy Method for Calculations in Fabric Mechanics Part I: Principles of the Method. *The Journal of The Textile Institute*, 69(4):81–91, April 1978.

[187] J. W. S. Hearle, P. Potluri, and V. S. Thammandra. Modelling Fabric Mechanics. *The Journal of The Textile Institute*, 92(3):53–69, January 2001.

[188] J. W. S. Hearle, P. Grosberg, and S. Backer. Structural mechanics of fibers, yarns, and fabrics. 1.

[189] J. W. S. Hearle. The Mechanics of Twisted Yarns: The Influence of Transverse Forces on Tensile Behaviour. *Journal of the Textile Institute Transactions*, 49(8):T389–T408, August 1958.

[190] M. Duhovic and D. Bhattacharyya. Simulating the deformation mechanisms of knitted fabric composites. *Composites Part A: Applied Science and Manufacturing*, 37(11):1897–1915, November 2006.

[191] Noboru Aisaka. Mathematical Considerations of Weft Knitting Process. *Journal of the Textile Machinery Society of Japan*, 17(3):82–91, 1971.

[192] S. Ghosh and P.K. Banerjee. Mechanics of the Single Jersey Weft Knitting Process. *Textile Research Journal*, 60(4):203–211, April 1990.

[193] R. Pietruszewska, K. Kowalski, and M. Kłonowska. Modelling of the Knitting Process during the Knitting-in of Elastomeric Threads Using Knitting Machines with Relanit and Classic Knitting Zone. *Fibres & Textiles in Eastern Europe*, Nr 4 (106), 2014.

[194] Yifan Zhang, Fei Sun, Yanjie Wang, Li Chen, and Ning Pan. Study on intra/inter-ply shear deformation of three dimensional woven preforms for composite materials. *Materials & Design*, 49:151–159, August 2013.

[195] Thomas Gereke and Chokri Cherif. A review of numerical models for 3D woven composite reinforcements. *Composite Structures*, 209:60–66, February 2019.

[196] R. H. Yang and S. Y. Wang. A linear dynamic model for rotor-spun composite yarn spinning process. *Journal of Physics: Conference Series*, 96:012039, February 2008.

[197] Resty Mayseptheny Hernawati, Valentinus Galih Vidia Putra, and Irfandhani Fauzi. Predicting the Actual Strength of Open-End Spun Yarn Using Mechanical Model, 2015.

[198] Q. Zhang, D. Beale, and R. M. Broughton. Analysis of Circular Braiding Process, Part 1: Theoretical Investigation of Kinematics of the Circular Braiding Process. *Journal of Manufacturing Science and Engineering*, 121(3):345–350, August 1999.

[199] F. Frenet. Sur les courbes à double courbure. *Journal de Mathématiques Pures et Appliquées*, pages 437–447, 1852.

[200] J.-A. Serret. Sur quelques formules relatives à la théorie des courbes à double courbure. *Journal de Mathématiques Pures et Appliquées*, pages 193–207, 1851.

[201] Dani Liu, Bahareh Shakibajahromi, Genevieve Dion, David Breen, and Antonios Kontsos. A Computational Approach to Model Interfacial Effects on the Mechanical Behavior of Knitted Textiles. *Journal of Applied Mechanics*, 85(4), April 2018.

[202] Rachael M. Granberry, Kevin P. Eschen, Amy J. Ross, Julianna M. Abel, and Bradley T. Holschuh. Dynamic Countermeasure Fabrics for Post-Spaceflight Orthostatic Intolerance. *Aerospace Medicine and Human Performance*, 91(6):525–531, June 2020.

[203] Henry Koon, Julianna Abel, Jeremy E. Schaffer, and Santo Padula. Design of knitted superelastic tire treads for next generation non-pneumatic rover tires. In *ASM International - International Conference on Shape Memory and Superelastic Technologies, SMST 2019*, ASM International - International Conference on Shape Memory and Superelastic Technologies, SMST 2019, pages 238–239, United States, January 2019. ASM International. International Conference on Shape Memory and Superelastic Technologies 2019, SMST 2019 ; Conference date: 13-05-2019 Through 17-05-2019.

[204] S. Qiu, B. Clausen, S. A. Padula, R. D. Noebe, and R. Vaidyanathan. On elastic moduli and elastic anisotropy in polycrystalline martensitic NiTi. *Acta Materialia*, 59(13):5055–5066, August 2011.

[205] S. Spinner and A. G. Rozner. Elastic Properties of NiTi as a Function of Temperature. *The Journal of the Acoustical Society of America*, 40(5):1009–1015, November 1966. Publisher: Acoustical Society of America.

[206] M. A. Qidwai and D. C. Lagoudas. On thermomechanics and transformation surfaces of polycrystalline NiTi shape memory alloy material. *International Journal of Plasticity*, 16(10):1309–1343, January 2000.

[207] R. P. Kusy and J. Q. Whitley. Effects of surface roughness on the coefficients of friction in model orthodontic systems. *Journal of Biomechanics*, 23(9):913–925, January 1990.

[208] Saeid Poorasadion, Jamal Arghavani, Reza Naghdabadi, and Saeed Sohrabpour. An improvement on the Brinson model for shape memory alloys with application to two-dimensional beam element. *Journal of Intelligent Material Systems and Structures*, 25(15):1905–1920, October 2014.

[209] T. W. Duerig, K. N. Melton, and D. Stöckel. *Engineering Aspects of Shape Memory Alloys*. Butterworth-Heinemann, October 2013. Google-Books-ID: y7QgBQAAQBAJ.

[210] Simeon Gill. A review of research and innovation in garment sizing, prototyping and fitting. *Textile Progress*, 47(1):1–85, January 2015.

[211] C.C. Gordon, C.L. Blackwell, S.P. Paquette, J.L. Parham, and B. Brandtmiller. Anthropometric change in the us army 1988-2012: Implications for design. *Anthrotech Inc.*, 2012.

[212] Rachael Granberry, Julia Duvall, Lucy E. Dunne, and Bradley Holschuh. An analysis of anthropometric geometric variability of the lower leg for the fit & function of advanced functional garments. In *Proceedings of the 2017 ACM International Symposium on Wearable Computers*, ISWC '17, pages 10–17, New York, NY, USA, 2017. ACM.

[213] Louis N. Awad, Jaehyun Bae, Kathleen O'Donnell, Stefano M. M. De Rossi, Kathryn Hendron, Lizeth H. Sloot, Pawel Kudzia, Stephen Allen, Kenneth G. Holt, Terry D. Ellis, and Conor J. Walsh. A soft robotic exosuit improves walking in patients after stroke. *Science Translational Medicine*, 9(400), July 2017.

[214] Fausto A. Panizzolo, Ignacio Galiana, Alan T. Asbeck, Christopher Siviy, Kai Schmidt, Kenneth G. Holt, and Conor J. Walsh. A biologically-inspired multi-joint soft exosuit that can reduce the energy cost of loaded walking. *Journal of NeuroEngineering and Rehabilitation*, 13(1):43, May 2016.

[215] Leonardo Cappello, Kevin C. Galloway, Siddharth Sanan, Diana A. Wagner, Rachael Granberry, Sven Engelhardt, Florian L. Haufe, Jeffrey D. Peisner, and

Conor J. Walsh. Exploiting Textile Mechanical Anisotropy for Fabric-Based Pneumatic Actuators. *Soft Robotics*, 5(5):662–674, July 2018.

[216] Michelle C. Yuen, R. Adam Bilodeau, and Rebecca K. Kramer. Active Variable Stiffness Fibers for Multifunctional Robotic Fabrics. *IEEE Robotics and Automation Letters*, 1(2):708–715, July 2016.

[217] Matthew J. Harrington, Khashayar Razghandi, Friedrich Ditsch, Lorenzo Guiducci, Markus Rueggeberg, John W. C. Dunlop, Peter Fratzl, Christoph Neinhuis, and Ingo Burgert. Origami-like unfolding of hydro-actuated ice plant seed capsules. *Nature Communications*, 2(1):1–7, June 2011.

[218] B. Kumar and J. Hu. 6 - Woven fabric structures and properties. In Menghe Miao and John H. Xin, editors, *Engineering of High-Performance Textiles*, The Textile Institute Book Series, pages 133–151. Woodhead Publishing, 2018.

[219] L. McDonald Schetky. Shape-Memory Alloys. In *Kirk-Othmer Encyclopedia of Chemical Technology*. John Wiley & Sons, Inc., 2000.

[220] Kevin Eschen, Julianna Abel, Rachael Granberry, and Brad Holschuh. Active-Contracting Variable-Stiffness Fabrics for Self-Fitting Wearables. pages V001T04A002–V001T04A002. American Society of Mechanical Engineers, September 2018.

[221] RAL-GZ 387/1. Medical compression hosiery: Quality assurance, 2008.

[222] Christopher B. Churchill and John A. Shaw. Shakedown response of conditioned shape memory alloy wire. volume 6929, pages 69291F–69291F–12, 2008.

[223] J E Huber, N A Fleck, and M F Ashby. The selection of mechanical actuators. *Proceedings of the Royal Society of London. Series A: Mathematical, Physical and Engineering Sciences*, 453(1965):2185–2205, 1997.

[224] C. B. Churchill, J. A. Shaw, and M. A. Iadicola. Tips and Tricks for Characterizing Shape Memory Alloy Wire: Part 4 – Thermo-Mechanical Coupling. *Experimental Techniques*, 34(2):63–80, 2010.

[225] R. Stalmans, J. Van Humbeeck, and L. Delaey. Effects of Training on the Shape Memory Behaviour of Cu-Zn-Al Alloys, 1992.

[226] Tom Borden. Shape-memory alloys: forming a tight fit. *Mechanical Engineering-CIME*, 113(10):66, 1991.

[227] G.B. Brook. Applications of titanium-nickel shape memory alloys. *Materials & Design*, 4(4):835–840, August 1983.

[228] Rachael Granberry, Santo Padula II, Kevin Eschen, Julianna Abel, and Brad Holschuh. Design and Control of Reduced Power Actuation for Active-Contracting Orthostatic Intolerance Garments. In *49th International Conference on Environmental Systems*, Boston, 2019.

[229] D. Stoeckel and T. Borden. Actuation and fastening with shape memory alloys in the automotive industry. *Mettallwissenschaft und technik*, 46(7):668–672, 1992.

[230] R Granberry, K Eschen, A Ross, J Abel, and B Holschuh. Medical Compression Capability of Dynamic Countermeasure Fabrics for Post-Spaceflight Orthostatic Intolerance. *under review.*

[231] Petr Šittner, Orsolya Molnárová, Lukáš Kadeřávek, Ondřej Tyc, and Luděk Heller. Deformation twinning in martensite affecting functional behavior of NiTi shape memory alloys. *Materialia*, 9(October 2019), 2020.

Appendix A

Appendix A

A.1 Supplemental Materials for Chapter 5

When utilizing a finite beam element approach, certain assumptions are inherently made: The fibers are assumed to be homogeneous, isotropic, perfectly round, and do not change their diameter upon extension or compression. The finite beam model assumes quasi-static loading conditions without contribution of dynamic effects. Forces, moments, and prescribed displacements are assumed to be applied to the centroid of the beam. The leading beam theories, Euler-Bernoulli and Timoshenko, are implemented and can be selected automatically or forced manually. The Euler-Bernoulli beam theory is a special case of the Timoshenko beam theory suitable for beams with high shear stiffness. The condition

$$\frac{E \cdot I}{\kappa \cdot A \cdot G \cdot L^2} \ll 1, \tag{A.1}$$

with the elastic modulus (E), the second moment of area (I), the Timoshenko shear coefficient (κ), the cross-sectional area (A), the shear modulus (G), and the length (L), is true for Euler-Bernoulli beams. The basic finite beam element between the nodes 1 and 2 supports tensile forces (f'_{1x}, f'_{2x}) and displacements (u'_1, u'_2), torsional moments (m'_{1x}, m'_{2x}) and displacements (Φ'_{1x}, Φ'_{2x}), shear forces ($f'_{1y}, f'_{2y}, f'_{1z}, f'_{2z}$) and displacements ($v'_1, v'_2, w'_1, w'_2$), as well as bending moments ($m'_{1y}, m'_{2y}, m'_{1z}, m'_{2z}$) and displacements ($\Phi'_{1y}, \Phi'_{2y}, \Phi'_{1z}, \Phi'_{2z}$) around the y'- and z'-axes with respect to the local coordinate system $\{x', y'z'\}$ (Figure 5.1). Local displacements and forces are related through the local stiffness matrix (k')

$$k'_a = \begin{pmatrix} \frac{AE}{L} & 0 & 0 \\ 0 & \frac{12EI_z}{L^3} & 0 \\ 0 & 0 & \frac{12EI_y}{L^3} \end{pmatrix}$$

$$k'_b = \begin{pmatrix} 0 & 0 & 0 \\ 0 & 0 & \frac{6EI_z}{L^2} \\ 0 & -\frac{6EI_y}{L^2} & 0 \end{pmatrix}$$

$$k'_c = \begin{pmatrix} 0 & 0 & 0 \\ 0 & 0 & -\frac{6EI_y}{L^2} \\ 0 & \frac{6EI_z}{L^2} & 0 \end{pmatrix}$$

$$k'_d = \begin{pmatrix} \frac{GJ}{L} & 0 & 0 \\ 0 & \frac{4EI_y}{L} & 0 \\ 0 & 0 & \frac{4EI_z}{L} \end{pmatrix}$$

$$k'_e = \begin{pmatrix} -\frac{GJ}{L} & 0 & 0 \\ 0 & \frac{2EI_y}{L} & 0 \\ 0 & 0 & \frac{2EI_z}{L} \end{pmatrix}$$

which assembles tensile, shear, torsional, and bending stiffness components

$$k' = \begin{pmatrix} k'_a & k'_b & -k'_a & k'_b \\ k'_c & k'_d & -k'_c & k'_e \\ -k'_a & -k'_b & k'_a & -k'_b \\ k'_c & k'_e & -k'_c & k'_d \end{pmatrix}$$

into a 12×12 matrix. Transformation to global coordinates is accomplished by the transformation matrix $[T]$

$$[k] = [T]^T [k'][T], \tag{A.2}$$

which transforms the local stiffness matrix $[k']_{\{12\times12\}}$ to the global coordinate system $\{x, y, z\}$, in which the global stiffness matrix $[k]_{\{\mathrm{DOF}\times\mathrm{DOF}\}}$ is assembled. [174] The degrees of freedom (DOF) of the system are $6 \times n_n$ where (n_n) is the number of nodes in the system. Upon solving the linear system of equations

$$\{F\} = [k]\,\{d\}, \tag{A.3}$$

where $\{F\} = \{f_{1x}, m_{1x}, f_{1y}, \ldots, f_{n_n z}, m_{n_n z}\}$ and $\{d\} = \{u_1, \Phi_{1x}, v_1, \ldots, w_{n_n}, \Phi_{n_n z}\}$, all nodal displacements and forces are known. Shape functions {N} of appropriate polynomial degree (bending-cubic, tension/torsion-linear) are used to perform Hermite interpolation between the nodal point displacements {d}. For example, a tensile shape function is

$$\{N\} = \left\{1 - \frac{x}{L}, \frac{x}{L}\right\}, \tag{A.4}$$

which, through multiplication with the nodal displacement vector {d} computes the interpolated displacements

$$\{u\} = \{N\}\{d\}, \tag{A.5}$$

of points along the element. Applying the tensile strain $\varepsilon_{xx} = \frac{\mathrm{d}u}{\mathrm{d}x}$ definition,

$$\varepsilon_{xx} = \frac{\mathrm{d}u}{\mathrm{d}x} = \frac{\mathrm{d}N}{\mathrm{d}x} d, \tag{A.6}$$

it is apparent that derivation of the shape function $\frac{dN}{dx}$ suffices for the calculation of strains. This procedure of strain calculation is applied to the torsion and bending displacement calculations as well. These tasks, the discretization of the spline unit cell geometry, assembly of the global stiffness matrix, and solution of the linear system of Equation A.3 with subsequent strain calculations are the computational tasks of the modeling framework.

A.2 Supplemental Materials for Chapter 6

A.2.1 Fitting Leg Sleeve Design Details

The allowable circumferential contractile force was calculated to keep the garment pressure below 10 mmHg, which is considered medically significant pressure. The allowable force (F_{max}) for each actuator-body pairing is defined

$$F_{max} = p_{max} r_n w \tag{A.7}$$

through the maximum allowable pressure ($p_{max} = 1333\,\text{Pa}$), the body cross-sectional radius (r_n), and the actuator x-axis width. SMA knitted actuators were selected based on the required %-actuation contractions while the number of courses was chosen to accomplish the required actuation displacements without exerting forces that exceed the calculated threshold F_{max}.

The calculated maximum allowable force and the panel-specific body circumference for each actuator-body pairing are represented in Figure A.2 and Figure A.3.

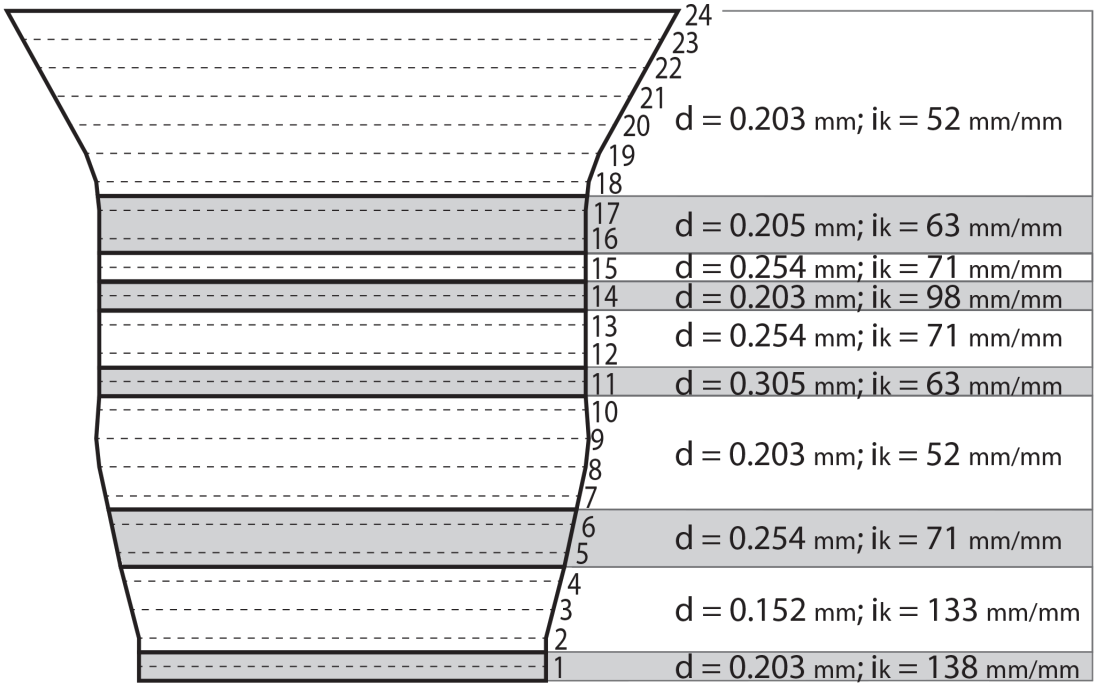

Figure A.1: **Garment Knit Panel Selection:** Full leg sleeve design details. Dashed lines 1-24 represent circumferential measurements taken around the participants leg in 2 cm increments. Dark outlines represent the boundaries of knitted panels, composed of a group of adjacent circumferences that require the same fabric actuation contraction behavior for fitting. The details of each SMA knitted actuator paired with each knit panel, specifically wire diameter (d) and knit index (i_k), are indicated on the right.

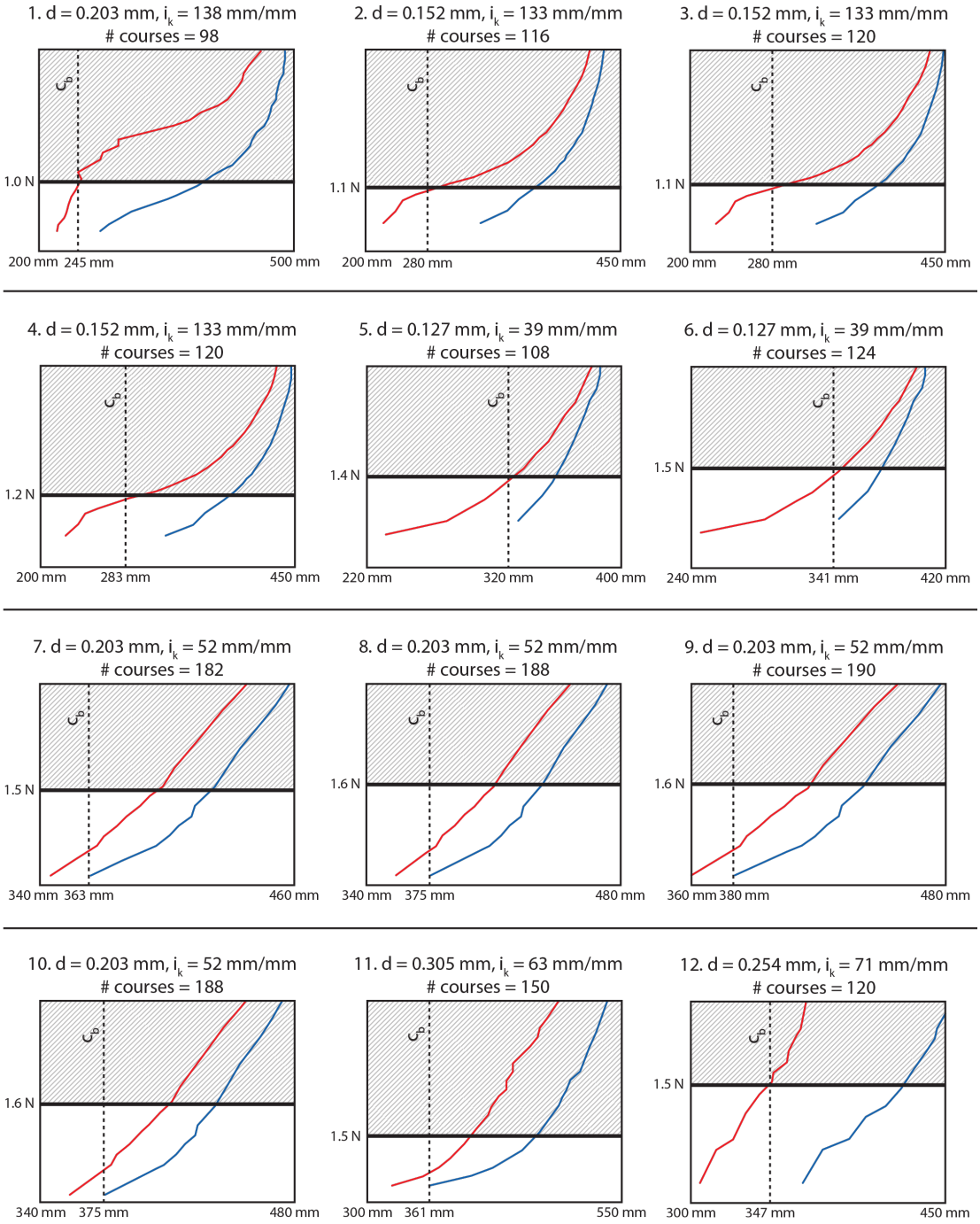

Figure A.2: **Knit Panel Performance Scaling:** Force-length plots for SMA knitted actuators paired with body circumference (c_b) measurements 1-12 in Figure A.1. The actuator data was gathered experimentally through force-control testing, detailed in prior work. The experimental data was scaled up or down by adding or subtracting knit courses so that the body circumference (c_b) was positioned between the austenite knit length (l_a) and the martensite knit length (l_m) at 0.5 N

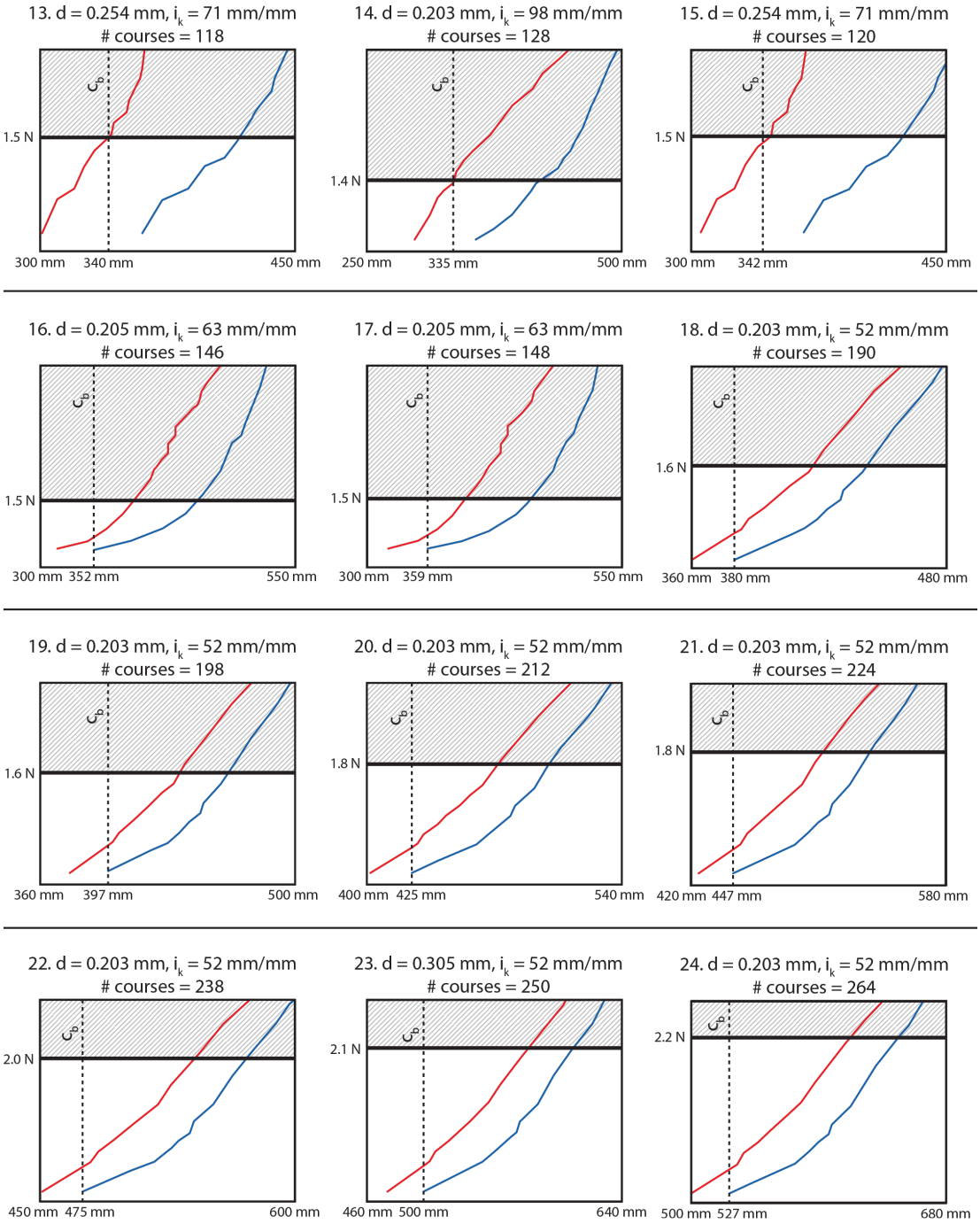

Figure A.3: **Knit Panel Performance Scaling:** Force-length plots for SMA knitted actuators paired with body circumference (c_b) measurements 1-12 in Figure A.1. The actuator data was gathered experimentally through force-control testing, detailed in prior work. The experimental data was scaled up or down by adding or subtracting knit courses so that the body circumference (c_b) was positioned between the austenite knit length (l_a) and the martensite knit length (l_m) at 0.5 N

A.2.2 SMA knitted actuator manufacturing

Adjacent fabrics cannot have a difference in wire diameter (d) greater than 0.1 mm without compromising stable connections between fabrics. Additionally, the knit index (i_k) is minimized in favor of dense fabric surfaces that are felt on the skin as uniform pressure. Finally, lighter and less expensive fabrics are prioritized over heavier and more expensive fabrics.

Flatbed Knitting

Weft knitting machines are composed of a flat bed of latch needles that form a series of interlocking loops (Figure A.4). Prototypes for this work were fabricated on a manual weft knitting machine (i.e., Taitexma); however, weft knitting machines used in the industrial production of knitted fabrics would enable a fully-automated fabrication process.

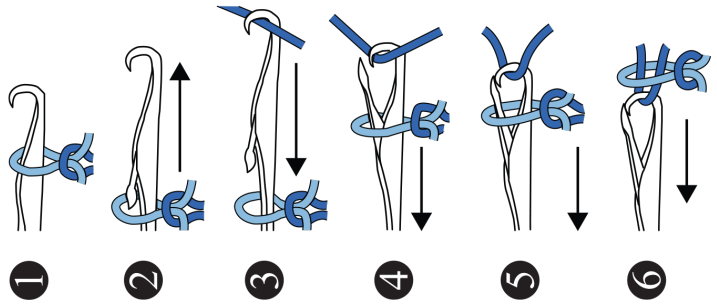

Figure A.4: **Knit Flatbed Machine Manufacturing Process:** Each latch needle forms a column of successive slip knots. (1) The latch needle must start out holding a filament loop. (2) The latch needle rises so that the filament loop falls below the latch. (3) The latch needle continue rising to hoop a new filament. (4) The latch needle lowers, carrying the new filament. (5) The pull-back action causes the latch to close and the previous loop filament to slide over the needle. (6) Upon returning to the initial state, the latch needle has formed a new loop.

Knit shaping on flatbed machines

To fabricate panels with non-rectangular shapes, specifically curved or diagonal shapes, latch needles can be selectively engaged or disengaged to increase or decrease the width of knitted fabric, respectively. This process of adding or subtracting active latch needles into the knitting process is called shaping. The process of subtracting active latch needles results in fabric curling upon actuation. Alternatively, the process of adding active latch needles results in further contraction. Consequently, all knit edge conditions were knit the same way to restrict the manufacturing process to added latch needles only. To accomplish this design restriction, knit patterns that required shaping were split at center front and joined vertically at center front and center back.

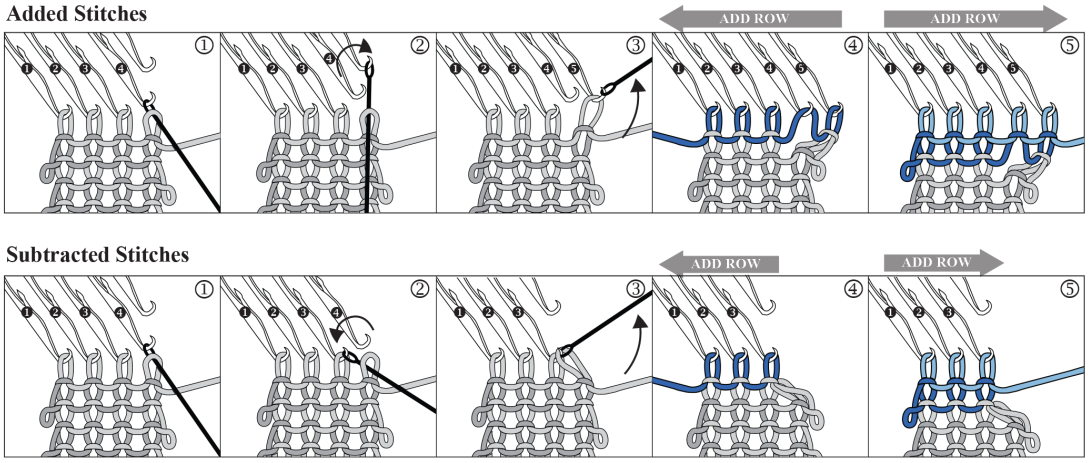

Figure A.5: **Knit Shaping:** Knit shaping on flatbed machines can occur through added stitches (i.e., to increase the knit dimensions) or through subtracted stitches (i.e., to decrease the knit dimensions). The following steps demonstrate the process on a manual knitting machine; however, these processes are automated in double-bed flat knitting. Added stitches: (1) A transfer tool is used to remove the looped filament from needle 4. (2) The transfer tool, carrying the looped filament, moves to an adjacent empty needle. (3) The transfer tool transfers the looped filament to needle 5, leaving needle 4 empty. (4) A new row of knitted courses is added, which adds a looped filament to all active needles 1-5. (5) A second knitted course completes to process. Subtracted Stitches: (1) A transfer tool is used to remove the looped filament from needle 4. (2) The transfer tool, carrying the looped filament, moves to an adjacent needle that already carries a knitted loop. (3) The transfer tool transfers the looped filament to needle 3, leaving needle 4 empty. Needle 4 is fully retracted so that it is no longer able to form knitted loops. (4) A new row of knitted courses is added, which forms looped filament to all active needles 1-3. (5) A second knitted course completes to process.

Crochet joining

Rather than using a traditional knit linking machine to join panels with a limited-compliance grafting seam, a compliant crochet joining stitch with cotton sewing thread and Kevlar® yarn was used to enable each panel to change dimensions without restriction. Depicted in Figure A.6, a crochet stitch is similar to a weft knit stitch in that the structure is composed of a series of interlocking loops. With more sophisticated industrial weft knitting machines, crochet joining would not be structurally necessary and could be eliminated in future works.

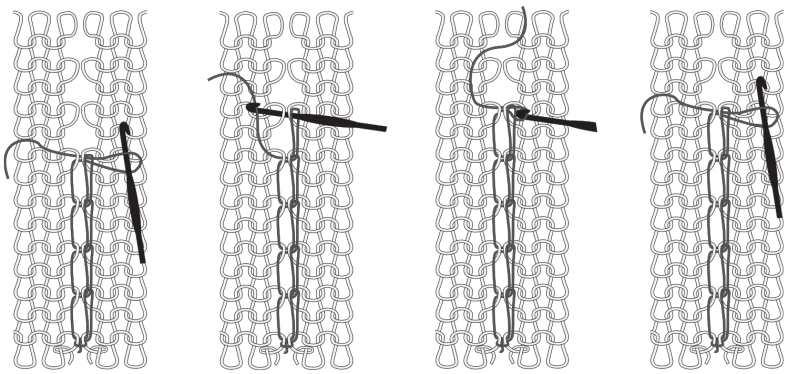

Figure A.6: **Garment Panel Joining:** A crochet stitch is a joining stitch used to connect SMA knitted actuator panels. (1) A crochet hook grasps a filament loop. (2) The crochet hook, holding the filament loop, passes through a knitted loop at the ends of adjacent knit panels. (3) The crochet hook catches the end of the free filament and pulls the filament through both knit panel loops and the previous filament loop. (4) Upon returning to the initial state, the crochet hook completes a full stitch.

A.2.3 Performance Stability

SMA knitted actuators undergo a combination of architectural and material shakedown leading to initial degrading and subsequently stabilizing cyclical thermo-mechanical performance. The self-fitting garment was analyzed for performance stability over ten tested cycles at the anterior and lateral views. Figure A.7 displays the mean deviation of all %-actuation contraction measurements on the self-fitting garment per cycle from the average of %-actuation contraction measurements over all cycles in the lateral and anterior view.

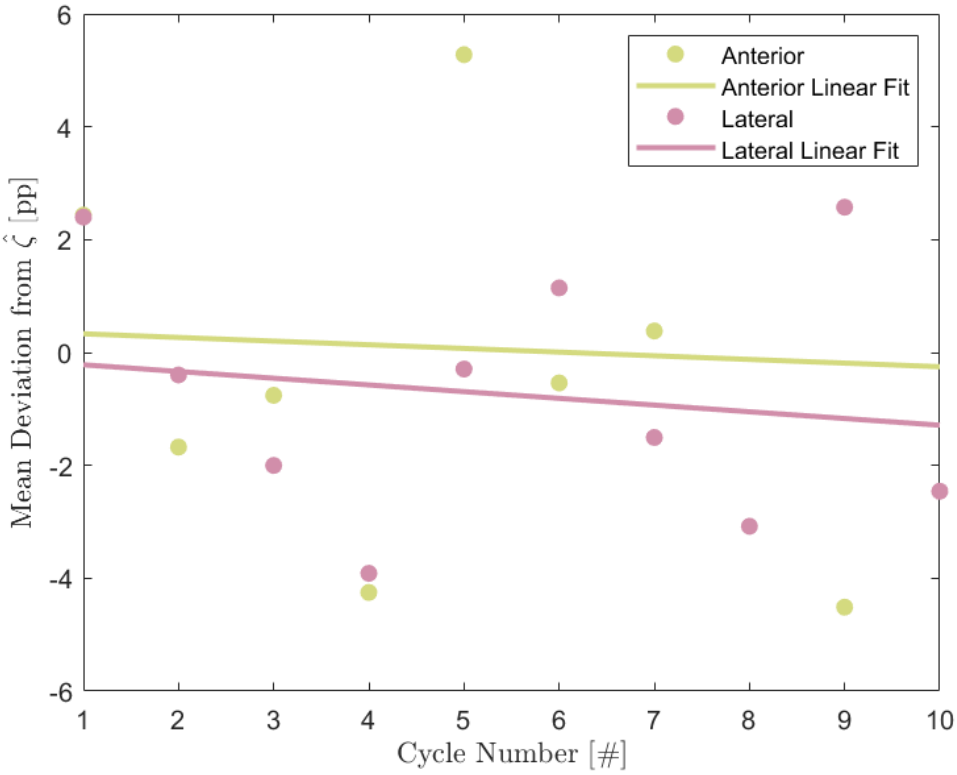

Figure A.7: **Garment Performance Stability:** Garment performance stability evaluated as the per cycle mean deviation of measured %-actuation contractions from the mean %-actuation contractions over all cycles. Linear fitting through the data collected for the anterior and lateral views shows a slow degradation of the garment's contractile ability.

Deviations of up to 6pp from the mean are reported. The linear fits calculated for the data in the anterior and lateral views reveal a marginal performance degradation in both views during these initial cycles. This degradation aligns with experimental data collected on a sample SMA knitted actuator with a wire diameter ($d = 0.203\,\mathrm{mm}, i_k = 138\,\mathrm{mm}^2\,\mathrm{mm}^{-2}$) as used in the self-fitting garment. The sample consisted of 15 loops in the wale- and course-wise directions. Performance degradation, i.e., a decrease in %-actuation contractions with increasing cycle numbers, occurs as the martensite knit length incrementally decreases while the austenite knit length increases. The rate of performance degradation decreases and stable performance is accomplished at a load- and geometry-dependent cycle number as shown in Figure A.8.

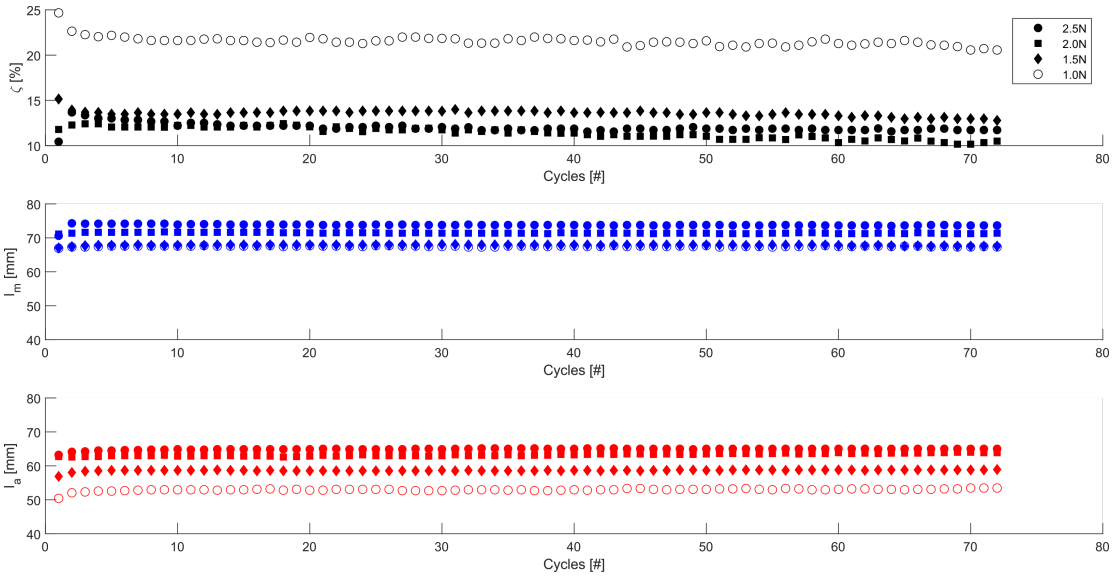

Figure A.8: **Cyclical Performance of SMA knitted actuators:** SMA knitted actuator performance stability evaluated under uniaxial loading under constant applied forces ($F_{app} = [1.0\,\text{N}, 1.5\,\text{N}, 2.0\,\text{N}, 2.5\,\text{N}]$). Plots show the %-actuation contraction (black), martensite knit length (blue), and austenite knit length (red) at the various cycles. Load-dependent cyclic performance degradation (%-actuation contraction) occurs through an increase of the austenite knit length and a decrease of the martensite knit length.

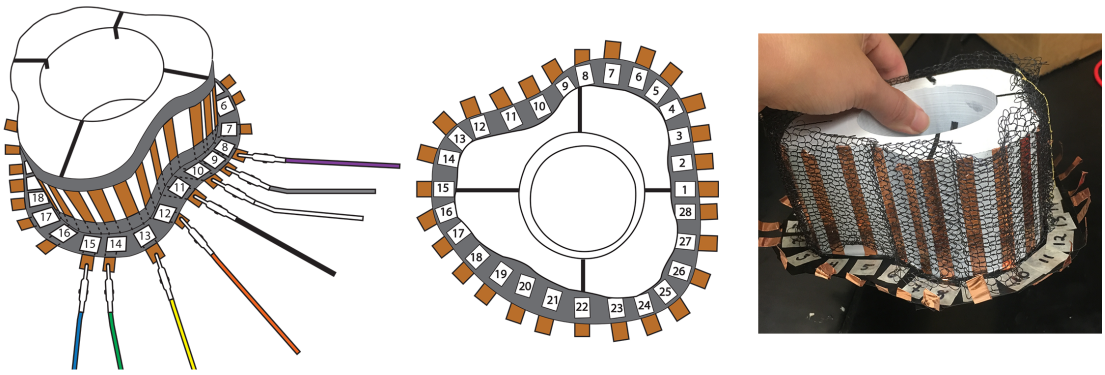

Figure A.9: **Contact Measurement Setup:** A custom setup was designed to accomplish contact sensing between SMA knitted actuator sleeves and the 3D printed leg cross-section to evaluate the fit (i.e., proximity) differences between the garment and the body across prototypes 1-3 (Figure 6.4a) through resistance measurement. An electrode was permanently connected to the sleeve being evaluated. Discrete, electrically conductive measurement points (MPs) (copper tape) were placed around the circumference of the leg cross-section (MP1 - MP28). The data acquisition device (NI-6341) was setup to collect 8 simultaneous resistance measurements at a time; therefore, MP1-8, MP8-15, MP15-22, MP22-1 for each sleeve prototype were collected in four different data collection trials.

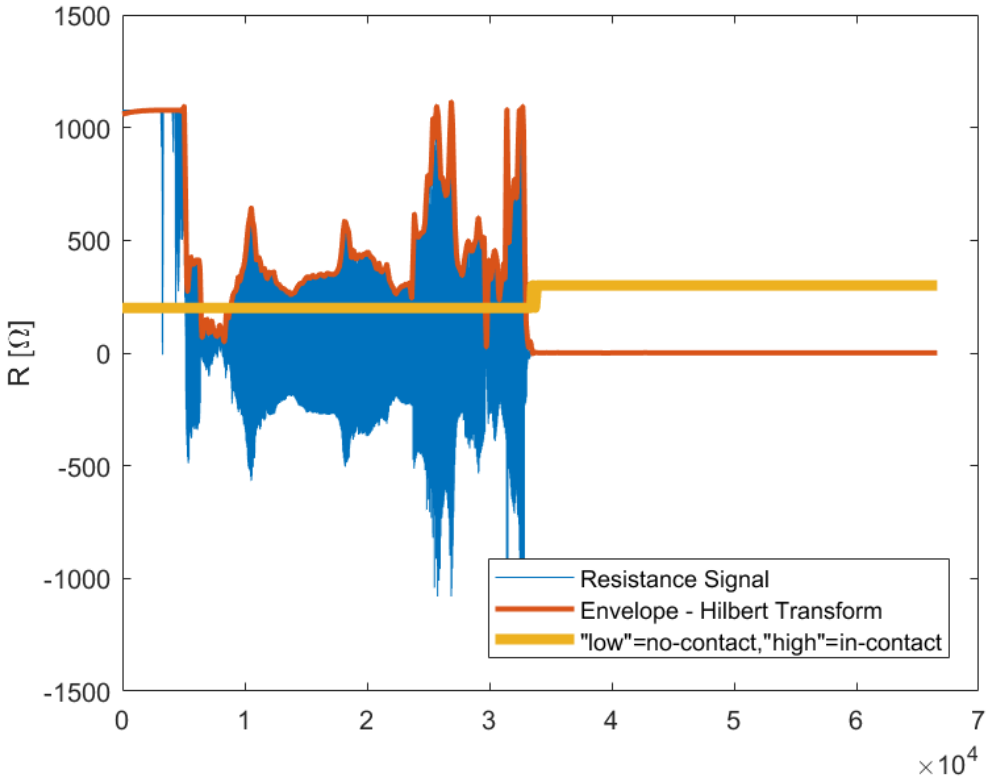

Figure A.10: **Contact Measurement Analysis:** Exemplary resistance measurement data (blue, sleeve 2, MP1) with highly unpredictable measurements before contact is established. Upon establishment of contact, the resistance value drops below 3 Ω. Hilbert transform is used to derive the upper envelope of the resistance signal (orange). The 3 Ω cut-off threshold is used to define the 'low'-no contact and 'high'-in contact levels (yellow). The entirety of the 'low'-no contact / 'high'-in contact plots is shown in Figure A.11. Upon data collection, a third contact condition "flutter" was defined as continuous switching between in-contact/no-contact levels.

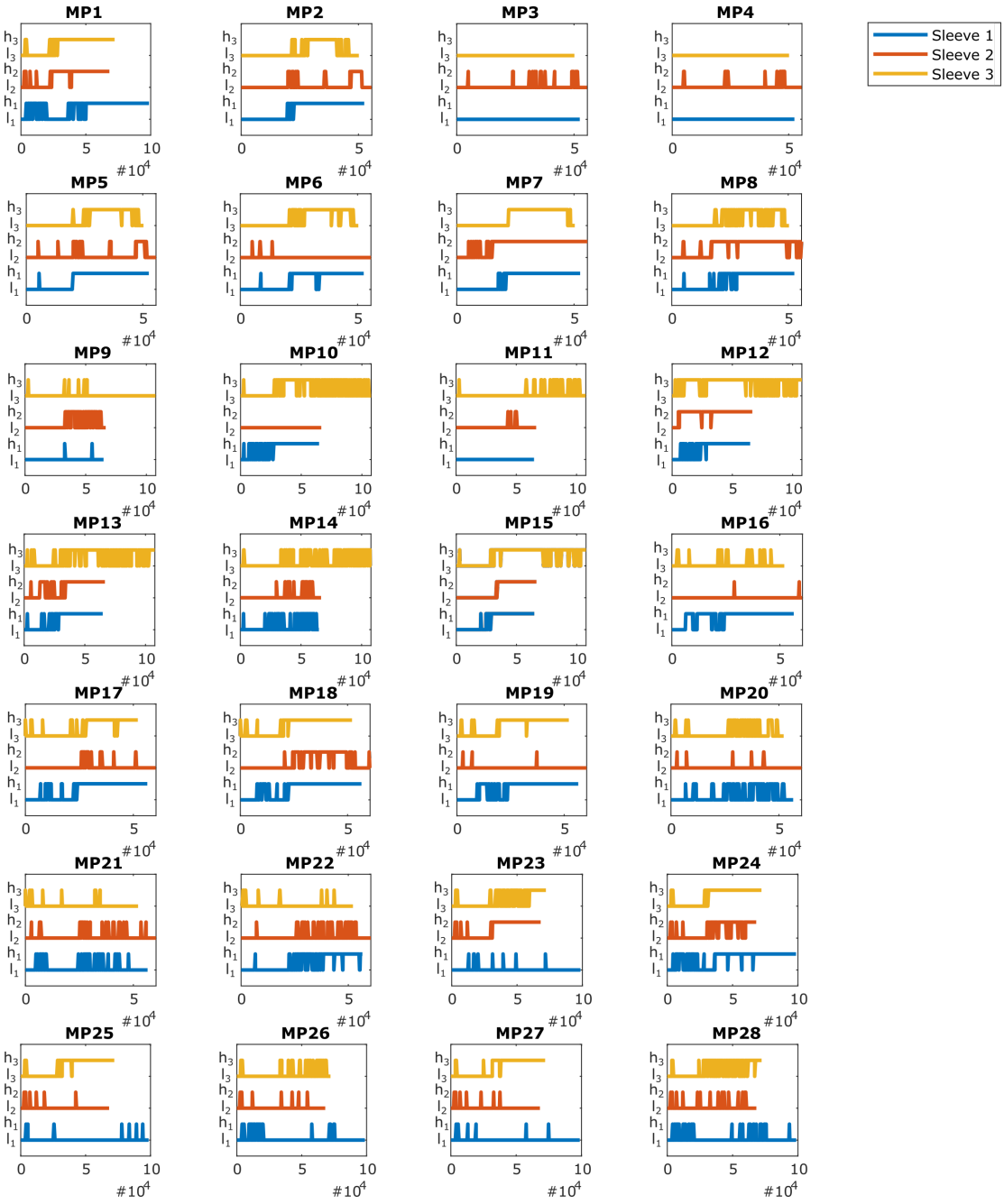

Figure A.11: **Contact Measurement Results:** Contact data from resistance measurements at the measurement positions MP1- MP28. 'Low'-no contact and 'high'-in contact levels are indicated for the three sleeves (Sleeve 1 - blue, Sleeve 2 - orange, Sleeve 3 - yellow). Flutter is defined as frequent changes between no-contact and in-contact levels.

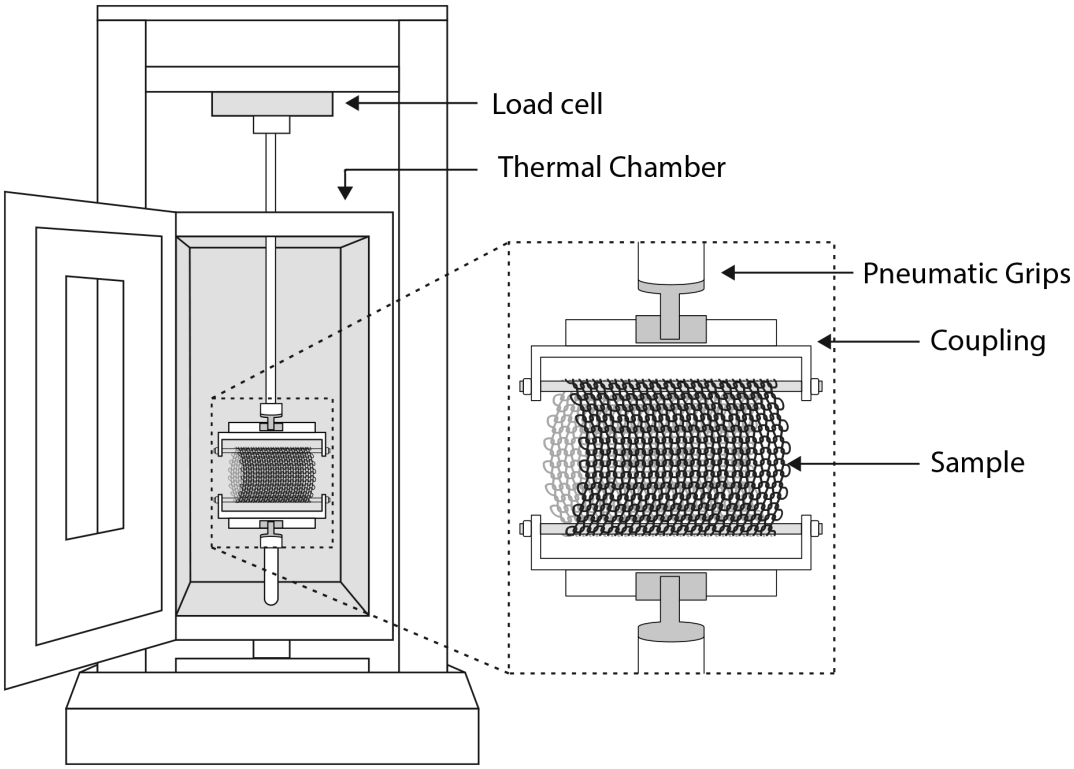

Figure A.12: **Instron Tensile Experiment:** NiTi tensile characterization for wire specimen as well as a prototype wrist sleeve were conducted in an Instron tensile testing machinse equipped with a 25-lb load cell (±1% of force reading from 1/200 to 1/500 load cell capacity) and housed in a thermal chamber. Wire specimen were gripped directly with pneumatic side-action grips pressurized to 50 psi. The prototype wrist sleeve required a mechanical couple that enabled the sample to loop around an upper and a lower rod. The setup allowed the sample to slide across the rods as needed in response to thermal-mechanical testing conditions.

A.3 Supplemental Materials for Chapter 7

A.3.1 Thermo-mechanical Training Procedure

The training procedure was conducted with a custom-built load frame housed inside an environmental chamber (Cincinnati Sub Zero). Length change was recorded with a linear encoder (250 CPI, US Digital) and temperature was measured with multiple k-type thermocouples. A load was applied to the sample while in a martensite state and the sample was subsequently exposed to 15 thermal cycles between 20 °C and 120 °C. The applied shakedown load was the load at which the particular SMA knitted actuator accomplished maximum work in prior characterizations ($F_{\hat{W}} = 1.7\,\mathrm{N},\ 90\,^{\circ}\mathrm{C},\ d = 0.203\,\mathrm{mm},\ i_k = 138\,\mathrm{mm}^2\,\mathrm{mm}^{-2},\ 15 \times 15$ loops, garter knit structure). [74] Figure A.13 depicts the thermo-mechanical training procedure for one prototype.

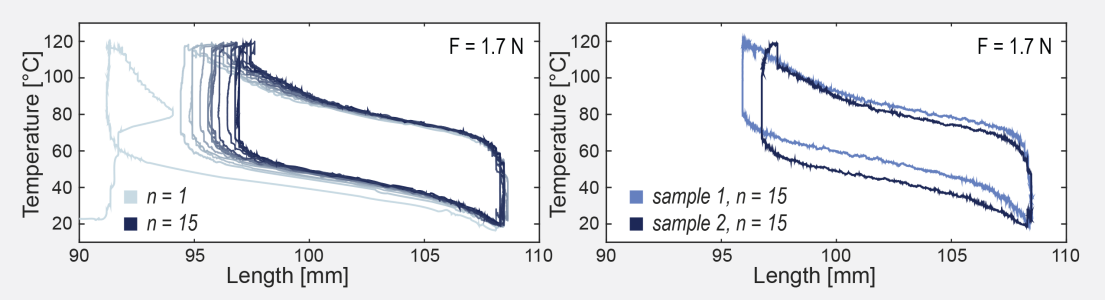

Figure A.13: **SMA Knitted Actuator Thermo-Mechanical Training:** (left) Shakedown response after 15 thermal cycles under applied load. (right) Length variation after between different manufactured samples at the end of the thermomechanical training procedure.

A.3.2 Rod-Beam-Model

In addition to the evidence in the literature and experiments that the force-increase behavior is caused by thermal expansion and contraction as a function of the NiTi temperature, an elementary model based on the fundamental beam and rod mechanics is presented. The model is intended to verify that the magnitude of force-increase observed in the experiment is plausible to be generated by thermal contraction.

The model simplifies the knitted loop into a connection of a rod and a beam (Figure A.14a) with a common Young's modulus (E), area (A), coefficient of thermal expansion

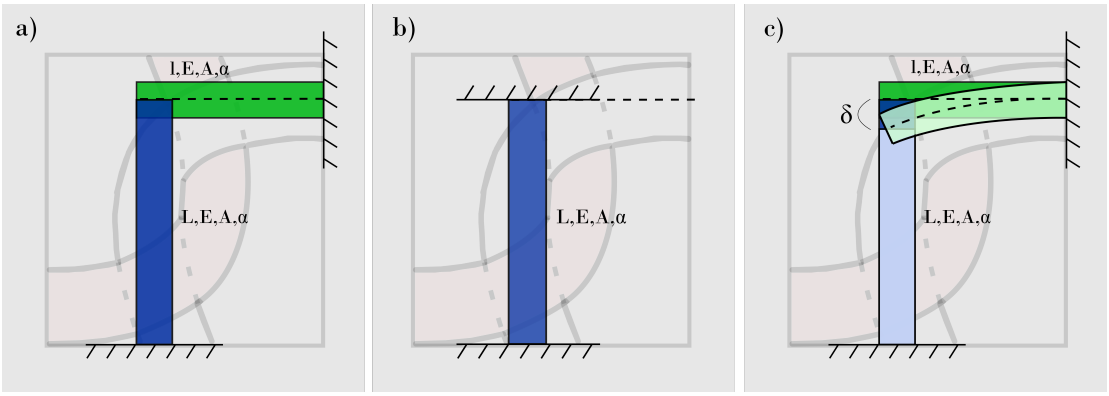

Figure A.14: **Rod-Beam Model Setup:** a) The model reduces the knitted loop to a rod of length (L), Young's modulus (E), area (A), and coefficient of thermal expansion (α) and a cantilever beam of length (l) which deform upon temperature changes. b) In a displacement-controlled rod, a force is generated upon cooling. c) This force provides the beam displacement required to accommodate the contraction of a free rod, as well as the characteristic force-increase upon cooling.

(α) and the beam length (l) and rod length (L). The displacement-controlled rod (Figure A.14b) generates a force

$$F_{r,\alpha} = \alpha \Delta\theta EA \tag{A.8}$$

upon the negative temperature change ($\Delta\Theta$). The same rod in a free-displacement configuration produces a contractile strain

$$\delta_{r,\alpha} = \alpha \Delta\theta L \tag{A.9}$$

under the same conditions. The force increase

$$F_{inc} = 2 \cdot n \cdot (F_{r,\alpha} - P) = 2 \cdot n \cdot \left(\alpha \Delta\theta EA - \frac{3\alpha \Delta\theta LEI}{l^3} \right) \tag{A.10}$$

is modeled as the difference between the contractile force $F_{r,\alpha}$ of the rod and the force (P) required to displace the cantilever beam to the displacement of the free rod. The determination of the lengths of the rod (L) and the beam (l) can be conducted through imaging, however, differences between loops can be relatively large. To investigate the plausibility of the force-increase based on thermal contraction, the Force increase is plotted against the ratio (l/L) and the rod length (L) in Figure A.15. The Young's

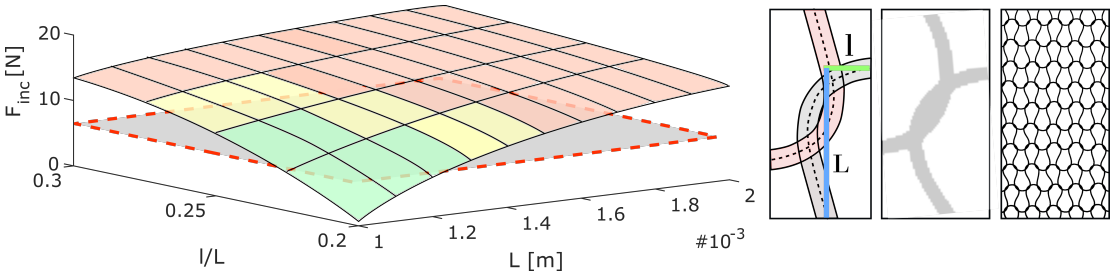

Figure A.15: **Rod-Beam Model Results:** The solution plane for the rod-beam model supports that thermal contraction produces force increases of the magnitude experimentally-obtained.

modulus ($E = E_A = 75\,\text{GPa}$) of austenitic NiTi, the area (A) and second moment of area (I) for a round cross-section of diameter ($d = 0.203\,\text{mm}$), the coefficient of thermal contraction ($\alpha = 8 \cdot 10^{-6}\frac{1}{\text{K}}$), and the temperature change ($\Delta\theta = -60\,\text{K}$) are inputs to the model. The solution plane for the variable beam and rod lengths shows the increase of the generated force F_{inc} as the rod length and the rod-beam-ratio increase. A combination of the rod length ($L = 1.3\,\text{mm}$) and a beam-rod-ratio ($l/L = 0.27$) produces a force-increase ($F_{inc} \approx 7\,\text{N}$) which represents a realistic simplification of the loop geometry and matches the experimental force-increase.

Appendix B

Appendix B

B.1 Biographical Sketch

Kevin was born in Karlsruhe, Germany in 1992, in a suburb of which he grew up before attending Karlsruhe Institute of Technology for his B.Sc. in Mechanical Engineering in 2011. After completing engineering internships at Edelstahl Rosswag GmbH and Volkswagen AG, he moved to the United States to live with his wife Julie and attend graduate school at the University of Minnesota. Through enjoying research at the Design of Active Materials and Structures Laboratory during the first year of his master's degree studies, Kevin decided to join the PhD program under the direction of Dr. Julianna Abel. From 2015 to 2020, Kevin worked as a research and teaching assistant at the University of Minnesota, where he conducted the research detailed in this thesis.